The Control of Solidification Kinetics of the Vacuum-cast Thin-wall Nickel-based Superalloys by Changing the Geometrical Characteristics of the Ceramic Mold

R. Cygan[a]*, D. Szeliga[b], P. Rokicki[b], J. Sieniawski[b], J.S. Suchy[c]

[a] Investment Casting WSK „PZL-Rzeszów" S.A.
[b] Rzeszow University of Technology
[c] AGH University of Science and Technology Krakow
* Corresponding author E-mail address: rafal.cygan@wskrz.com

Abstract

This paper provides an analysis of experimental research and results of investment casting process. Temperature field in a ceramic mold is one of the problems during numerical simulation. Reducing the costs of production in precision casting involves the reduction of scraps, which is one of the fundamental problems of the foundry industry. Reducing these costs is associated with optimization of precision casting technology of aircraft engines critical parts, including control of the solidification front in thin-walled castings of nickel super alloys cast in a vacuum. It is achieved by changing the geometrical characteristics of the ceramic mold. The results of the tests were used to optimize the industrial production of aircraft components in Precision Foundry of WSK Rzeszów. Temperature distribution gained in the conducted tests allowed verification and optimization of computer simulations.

Keywords: Nickel-based superalloys, Ceramic mold, Thin-walled castings, Investment casting

1. Introduction

The important technological problems occurring in the production of nickel-based superalloy casts include: developing conditions for pouring and solidification of casting and, what's involved, determining the effect of all factors on the orientation of the liquid metal solidification front and the cooling of it [1-3].
The problem of defects appearance in precision castings, despite the use of advanced technology, is not yet solved. There is no comprehensive study and evaluation of changes in temperature field in the cross-section of the ceramic mold during annealing, pouring and solidification processes of molten metal in the area of

thin-walled castings, such as the trailing edge of nickel-based superalloy blades cast in vacuum. These elements are used in low-pressure turbine aircraft engines. Lack of an access to knowledge about the distribution of temperature in the cross section of the ceramic mold during annealing, casting, solidification and cooling of the casting makes it impossible to determine the causes of defects, especially in thin-walled castings. This is due to a reserve of technological knowledge by global foundries which produce components for hot engines. In many precise foundries it is necessary to address these issues in case of changing types of castings as well as in the introduction of new types of materials [4-8].

The results of researches will allow to determine a precise effect of the ceramic layer thickness (the number of layers made) on the ceramic mold temperature distribution during annealing process as well as during the pre-filling process and solidification of nickel-based superalloy super thin-walled cast components. These data are necessary to determine the impact that the change of geometrical characteristics has on the temperature distribution of the ceramic mold. Hence, also on the direction of the solidification front. Obtained results will also be helpful to determine the correct annealing time of the ceramic mold. This knowledge will significantly contribute to the labour reduction, thus, to a substantial reduction of the cost of manufacturing of casting, not just airlines ones, but also other casting machine components manufactured by precise casting.

2. Methodology

The molds were performed at the precise foundry WSK PZL Rzeszów. Methodology for the molds execution was similar as in the case of production ones keeping all the process parameters so that the molds were made as similar as possible to the production ones in the means of physico-chemical properties.

Two model sets for casting wax plates were designed and built with dimensions shown in (Fig. 1). The shape of this cast provides enough flat surface for the precise placement of thermocouples. Four wax models with H-type gating system were combined into a model set. In order to stabilize and strengthen the model set and for better wax melting, 4 vents were applied in a further stage (Fig. 2a).
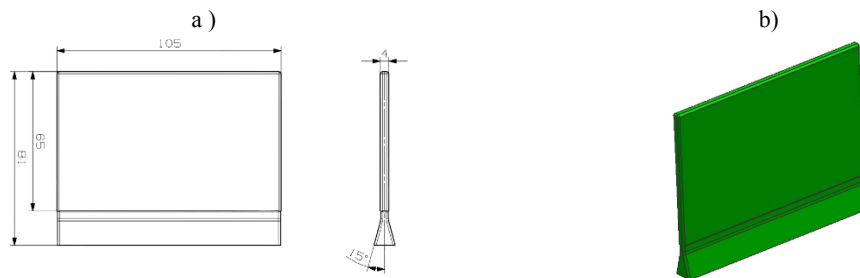

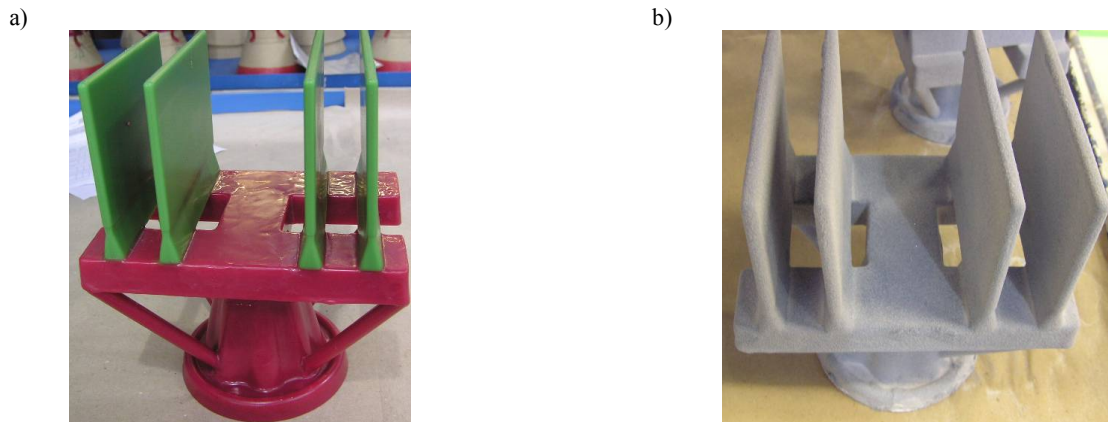Fig. 1. Plates models a) geometrical dimensions, b) 3D model

Fig. 2. a) Wax model set b) ceramic mold - after first layer application

Two wax sets formed the basis for the implementation of multi-layer ceramic molds. Ceramic molds were made with the use of alcohol coating. For the first layer $CoAl_2O_4 + ZrSiO_4$ were used (Fig.2b). This layer is characterized by good thermal conductivity and durability, and prevents the reaction of molten metal with a ceramic material. Afterwards, the next layers were applied with placing thermocouples: Thermocouple #1 after 2nd layer, thermocouple # 2 after 3rd layer, thermocouple #3 after 4th layer and thermocouple #4 after 7th layers. Two molds fabricated with 9 and 11 layers coated. B-type thermocouples with 0.8 mm wire diameter were used for the measurement.

a)

Thermocouples 3 and 4 mounting places
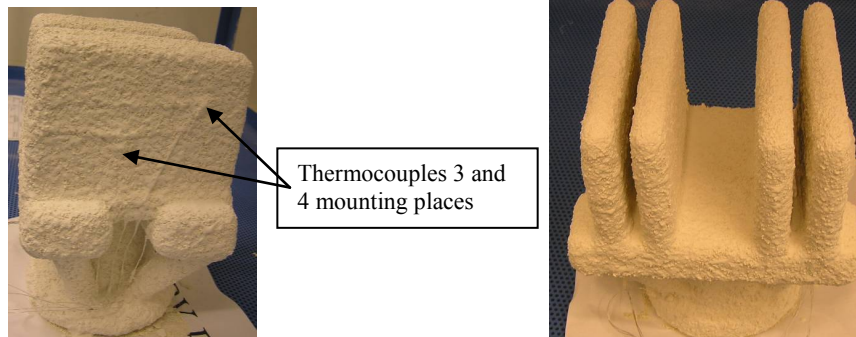
b)

Fig. 3. Ceramic mold a) with 9 ceramic coatings, b) with 11 ceramic coatings

When all the sets of ceramic layers were ready, the assembly was dried for 48 hours at a suitable temperature and humidity. After drying the ceramic mold was placed in high-pressure autoclave to fuse out the wax. Pre-annealing was performed at 600°C for 2 h in order to remove the wax model residue. Then, insulating of the mold and pouring were performed (Fig. 4).

The solidification process of nickel-based superalloy IN713C castings was performed in Research and Development Laboratory for Aerospace Materials at Rzeszów University of Technology, in a vacuum oven VIMIC 2 E - DS / SC produced by ALD Vacuum Technologies company. 6 kg load was inductively melted in vacuum - 2x10-3 [Pa]. Ceramic mold was placed in the heating chamber of the furnace and annealed at 1250°C in 110 min time. The molds were poured with nickel-based superalloy IN713C at a temperature of 1470°C and moved from the heating to cooling zone of the furnace in about 10 seconds. Afterwards, the cooling chamber was ventilated in about 60 seconds. The molds were cut (Fig. 5) removing the remains of the ceramic mold.

a)   b)
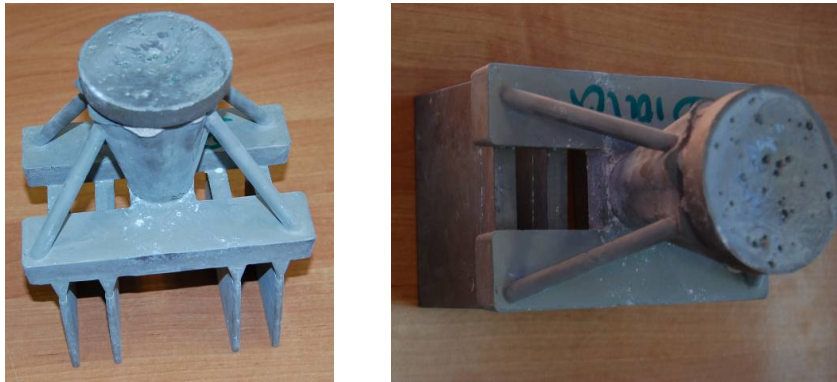

Fig. 4. a) insulated ceramic mold, b) mold after pouring

Fig. 5. Molds after pouring with molten metal and the removal of ceramics.

3. Results and discussion

After the experiment, the temperature change on the cross-section of the mold during annealing, pouring, solidification and cooling was received. Depending on the quantity of the ceramic layers in the mold, temperature distribution was as follows (Figures 6-8):
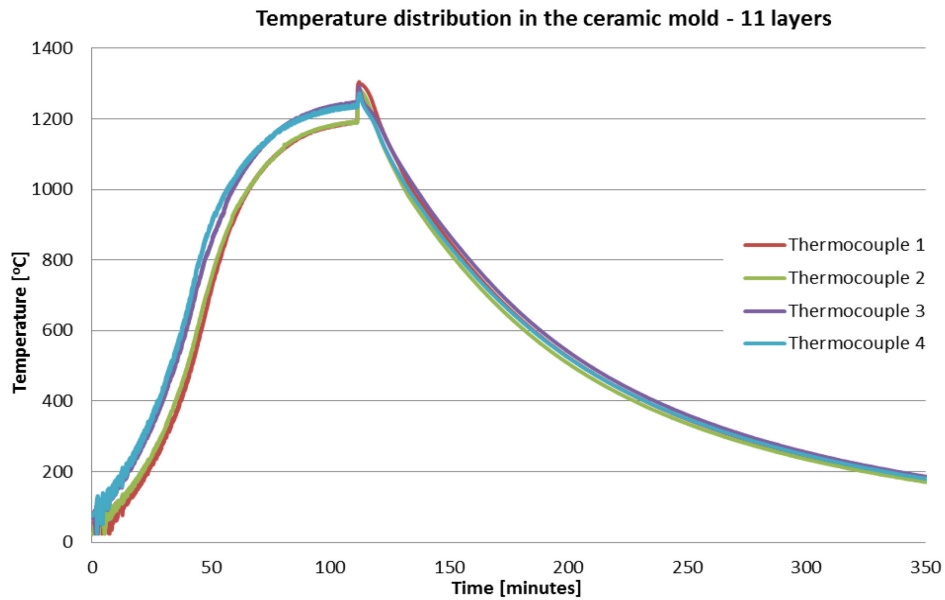

Fig. 6. Temperature distribution in the ceramic mold - 11 layers
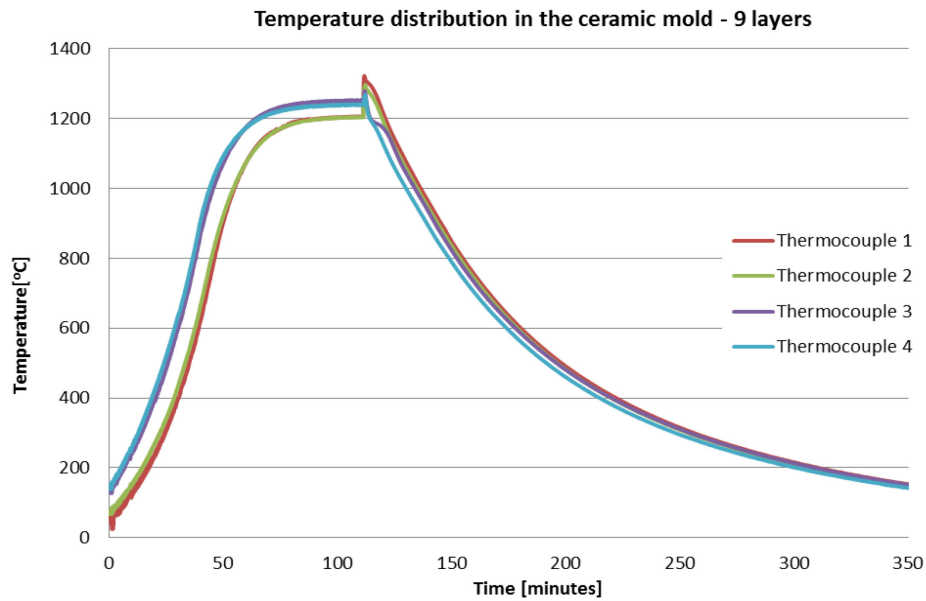
Temperature distribution in the ceramic mold - 9 layers

Fig. 7. Temperature distribution in the ceramic mold - 9 layers
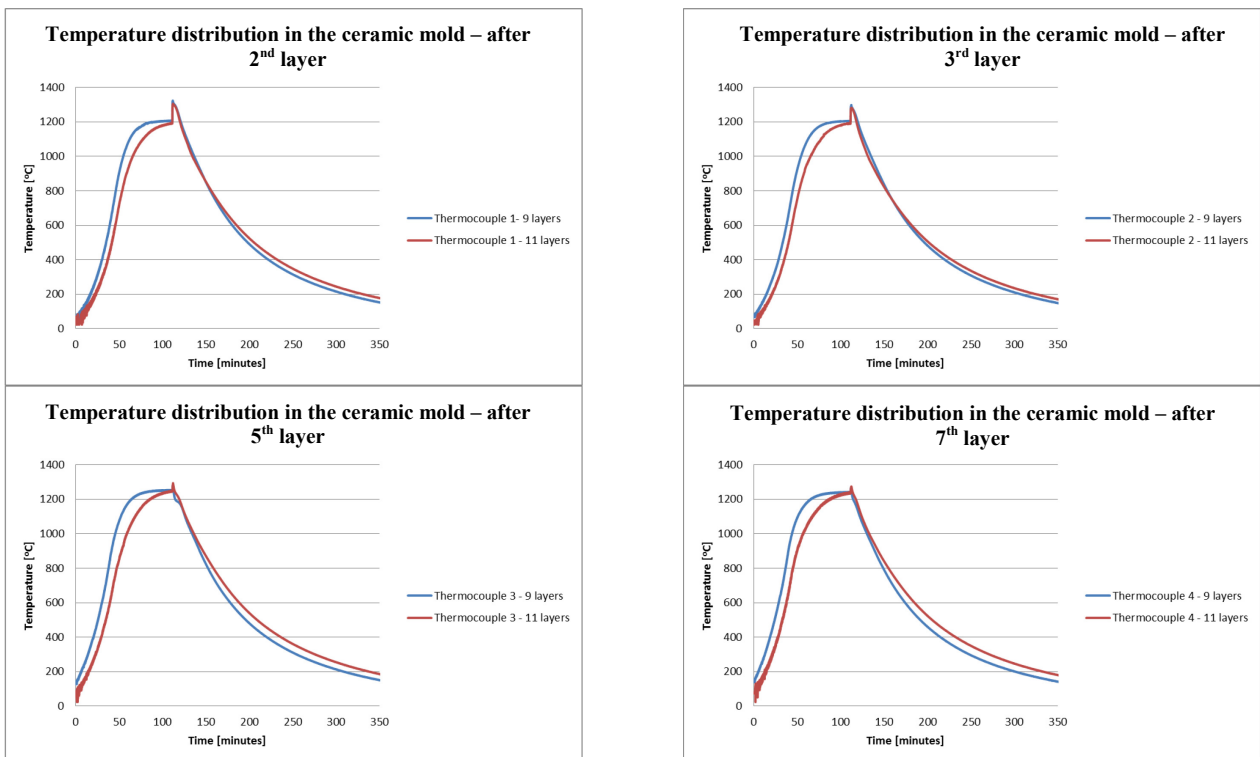
Fig. 8. Comparison of temperature distribution in the ceramic molds

The next step was to analyse the distribution of temperature on the cross-section of the ceramic mold during annealing, pouring of molten metal, solidification and cooling (Fig. 9). The aim of the study was:

a) Determination and comparison of the temperature distribution in tested ceramic molds during annealing process after 30, 45, 60, 75 and 90 [min].
b) Determination and comparison of the temperature distribution in tested ceramic molds during pouring of molten metal.

c) Determination and comparison of the temperature distribution in tested ceramic molds during solidification and cooling processed after 0 [s], 63 [s], 93 [s], 123 [s], 153 [s], 213 [s], 49 [min] 89 [min], 189 [min] and 268 [min] from the moment of molten metal pouring.

Temperature distribution after 30 minutes heating

Temperature distribution after 45 minutes heating

Temperature distribution after 60 minutes heating

Temperature distribution after 75 minutes heating

Temperature distribution after 90 minutes heating

Temperature distribution while pouring after 111 minutes

Temperature distribution after 30 seconds since filling

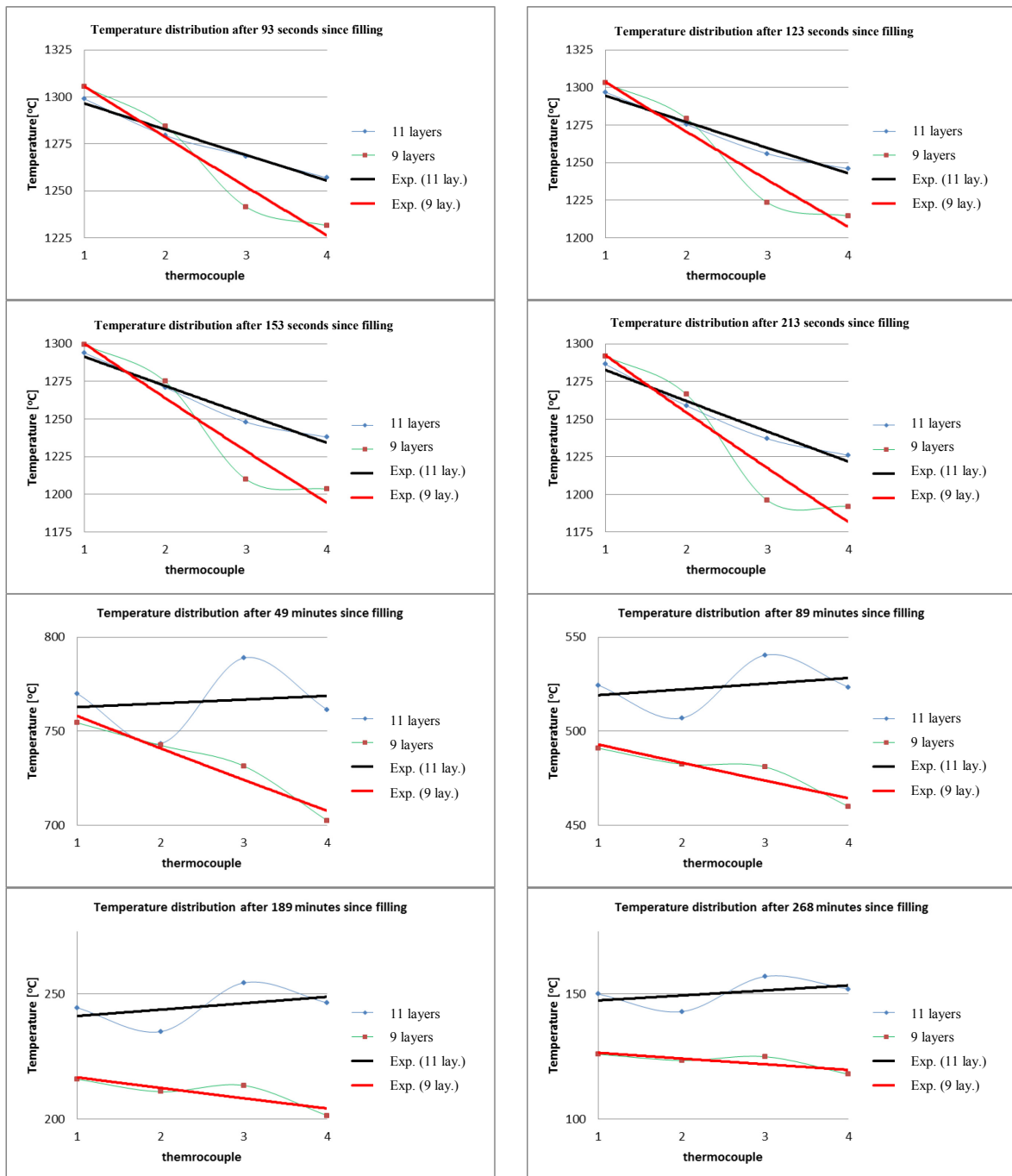Temperature distribution after 63 seconds since filling

Fig. 9. Comparison of the temperature distribution in the studied sections of the ceramic molds

4. Summary

As a result of the experiment, the temperature distribution curves of ceramic molds with 9 and 11 layers (shells) were made. These curves allowed to determine the effect of selected geometric features changes on the temperature distribution in the studied ceramic mold system, during annealing, pouring, solidification and cooling processes.

In the molds with 9 ceramic layers after 80 minutes of heating, temperature had been stabilized, however, it had not reached the ambient temperature (1250°C) throughout the section.

In the molds with 11 ceramic layers after 110 minutes of heating, temperature had been stabilized, however, it had not reached the ambient temperature (1250°C) throughout the section.

The temperature difference in the molds while pouring was slightly higher for the mold with 9 ceramic layers.

The maximum temperature recorded by the measuring system during pouring was 1305°C for 11 layers and 1322.5 ^{o}C for 9 layers.

For the mold with 9 layers a much larger temperature gradient was observed.

Mold with 9 layers cools down much faster by handing over the accumulated heat to the surroundings.

The results of the tests were used to optimize the industrial production of aircraft components in Precision Foundry of WSK Rzeszów. Temperature distribution gained in the conducted tests allowed verification and optimization of computer simulations. The results will also be used when designing the ceramic molds for new implemented products.

Acknowledgements

References

[1] Cygan, R., Sobczak, N. & Suchy, J.S. (2010). Thermal and physical properties of nickel superalloy and ceramic mold used for computer simulation. *International Foundry Research, 62, No.1,* 30 – 34.

[2] Cygan, R., Sobczak, N. & Suchy, J.S. (2009). Interaction: Ceramic mold – metal in nickel superalloy casting. *International Foundry Research, 61, No.3,* 16 – 21.

[3] Furgał, G. & Cygan, R. (2009). Quality problems root cause identification and variability reduction in casting processes. *Archives of Foundry Engineering, Volume 9, Issue 1/2009,* 13 – 16

[4] Budzik, G., Matysiak, H., Cygan, R., Bąk, S. & Cygnar, M. (2010). Rapid prototyping process of monocrystal aircraft engine blades. *Journal of Kones Powertrain and Transport*, Warszawa, 81-86

[5] Moskal, G., Cwajna, J., Bińczyk, F., Cygan, R., Witala, B. (2010). Influence of measurement results of thermal conductivity and heat transfer coefficients on the simulation results of casting process of aircraft engine elements made of monocrystalline and directionally crystallized superalloys, 6th International Conference on Diffusion in Solids and Liquids: Mass Transfer, Heat Transfer and Microstructure and Properties, DSL 2010, Paris, France 5-7 July, pp. 266

[6] Sieniawski, J. (2002). Development of design methods and the assessment of the microstructure and properties of structural materials for aircraft technicians, Red. M. Hetmańczyk: *Postępy nauki o materiałach i inżynierii materiałowej*. Wyd. Pol. Śląskiej, Katowice (in Polish),

[7] Sieniawski, J. (1995). *Criteria and methods of evaluation of the components of turbine aircraft engines*, Oficyna Wydawnicza Politechniki Rzeszowskiej, Rzeszów

[8] Beeley, P.R., Smart, R.F. (1995). *Investment casting*, University Press, Cambridge UK,

Original Research Article

Analysis of temperature distribution in shell mould during thin-wall superalloy casting and its effect on the resultant microstructure

Łukasz Rakoczy [a,*], Rafał Cygan [b]

[a] AGH University of Science and Technology, Faculty of Metals Engineering and Industrial Computer Science, Department of Physical and Powder Metallurgy, Mickiewicza 30, 30-059 Cracow, Poland
[b] Consolidated Precision Products, Investment Casting Division CPP-Poland, ul. Hetmanska 120, 35-078 Rzeszow, Poland

ABSTRACT

This work focuses on the influence of temperature distribution in a shell mould during investment casting of thin wall parts on macrostructure, chemical composition of microstructural constituents and γ/γ' misfit parameter. A reduction of production costs is associated with the optimization of precision casting technology of aircraft engine critical parts, including control of the solidification front in thin-walled castings of nickel superalloys.

Appropriate lost-wax casting parameters lead to the creation of coarse grained structure, desired for high-temperature service applications. As a result of non-equilibrium solidification, substantially large chemical inhomogeneities in the dendrite core and interdendritic spaces are formed. Interdendritic spaces are occupied by constituents formed as a consequence of segregation of alloying elements, namely eutectic islands γ/γ', borides, carbides, and an intermetallic compound of Ni and Zr. Dendrite cores consist of cubic-shaped γ' precipitates surrounded by Ni-rich γ channels. Low lattice misfit influences cubic morphology of γ' precipitates, which is favourable for jet engine application because it can guarantee good creep resistance.

1. Introduction

Precipitation strengthened nickel-based alloys called also superalloys are widely used in the aerospace industry as components in the hot section of engines. Today, the construction of aircraft engines without the use of materials from this group is impossible, as evidenced by the fact that nearly half of the mass of currently produced units are nickel alloys [1,2]. One of the representatives of this group is Inconel 713C, precipitation strengthened by the γ' intermetallic phase. This alloy is extensively use in the aerospace, but also in the energy and oil & gas industries due to its unique combination of high strength at service temperature, excellent oxidation and hot corrosion resistance. This exceptional set of mechani-

cal properties originates from many alloying elements like Nb, Al and Cr that create a solid solution and precipitation strengthening, and also the creation of protective layer of oxides on the inner surface. Normally, nickel superalloys, after the casting process, are subjected to heat treatment (solution + ageing), however Inconel 713C achieves high properties directly after casting i.e. in the ''as cast'' condition [3,4]. Optimization of the casting process is therefore crucial to achieving much higher mechanical properties than in previously produced parts. Investment casting, also known as lost-wax casting, is the only commercially used technique for fabrication of turbine blades and vanes which are one of the most important structural components of jet engines [5,6]. Manufacturing of such complex components is always a great challenge. Increased efficiency of engines can be obtained with new more complex geometry and thinner walls. Innovations, however, are impeded by the complexity of the fabrication process, which leads to an increasing amount of metallurgical discontinuities. These parts have to fulfill strict quality requirements in order to withstand high mechanical loads at temperature even up to 1050 °C for several thousand hours [7,8]. One of the most important steps in the investment casting process is shell fabrication, because, during the solidification, the interfacial heat transfer between the metal and the shell mould is ones of the most important factors that influence the microstructure and strength of resulting casting product [9]. Example of the geometry which is usually chosen to produce testing plates for microstructural and thermal analysis is H-type gating system like in Fig. 1.

One of the basic technological problems is cracking and deformation of ceramic mould at high temperature, whereas the main influence is the type of material that is used and the shape of mould. Results of the research will allow determining the precise effect of the ceramic layers thickness (the number of layers) on the temperature distribution in the shell mould during preheating, as well as during the pouring and solidification of nickel-based superalloy thin-walled casting. These data are necessary to determine the influence of the geometrical characteristic of the mould on temperature distribution, hence, also on the solidification process. Obtained results will also be helpful to determine the correct preheating time of the mould. This knowledge will contribute to a substantial reduction of the cost of manufacturing of casting, not just in the aviation industry, but also other castings of machine components.

There is still is a lack of information about influence of shell mould design, the temperature distribution in moulds and casting parameters on the microstructure of equiaxed Ni-based superalloys. Scientific papers focus on cracking during welding, the influence of pouring temperature on microstructure and degradation during creep but reports about the relation of temperature distribution in shell moulds to microstructure is still rare [10,11]. The aim of work was to investigate the influence of temperature distribution in a shell mould during investment casting on microstructure and misfit γ/γ′ parameter of Inconel 713C superalloy.

2.   Experimental procedure

The Inconel 713C nickel superalloy was used as the experimental casting and the gating system. The material was provided by Canon Muskegon Company. Result of chemical composition analysis obtained by optical emission spectroscopy (OES) is presented in Table 1. The mould was prepared in the Investment Casting division of CPP Corp. and all
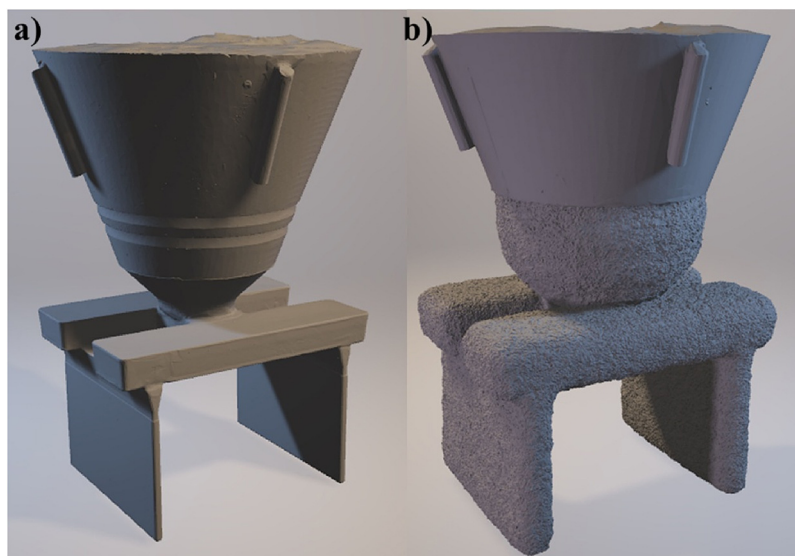

Fig. 1 – Geometry of wax model: (a) before; (b) after coating.

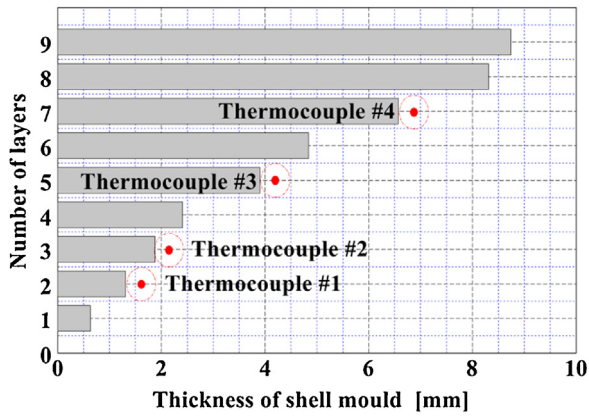| Table 1 – Chemical composition of Inconel 713C.												
Element	Cr	Al	Mo	Nb	Ti	C	Zr	Co	B	S	P	Ni
wt.%	14.24	5.93	4.29	2.45	0.92	0.11	0.08	0.04	0.012	0.003	0.004	Bal.

Fig. 2 – Number of layers and location of thermocouples.

technological conditions were as similar as possible to internal standards accepted by aerospace customers.

A model set for casting wax plates was designed and built with plate dimensions 105 mm × 65 mm × 4 mm. The shape of this casting provides enough flat surface for the precise placement of thermocouples. Wax models with H-type gating system (like in Fig. 1) were combined into a set. Wax set formed the basis for the implementation of multi-layer ceramic mould. In order to stabilize and strengthen the model set and for better wax melting four vents were included in a further stage. The shell mould was fabricated by the "dip and stucco" technique. The ceramic mould was made with $ZrSiO_4$ matrix and an alcohol-based coating. The layer is characterized by good thermal conductivity and durability and prevents a reaction of molten metal with a ceramic material. As a shell mould backup alumina silicate powders were applied.

ATOS Triple Scan III device scanned the wax model on which each of the nine layers was deposited (Fig. 2). Results of measurements and location of the thermocouples are presented in Table 2. B-type (PtRh30–PtRh6) thermocouples with 0.8 mm wire diameter were used for measurement. The junctions of thermocouples were located parallel to the surface of plate casting (in the middle region of the plate).

(a) The first thermocouple was mounted in the middle of external plate surface after application of the second layer. Subsequently, the model was scanned by a high resolution, optical device.

(b) The second thermocouple was mounted in the middle of external plate surface after application of the third layer. Subsequently, the model was scanned by a high resolution, optical device.

(c) The third thermocouple was mounted in the middle of external plate surface after application of the fifth layer.

Subsequently, the model was scanned by a high resolution, optical device.

(d) The fourth thermocouple was mounted in the middle of external plate surface after application of the seventh layer.

The procedure of layering is widely known in the foundry industry. The first thermocouple was fixed at about 1.31 mm from the wax model, the next about 1.88 mm, the third at ~3.9 mm and the fourth ~6.57 mm from the pattern. All activities connected with the preparation of mould and measurements were performed by a foundry engineer. When all the sets of ceramic layers have been deposited, the assembly was dried for 48 h at suitable temperature and humidity. After drying the ceramic mould was placed in a high-pressure autoclave to dewax. Pre-annealing was performed at 600 °C for 2 h in order to remove the wax model residue. The pouring process of casting was performed in the Research and Development Laboratory for Aerospace Materials at the Rzeszow University of Technology in a vacuum oven VIMIC2E – DS/SC produced by ALD Vacuum Technologies company. The 4 kg IN713C ingot was inductively melted in vacuum of 2×10^{-3} Pa. The ceramic mould was placed in the heating chamber of the furnace and preheated at 1250 °C for 127 min. The liquid metal was poured at 1470 °C and moved from the heating to cooling zone of the furnace in about 10 s. Afterwards the cooling chamber was ventilated in about 60 s.

The surfaces of the cast plates were cut from the assembly, then sand blasted and macroetched with a No. 17 Etch solution (0.75 g molibdic acid, 25 ml nitric acid, 25 ml hydrohloric acid, 25 ml water). Images were captured by microscope Optimus, and then analyzed by ImageJ commercial software. Following stereological parameters were calculated: the mean area, size, perimeter and number of grains per mm^2. Microstructure investigation was performed by light (etching in No. 17 Etch) and with a scanning electron microscopy (electrochemically etched in 10% CrO_3 solution) equipped with EDS spectrometer. For the imaging and EDS analyses, a 20-kV accelerating voltage was applied. Based on the results segregation coefficient k for the selected alloying elements was determined. X-ray diffraction was carried out on a Siemens/Bruker D5005 device and Cu K_α ($\lambda = 0.15418$ nm) radiation source. The angles were read off from the positions of the peaks on a diffractogram and the interplanar spacings d_{khl} were calculated using the Bragg–Wulff equation (Eq. (1)). Based on the computed lattice parameter of matrix a_γ and precipitates γ' $a_{\gamma'}$ (Eq. (2)), the γ/γ' misfit coefficient (Eq. (3)) was determined.

$$d_{hkl} = \frac{\lambda}{2 \sin \theta} \tag{1}$$

Table 2 – Thickness of layers and location of thermocouples.

No. of layer	1	2	3	4	5	6	7	8	9
Mean value of thickness (mm)	0.63	1.31	1.88	2.41	3.90	4.84	6.57	8.31	8.74
Standard deviation (mm)	0.19	0.27	0.34	0.60	0.68	0.79	0.94	1.39	1.16
Number of thermocouple		1	2		3		4		
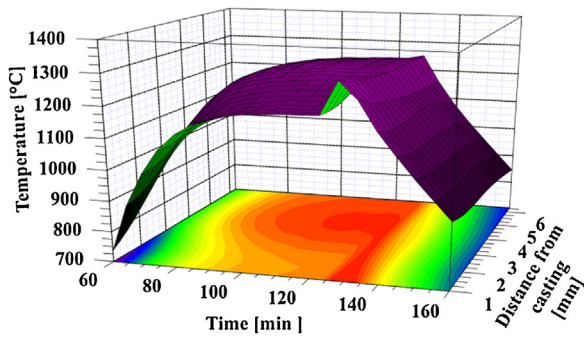
Fig. 3 – Distribution of temperature in shell mould.

Table 3 – Registered temperatures after 50, 100, 130 and 150 min.

Time (min)	Thermocouple	1	2	3	4
		Temperature (°C)			
50		479	515	691	729
100		1194	1192	1244	1231
130		1298	1273	1206	1201
150		1028	1010	998	956

$$a = \frac{\lambda \sqrt{h^2 + k^2 + l^2}}{2 \sin \theta} \qquad (2)$$

$$\delta = \frac{2(a'_\gamma - a_\gamma)}{a'_\gamma + a_\gamma} \qquad (3)$$

3. Results and discussion

3.1. Temperature distribution in shell mould

The temperature distribution recorded during the casting process, i.e. during preheating, pouring, crystallization and cooling is shown in Figs. 3 and 4. The designed preheating temperature was 1250 °C and, in order to ensure a uniform temperature in the inner layers of mould, preheat time of 127 min chosen. In Table 3 temperature information originating from thermocouples after 50, 100, 130 and 150 min is presented. After 50 min, the difference between the highest and lowest temperature recorded was almost 250 °C. Experimental data show that after about 100 min the temperature inside the mould stabilized at all measuring points and the difference between the lowest and the highest temperature was barely over 50 °C. The heating rate in the 0–100 min range was between 11.69 and 12.31 °C/min (initial temperature of 25 °C). Taking into account the stabilization of the temperature after 100 min, the preheating time could be considerably shortened. Immediately after preheating, the liquid metal at 1470 °C was poured into the shell mould. After approximately 10 s from

pouring, the shell mould was withdrawn from the heating area to the cooling chamber of the furnace. The maximum temperature recorded by thermocouples were: (1) 1322 °C, (2) 1297 °C, (3) 1279 °C and (4) 1268 °C. The difference between the highest and the lowest is 54 °C, while during the crystallization the difference increased even to nearly 100 °C after 130 min. The decrease of temperature below the liquidus and with sufficient undercooling leads to the nucleation of γ phase in the liquid phase. Based on differential thermal analysis (DTA) [12] the solidification of IN713C occurs in the range 1342–1263 °C, while the maximum of the exothermic peak is at 1338 °C.

Szeliga [13] described the solidification path of Inconel 713C for similar casting parameters using thermocouples mounted inside shell mould. He indicated that the solidification of γ phase starts at 1327 °C (liquidus temperature) and lasts for about 41 s. After about 160 s at 1300 °C, the precipitation of the γ′ phase in the form of γ/γ′ eutectic islands begins. The end of the solidification process takes place after about 222 s at 1240 °C (solidus temperature), and so is lower by 23 °C compared to the DTA results [12]. The precipitation of the γ′ phase takes place in the solid state from a supersaturated γ matrix after about 258 s at 1173 °C and ends after 426 s at 1004 °C. In this work, after about 135 min, the temperature drop stabilized, whereas cooling rate between 128–300 min, to approximately 225 °C, was in the range 5.0 °C/min (thermocouple 4)–6 °C/min (thermocouple 2). The temperature drop at all measuring points also stabilizes after about 7 min, i.e. after the end of the precipitation processes.

3.2. Macro, microstructure and chemical composition of constituents in the Inconel 713C superalloy

Long-term service of nickel superalloy at high homologous temperature, at which gas turbine components are exposed to degradation through creep, requires forming a coarse grained
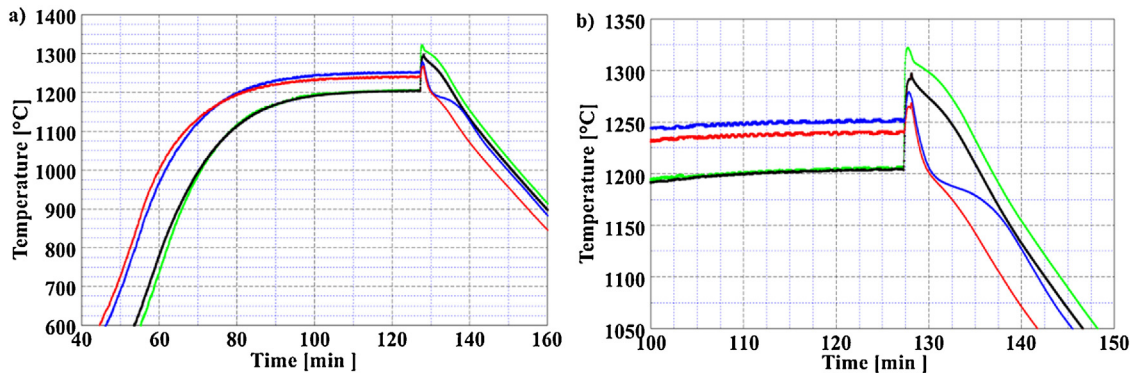

Fig. 4 – Temperatures registered by thermocouples: 1 – green curve, 2 – black curve, 3 – blue curve, 4 – red curve: (a) range 600–1400 °C; (b) 1050–1350 °C.
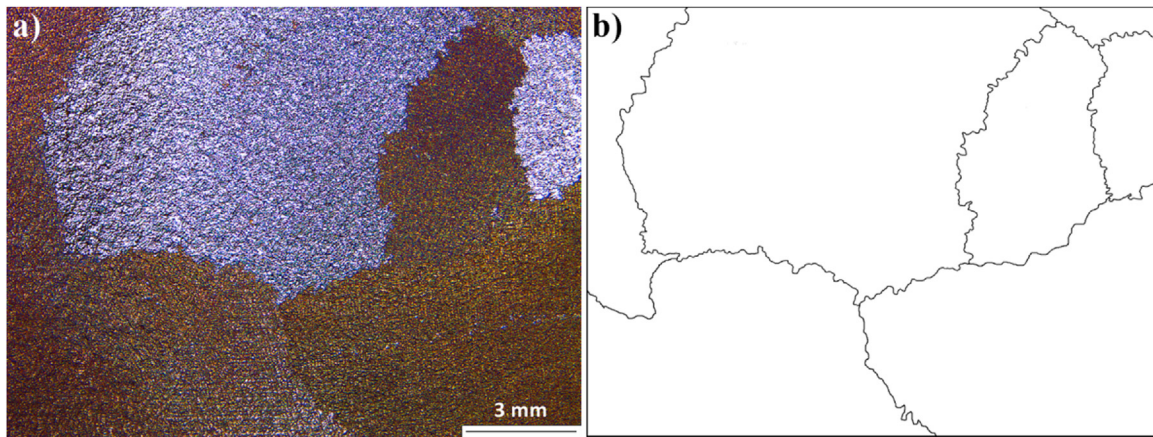
Fig. 5 – Macrostructure of Inconel 713C: (a) etched sample; (b) binary image.

Table 4 – Stereological parameters of microstructure.				
Parameter	Mean surface area (mm^2)	Mean perimeter (mm)	Mean size (mm)	Number of grains per mm^2
Value	26.22	26.47	5.10	0.04
Standard deviation	22.90	12.07	1.66	0.02

structure. The macrostructure of the Inconel 713C casting along with the binary image is shown in Fig. 5. Equiaxed grains of various sizes are observed, and so the image was subjected to computer analysis and the results are included in Table 4. The average grain area and the perimeter were 26.22 mm^2 and 26.27 mm respectively. The mean size of the grain was slightly over 5 mm. Due to the coarse grain structure, the number of grains per unit area was 0.04. The calculated stereological parameters indicate that the structure of the casting is beneficially favourable for the anticipated applications in aircraft engines.

The uniform temperature distribution shown in Figs. 3 and 4 is very desirable during investment casting because it guarantees appropriate heat transfer after pouring. The non-uniform temperature distribution exposes the shell mould to a greater thermal shock when in contact with liquid metal, which can lead to cracking or erosion of the primary coat which promotes the formation of non-metallic inclusions. Too high heat dissipation during pouring and the solidification of castings leads to the undercooling of the metal. As a consequence, a chill zone structure is formed, which significantly reduces the mechanical properties of castings, especially at high service temperatures. In addition, significant undercooling of the mould may lead to misruns, if the metal solidified before completely filling mould cavity [5,6,9]. The pouring process report stated that casting is characterized by high quality in line with the foundry's requirements. In the obtained microstructure there were no foundry defects, including chill zone structure, hot tears, misruns and coldshuts.

Observations of the Inconel 713C superalloy structure at a higher magnification revealed significant microstructural heterogeneity (Fig. 6a). Carbides had a morphology from regular blocky-shaped to Chinese script. Etching of the sample revealed the dendritic structure of the alloy with a secondary

dendrite arm spacing was 75 μm (±10 μm). In the dendrite cores, the cubic-shaped γ′ phase is surrounded by the channels of the matrix, whereas microstructure of interdendritic region was much more complex (Fig. 6b) in some places, which has been analyzed in detail.

The average concentrations of the main alloying elements in the cores of dendritic arms and the interdendritic spaces were determined using EDS (Fig. 7). Due to the microsegregation during crystallization, the values in selected regions were quite different and so, in order to show these differences, segregation coefficients have been calculated. The coefficient denoted as k is the relationship of concentration of alloying elements in the centerline of dendrites to that in the interdendritic spaces, namely $k = \frac{C_D^i}{C_{ID}^i}$. The coefficient k for Cr and Mo has a value less than one, namely 0.89 and 0.90, so the concentration of these elements was higher in interdendritic spaces. In dendrite cores, where a high volume fraction of the main strengthening phase was observed, the concentration γ′ formers exceed the value of one, namely 1.11 and 1.15 for Al and Ti respectively. The values of the coefficient k can approach one through diffusion as a result of heat treatment (solution + ageing) and by raising the pouring temperature [12].

As a result of the segregation of alloying elements in interdendritic spaces, numerous constituents with a relatively complex morphology were observed when compared to dendrite arms. Ten locations of EDS analysis were selected to characterize the chemical composition and identification of precipitates (Figs. 8 and 9). The results of the analysis (Table 5) from points 1, 4 and 9 indicate increased contents of Ni and Al (Figs. 8a and 9a), while the morphology confirms that precipitates were results of an eutectic reaction. At the end of solidification, the L → γ + γ′ reaction occurred, the Ni$_3$(Al, Ti) phase took up a large irregular morphology, and this area is commonly called eutectic γ/γ′ islands. The liquid in the
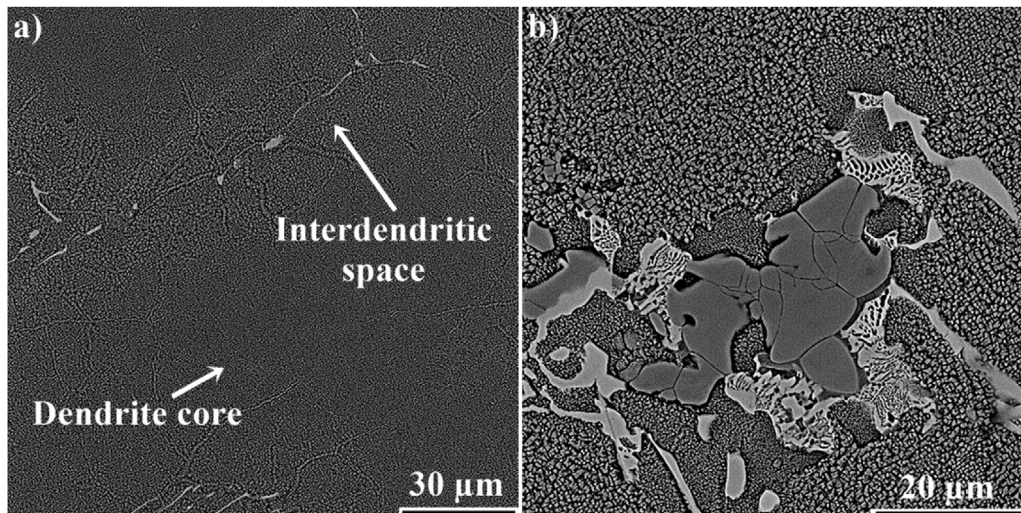
Fig. 6 – Microstructural constituents in IN713C: (a) dendrite core; (b) interdendritic space.

interdendritic spaces was then enriched with γ' formers, namely Al and Ti. The concentration of these elements at the analyzed points was 16.3–16.6 at.% and 2.3–2.4 at.%, respectively. The presence of eutectic islands is undesirable for final mechanical properties, hence heat treatment is performed in order to reduce the volume fraction of this residual phase [14,15]. In order to strengthen grain boundaries, B and Zr were added to IN713C, 0.08 wt.% and 0.012 wt.%, respectively, which elements are characterized by very low solubilities in the γ and γ' phases. In points 2, 3, 7 and 8 a significant enrichment was observed in Mo and Cr (Figs. 8b, c and 9b), whose total content exceeded even 82 at.%. The concentration of Mo was in the range of 49.9–53.8 at.%, Cr 28.7–29.4 at.%, and the third in order Nb was 6.5–7.9 at.%. Similar enrichment in Cr and Mo was observed in numerous nickel superalloys [16–21]. During the TEM studies on the influence of inoculant concentration on grain size in IN713C, the presence of borides M_3B_2 was shown [12]. Research on the atomic scale conducted by Hu [22] on M_5B_3 and M_3B_2 borides indicated that, despite the similar spectrum obtained from STEM-EDS, M_5B_3 borides are much richer in W, while in Inconel 713C this element is absent. Matysiak [12] observed that in the vicinity of
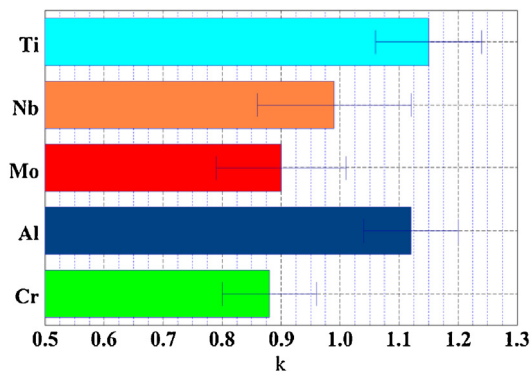
M_3B_2 borides the intermetallic compound Ni_7Zr_2 are formed. The morphology of the precipitates in which EDS points 5 and 6 were located, confirms, as well as strong enrichment in the Zr, these observations in the castings (Fig. 9c). Important conclusions can be reached by comparing the equilibrium Ni–Zr binary diagram [23] with above-mentioned observations. At 1438 °C congruent reaction L → Ni_7Zr_2 occurs. Subsequently, at 1304 °C and 1181 °C two peritectic reactions, namely L + Ni_7Zr_2 → Ni_5Zr and L + Ni_7Zr_2 → $Ni_{21}Zr_8$ take place. Binary diagram Ni–Zr indicates that the only eutectic reaction L → γ + Ni_5Zr can occur at 1164 °C, which implies that Ni_7Zr_2 can be present in IN713C microstructure, but not in a form of an eutectic. Motejadded [24] observed that liquid phase rich in Zr reacts with the eutectic or primary γ' phase through peritectic reaction L + γ' → γ + Ni_7Zr_2. It can be concluded that lamellar structure γ/Ni_7Zr_2 was a product of a peritectic reaction or eventually due to enrichment to Zr and B as a ternary eutectic L → γ + Ni_7Zr_2 + M_3B_2. During the solidification, as the γ' phase grew, the liquid was enriched by elements like Al and Ti. The enrichment reached a critic level, satisfying the thermodynamic requirements, and an eutectic reaction is initiated L → γ + γ'. Babu [25] suggests that in complex alloys, the eutectic reaction can be a more complicated. The negligible volume of eutectic γ–γ' phase can cause that the solute enrichment in the last solidifying liquid to be insufficient to induce the typical eutectic reaction. This can be the explanation of γ + Ni_7Zr_2 + M_3B_2 being present in Inconel 713C microstructure. Point 10 indicates the enrichment of elements called carbide formers, namely Nb, Mo and Ti, mainly the first one (Figs. 8d and 9d). Niobium creates MC-type carbides in Ni-based superalloys, which are precipitated directly from the liquid according to L → MC or via eutectic reaction L → γ + MC. During cooling, carbides are moved into interdendritic regions by solidified γ.

3.3.   Lattice parameter of γ matrix and γ' precipitates

Peaks {111} and {113} were in fact superpositions of reflections because both are combinations of the overlapping peak of the γ matrix and the corresponding peak of the γ' phase. Lattice

Fig. 7 – Segregation of alloying elements between the dendrite core and the interdendritic space (coefficient *k* with a standard deviation).
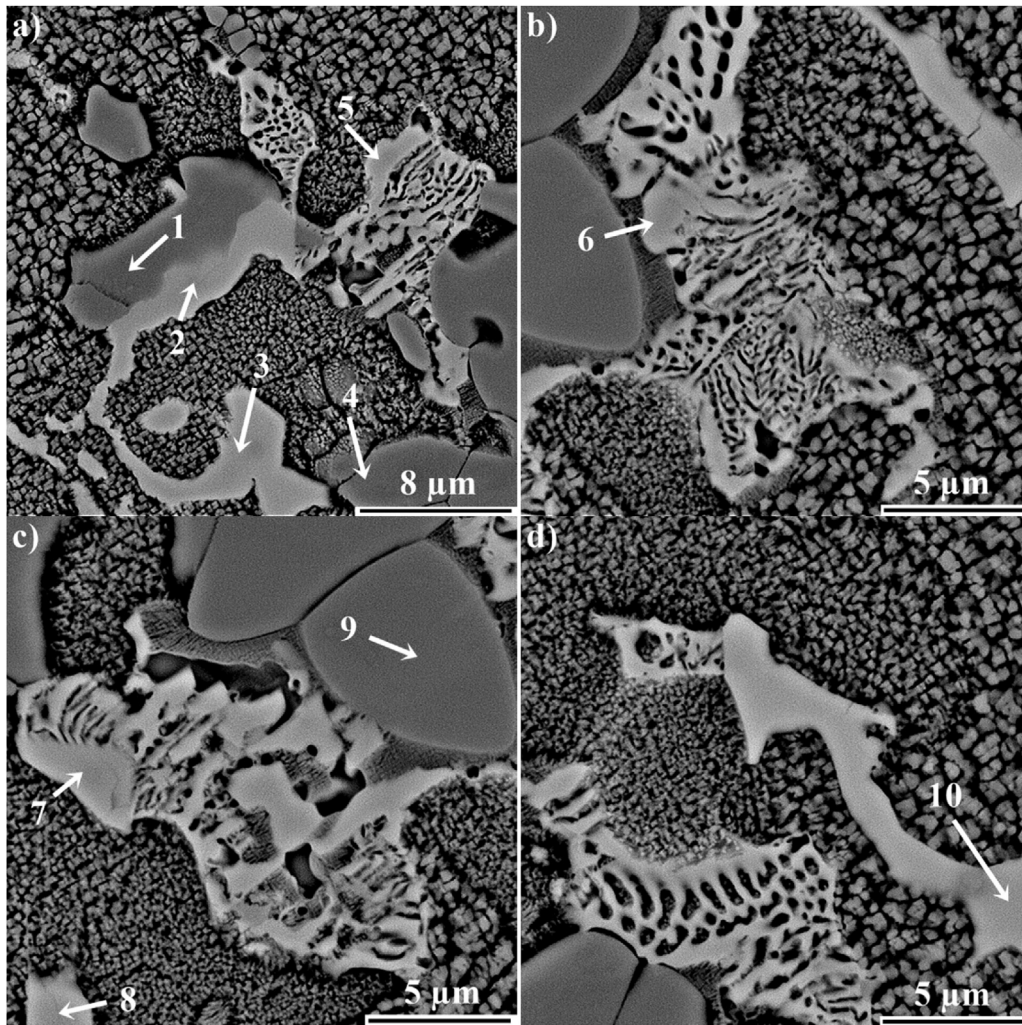
Fig. 8 – Location of EDS point analysis: (a) 1–5; (b) 6; (c) 7–9; (d) 10.

parameters of the γ matrix and γ′ precipitates were very similar, and so by analysing the XRD diagram, it is not possible to detect any difference in lattice constants of both phases. In order to match the peaks originated from γ and γ′, the least square method was applied. The interplanar distance both (111) and (113) planes were higher for the γ′ phase being 2.05603 Å and 1.07708 Å respectively (Table 6). Lattice parameter (a) calculated according to Eq. (1) was 3.56115 Å for (111) and 3.57227 Å for (113). Interplanar distances for (111) and (113) planes of intermetallic phase γ were 2.05077 Å and 1.07504 Å respectively. Calculation of the lattice parameter both for (111) and (113) planes gave, $a_{(111)} = 3.55204$ Å and $a_{(113)} = 3.565504$ Å. The so-obtained lattice parameters of γ and γ′ phases have been used to calculate lattice parameter misfit. Misfit parameter in both case was positive: $\delta_{(111)} = 0.256\%$, while $\delta_{(113)} = 0.190\%$. The δ parameter was small for both peaks, so it can be concluded that the nucleation energy is relatively small and so the formation of γ′ phase precipitates occurred under small undercooling [26]. A significant determinant of the lattice misfit is the internal misfit stress, which is the fundamental reason for the development of a raft structure comprising γ and γ′ alternately stacked in the <001> loading direction [27]. Ni-based superalloys usually attain sufficiently high rupture life in the full heat treatment (FHT) condition, namely after solution + ageing treatment [28–30]. One of the important characteristics of Inconel 713C is that it is able to fulfill the minimum rupture life requirement in as-cast condition [31]. Azadi reported that rupture life of Inconel 713C during creep testing can be longer in the as-cast condition in comparison with the alloy in the FHT condition. This influences the casting technology and appropriate parameter selection is crucial in achieving the desired microstructure and properties. Creep is controlled by dislocation movement in the γ matrix, induced by the applied tensile stresses, which is superimposed on the stresses originated from misfit [32,33].

4. Summary

The results show the influence temperature distribution in the ceramic mould with 9 layers (shells) on the microstructure and γ/γ′ misfit coefficient of Inconel 713C
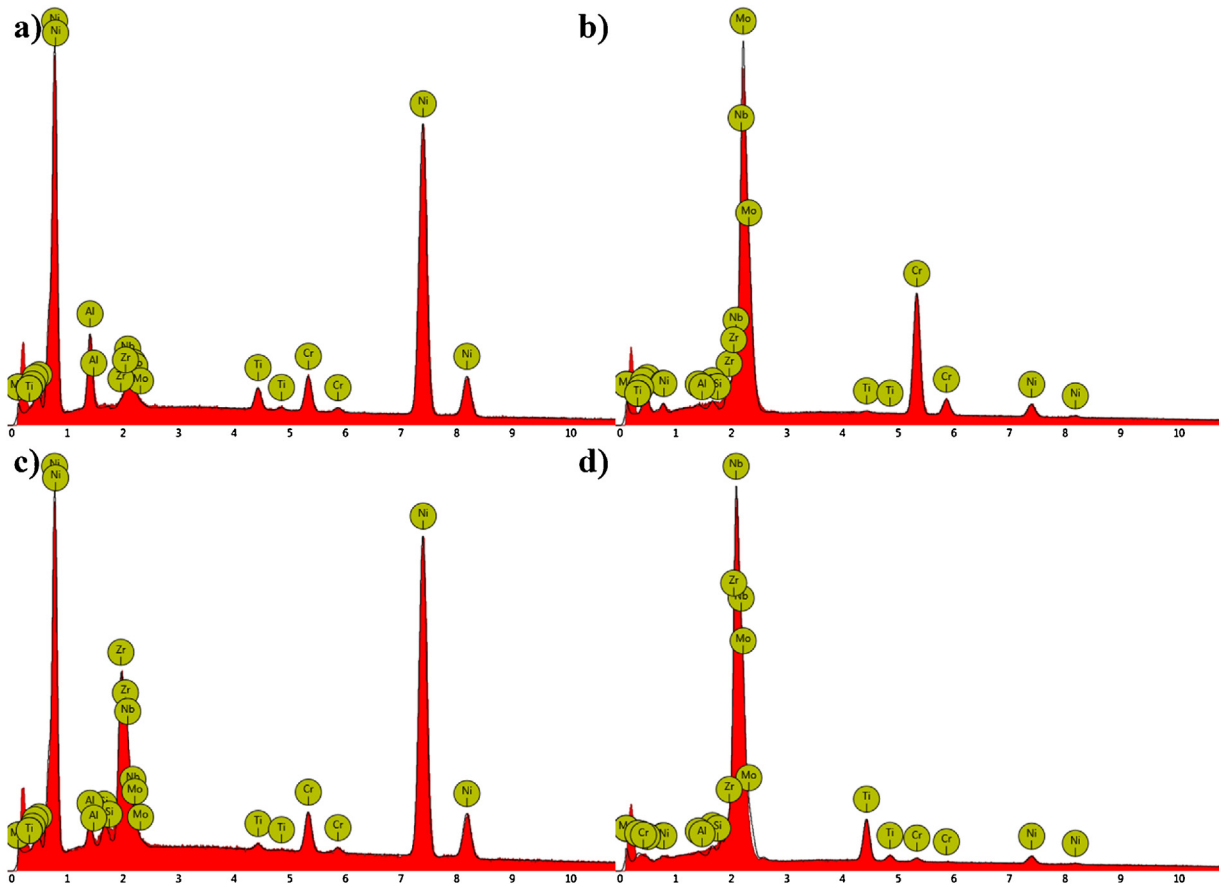
Fig. 9 – EDS spectrum: (a) γ' in eutectic island; (b) M_3B_2; (c) Ni_7Zr_2; (d) NbC.

superalloy. In order to prevent the cracking of the shell mould, formation of chill zone structure and misruns, a preheat of shell moulds was carried out. Two main temperatures of casting, namely preheating and pouring were 1250 °C and 1470 °C respectively. The preheating time was 127 min while and 1250 °C was reached almost half an hour earlier. Selected casting parameters and composition of shell mould created conditions favourable to coarse grain structure with a mean size of grain 5.1 mm desired for a

typical service temperature. The microstructure of Inconel 713C castings was characterized by substantially large local inhomogeneities originating from segregation of alloying elements during solidification of casting. Dendrite cores consisted of coherent cubic shaped γ' precipitates divided by channels of γ matrix. Enrichment of interdendritic liquid in Al and Ti in the final stage of casting solidification caused the eutectic reaction L $\rightarrow \gamma + \gamma'$. Due to the low solubility of B and Zr in γ' and matrix, in the close vicinities of the eutectic islands, borides and an intermetallic compound of Ni with Zr were observed. Borides were enriched in molybdenum and chromium, while MC-type carbides, which were also present in interdendritic spaces, in niobium, molybdenum, and titanium. X-ray diffraction investigation revealed good

Table 5 – Results of EDS analysis (at.%).

Element	Cr	Al	Nb	Mo	Ti	Zr	Si	Ni
Point								
1	4.4	16.3	4.2	1.3	2.3	1.2	–	70.3
2	29.3	0.9	7.8	53.0	0.4	2.2	1.3	5.1
3	28.8	1.2	7.9	53.8	0.6	1.9	1.3	12.1
4	4.1	16.5	4.3	1.4	2.4	1.4	–	69.9
5	5.3	3.2	5.6	2.9	0.4	17.6	2.1	62.9
6	4.4	3.7	5.7	1.4	0.6	17.2	2.1	64.9
7	28.7	1.3	6.5	49.9	0.5	2.8	1.4	8.9
8	29.4	0.8	7.1	53.2	0.5	2.2	1.3	5.5
9	4.0	16.6	3.7	1.4	2.4	1.2	–	70.7
10	1.1	0.9	60.4	14.5	11.5	5.9	1.9	3.8

Table 6 – Results of X-ray diffraction.

hkl		111		113	
Phase	γ'	γ	γ'	γ
2Θ [deg]	44.003	44.122	91.308	91.531
Interplanar distance d_{hkl} [Å]	2.05603	2.05077	1.07708	1.07504
Lattice parameter a [Å]	3.56115	3.55204	3.57227	3.565504
Misfit δ	0.256%		0.190%	

crystallographic matching between γ matrix and γ′ precipitates. Peaks (111) and (113) were superpositions of reflections and so least square method was used in order obtain lattice parameters of γ and γ′ phase. Lattice misfit (δ) was positive for both peaks, namely 0.256% (111) and 0.190% (113). Such values indicate on good creep resistance, which is important taking into account that Inconel 713C can fulfil international standards and be used in as-cast condition.

Ethical statement

The article was conducted according to ethical standards.

Funding body

Acknowledgements

REFERENCES

[1] E. Benini, Advances in Gas Turbine Technology, Intech, 2011, http://dx.doi.org/10.5772/664.

[2] Ł. Rakoczy, et al., Microstructure and properties of a repair weld in a nickel based superalloy gas turbine component, Adv. Mater. Sci. 17 (2) (2017) 55–63.

[3] A. Szczotok, J. Pietraszek, N. Radek, Metallographic study and repeatability analysis of γ′ phase precipitates in cored thin-walled castings made from IN713C superalloy, Arch. Metall. Mater. 62 (2) (2017) 595–601.

[4] T. Pollock, S. Tin, Nickel-based superalloys for advanced turbine engines: chemistry, microstructure and properties, J. Propuls. Power 22 (2) (2006) 361–374.

[5] C.H. Konrad, et al., Determination of heat transfer coefficient and ceramic mold material parameters for alloy IN738LC investment castings, J. Mater. Prop. Technol. 211 (2011) 181–186.

[6] Y.W. Dong, et al., Modelling of shrinkage during investment casting of thin-walled hollow turbine blades, J. Mater. Process. Technol. 244 (2017) 190–203.

[7] J. Coakley, et al., Lattice strain evolution and load partitioning during creep of a Ni-based superalloy single crystal with rafted γ′ microstructure, Acta Mater. 135 (2017) 77–87.

[8] ASTM E139-11 Standard Test Methods for Conducting Creep, Creep-Rupture, and Stress-Rupture Tests of Metallic Materials.

[9] L. Qin, et al., A design of non-uniform thickness mould for controlling temperature gradient and S/L interface shape in directionally solidified superalloy blade, Mater. Des. 116 (2017) 565–576.

[10] M. Lachowicz, et al., Microstructure transformations and cracking in the matrix of γ–γ′ superalloy Inconel 713C melted with electron beam, Mater. Sci. Eng. A 479 (2008) 269–276.

[11] H. Matysiak, et al., The microstructure degradation of the IN713C nickel-based superalloy after stress rupture tests, J. Mater. Eng. Perform. 23 (9) (2014) 3305–3313.

[12] H. Matysiak, et al., The influence of the melt-pouring temperature and inoculant content on the macro and microstructure of the IN713C Ni-based superalloy, J. Miner. 68 (1) (2016) 185–197.

[13] D. Szeliga, et al., Investigation of casting–ceramic shell mold interface thermal resistance during solidification process of nickel based superalloy, Exp. Therm. Fluid Sci. 87 (2017) 149–160.

[14] L. Cao, et al., Formation of the surface eutectic of a Ni-based single crystal superalloy, J. Mater. Sci. Technol. 33 (2017) 347–351.

[15] S. Hedge, R. Kearsey, J. Beddoes, Designing homogenization – solution heat treatments for single crystal superalloys, Mater. Sci. Eng. A 527 (2011) 5528–5538.

[16] B. Du, et al., M_5B_3 boride at the grain boundary of a nickel-based superalloy, J. Mater. Sci. Technol. 32 (2016) 265–270.

[17] A. Shulga, Boron and carbon behavior in the cast Ni-base superalloy EP962, J. Alloys Compd. 436 (2007) 155–160.

[18] B. Zhang, et al., Precipitation and evolution of boride in diffusion affected zone of TLP joint of Mar-M247 superalloy, J. Alloys Compd. 695 (2017) 3202–3210.

[19] J. Wei, et al., The effects of borides on the mechanical properties of TLPB repaired Inconel 738 superalloy, Metall. Trans. A 48 (10) (2017) 4622–4631.

[20] S. Seo, et al., Eta phase and boride formation in directionally solidified Ni-base superalloy IN792 + Hf, Metall. Trans. A 38 (4) (2007) 883–893.

[21] A. Chamanfar, et al., Cracking in fusion zone and heat affected zone of electron beam welded Inconel-713LC gas turbine blades, Mater. Sci. Eng. A 642 (2015) 230–240.

[22] X.B. Hu, et al., The Wyckoff positional order and polyhedral intergrowth in the M3B2- and M5B3-type boride precipitated in the Ni-based superalloys, Sci. Rep. 4 (2014) 1–9, Article 7367.

[23] P. Franke, D. Neuschütz, Binary Systems. Part 4: Binary Systems From Mn–Mo to Y–Zr. Landolt-Börnstein – Group IV Physical Chemistry (Numerical Data and Functional Relationships in Science and Technology), vol. 19B4, Springer, Berlin, Heidelberg, 2006.

[24] H. Motejadded, et al., Dissolution mechanism of Zr rich structure in a Ni_3Al base alloy, J. Mater. Sci. Technol. 27 (2011) 885–992.

[25] S. Babu, et al., Atom-probe field-ion microscopy investigation of CMSX-4 Ni-base superalloy laser beam welds, in: International Field Emission Society IFES'96 Proceedings of the 43rd International Field Emission Symposium, 1996.

[26] F. Masoumi, et al., Kinetics and mechanisms of γ′ repreciptation in a Ni-based superalloy, Sci. Rep. 6 (28650) (2016) 1–16.

[27] L. Nguyen, et al., Quantification of rafting of γ′ precipitates in Ni-based superalloys, Acta Mater. 103 (2016) 322–333.

[28] V. Caccuri, et al., γ′-Rafting mechanisms under complex mechanical stress state in Ni-based single crystalline superalloys, Mater. Des. 131 (2017) 487–497.

[29] P. Nörtershäuser, et al., The effect of cast microstructure and crystallography on rafting, dislocation plasticity and creep

anisotropy of single crystal Ni-base superalloys, Mater. Sci. Eng. A 626 (2015) 306–312.

[30] C. Li, et al., Microstructure and mechanical properties of a Ni-based superalloy after heat treatment in a steady magnetic field, J. Mater. Process. Technol. 246 (2017) 176–184.

[31] M. Azadi, et al., Effects of solutioning and ageing treatments on properties of Inconel 713C nickel-based superalloy under creep loading, Mater. Sci. Eng. A 711 (2018) 95–204.

[32] M. Li, et al., Creep deformation mechanisms and CPFE modelling of a nickel-base superalloy, Mater. Sci. Eng. A 718 (2018) 147–156.

[33] R. Reed, The Superalloys: Fundamentals and Applications, Cambridge University Press, Cambridge, 2006.

CrossMark

The Influence of the Melt-Pouring Temperature and Inoculant Content on the Macro and Microstructure of the IN713C Ni-Based Superalloy

HUBERT MATYSIAK,[1] MALGORZATA ZAGORSKA,[2,6] ALICJA BALKOWIEC,[2] BOGUSLAWA ADAMCZYK-CIESLAK,[2] KRZYSZTOF DOBKOWSKI,[2] MATEUSZ KORALNIK,[2] RAFAL CYGAN,[3] JACEK NAWROCKI,[4] JAN CWAJNA,[5] and KRZYSZTOF J. KURZYDLOWSKI[2]

1.—Functional Materials Research Center, Warsaw University of Technology, 02-507 Warsaw, Poland. 2.—Faculty of Materials Science and Engineering, Warsaw University of Technology, 02-507 Warsaw, Poland. 3.—Wytwornia Sprzetu Komunikacyjnego PZL Rzeszow S.A., 35-078 Rzeszow, Poland. 4.—Faculty of Mechanical Engineering and Aeronautics, Rzeszow University of Technology, 35-959 Rzeszow, Poland. 5.—Faculty of Materials Engineering and Metallurgy, Silesian University of Technology, 40-019 Katowice, Poland. 6.—e-mail: m.zagorska@inmat.pw.edu.pl

The aim of this work was to determine the effect of melt-pouring temperature T_m and inoculant (cobalt aluminate—$CoAl_2O_4$) concentration in the prime coat of the shell mold on the macro- and microstructure of the IN713C superalloy. The results show that cobalt aluminate is an effective modifier of the IN713C superalloy, which causes refinement of the equiaxed grains (EX) and a reduction of the fraction and size of the columnar grains on the casting surface. Also, the melt-pouring temperature in the range of 1450–1520°C was found to influence the mean EX grain size. Based on the results of differential thermal analysis of the alloy and detailed microstructure characterization, a sequence of precipitations has been proposed that advances current understanding of processes that take place during alloy solidification and casting cooling.

INTRODUCTION

IN713C is a nickel-based superalloy adequate for use at high temperatures. Its good resistance to high-temperature corrosion and creep, good castability, and high structural stability at elevated temperatures[1–7] make it suitable for fabrication; therefore, this superalloy is widely used in aircraft engine turbines parts,[4,5,8,9] such as low-pressure turbine (LPT) blades and LPT vane clusters. For example, the designers of the large aircraft turbofan engine GP7200 selected this alloy for the production of LPT blades and LPT vane clusters. These complicated castings must meet all quality requirements, which in this case are highly strict. Every IN713C superalloy master ingot has to undergo a number of tests. Examined are the chemical composition (the content of the main alloying elements and the trace elements) and the mechanical properties (employing static tensile testing at elevated temperatures and stress rupture tests).

The as-cast IN713C superalloy has a dendritic microstructure. The matrix of the alloy is the γ phase, strengthened by cubic and coherent precipitations of the γ' $Ni_3(Al,Ti)$ phase.[1,2,10,11] Carbon present in the alloy segregates into the interdendritic areas and reacts with carbide-forming elements, such as niobium, titanium, or tantalum, thus, forming metal carbides (MC) with the NbC structure.[1,2,10–14] To obtain optimal mechanical properties of the IN713C alloy, it is common practice to maximize the volume fraction of the γ' phase and to promote a uniform EX grain size distribution. This can be achieved by proper selection of melting and pouring parameters, as well as by inoculation.[15–18]

The predominant feature of investment cast superalloys is the macrostructural coarseness and nonuniformity of surface grain size, which may reduce the fatigue performance and reliability of cast LPTs in the intermediate temperature range. In the LPT section, the operating temperature is within the range of 650°C and 700°C, which is usually below the

creep range where stresses from centrifugal loads are high. Thus, high tensile strength and good low cycle fatigue (LCF) resistance are primarily required. In this temperature range, a uniform and relatively fine surface grain size is desired to promote fatigue properties and resistance to crack growth.[19–23] For this reason, in the presented work, castings were modified by adding the $CoAl_2O_4$ inoculant to the prime coat of the shell mold. This technique of modification was chosen due to the ease of implementation, the acceptable cost, and satisfactory results (for thin-wall castings), in accordance with the requirements put forward by turbine parts purchasers. The modification mechanism of the nickel superalloys with the use of the cobalt aluminate is widely discussed in the literature.[19–24] The alloying elements (e.g., Cr, C, Ti, and Al) react with $CoAl_2O_4$ to form Co particles formed on the surface of the shell mold. The particles act as nucleation sites for the heterogeneous crystallization of the γ phase. The crystallographic similarity and low value of lattice misfit between the nucleation sites and γ phase guarantee effective refinement of the surface macrograins.[25]

The aim of the current research was to determine the effect of the melt-pouring temperature and the inoculant concentration (cobalt aluminate) in the prime coat of the shell mold on the macro- and microstructure of IN713C superalloy castings.

MATERIAL AND EXPERIMENTAL PROCEDURE

The IN713C superalloy was provided by Canon Muskegon. The chemical composition of the alloy is presented in Table I.

As-received "master heat" ingots were cut into charges of 3.5 kg. These were later melted in a zirconia ramming crucible installed in the industrial VIM IC Consarc furnace. General technical conditions of the casting trials are listed in Table II.

Vacuum during melting and pouring was maintained at a level of 2×10^{-2} mbar. Three melt-pouring temperatures (T_m) were used: 1450°C, 1480°C, and 1520°C, which were controlled by Pt/Pt–Rh thermocouples. The molten alloy was cast into ceramic shell molds fabricated through the "dip and stucco" technique. The assembly consisted of five plate cast samples, each of 0.2 kg with a height of 100 mm, a width of 70 mm, and a wall thickness of 5 mm.

Three different prime coats of shell molds were used for the casting trials:

a) Trials 1–3: with a zircon filler and colloidal silica binder.
b) Trials 4–6: same as Trials 1–3 plus 5 wt.% of cobalt aluminate ($CoAl_2O_4$) inoculant.
c) Trials 7–9: same as Trials 1–3 plus 10 wt.% of cobalt aluminate ($CoAl_2O_4$) inoculant.

Alumina silicate powders were applied as a shell mold backup. The molds were dewaxed in boilerclave, burned out at 750°C, heat insulated with alumina-silicate Fiberfrax®, and fired in air at 1250°C for 2 h. During the pouring process, the temperature of all the shell molds (T_s) was 1200°C. The temperature changes during the alloy solidification and casting cooling were evidenced using Pt/Pt–Rh thermocouples and the multichannel recorder HIOKI. By using these data, the average cooling rate was calculated in the temperature range from T_m to 650°C. Regardless of the T_m measured, the average cooling rate at the center of the castings was within the range of 10–12°C/min.

To estimate the main temperature characteristics during solidification of the IN713C superalloy, differential thermal analysis (DTA) was performed by using Labsys DTA/DSC Staram. Specimens weighing 0.14 g were cooled from 1500°C to 500°C under a flowing argon atmosphere at a cooling rate of 10°C/

Table I. Chemical composition of the IN 713C superalloy

Element	C	Si	Al	B	Nb + Ta	Cr	Fe	Mo	Ti	Zr	Ni
wt.%	0.069	0.010	6.080	0.010	2.160	13.580	0.090	4.210	0.840	0.060	Balance

Table II. Technical conditions of the casting trials

	Melt-pouring temperature, T_m (°C)		
	Trial acronym		
Shell mold system and firing temperature (T_s)	**1450**	**1480**	**1520**
0 wt.% of $CoAl_2O_4$ inoculant, T_s = 1200°C	T1	T2	T3
5 wt.% of $CoAl_2O_4$ inoculant, T_s = 1200°C	T4	T5	T6
10 wt.% of $CoAl_2O_4$ inoculant, T_s = 1200°C	T7	T8	T9

The Influence of the Melt-Pouring Temperature and Inoculant Content on the Macro and Microstructure of the IN 713c Ni-Based Superalloy
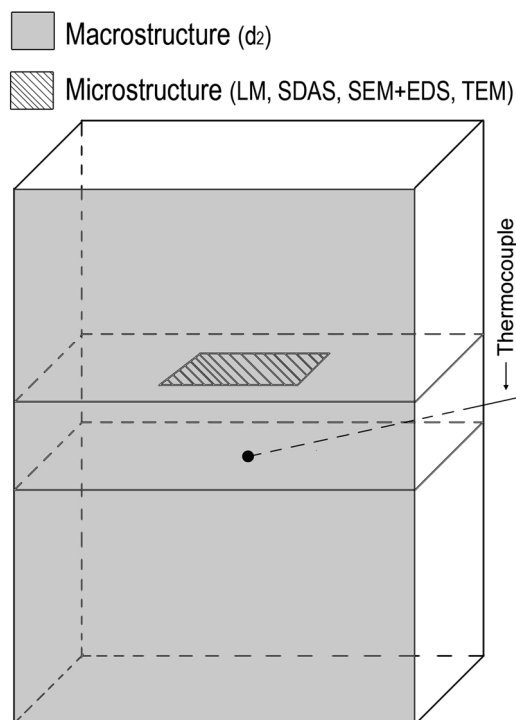
187

Fig. 1. Sampling areas for macro- and microstructure investigations.

min. A 99.99% pure corundum was used as the reference material. The enthalpy of the observed transformations during solidification and casting cooling were determined by measuring the exothermic peak areas with a numerical integrator method.

The surface of the cast plates (Fig. 1) were macroetched with a solution of analytically pure HNO_3 (20 g/L), HCl (300 g/L), $FeCl_3$ (160 g/L), and H_2O (100 mL/L) at 50°C (time of etching was 2–4 min). A digital microscope (VHX Kayence) was used to capture the macrostructure images. Image processing and quantitative image analyses were performed by using MicroMeter software.[26] The size of the macro grains on the surface of the castings was measured in terms of equivalent grain diameter d_2 (diameter of a circle with the same surface area). An average value of d_2, out of 100 equiaxed surface macro grains, was obtained for each of five castings from each assembly.

Microstructure characterization and analyses were carried out by using the following techniques: light microscopy (LM) equipped with Vickers microhardness device (μHV), scanning electron microscopy (SEM), transmission electron microscopy (TEM), and x-ray spectroscopy (EDS).

The samples for LM and SEM observations were sectioned along the transverse cross section of the cast plates (Fig. 1). The specimens were then ground, polished, and chemically etched with Kalling's reagent, consisting of analytically pure 5-g $CuCl_2$, 100-mL HCl, and 100-mL ethanol. The dendritic microstructure and the secondary dendrite

arm spacing (SDAS) were investigated in the center of the cross-sectioned samples by using a Nikon Epiphot 220 LM and were quantitatively analyzed by employing MicroMeter software. The sample cross sections were also analyzed by a SEM Hitachi S-3500 N equipped with energy-dispersive x-ray spectroscopy (EDS). For the imaging and EDS analyses, a 15-kV accelerating voltage was used. SEM microstructure images were analyzed quantitatively in terms of the γ' phase size in dendrites and interdendritic areas. An equivalent diameter d_2 of the γ' phase was measured.

Samples for TEM observations of the IN713C matrix were cut from 3-mm-diameter cylinders cut from the castings by spark erosion. Thin foils of 0.2-mm thickness were sliced by a wire saw and mechanically grounded using a Gatan Dimple Grinder. Finally, thin foils were electrochemically polished by the double-jet method on a Struers device in a mixture of acetic and perchloric acids (95/5 vol.%). Samples for TEM observations of the IN713C superalloy constituents (M_3B_2 and Ni_7Zr_2) were prepared by using a single focused ion beam (FIB) system (Hitachi FB-2100) and a lift-out preparation technique. The sampling area was selected on the basis of SEM observations. The obtained material underwent microstructure observations and selected area electron diffraction analyses (SAED), which were performed with a Jeol JEM 1200EX II TEM (operating at 120 kV). The diffraction aperture with a diameter of 500 nm was used.

RESULTS

Differential Thermal Analysis (DTA) Results

The results of the DTA of the IN 713C superalloy are shown in Fig. 2 and Table III.

The cooling curve exhibits an exothermic peak with two maxima related to solidification processes. The beginning of the solidification (formation of γ phase dendrites, $L \rightarrow \gamma$) was recorded at $T_1 = 1342$°C—the liquidus temperature. The maximum at which the transformation occurs with the highest intensity is at $T_2 = 1338$°C. The second maximum is related to the precipitation of MC primary carbides from the liquid ($L \rightarrow MC$) and the formation of the MC/γ eutectic ($L \rightarrow MC + \gamma$). This transformation begins at $T_3 = 1305$°C, and its maximum is observed at $T_4 = 1299$°C. The solidification ends at $T_5 = 1263$°C—the solidus temperature. The solidification enthalpy (ΔH_{SOL}) can be estimated as -125 J/g. During the cooling, a minor effect was also observed related to an exothermic transformation in the solid state with a maximum at $T_7 = 1151$°C. This is caused by the precipitation of γ' phase from γ phase ($\gamma \rightarrow \gamma'$), which starts at $T_6 = 1169$°C and ends at $T_8 = 929$°C. The enthalpy of the phase transformation ($\Delta H_{\gamma'}$) in the solid state equals -9 J/g. Further cooling of the alloy below 929°C does not cause any significant thermal effects on the DTA curve.
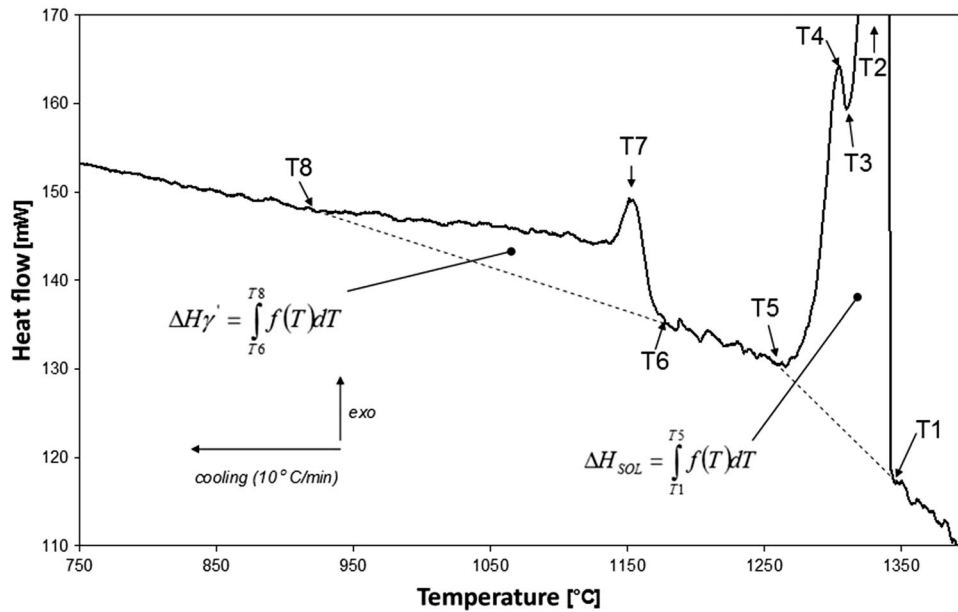
Fig. 2. DTA curve (cooling range) for the IN713C superalloy obtained at a cooling rate of 10°C/min in the temperature range 1400°C to 750°C.

Table III. DTA results for the IN 713C superalloy

			Cooling rate		
			10°C/min		
				Literature data (Refs. 2 and 27)	
Transformation	Parameter		Present study		
Alloy solidification	T_1 liquidus	°C	1342	1335	1338
	T_2		1338	Not given	1289
	T_3		1305	Not given	Not given
	T_4		1299	1278	1238
	T_5 solidus		1263	1235	1219
	ΔH_{SOL}	J/g	−125	Not given	Not given
Solid phase trasformation	T_6	°C	1169	1135	1175
	T_7		1151	Not given	Not given
	T_8		929	700	996
	$\Delta H_{\gamma'}$	J/g	−9	Not given	Not given

The temperatures determined from the DTA measurements are generally in agreement with the literature data (Table III). Observed scatter of data is influenced by several factors, which can be divided into three categories: (I) associated with the DTA device, (II) associated with the sample, and (III) associated with the "interpretation" of the DTA thermogram.[28,29]

For the first, one can distinguish uncorrectable and variable parameters. Uncorrectable parameters are those that are connected with the design of the DTA device components. The uncorrectable parameters are not taken into consideration here. In the group of variable parameters, the cooling/heating rates and the type of

atmosphere are the most important. If the cooling/heating rates (the basic factor determining the location of characteristic temperatures on a thermogram) are the same, the type of atmosphere used and its flow rate may influence the data. For the second, the most important factors affecting the results are the mass of the tested sample (varying in discussed works), its chemical composition, and the type of reference material. The mass of the test sample has to be selected in such a way that the temperature gradient in the sample during the measurements is as low as possible. Thus, for different DTA devices, sample masses may vary; however, all of them are low and within the range of tens to hundreds of milligrams. In the case of

The Influence of the Melt-Pouring Temperature and Inoculant Content on the Macro and Microstructure of the IN 713c Ni-Based Superalloy
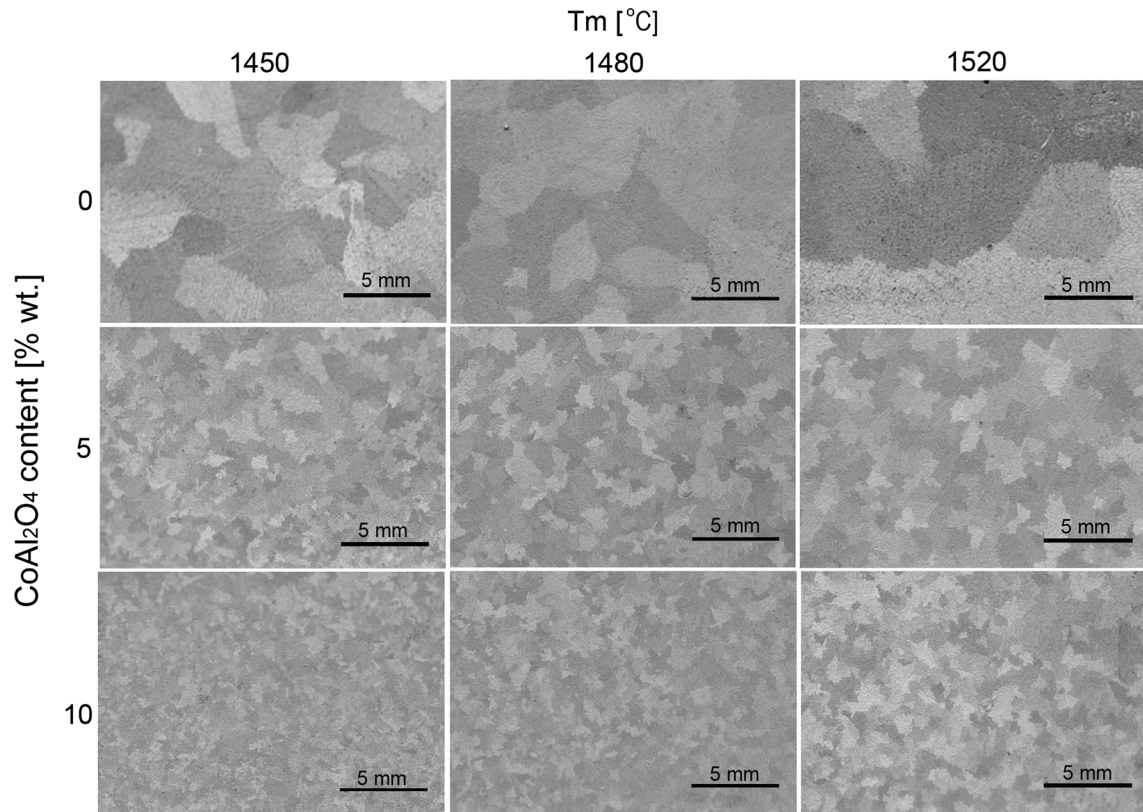
189

Fig. 3. Representative macrostructure images (LM) of the cast surface after sand blasting and etching.

multicomponent as-cast alloys, such a small volume of material should be considered unrepresentative due to local changes in the chemical composition caused by the segregation of alloying elements. In addition, the content of individual alloying elements, including trace elements, may vary in the ranges provided by the standard for a particular alloy grade. These differences occur in the discussed cases. Ceramic and metallic materials, in which there are no phase transitions in the range of temperature measurements, are successfully used as reference samples for the DTA technique. These materials, however, are characterized by significantly different thermal properties (such as heat capacity and thermal conductivity), which may result in noticeable differences in the obtained results. For instance, in Ref. 29, a solution suggested to increase measurement accuracy is to use platinum as a reference for defining characteristic temperatures during the melting and solidification of superalloys and to employ nickel as a reference for analyzing phase transformations in the solid state.

Finally, the "interpretation" of the DTA thermogram stems from the fact that each superalloy reaction occurs over a temperature range. Determining the onset and completion of a reaction may differ in various studies. Usually, the beginning of a reaction will be the point at which the DTA curve departs from the baseline. In the case of the end of a

reaction, similarly as in the case of the beginning of a reaction, the literature points out that some researchers assume that the end is determined by the point at which the curve returns to the baseline (like in the present study), while according to others, a reaction ends at the minimum or maximum of the reaction peak. All of the aforementioned factors significantly influence the obtained results and should be taken into consideration in a comparative analysis.

Macro- and Microstructure Analysis

Microstructure images representative of the surface of the castings are presented in Fig. 3. The results of the surface grain size measurements versus the melt-pouring temperature and the cobalt aluminate content are shown in Fig. 4. On the basis of the obtained results, it should be stated that increasing the melt-pouring temperature from $T_m = 1450°C$ to $T_m = 1520°C$ causes an increase in the grain size. In the case of unmodified castings, the grain size increased 2.3 times, whereas for modified castings, it was 1.8 and 1.4 times for 5 wt.% and 10 wt.% inoculant content, respectively.

The results also show that the cobalt aluminate $(CoAl_2O_4)$ is a very effective modifier for the alloy IN713C in the whole range of melt-pouring temperatures. It both refines the equiaxed grains (EX) and significantly reduces the size and fraction of the
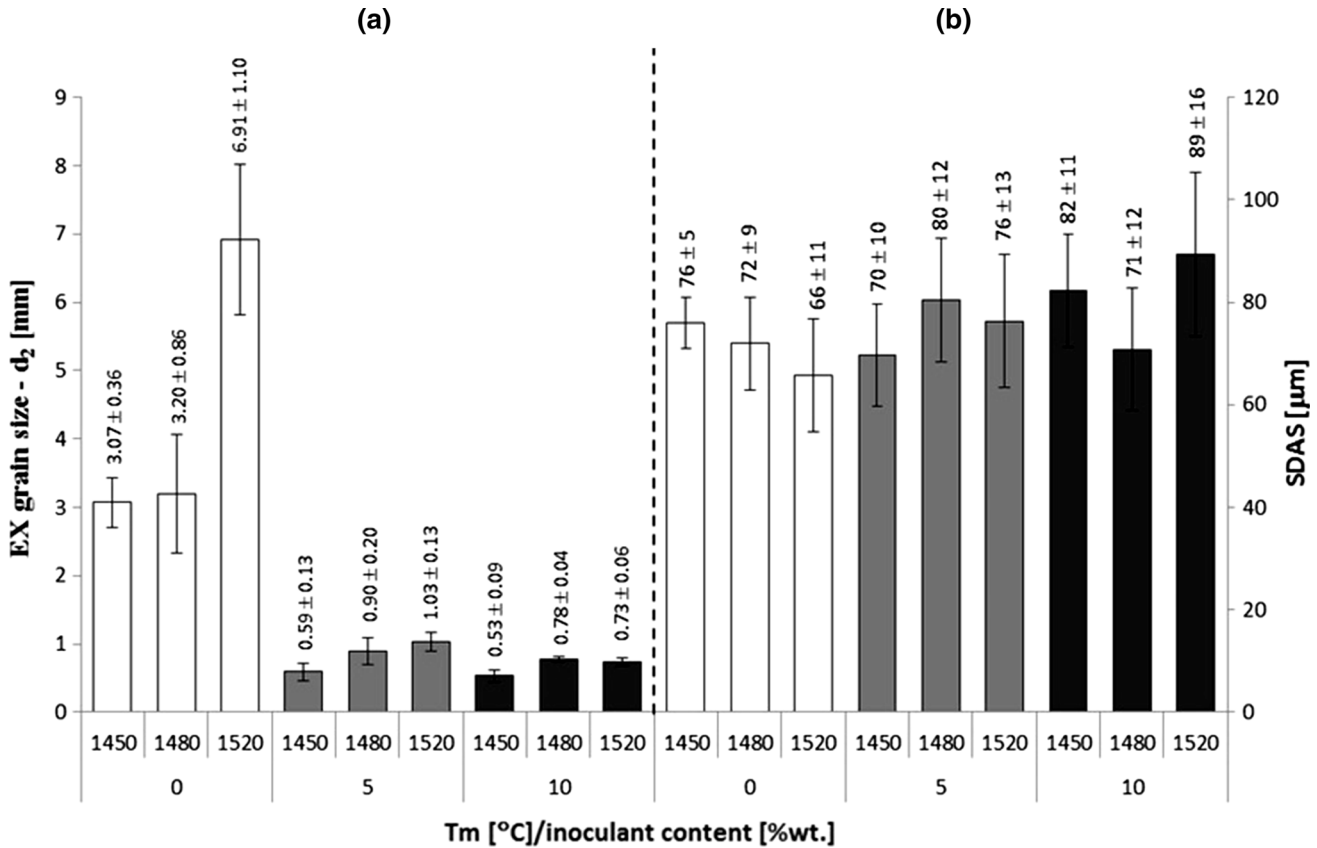
(a)   **(b)**

Fig. 4. Effect of inoculant content and melt-pouring temperature on the size of surface EX grains (a) and secondary dendritic arm spacing (SDAS) (b).

columnar ones. It should, however, be noted that the increase of the inoculant concentration from 5 wt.% to 10 wt.% brings about only a minor improvement.

The LM and SEM microstructure observations of the casting cross sections indicated (regardless of the melt-pouring temperature and the inoculant content) the presence of a dendritic microstructure typical of the as-cast state. Dendrites of the γ phase and interdendritic areas with numerous precipitations were observed, as illustrated in Fig. 5a and b.

MC primary carbides, rich in Nb (Figs. 5b–e and 6a), appear in large numbers in the interdendrictic areas. They occur in the form of "Chinese script" and in a eutectic mixture γ + MC. In a few NbC carbides, one could observe oxide nonmetallic inclusions containing Al and Mg (Figs. 5e and 6b), which were probably present in the "master heat" ingot as an "impurity" after manufacturing of the alloy ingots. The $\gamma + \gamma'$ eutectic (Fig. 5d and f) and a eutectic, in which one of the phases is rich in Ni and Zr (Figs. 5c, d and 6c), were also found. In the vicinity of this eutectic, particles of a phase M_3B_2 rich in Mo (Figs. 5c and 6d), eutectic $\gamma + \gamma'$, and MC constituents (Fig. 5c and d) were observed.

The images of the dendritic structure (Fig. 5a) have been analyzed with the purpose of determining the secondary dendrite arm spacings (SDAS). The

obtained results are presented in Fig. 4. No evidence for correlation between SDAS and the melt-pouring temperature or the inoculant content was found. The mean values of SDAS are within the range of 66–89 μm.

Still, one may observe a significant difference in the microhardness values between the dendrites and the interdendritic areas, as shown in Fig. 7. Regardless of the pouring temperature and the inoculant content, a higher hardness value was recorded in the interdendritic regions, from 351 HV0.2 to 401 HV0.2 compared with 314 HV0.2 to 347 HV0.2 for the dendrites.

The increased microhardness of the interdendritic areas is connected with the segregation of the alloying elements taking place during solidification. The interdependence was confirmed by measurement of the chemical composition (EDS). The values of the segregation coefficient k,[2] compiled in Table IV, indicate significant enrichment of the interdendritic areas ($k < 1$) with Mo and Nb. Chromium also has a tendency to segregate to the interdendritic regions, whereas Al enriches the cores of the dendrites ($k > 1$).

The segregation of the alloying elements during solidification also affects the size of the γ' phase precipitations. Regardless of the pouring temperature and the inoculant content, coarser precipitations
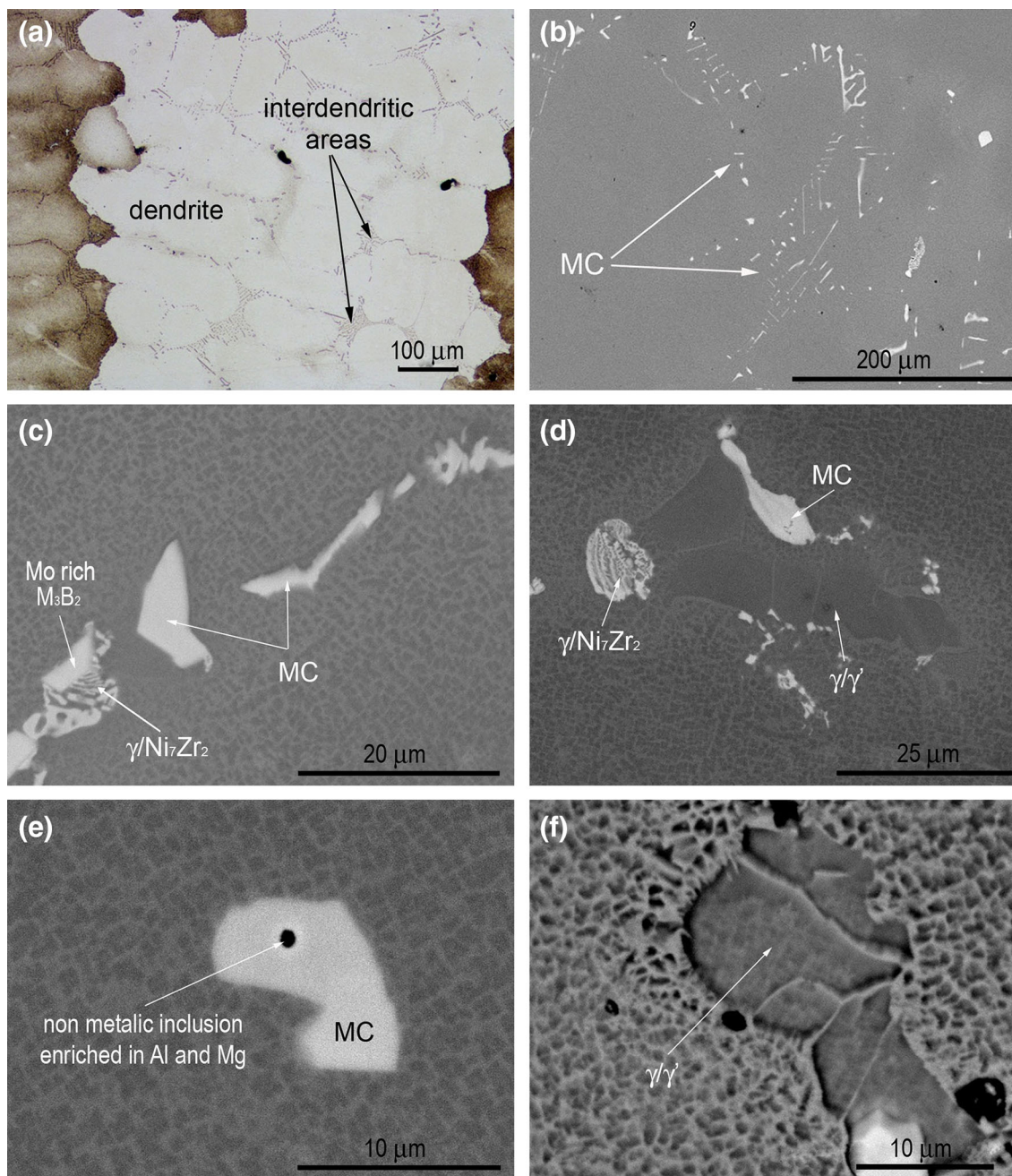
Fig. 5. LM (a) and SEM (b–f) images of the IN713C superalloy microstructure.

were observed in the interdendritic areas, as shown in Fig. 8. Such tendency is commonly observed in cast nickel-based superalloys.[30–32]

TEM Analysis

TEM images (bright field) representative of the alloy γ-matrix, a eutectic mixture in which one phase is rich in Ni and Zr, and precipitates of a phase rich in Mo are shown in Figs. 9 and 10, respectively.

The results of the SAED analysis corresponding to the microstructure images are given in Figs. 9 and 11 and in Table V. On the basis of the obtained

results, it can be stated that the alloy matrix is a γ-Ni solid solution strengthened by cubic, coherent precipitates of the γ' (Ni_3AlTi) phase. These observations are in agreement with the literature data.[2,13]

It was found that the phase rich in Ni and Zr is Ni_7Zr_2 (Table V). It has a monoclinic structure (mC36; C2/m(12)), with a = 4.698 Å, b = 8.235 Å, c = 12.193 Å, and the angle β = 95.83°. The following crystallographic relationships between the Ni_7Zr_2 phase and the γ matrix were identified:

$[013]\gamma//[21\text{-}1]Ni_7Zr_2$ and $(\text{-}13\text{-}1)\gamma// \sim (022)\ Ni_7Zr_2$— see Fig. 11a
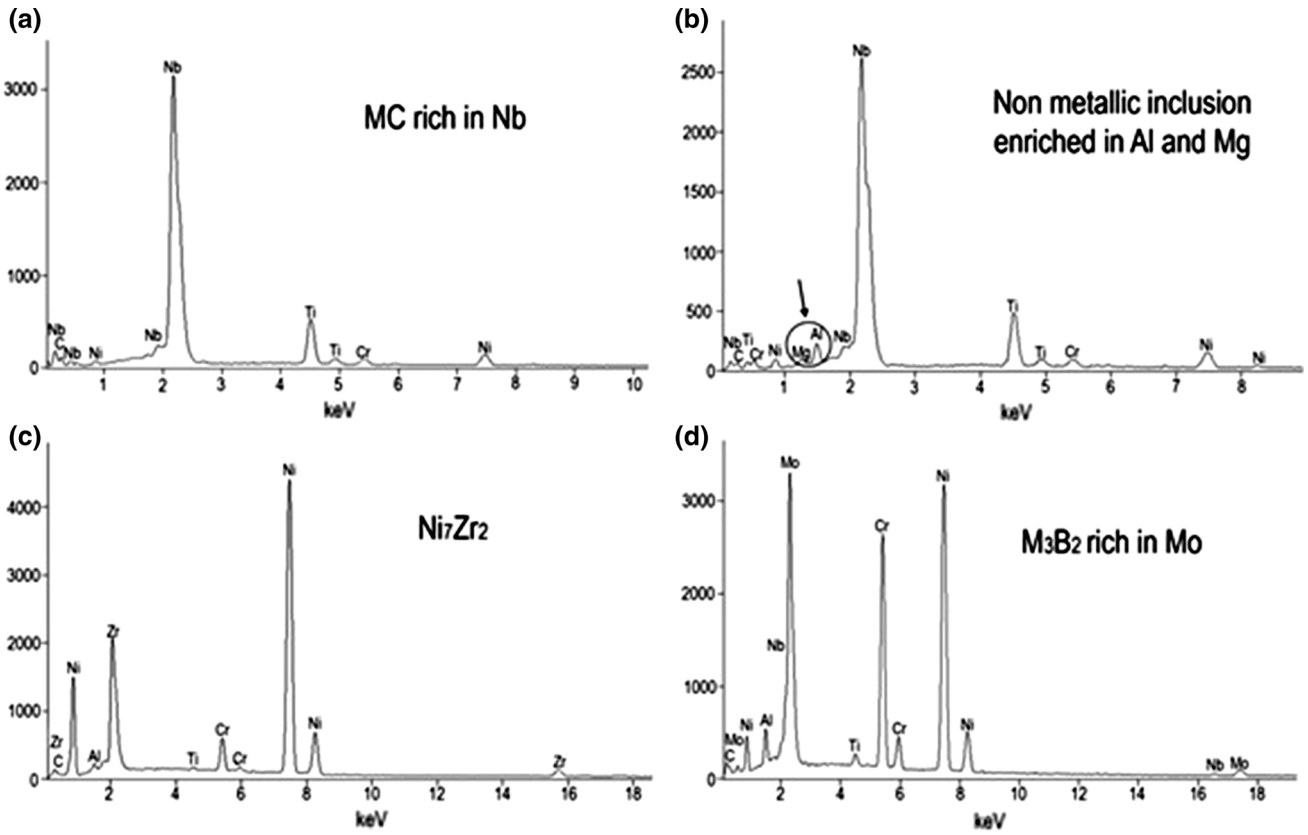
Fig. 6. Spectrograms for NbC (a), nonmetallic inclusion rich in Al and Mg observed in the cores of NbC carbides (b), Ni_7Zr_2 (c), and M_3B_2 (d).
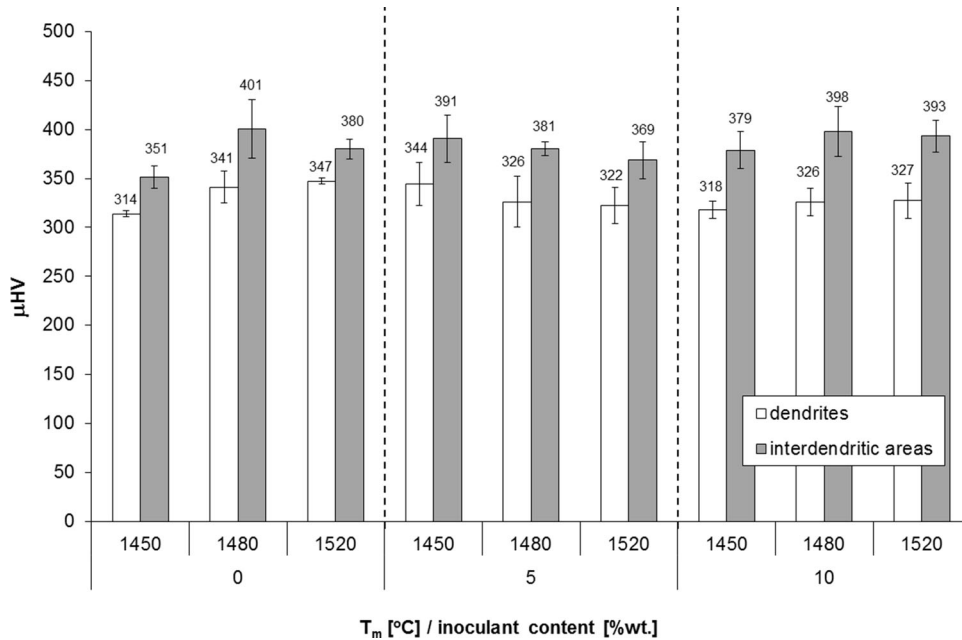

Fig. 7. Microhardness of the dendrites and the interdendritic areas for different melt-pouring temperatures and $CoAl_2O_4$ contents.

The Influence of the Melt-Pouring Temperature and Inoculant Content on the Macro and Microstructure of the IN 713c Ni-Based Superalloy

193

Table IV. Segregation of main alloying elements in the IN 713C superalloy

Trial parameters		$k = C_D^i/C_{ID}^i$				
CoAl$_2$O$_4$ content (wt.%)	T_m (°C)	Al	Ti	Cr	Mo	Nb
0	1450	1.19	0.93	0.92	0.76	0.73
	1480	1.07	1.01	0.93	0.78	0.82
	1520	1.03	0.90	0.99	0.85	0.59
5	1450	1.03	1.10	0.99	0.91	0.94
	1480	1.09	0.88	0.93	0.79	0.75
	1520	1.08	0.89	0.97	0.85	0.89
10	1450	1.11	0.95	0.91	0.73	0.53
	1480	1.13	1.00	0.84	0.78	0.63
	1520	1.04	0.95	1.02	0.66	0.64

C_D^i stands for the element concentration in dendrite and C_{ID}^i for the element concentration in interdendritic areas.
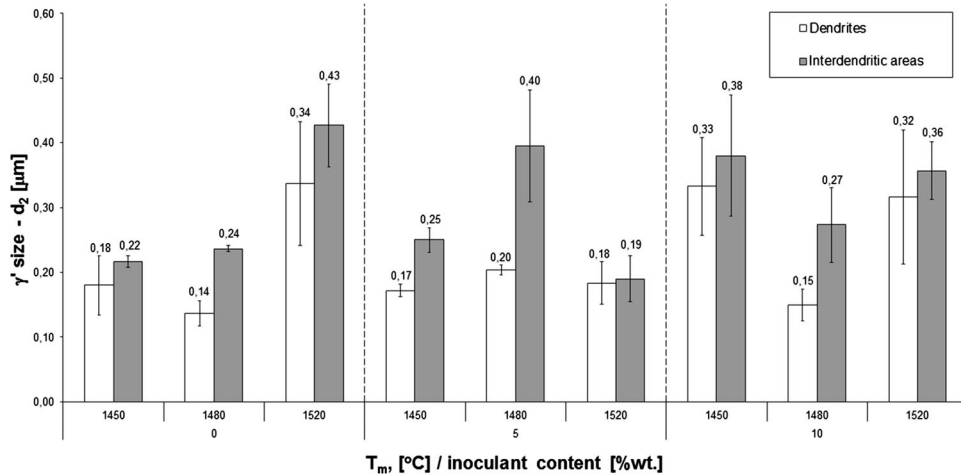

Fig. 8. Size of the γ' phase precipitates in the dendrites and the interdendritic areas for different melt-pouring temperatures and CoAl$_2$O$_4$ contents.

[-112]γ//[101]Ni$_7$Zr$_2$ and (-11-1)γ// ∼ (-202)Ni$_7$Zr$_2$ —see Fig. 11b
[011]γ//[201]Ni$_7$Zr$_2$ and (-200)γ//∼ (-204)Ni$_7$Zr$_2$ —see Fig. 11c

The phase rich in Mo is M$_3$B$_2$ boride with a tetragonal lattice (tP10, F4/mbm) and a = b = 5.775 Å and c = 3.145 Å.

DISCUSSION

Influence of T_m on SDAS and Surface Grain Size

The secondary dendrite arm spacing is correlated with the local solidification time t_{SOL}, cooling rate, temperature gradient G, and solidification rate v (Eq. 1).[33] The cooling rate, thermal gradient, and solidification rate are determined by the thermophysical properties of the alloy and shell mold, the casting process conditions (e.g., melt-pouring temperature, shell temperature, temperature of the shell cooling chamber after casting, casting, and

shell wall cross-section thicknesses), and the heat transfer coefficients between the casting and shell mold:

$$\text{SDAS} \sim \left(t_{SOL}\right)^{1/3} \sim \left(\frac{1}{Gv}\right)^{1/3} \qquad (1)$$

In the present study, no evidence for correlation between SDAS and the melt-pouring temperature or the inoculant content was found (Fig. 4). The works[21,22] present results that show that when the melt-pouring temperature is constant and the variable is the inoculant content, there are no meaningful differences between SDAS values, despite significant differences in the grain size, which is confirmed by our results. It means that if the constant melt-pouring temperature cooling rate, thermal gradient, and solidification rate are constants, the introduction of inoculant to the prime coat is negligible. However, an increase in the melt-pouring temperature accompanied by a decrease in the cooling rate will be manifested in an increase in

SDAS. The investment casting of nickel alloys into ceramic molds is characterized by very low cooling rates (in the presented work an average of 10°C/min to 12°C/min in the temperature range from T_m to 650°C). It stems from the fact that the ceramic mold has a very low thermal conductivity value (for castings used by the authors, it is 1.09 W/(mK) at 1200°C and 0.77 W/(mK) at 600°C). Additionally, heat insulating materials (Fiberfrax® wrapping)
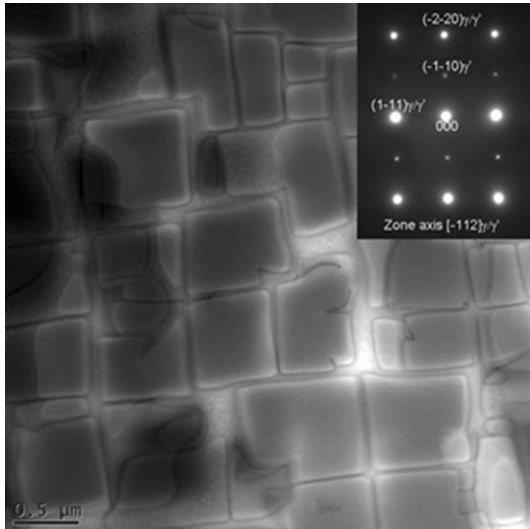

Fig. 9. TEM image (bright field) and corresponding SAED pattern for cubic precipitates of the γ' phase in the matrix of the γ phase.
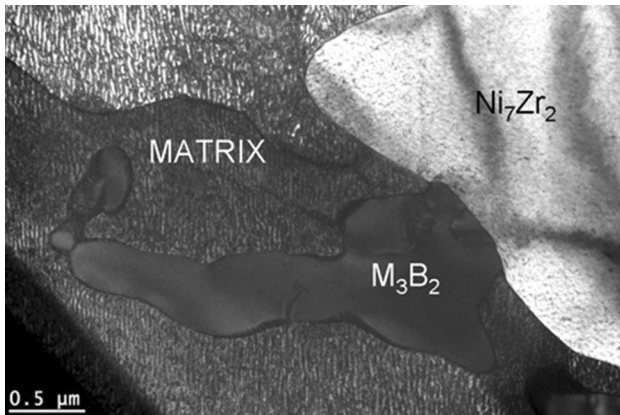

Fig. 10. TEM image (bright field) of Ni7Zr2 and M3B2 phases.

were used, which also decreases the cooling rate. Another fact worth mentioning is that the maximum difference between the melt-pouring temperatures is only 70°C, and the temperature of the mold during casting is quite high (1200°C).

In the work,[33] it has been shown for plate castings (width of 40 mm and thickness of 4 mm) of the superalloy IN738LC, a substantial change in temperature gradient occurs in the surface zone of the casting. On the basis of the casting cross section, it has been found that the gradient was 2.75 K/mm on the surface and then decreased rapidly away from the surface. At the distance of 10 mm from the surface, the gradient was 0.25 K/mm and remained constant in the central part of the plate. Close to a tenfold decrease in the gradient caused a one-third increase in SDAS, or 30 μm in the surface zone and 40 μm in the volume of the casting, respectively.

It should also be noted that the mentioned measurements of SDAS were made in the volume of the material and not on its surface, as it was in the case of determining the grain size. By taking into account the parameters of our process discussed earlier (small differences in melt-pouring temperatures, and irrespective of the temperature cooling rates caused by thermophysical properties of the mold material), as well as the area selection for determining SDAS, the minor changes in cooling rate, thermal gradient, and solidification rate in this study provide evidence for a correlation between SDAS and the melt-pouring temperature or the inoculant content. In commercial practice, this means that some scatter between melt-pouring temperatures can be allowed without the consequence of a significant influence on SDAS in the casting volume and, therefore, on its mechanical properties.

It has to be remembered, however, that some significant differences in both the macro- and microstructure of the casting may occur on the surface and in the surface zone in relation to the casting volume for different melt-pouring temperatures, as evidenced by the grain size results in Fig. 4. A rise of 70°C in the melt-pouring temperature causes an increase in the grain size on the casting surface of each case analyzed. It is consistent with the expectation that an increase in the melt-pouring temperature lowers the cooling rate and may result in grain coarsening. The differences

Table V. Comparison of the experimental $d_{(hkl)}$ spacings with values from *powder diffraction files*

Ni_7Zr_2	(hkl)	(020)	(022)	(–112)	(1–11)	(113)	(–131)
	$d_{(hkl)}$ (Å)	4.04	3.52	3.42	3.80	2.94	2.31
		4.12[a]	3.51[a]	3.41	3.76[a]	2.75[a]	2.30[a]
M_3B_2	(hkl)	(010)	(111)	(101)	(211)	(110)	(120)
	$d_{(hkl)}$ (Å)	5.72	2.49	2.76	2.00	4.07	2.56
		5.74[b]	2.49[b]	no data[b]	1.99[b]	4.09[b]	2.58[b]

[a]PDF 71-0543. [b]PDF 18-0839.

The Influence of the Melt-Pouring Temperature and Inoculant Content on the Macro
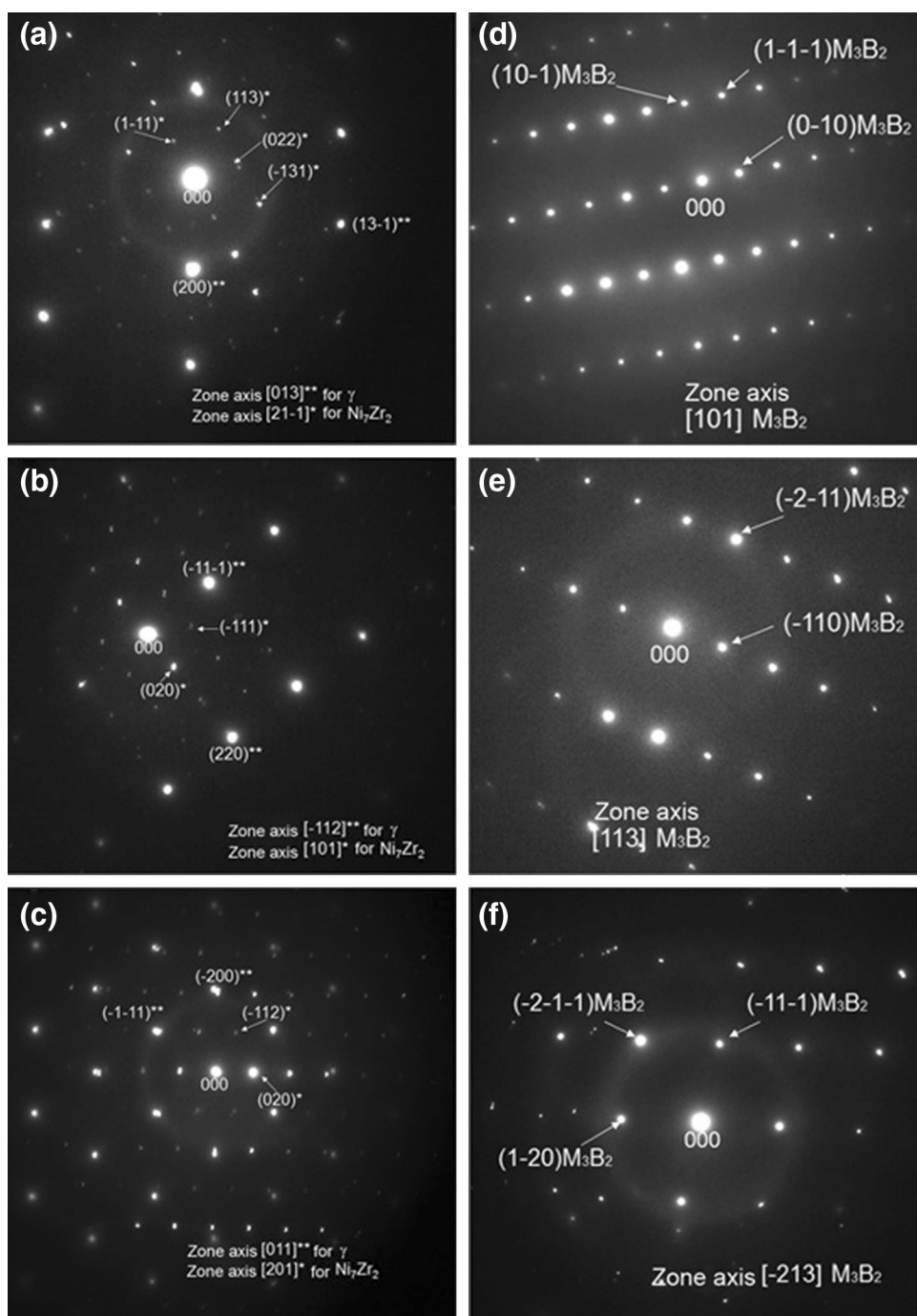and Microstructure of the IN 713c Ni-Based Superalloy
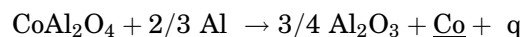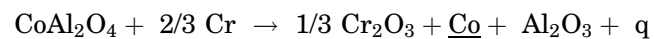
195

Fig. 11. SAED patterns for precipitations of Ni7Zr2 (a–c) and M3B2 (d–f)—corresponding to Fig. 10.
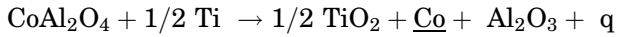
in macro- and microstructure (SDAS, morphology, and the size of constituents and γ' precipitates) in the surface zone and in the volume of the casting will be the topic of our next study.

Refining Mechanism of Surface Macro Grains

The modification mechanism of nickel alloys with the use of cobalt aluminate is widely discussed in the literature.[19–24] The alloying elements react with CoAl$_2$O$_4$. As a result of the process on the surface of the shell mold, Co particles are formed that act as nucleation cites for heterogeneous crystallization of the γ phase (q is the latent heat of the presented reactions):

$$CoAl_2O_4 + 2/3\ Cr \rightarrow 1/3\ Cr_2O_3 + \underline{Co} + Al_2O_3 + q$$

$$CoAl_2O_4 + 2/3\ Al \rightarrow 3/4\ Al_2O_3 + \underline{Co} + q$$

$$CoAl_2O_4 + 1/2\ Ti\ \rightarrow 1/2\ TiO_2 + \underline{Co} +\ Al_2O_3 +\ q$$

At a temperature above 450°C, cobalt has the same crystallographic system (FCC) as the IN713C matrix (γ phase). The lattice constants of both phases, $a_{Co} = 3.5447$ Å and $a_\gamma = 3.5975$ Å, are similar, and the lattice misfit (defined as $f = \frac{a_\gamma - a_{Co}}{a_{Co}} 100\%$) of the nucleation sites (Co) and the γ phase equal only 1.5%. The similarity of crystallographic systems and a low value of lattice misfit guarantees effective refinement of the surface macrograins.[25]

In earlier studies,[23,24] it has been confirmed that Co-generated nucleation sites are mainly observed on the surface of the shell mold and that their size reaches up to 4 μm. In Ref. 24, it has also been shown that as a result of the modification, there is a refinement of Co to a depth of about 10 μm. It should be noted, however, that in this case the prime coat of the shell mold contained only $CoAl_2O_4$ and a binder. In Ref. 34 the depth of the refinement was only 0.01 μm for 10% inoculant content. This is substantiated by the fact that the effectiveness of the modification significantly decreases with distance from the surface of the casting. Thus, this type of modification is not applicable for thick-walled castings.

In contrast, the unquestionable advantage of this type of modification is the fact that the $CoAl_2O_4$ reduction reaction is an exothermic reaction, which effectively prevents the formation of the so-called "chill grains" considered to be a casting defect. These defects were not observed in our castings.

As it has already been mentioned, for castings that underwent modification and an increase of T_m, there is an increase in the grain size. In the case of unmodified castings, the grain size increases 2.3 times. For modified castings, it increases 1.8 and 1.4 times for 5% and 10% inoculant content, respectively. An increase in the grain size is primarily associated with a decrease in the cooling rate during increasing T_m; it can be, however, supposed that in the case of high melt-pouring temperatures (and a relatively high temperature of the shell mold), some nucleation cites can be remelted, which would also contribute to the increase of the grain size. Consequently, the increase in the inoculant content, while applying high T_m, is desirable. Additionally, when $CoAl_2O_4$ content in the prime coat is increased, a greater number of nucleation cites may be "generated." If some of them remelt, then a sufficiently large number of nucleation cites remains, ensuring grain refinement.

Microstructure Constituents and Solidification Path

Based on the DTA investigations and microstructure characteristic of the IN713C superalloy, it may be concluded that in the first stage of solidification, γ-phase crystals are formed. Next, with the decrease of temperature, the solubility of alloying elements (such as Nb, Mo, Ti, C, and B) in the γ-phase is reduced, which is manifested by their segregation at the γ-phase dendrite–interdendritic liquid interface. Favorable conditions for the precipitation of NbC primary carbides occur (according to the typical reactions L $\rightarrow$ MC or L $\rightarrow$ γ + MC) in the interdendritic areas. These areas offer some solubility of other carbide-forming elements, such as Ti, Mo, or Cr. The precipitation of MC in the interdendritic liquid depletes these elements and enriches them with Al and Ti—the elements that are γ' formers.

In the final stage of solidification, a eutectic reaction L $\rightarrow$ γ + γ' in the areas where the interdendritic liquid is enriched with Al and Ti takes place. The solubility of Zr and B in γ and γ' is extremely low,[31,32,35,36] and thus, the aforementioned elements segregate into the boundary (γ/γ') eutectic–residual liquid interface, thus, providing favorable conditions for the precipitation of phases rich in Zr like Ni_5Zr or Ni_7Zr_2 and phases rich in B like M_5B_3 or M_3B_2 borides.[31,32,35,36]

On the basis of phase equilibrium[37] for the binary alloy Ni-Zr, it can be clearly stated that only one eutectic reaction occurs (which takes place at 1170°C), in which L $\rightarrow$ γ + Ni_5Zr. This stands in clear contrast with our observations.

According to the equilibrium system,[37] the Ni_7Zr_2 phase is formed directly from the liquid at 1420°C. Next, at 1300°C and 1180°C, two peritectic reactions take place: L + Ni_7Zr_2 $\rightarrow$ Ni_5Zr and L + Ni_7Zr_2 $\rightarrow$ $Ni_{21}Zr_8$. It can be concluded that, at ambient temperature, no Ni_7Zr_2 phase occurs in the alloy eutectics. This phase might be present in the microstructure but not in the eutectic.

To explain the presence of the Ni_7Zr_2 phase in the eutectic, one should refer to the equilibrium systems of multi-element alloys. Examinations of alloy Ni-7.9Al-7.7Cr-1.4Mo-1.7Zr-0.008B in Ref. 38 suggest that the residual liquid rich in Zr reacts with the eutectic phase or the primary phase γ' according to the peritectic reaction L + γ' $\rightarrow$ γ + Ni_7Zr_2. The eutectic reaction L $\rightarrow$ γ +Ni_7Zr_2 + Ni_5Zr is also possible.[38] However, in our studies, we did not observe the presence of the Ni_5Zr phase. This suggests that the lamellar structure of γ/Ni_7Zr_2 can be a result of the peritectic reaction. It should be noted, however, that in the immediate vicinity of the phase mixture γ/Ni_7Zr_2, precipitates of M_3B_2 borides were found. In Ref. 39 it was proven that the formation of eutectic ($\gamma + \gamma'$) may be accompanied by the precipitation (from the residual liquid rich in Zr and B) of a ternary eutectic, according to the equation L $\rightarrow$ γ + Ni_7Zr_2 + M_3B_2, which is in agreement with our observations.

CONCLUSION

The results show that the cobalt aluminate (added in the range of 5–10 wt.% to the prime coat of the shell mold) significantly reduced the size of the EX grains. Additionally, the presence of an inoculant decreases the size and fraction of the columnar

The Influence of the Melt-Pouring Temperature and Inoculant Content on the Macro and Microstructure of the IN 713c Ni-Based Superalloy

197

grains. However, the increase of the inoculant concentration from 5 wt.% to 10 wt.% causes no significant improvement. Also, the increase of the melt-pouring temperature from $T_m = 1450°C$ to $T_m = 1520°C$ results in an increase in the mean equivalent diameter of the EX grains in all the analyzed cases.

Independent of the melt-pouring temperature, the IN713C superalloy has a nonhomogenous dendritic structure in the as-cast state; however, no significant differences were found between the SDAS. The mean values of SDAS are within the range of 66 μm to 89 μm.

The melt-pouring temperature and the inoculant content do influence the phase composition of the alloy. The alloy matrix consists of the γ-Ni phase strengthened by cubic, coherent precipitates of γ'-Ni$_3$(AlTi) phase. The interdendritic areas reveal the presence of NbC primary carbides, as well as that of eutectics: $\gamma + NbC$, $\gamma + \gamma'$ and $\gamma + Ni_7Zr_2 + M_3B_2$.

Examinations of the chemical composition of the dendrites and interdendritic areas confirmed the segregation of molybdenum, niobium, and chromium into the interdendritic areas, whereas aluminum enriched the cores of the dendrites, regardless of the conditions of the casting process. The segregation of elements of large atomic radii (Nb-146 pm and Mo-137 pm) significantly affects the matrix solid solution strengthening, as well as the size of γ', which causes an increase in hardness of the interdendritic areas.

ACKNOWLEDGEMENT

OPEN ACCESS

REFERENCES

1. J.R Brinegar, J.R Mihalisin, J. VanderSluis, *Proc. Int. Symp. Super.* 53 (1984).
2. F. Zupanic, T. Boncina, A. Krizman, and F.D. Tichelaar, *J. Alloy. Compd.* 329, 290 (2001).
3. D. Gelmedin and K.H. Lang, *Proc. Eng.* 2, 1343 (2010).
4. T.M. Maccagno, A.K. Koul, J.-P. Immarigeon, L. Cutler, R. Allem, and G. L'esperance, *Metall. Mater. Trans. A* 21, 3115 (1990).
5. N. Elliaz, G. Shemesh, and R.M. Latanision, *Eng. Fail. Anal.* 9, 31 (2002).
6. M. Tabuchia, K. Kubo, K. Yagi, A.T. Yokobori Jr, and A. Fuji, *Eng. Fract. Mech.* 62, 47 (1999).
7. A. Ges, H. Palacio, and R. Versaci, *J. Mater. Sci.* 29, 3572 (1994).
8. G.A. Kool, *J. Thermal Spray Technol.* 5, 31 (1996).
9. C. Persson and P.-O. Persson, *J. Mater. Eng. Perform.* 2, 565 (1993).
10. A.K. Bhambri, T.Z. Kattamis, and J.E. Morral, *Metall. Trans. B* 6B, 523 (1975).
11. A. Somoza, G. Santos, A. Ges, R. Versaci, and F. Plazaola, *Phys. Stat. Solidi (a)* 174, 189 (1999).
12. M. Lachowicz, W. Dudziński, K. Haimann, and M. Podrez-Radziszewska, *Mater. Sci. Eng. A* 479, 269 (2008).
13. M. Lachowicz, W. Dudziński, and M. Podrez-Radziszewska, *Mater. Charact.* 59, 560 (2008).
14. M.B. Lachowicz, *Arch. Foundry Eng.* 10, 11 (2010).
15. C.T. Sims, N.S. Stoloff, and W.C. Hagel, *Superalloys II* (New York: Wiley, 1987).
16. J.R. Davis, *Nickel, cobalt and their alloys* (Almere: ASM International, 2000), pp. 68–85.
17. F. Binczyk, J. Śleziona, and A. Kościelna, *Arch. Foundry Eng.* 9, 13 (2009).
18. F. Binczyk and J. Śleziona, *Arch. Foundry Eng.* 10, 195 (2010).
19. Y. Xiong, A. Yiping Guo, W. Liu, and L. Liu, *Sci. Technol. Adv. Mater.* 2, 13 (2011).
20. L. Liu, R. Zhang, L. Wang, S. Pang, and B. Zhen, *J. Mater. Process. Technol.* 77, 300 (1998).
21. P. Zhijiang, J. Shuqin, Z. Zehai, and L. Yan, *China Foundry* 7, 121 (2010).
22. L. Liu, T. Huang, Y. Xiong, A. Yang, Z. Zhao, R. Zhang, and J. Li, *Mater. Sci. Eng. A* 394, 1 (2005).
23. W. Jin, F. Bai, T. Li, and G. Yin, *Mater. Lett.* 62, 1585 (2008).
24. F. Jian and Y. Bin, *High temperature alloys for gas turbines*, ed. R. Brunetaud (New York: Springer, 1982), pp. 987–997.
25. W. Kurz and D.J. Fisher, *Fundamentals of solidification* (Dürnten: Trans Tech, 2005).
26. T. Wejrzanowski, M.Sc. Thesis, Warsaw University of Technology, Warsaw, Poland, 2000.
27. S. Zlá, B. Smetana, M. Žaludová, J. Dobrovská, V. Vodárek, K. Konečná, V. Matějka, and H. Francová, *J. Therm. Anal. Calor.* 110, 211 (2012).
28. W.J. Boettinger, U.R. Kattner, K.-W. Moon, and J.H. Perepezko, *Special Publication 960* (Institute of Standards and Technology, 2006).
29. C.J. Burton, *TMS Superalloys* (1976), p. 147.
30. R.K. Sidhu, O.A. Ojo, and M.C. Chaturvedi, *Metall. Mater. Trans. A* 40A, 150 (2009).
31. O.A. Ojo, N.L. Richards, and M.C. Chaturvedi, *Scripta Mater.* 51, 683 (2004).
32. R.K. Sidhu, O.A. Ojo, and M.C. Chaturvedi, *J. Mater. Sci.* 43, 3612 (2008).
33. M.M. Franke, R.M. Hilbinger, C.H. Konrad, U. Glatzel, and R.F. Singer, *Metall. Mater. Trans. A* 42A, 1847 (2011).
34. F. Binczyk, J. Śleziona, and P. Gradoń, *Kompozyty* 11, 49 (2011).
35. H.R. Zhang, O.A. Ojo, and M.C. Chaturvedi, *Scripta Mater.* 58, 167 (2008).
36. L.O. Osoba, R.G. Ding, and O.A. Ojo, *Metall. Mater. Trans. A* 43a, 4281 (2012).
37. P. Nash and C.S. Jayanth, *Bull. Alloy Phase Diagr.* 5, 144 (1984).
38. H.B. Motejadded, M. Soltanieh, and S. Rastegari, *J. Mater. Sci. Technol.* 27, 885 (2011).
39. S.S. Babu, S.A. David, J.M. Vitek, and M.K. Miller, International Field Emission Society IFES'96 Proceedings of the 43rd International Field Emission Symposium 1996.

Nowoczesne spoiwa ceramiczne w odlewnictwie precyzyjnym

Modern ceramic binders using in investment casting technology

Rafał Cygan[1,2]

[1]Politechnika Rzeszowska, Wydział Budowy Maszyn i Lotnictwa, Laboratorium Badań Materiałów dla Przemysłu Lotniczego Al. Powstańców Warszawy 8, 35-029 Rzeszów

[2]CPP Poland Sp. z o.o., ul. Hetmańska 120, 35-079 Rzeszów

Słowa kluczowe: odlewnictwo precyzyjne, spoiwo ceramiczne, mieszanki formierskie, formy ceramiczne, turbinowe silniki lotnicze

Kay: investment casting, binder, slurry, ceramic moulds, turbine aircraft engines

Streszczenie:

W artykule przedstawiono wyniki badań nowoczesnych materiałów ceramicznych stosowanych w produkcji krytycznych elementów części gorącej silników lotniczych z wykorzystaniem technologii odlewania precyzyjnego. W procesie wytwarzania części lotniczych stosowana jest powszechnie technologia precyzyjnego odlewania w wielowarstwowych formach ceramicznych. Technologia ta umożliwia precyzyjne odtwarzanie, skomplikowanych geometrycznie, przestrzennych kształtów części lotniczych. Ekstremalnie wysokie i rosnące wymagania jakościowe, jakie muszą być spełnione przez gotowy wyrób (precyzyjny odlew części gorącej turbinowego silnika lotniczego), powodują konieczność bieżącego permanentnego rozwiązywania, złożonych pod względem technologicznym, problemów związanych z powstawaniem wad odlewniczych oraz wad powierzchni odlewów generowanych przyczynami zależnymi od jakości technologicznej ceramicznej formy odlewniczej. Zapobieganie powstawaniu wad odlewniczych realizowane jest poprzez optymalizowanie parametrów procesu metalurgicznego oraz poprzez optymalizowanie konstrukcyjnej i technologicznej budowy form odlewniczych. Natomiast zapobieganie powstawaniu wad generowanych przyczynami zależnymi od jakości technologicznej formy odlewniczej może być realizowane poprzez poprawny dobór materiałów technologicznych i pomocniczych do budowy samonośnych form ceramicznych oraz parametrów procesu ich wytwarzania.

Streszczenie en:

In the present paper study on modern ceramic materials used in the precision casting technology during the production of hot gas path components for aircraft engines was performed. In the manufacturing of engines components, lost-wax casting technology using multi-layer ceramic moulds is commonly used. This technology enables precise and repeatable production of geometrically complex shapes of aircraft parts such as thin-walled turbine blade and vanes. The extremely high and ever-increasing quality requirements that must be met by a finished product (castings) cause the need to solve on a current basis, technologically complex problems. They are related to the formation of casting defects, both volume and surface ones, generated by reasons dependent on the technological quality of the ceramic moulds. Prevention of foundry defects is accomplished by optimizing the parameters of the metallurgical process and by optimizing the construction of shell moulds. Prevention of defects generated by causes dependent on the quality of the shell mould can be realized by refining the quality of technological and reinforcing materials for the mould construction and by optimizing the parameters of their manufacturing process.

Odlewnictwo precyzyjne jest jedną z najstarszych metod wytwarzania. W starożytności, w Azji Środkowej (3000 p.n.e.) oraz Grecji (500 p.n.e.) wykonywano ta metodą przedmioty codziennego użytku (rys. 1). Początkowo, materiałem stosowanym w produkcji form odlewniczych była glina, która następnie została zastąpiona przez materiały ceramiczne [1].
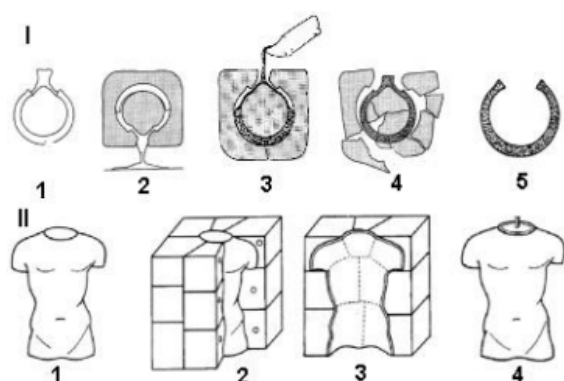
Rys. 1. Zarys technologii odlewania z wykorzystaniem wosku. I – technologia stosowana w Indiach i Azji Środkowej ok. 3000 r. p. n. e. : 1 – model woskowy, 2 – gliniana forma, 3 – zalewanie wnęki formy, 4 – rozbijanie formy, 5 – odlew. II – technologia stosowana w Grecji

500 r. p. n. e.: 1 – model z gliny, 2 – forma z gliny, 3 – wnęka formy pokryta warstwą wosku, 4 – model woskowy [2].

Stosowanie procesów metalurgicznych do wytwarzania przedmiotów użytkowych datuje się od 7000 lat p. n. e (tab. 1) [1].

Tabela 1. Zastosowanie metali nieżelaznych do wytwarzania przedmiotów użytkowych

| Lata p.n.e.	Rodzaj materiału i procesu
Ok. 7000	Przetapianie samorodków złota - odlewanie, kucie
Ok. 7000	Przetapianie samorodków miedzi - odlewanie, kucie
Ok. 6000	Wytapianie ołowiu z rudy - odlewanie
Ok. 5000	Wytapianie miedzi z rudy - odlewanie, kucie
Ok. 4000	Wytapianie miedzi stopowej z rud mieszanych zawierających As i Pb - odlewanie, kucie
Ok. 3000	Wytapianie cyny z rudy - odlewanie
Ok. 2500	Otrzymywanie brązu przez stapianie miedzi z rudą cyny i miedzi z cyną - odlewanie, kucie
Ok. 1000	Otrzymywanie mosiądzu przez stapianie miedzi z rudą cynku w obecności węgla - odlewanie, kucie

W okresie średniowiecza odlewanie jest już powszechnie stosowane do produkcji wyrobów artystycznych i jubilerskich niemal we wszystkich częściach świata (Europa, Ameryka płd., Afryka, Azja) [3].

Dynamiczny rozwój procesów otrzymywania metali i ich stopów, jak również technik odlewania precyzyjnego (metoda traconego wosku) pozwolił na uzyskanie odlewów o wysokiej jakości (właściwości mechaniczne, dokładność wymiarów) (rys. 2). Obecnie tą metodą produkuje się odlewy dla przemysłu lotniczego, zbrojeniowego, maszynowego, motoryzacyjnego, elektronicznego, optycznego i na potrzeby medycyny (ale również w dalszym ciągu odlewy artystyczne) [4].
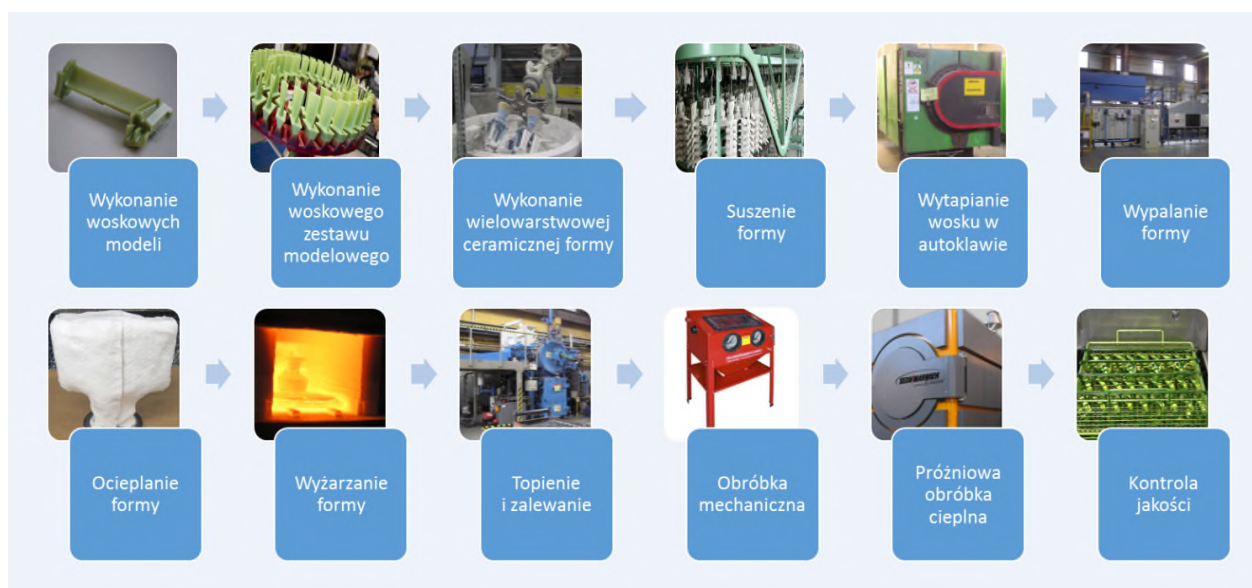
Rys. 2. Schemat procesu odlewania metodą traconego wosku

Do wykonywania odlewniczych form ceramicznych stosuje się obecnie różne rodzaje spoiw, będących głównym składnikiem lejnych mas ceramicznych. Jednym z podstawowych materiałów wykorzystywanych w tej technologii jest krzemian etylu $(C_2H_5O)_4Si$, który poddawany jest procesowi hydrolizy zgodnie z reakcją (1):

$$(C_2H_5O)_4Si + 4H_2O \longrightarrow Si(OH)_4 + 4C_2H_5OH \qquad (1)$$
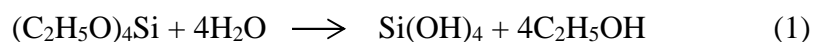
W wyniku hydrolizy powstaje nierozpuszczalna w wodzie krzemionka $Si(OH)_4$, która jest chemicznie obojętna, odporna na działanie wysokiej temperatury i posiada zdolność wiązania sypkich materiałów ceramicznych, wskutek hydrolizy z alkoholem etylowym kwasu chlorowodorowego i amoniaku. Spoiwa te charakteryzują się dobrymi właściwościami technologicznymi oraz krótkim czasem schnięcia. Ich wadą jest szkodliwy wpływ na zdrowie pracowników oraz środowisko naturalne. Dlatego spoiwa zawierające krzemionkę $Si(OH)_4$ są obecnie wycofywane z produkcji. Zastępuje się je spoiwami na bazie krzemionki koloidalnej, która jest zawiesiną koloidalnych cząstek krzemionki (SiO_2) w wodzie i charakteryzuje się przydatnością technologiczną w długim czasie oraz obojętnością dla środowiska naturalnego [5]. Wadą mieszanek ceramicznych na bazie spoiw wodnych jest dłuższy czas schnięcia poszczególnych warstw oraz nierównomierne pokrywanie skomplikowanych geometrycznie kształtów, w szczególności ostrych krawędzi.

Do podstawowych materiałów ceramicznych stosowanych w odlewnictwie precyzyjnym nadstopów niklu należą korund, mulit i glinokrzemiany. Do wykonania masy lejnej scharakteryzowanej w powyższym artykule zastosowano mulit, szeroko używany w

technologii form ceramicznych. Charakteryzuje się on małą gęstością 3,05g/cm^3 (niezależną od temperatury), wysoką temperaturą topnienia 1810°C, dobrą odpornością na pełzanie oraz wstrząsy cieplne (z uwagi na niski liniowy współczynnik rozszerzalności cieplnej), małą przewodnością cieplną oraz dużą odpornością chemiczną. Należy zaznaczyć, że współczynnik liniowej rozszerzalności cieplnej α mulitu zależy od temperatury - w temperaturze pokojowej wynosi 3,55*10-7 1/K podczas gdy w temperaturze 1173K jest o rząd wielkości wyższy. Przewodność cieplna mulitu jest porównywalna z przewodnością cieplną krzemianu cyrkonu. Syntetyczny mulit charakteryzuje się dużą czystością chemiczną - zawartość zanieczyszczeń nie przekracza 0,5%. Dostępne gradacje mączek, umożliwiają zastosowanie mulitu jako materiału na osnowę ciekłych mas ceramicznych stosowanych na tzw. konstrukcyjne warstwy form, a także jako materiał na ich obsypki. Jednak z uwagi na wysokie ceny (2,0 - 2,5 euro/kg) mulit stosuje się do wytwarzania form ceramicznych do odlewania odpowiedzialnych elementów części gorącej turbinowych silników lotniczych.

Podstawowymi materiałami (oprócz spoiwa) do wytwarzania mieszanek formierskich wykorzystywanych w odlewnictwie precyzyjnym są również proszki ceramiczne stanowiące wypełniacz dodawany do spoiwa podczas wytwarzania masy lejnej. Ceramiczne materiały formierskie (osnowy mieszanin formierskich oraz obsypki) są najczęściej tlenkami metali, które muszą spełniać określone wymagania. Materiały na pierwszą warstwę formy odlewniczej powinny charakteryzować się niską reaktywnością w kontakcie z ciekłym stopem, stabilnością chemiczną w temperaturze do 1500 °C i próżni 10^{-4} Tr, odpornością na erozję i łatwością formowania gładkich powierzchni. Materiały na konstrukcyjne warstwy formy odlewniczej powinna cechować wysoka wytrzymałość zarówno w stanie surowym jak i temperaturze ok. 1400 °C i próżni 10^{-4} Tr, odporność na pełzanie, łatwość formowania i wybijania odlewów - nie powinny charakteryzować się przemianami alotropowymi i mieć relatywnie niską cenę.

W celu opracowania nowych materiałów ceramicznych Odlewnia Precyzyjna Consolidated Precision Products Rzeszów współpracuje z Laboratorium Badań Materiałów dla Przemysłu Lotniczego Politechniki Rzeszowskiej. Jednym z przykładów takiej współpracy jest realizacja projektu badawczego „Opracowanie technologii odlewania krytycznych elementów części gorącej silników lotniczych z zastosowaniem materiałów ceramicznych nowej generacji", w ramach IV edycji programu LIDER. Jednym z jego celów jest opracowanie składu chemicznego i zastosowanie w praktyce przemysłowej nowoczesnych spoiw formierskich, przyjaznych zdrowiu ludzkiemu i środowisku naturalnemu. W ramach badań opracowano spoiwo na osnowie polimerowej emulsji akrylowej, zawierającej fazę stałą o objętości

względnej ok. 48-50% oraz dodatkowo 1-10 % mas. włókien szklistych. Zastosowanie włókien szklistych zwiększyło gazoprzepuszczalność, właściwości mechaniczne odlewniczych form ceramicznych oraz pozwoliło zmniejszyć liczbę nakładanych warstw, a tym samym grubość form.

Do wytwarzania ceramicznych mas odlewniczych stosowano włókna szklane o grubości 5-10 μm, przepuszczające światło (rys. 3).
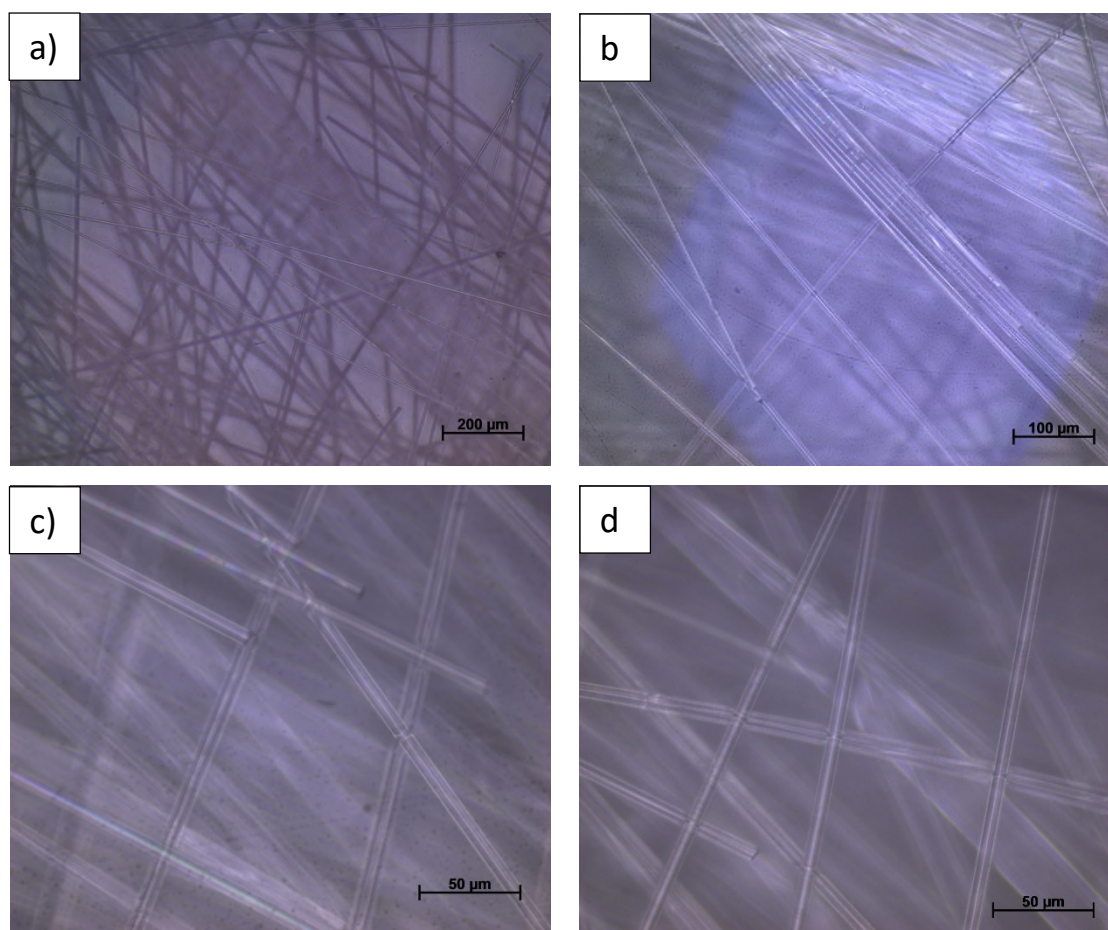
Rys. 3. Włókna szklane stosowane do wytwarzania odlewniczych mas ceramicznych na osnowie polimerowej emulsji akrylowej

Na podstawie analizy wyników badań metodą skaningowej mikroskopii elektronowej SEM z zastosowaniem metody dyssypacji energii EDS stwierdzono, że badane włókna szklane składają się z wapnia, krzemu i aluminium (rys. 4, tab. 2).
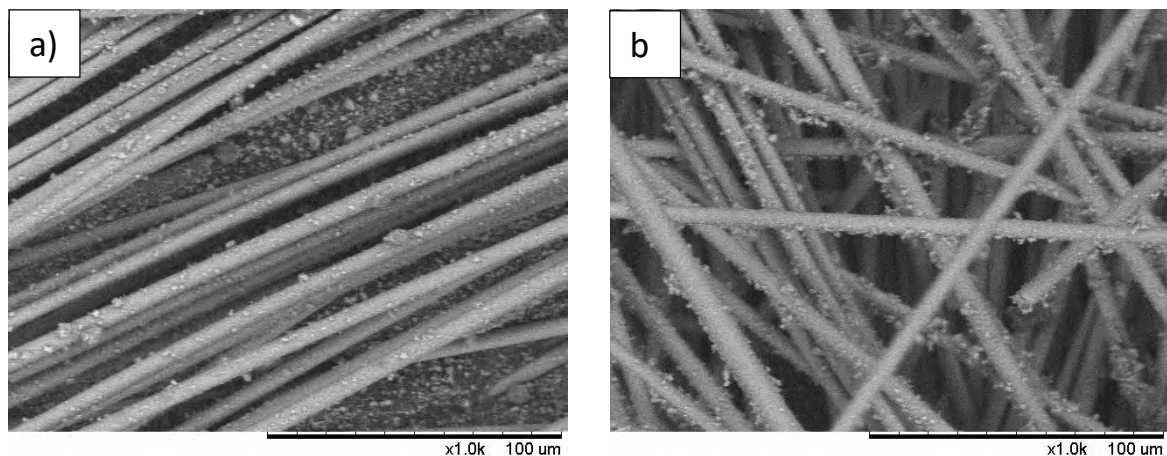
Rys. 4. Kształt i rozmiary włókien szklanych zastosowanych w spoiwie, SEM

Tabela 2. Skład chemiczny włókien zastosowane w spoiwie, EDS

Pierwiastek	Zawartość, % mas.
Al	3
Si	10
Ca	87

Próby technologiczne prowadzono w formach odlewniczych wykonanych z opracowanych mieszanek ceramicznych. Wykonane metodą wtrysku modele woskowe segmentów aparatów kierujących oraz układów wlewowych połączono w woskowe zestawy modelowe, które odtłuszczono w środku myjącym. Tak przygotowane woskowe zestawy modelowe zanurzano w lejnej masie ceramicznej a następnie obsypywano proszkiem ceramicznym w obsypywarce deszczowej. Łącznie nakładano 6 warstw ceramicznych uzyskując grubość ścianki formy ok. 8 mm (rys. 5a). Następnie formy ceramiczne umieszczono w autoklawie i poddano procesowi wytapiania wosku (temperatura 165 °C, ciśnienie 7 bar). Resztki wosku wypalano z form ceramicznych w elektrycznym piecu komorowym w temperaturze 600°C, myto w wodzie w celu usunięcia pozostałości mas lejnych i proszków ceramicznych z wnęki formy, suszono w temperaturze 80°C w czasie 4 godz,. Następnie formy ocieplano 2 warstwami maty izolacyjnej. Zalewanie form nadstopem niklu wykonano w indukcyjnym piecu próżniowym (temperatura ciekłego **stopu IN713C** 1550°C, próżnia 2x10^{-3} Tr). Odlewy segmentów aparatów kierujących (rys. 5b) poddano obróbce poodlewniczej oraz operacjom kontrolnym.
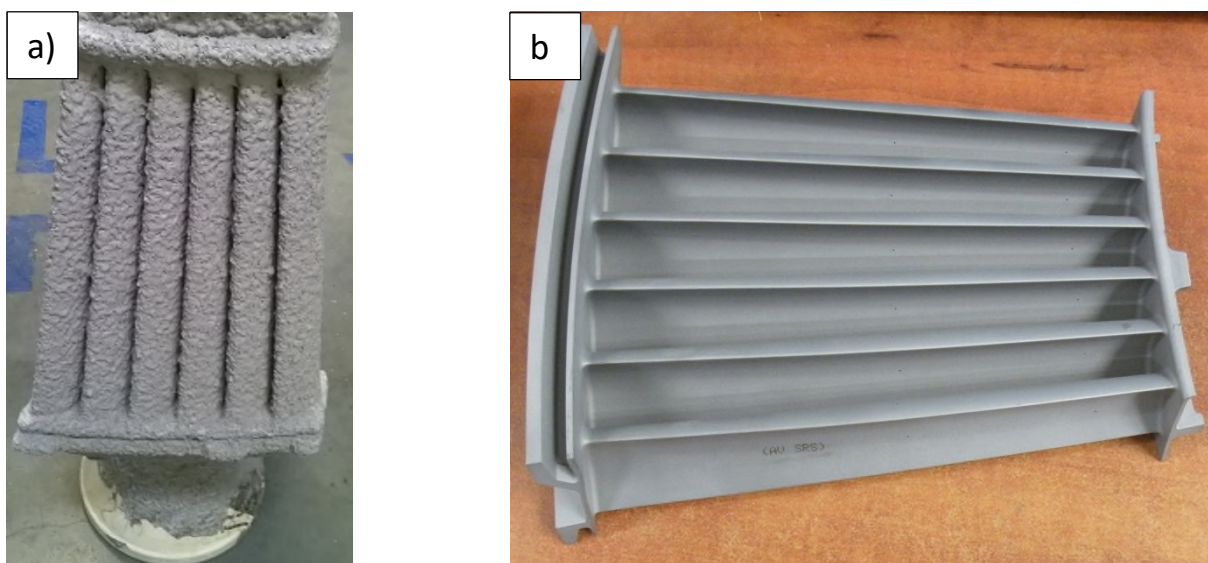
Rys.5. Ceramiczna forma odlewnicza (a), odlew segmentu aparatu kierującego turbiny niskiego ciśnienia lotniczego silnika turbinowego (b)

Podsumowanie

Skomplikowana geometria oraz rosnące wymagania jakościowe stawiane odlewom precyzyjnym z nadstopów niklu wymuszają poszukiwanie zarówno nowych materiałów ceramicznych na formy odlewnicze jak i rozwiązań technologicznych zapewniających obniżenie kosztów wytwarzania, w szczególności zmniejszenia liczby wadliwych odlewów. Jednym z kierunków obecnie intensywnie rozwijanych jest wytwarzanie form ceramicznych z zastosowaniem nowych materiałów oraz efektywniejszych metod. Przedstawiona w artykule tematyka wykonywania ceramicznych form odlewniczych jest zgodna z najnowocześniejszymi trendami. Zastosowanie spoiw wodnych, emulsji akrylowych oraz włókien szklanych jako wypełniaczy przyczyni się do zmniejszenia zanieczyszczenia środowiska oraz zwiększy efektywność procesu odlewania precyzyjnego.

Odlewy segmentów aparatów kierujących wykonane w formach ceramicznych z opracowanej mieszanki, spełniają wszystkie wymagania jakościowe (wymiary, wady odlewnicze, chropowatość powierzchni, porowatość) stawiane przez odbiorców. Opracowana mieszanka ceramiczna zawierająca włókna szklane, pozwoliła na zmniejszenie liczby wykonywanych warstw z 8 do 6, co ma bezpośredni wpływ na wzrost oszczędności wynikających ze skrócenia czasu produkcji form ceramicznych o około 25% oraz zmniejszenia masy stosowanych materiałów ceramicznych o 15%. Ceramiczne formy

odlewnicze wykonywane są w firmie CPP Polska na zrobotyzowanym stanowisku produkcyjnym a zmniejszenie liczby warstw przyczynia się bezpośrednio do wzrostu przepustowości linii produkcyjnej. Ponadto formy te charakteryzują się wyższymi właściwościami mechanicznym oraz większą gazoprzepuszczalnością co również zwiększa obszar ich zastosowania w firmie CPP Polska.

Podziękowania:

Literatura:

[1] Wasilewski P.: Odlewnictwo jako jedna z najstarszych metod wytwarzania. *Archiwum Odlewnictwa* 1 (2001) 1 str.9-38

[2] Stölzel K.: Giesserei über Jahrtausende. VEB Deutscher Verlag, Leigzig 1978.

[3] Baker J.: Five Thousand Years of Investment Castings. BICTA Bulletin, (1997) 26, pp. 6–8.

[4] Stachańczyk J.: Odlewnictwo precyzyjne na świecie – stan aktualny, perspektywy rozwoju. *Modern Foundry Poland and the World* (2011) 2

[5] Małek M., Wiśniewski P., Matysiak H., Michalski J., Kopta M., Cygan R., Kurzydłowski K.J.: Wpływ rodzaju spoiwa na właściwości mechaniczne ceramicznych form odlewniczych. XLI Szkoła Inżynierii Materiałowej Kraków-Krynica 24-27 IX 2013

[6] Gromada M., Świeca A., Kostecki M., Olszyna A., Cygan R.: Ceramic cores for turbine blades via injection moulding. *Journal of Materials Processing Technology* (2015) 220 pp. 107-112.

[7] Furgal G., Cygan R.: Quality problems root cause identification And variability reduction in casting processes. *Archives of Foundry Engineering* 9 (2009) 1 pp.13-16.

[8] Kwiatkowski M.: Wykorzystanie metod skanowania 3D, termowizji i tomografii komputerowej do sterowania jakością w procesie wytwarzania krytycznych części silników lotniczych. Rozprawa doktorska Akademia Górniczo-Hutnicza. Kraków 2017.

Ł. RAKOCZY*#, M. GRUDZIEŃ**, R. CYGAN***, A. ZIELIŃSKA-LIPIEC*

EFFECT OF COBALT ALUMINATE CONTENT AND POURING TEMPERATURE ON MACROSTRUCTURE, TENSILE STRENGTH AND CREEP RUPTURE OF INCONEL 713C CASTINGS

The effect of cobalt aluminate inoculant addition and melt-pouring temperature on the structure and mechanical properties of Ni-based superalloy was studied. The first major move to control the quality of investment cast blades and vanes was the control of grain size. Cobalt aluminate ($CoAl_2O_4$) is the most frequently utilized inoculant in the lost-wax casting process of Ni-based superalloys. The inoculant in the prime coat of moulds and pouring temperature play a significant role in grain size control. The finest surface grains were obtained when the internal surface of shell mould was coated with cobalt aluminate and subsequently pouring was at 1480°C. The influence of selected casting parameters and inoculant addition on mechanical properties was investigated on the basis of tensile, creep and hardness testing. The effect of grain refinement on mechanical properties were consistent with established theories. Tests conducted at ambient temperature indicated a beneficial effect of grain refinement both on tensile strength and hardness. In contrast at elevated temperature during creep, the reverse trend was observed.

Keywords: pouring, investment casting, lost wax, superalloy, creep

1. Introduction

Inconel 713C belongs to the group of nickel based alloys which are characterized by an unique combination of properties at elevated temperatures. High mechanical properties, excellent resistance to oxidation and hot corrosion make them suitable to manufacturing components in jet engines and industrial gas turbines [1-3]. The usefulness of superalloys for harsh environment applications is given by few physical factors. Face centered cubic (FCC) crystallographic system is characterized by low rates of thermally activated processes and so creep deformation is relatively small. Furthermore, this polymorph is thermodynamically stable from liquid nitrogen temperature up to the melting point; thus phase transformations of γ-matrix do not occur. Nickel is able to promote the precipitation of the intermetallic phase $Ni_3(Al, Ti)$, denoted as γ′, which exhibits the $L1_2$ crystal structure. In doing so, the so-called yield stress anomaly arises: the flow stress rises with temperature, an effect exploited for high temperature components [4-6]. Inconel 713C is widely used in the production of low pressure turbine (LPT) blades and vane clusters. Due to high costs of machining, investment casting is a fundamental method for the fabrication of parts with complex geometries. Exceptional properties are gained with the lost wax process, especially high dimensional accuracy due to monolithic ceramic moulds, and better metallurgical features originating from the use of preheated moulds [7]. Cost disparity between investment casting and other casting methods results from the necessity to create expendable patterns and construct individual moulds from these. The primary field for investment casting of Inconel 713C is the production blades and vane clusters, usually for low pressure turbine (LPT) section. This specialized area of investment casting technology demands various processing techniques to provide the high metallurgical quality in critical gas turbine components [8]. Development over the years in the complexity and integrity of lost-wax castings has led a continuous improvement in capability of the manufacturing process. Superior mechanical properties of nickel based superalloy generally originate also from alloying elements in Ni-matrix and properly conducted heat treatment, namely solution and ageing [9]. It is noteworthy that the high resistance to creep and low cycle fatigue of Inconel 713C alloy are sufficiently achievable in the "as cast state", thus costly heat treatment is eliminated [10]. Development in the manufacturing technology to attain the highest properties requires intensive investigations and testing. For this reason it is important to make a correlation betwixt process parameters, constituents in the shell mould and mechanical properties of Inconel 713C in as cast condition. Continuous improvement of engines makes the LPT section much more complex in structure. Service temperature reaches even 700°C and so fine grained microstructure characterized by high

* AGH UNIVERSITY OF SCIENCE AND TECHNOLOGY, FACULTY OF METALS ENGINEERING AND INDUSTRIAL COMPUTER SCIENCE, DEPARTMENT OF PHYSICAL AND POWDER METAL-LURGY, AL. MICKIEWICZA 30, 30-059 KRAKÓW
** FOUNDRY RESEARCH INSTITUTE, 73 ZAKOPIAŃSKA STR., 30-418 KRAKÓW, POLAND
*** CONSOLIDATED PRECISION PRODUCTS POLAND, 120 HETMANSKA STR., 35-078 RZESZOW, POLAND

\# Corresponding author: lrakoczy@agh.edu.pl

strength is required. However, it is important to remember that the grain refinement leads to a decrease in creep resistance. High strength is favoured by fine grain size, in turn creep favoured by coarse grain size, so optimum range of sizes is required by end users. Cast components operating in the turbine, due to service conditions, must have appropriate microstructure and lack casting defects that can contribute to catastrophic failure. Mentioned features can be controlled by melt-pouring temperature and composition of the prime coat [11]. Filling ability of thin wall blades and vanes can be improved through increase of pouring temperature, however on the other hand, it leads to grain coarsening. In the LPT section operating temperature is usually below the creep range, and so stresses originating from centrifugal loads are relatively low [12]. In order to overcome this problem, castings are usually modified by the addition of refiners which contain high stability particles or adding inoculant to the prime coat of the ceramic mould. Grain refinement of the cast microstructure is directly connected with increasing the heterogeneous nucleation sites during solidification [13]. Some information is available in the literature [10,14-16] about modification of Inconel 713C superalloy, but the aviation industry continues to seek new solutions and improvements to increase durability of critical components, also called flight safety parts. The effect of the selected process parameters, geometry of castings as well as the preparation of ceramic mould on the mechanical properties of the Inconel 713C superalloy, presented in this work, has not yet been analyzed. The aim of the investigation was to establish the influence of the $CoAl_2O_4$ content in the prime coat and melt-pouring temperature on the macrostructure, microstructure and also mechanical properties at room and elevated temperatures.

2. Experimental procedure

Four Inconel 713C investment castings with different pouring temperatures and prime coatings of shell mould were fabricated. The superalloy used in this experiment was provided by Canon Muskegon Company. The wax patterns were injection moulded and then ceramic monolithic mould was built up around these patterns by a series of dip coatings. Two prime coats were produced for the casting:

a) Shell mould 1-2: The prime coat consisted zircon filler and colloidal silica binder,
b) Shell mould 3-4: Similar to 1-2 plus 5 wt. % of $CoAl_2O_4$ inoculant.

Grit of alumina was used as a primary stucco, and then few coat mould backups made of ceramic slurries based on alumina silicate powders and colloidal silica binder. As a backup stucco aluminate silicate grit was used. One of prepared shell mould is shown in Fig. 1. The wax patterns were removed from the shell molds in boilerclave and then covered with alumina silicate Fiberfrax® insulation. Whole assemblies were fired in air in order to harden the moulds. Master heat charges were melted in a zirconia crucible mounted in the VIM IC Consarc furnace. Directly before melting the moulds were preheated up

to 1000°C. During melting and subsequent pouring, the vacuum was 2×10^{-3} mbar. Two melt-pouring temperatures, controlled by Pt/Pt-Rh thermocouples, were selected: 1480°C (shell 1, 3) and 1520°C (shell 2, 4).

Fig. 1. One of the shell mould prepared in the experiment

TABLE 1

Experimental conditions

Content of inoculant [wt. %]	Preheat temperature [°C]	Melt pouring temperature [°C]	
		1480	1520
		Description of shell	
0	1000	**N1**	**N2**
5	1000	**M1**	**M2**

After the alloy has solidified and cooled, the moulds were broken away and the castings subjected to further investigation. The geometry of cast element after excision from assembly and machining is presented in Fig. 2. Measuring length is equal 32 mm.

Fig. 2. Geometry of prepared element after: a) excision b) machining

In order to establish influence of inoculant content and melt-pouring temperature on mechanical properties and macrostructure of Inconel 713C, light microscopy and scanning electron microscopy observations were made, and creep, tensile and hardness testing were performed. Chemical composition of the alloy was estimated by Optical Emission Spectroscopy (OES) and the results are included in Table 2.

TABLE 2

Chemical composition of Inconel 713C

Element	Cr	Al	Mo	Nb	Ti	Co	C	Zr	Ni
Wt. [%]	13.31	6.13	4.20	2.45	0.89	0.27	0.12	0.08	Bal.

Samples for macroscopic and microscopic examinations of base metals were taken from the top surface of the cast elements. Afterwards they were mounted in resin, metallographically prepared (grinding, polishing) and finally chemically etched in AG21 (macro) and no. 17 Etch (micro) reagents. Macroscopic and macroscopic observations were conducted on Nikon, Leica and FEI devices. Tensile tests were performed at ambient temperature according to ASTM E8M-13a standard on an INSTRON 3382 device. Vickers hardness was measured in accordance with the requirements of PN EN ISO 6507-1. Creep tests were carried out on Walter+Bai AG LFMZ-30 machine in accordance to the requirements of ASTM E139 standard. Specimens were heated up to 982°C with a final holding time 60 minutes. Subsequently they were loaded with an axial force which produces on their cross sections an initial tensile stress of 151.8 MPa.

3. Results

3.1. Macro and microstructure

The macrostructures representative different as cast samples are presented in Fig. 3. The results of the grain size analysis depending on pouring temperature and content of cobalt aluminate are shown in Table 3. It is to be noted that the increase in the melt-pouring temperature leads to grain growth due to the lower cooling rate of the crystallization process. The increase in pouring temperature by 40°C (N1→N2) results in an increase in the average surface of grain by more than 70%, thus decreasing the number of grains per millimeter. Captured images indicate that a 5% addition of cobalt aluminate is a great modifier for this Ni-based superalloy. Surface modification conducted at 1480°C led to a 2.6-fold decrease in the average surface of grain from 6.42 mm² to 2.44 mm². For the modified and non-modified alloy the number of grains per square millimeter was 0.16 and 0.41, respectively.

TABLE 3

Stereological parameters of non-modified and modified alloys

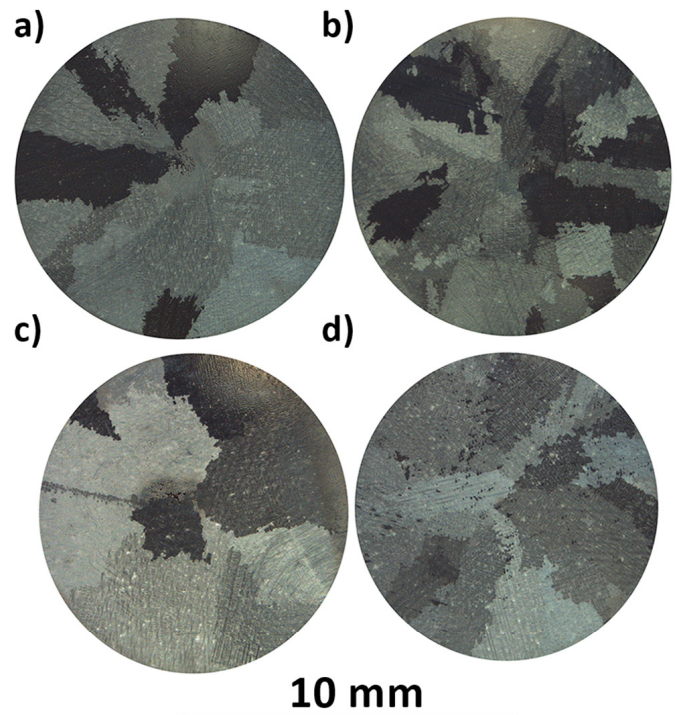| Variant	N1	M1	N2	M2
Average surface of grain [mm²]	6.42	2.44	11.03	5.56
Number of grains per mm²	0.16	0.41	0.09	0.18

Fig. 3. Macrostructure of prepared castings: a) N1; b) M1; c) N2; d) M2

The average surface of the grain size of the specimen cast at 1520°C was 11.03 mm². Addition of 5% of cobalt aluminate to the prime coat caused an almost twice decrease to 5.56 mm². In the first case (sample N2), the number of grains per unit area was 0.09 and in the second (sample M2), the value was twice as high. Analysis of the macrostructures for casting defects showed that the unmodified samples (coarse grained) exhibited higher porosity. It is important to emphasize that in the prepared castings chill zone structure, which is generally unacceptable, was not observed.

Regardless of the pouring temperature and the inoculant addition inside the equiaxed grains a dendritic structure with high local inhomogeneity was observed. Example of the microstructure of as-cast Inconel 713C is shown in Fig. 4. Segregation of alloying elements occurs during solidification of casting (Fig. 4a). Dissimilarity between microstructure of dendrite core and interdendritic spaces originates from decrease of solubility of elements in γ-matrix during cooling. The main strengthening phase γ' is surrounded by matrix fulfill cores, in turn enrichment of interdendritic spaces with elements additionally caused formation of γ/γ' eutectic island and carbides (Fig. 4b). In dendrite cores intermetalic phase γ' has a cubic shape, whereas in eutectic particles it is more globular. Interdendritic regions are strongly enriched in niobium, and so carbides precipitated mainly in these areas. Fig. 4c shows a scanning electron microscopy microstructure with marked field of EDS analysis. In Fig. 4d and 4e EDS spectra originating from the dendrite core and MC-type primary niobium rich carbide are presented. Carbides assumed different morphology from the blocky-shape, through the parallelograms, to the characteristic shape referred to in the literature as Chinese script. Dendrite cores are enriched in Cr and Mo which suggest that during solidification these elements likely segregate into γ.
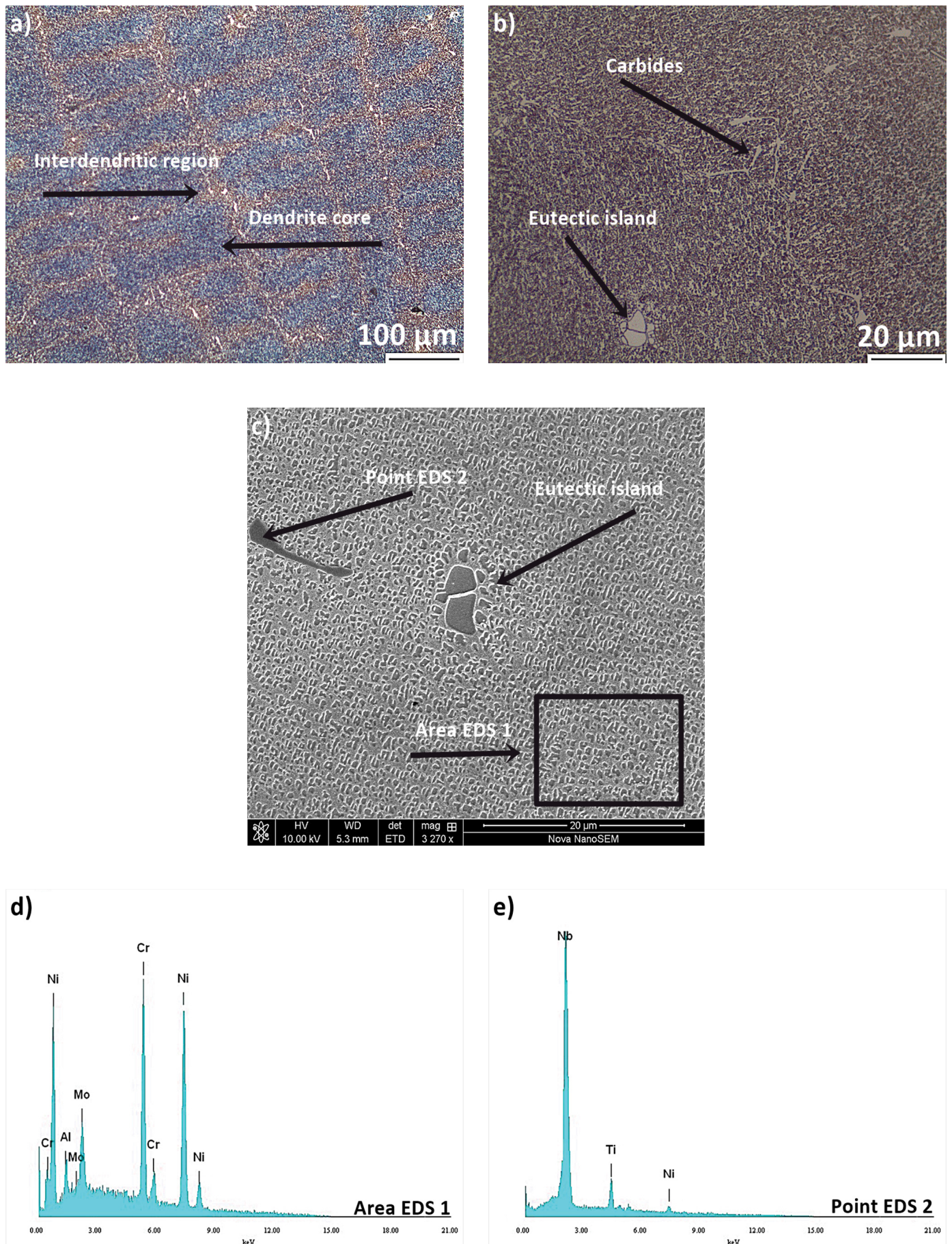
Fig. 4. Inconel 713C structure in the as cast state: a) dendritic structure; b) eutectic γ/γ' island and carbides; c) location of EDS analysis regions; d) EDS spectrum of the dendrite core; e) EDS spectrum of a Nb-rich carbide

3.2. Mechanical properties

Stress-strain curves obtained during tensile testing at ambient temperature are presented in Fig. 5. All the test results are shown in Table 4. Irrespective of the melt-pouring temperature, similar yield strength results were obtained for unmodified and surface modified samples. The addition of cobalt aluminate to prime coat improved the yield strength by 70 MPa for 1480°C and 72 MPa for 1520°C, which is almost identical. A slightly larger difference in the obtained values was observed for the ultimate tensile strength.

The results indicate that maximum values of ultimate tensile strength and strain are achieved for modified castings. Sample M1 broke at stress 1030 MPa, ie. at 104 MPa greater than sample N1. The surface modification subjected for the 1480°C pouring temperature increased the UTS by 11%. The values obtained for samples poured at 1520°C were slightly lower and were respectively 861 MPa for the unmodified sample and 980 MPa for the sample with $CoAl_2O_4$ addition. An addition of inoculant to prime coat and pouring temperature of 1480°C consequently attained the optimal combination of mechanical properties.

Macrostructure of the fractures and their cross-sections after a tensile test, are shown in Fig. 6 and 7. The complex character of cracking was observed and it indicates structural heterogeneity of the cast superalloy. Cracks propagated through equiaxed grains of the castings along the interdendritic areas. Few secondary cracks were observed, namely two on the inner surface of sample M1 and one inside of sample N2.
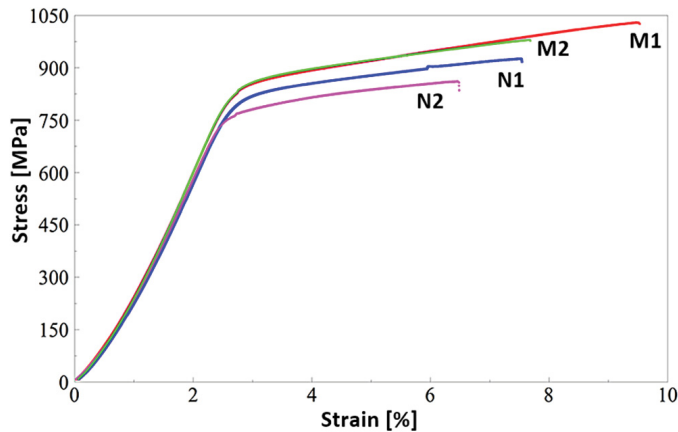

Fig. 6. Fractures of tensile test specimens: a) N1; b) M1; c) N2; d) M2

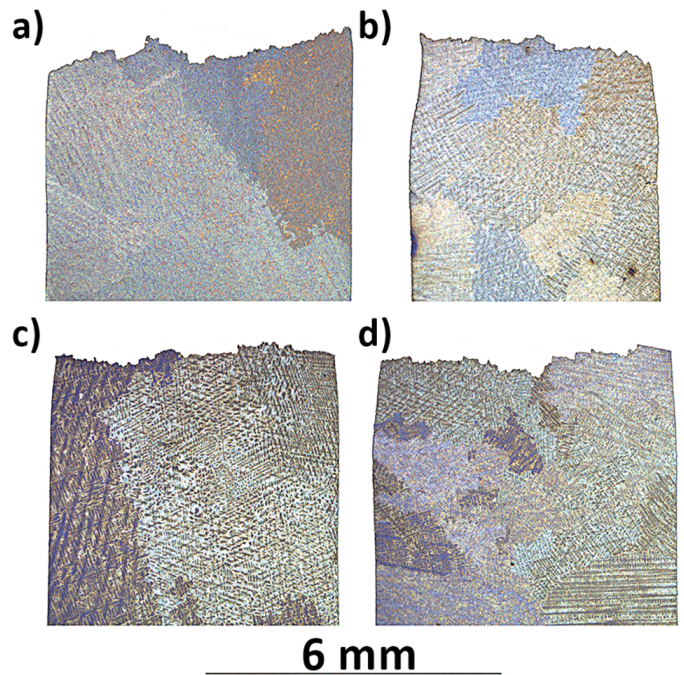Fig. 5. Tensile testing curves

Fig. 7. Cross sections of tensile test fractures: a) N1; b) M1; c) N2; d) M2

At high temperature/low stress (e.g. 982°C/151.8 MPa), superalloys show steady creep with a short primary stage and steady state represented by a plateau and pronounced strain appearing at the tertiary stage. Fig. 8 shows the percentage strain as a function of rupture time, creep curves have the classical shape, while the detailed results are in Table 5. It was noted that Inconel 713C modified with cobalt aluminate independently of the melt-pouring temperature, showed lower rupture life comparison with the unmodified alloy. For the specimens poured from 1520°C,

TABLE 4

Ambient temperature tensile test results of Inconel 713C

Pouring Temperature [°C]	Content of inoculant [%]	Description	Yield strength 0.2% [MPa]	Tensile strength [MPa]
1480	0	N1	750	926
1480	5	M1	820	1030
1520	0	N2	749	861
1520	5	M2	821	980

the decrease was almost 10%, while for the specimens poured from 1480°C more than 11%. Time to rupture of sample M1 was 4.8 h shorter in comparison with sample N1 (41.4 h), in turn for sample M2 poured from the higher temperature, time to rupture was 38.1, and so 4.2 h shorter than for non-modified specimen. The shorter time to rupture results essentially from grain refinement, because the surface areas of the grain boundaries being the preferred deformation sites during creep and creep rate is increased. The longest time to fracture was 42.3 h for the sample N2, and the shortest 36.6 h for the M1 variant. Materials characterized by coarse grains withstood the applied stress the longest time. Creep rate in steady state is increase with grain refinement for both melt-pouring temperatures. At 1480°C creep rate for sample N1 is equal 0.035% per hour, whereas modification increases this rate by more than 40%. At 1520°C creep rates both modified and non-modified samples are close with a little higher value for the fine-grain specimen.
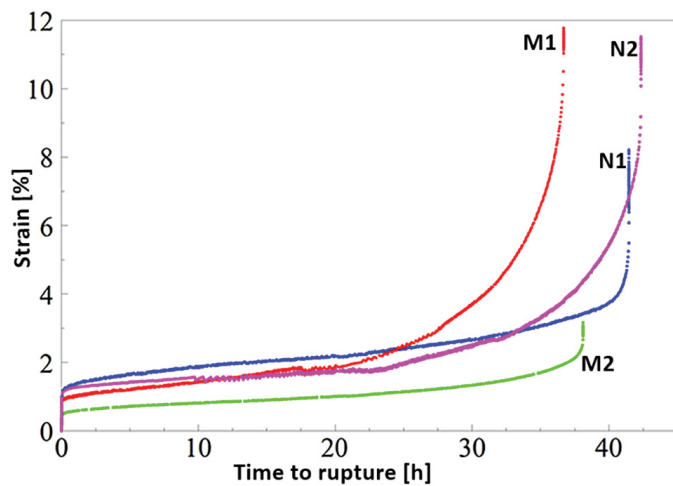

Fig. 8. Creep curves

TABLE 5

Creep resistance of Inconel 713C

Pouring Temperature [°C]	Content of inoculant [%]	Description	Time to rupture [h]	Steady state creep rate [%/h]
1480	0	N1	41.4	0.035
1480	5	M1	36.6	0.050
1520	0	N2	42.3	0.022
1520	5	M2	38.1	0.025

Fig. 9 and 10 show macrostructures of the fractures and cross sections, respectively of the specimens after stress rupture. The test was carried out at a temperature of nearly 1000°C (above potential service temperature) in air, so an oxide layer was observed on the fractures. Dark green colouration indicates the formation of chromium rich oxide on their inner area. Fractures are characterized by a highly developed surface due to uneven plastic deformation. The cross-sectional microstructures show the intergranular fracture mode. In the N1 sample, the grains are larger than in the sample M1; direction of the crack propaga-

tion indicates that relatively high "jumps" are associated with separation of larger grains. Similar tendency occurs in N2 and M2 samples. There are also numerous secondary cracks that have been initiated and run along the inside of the material,
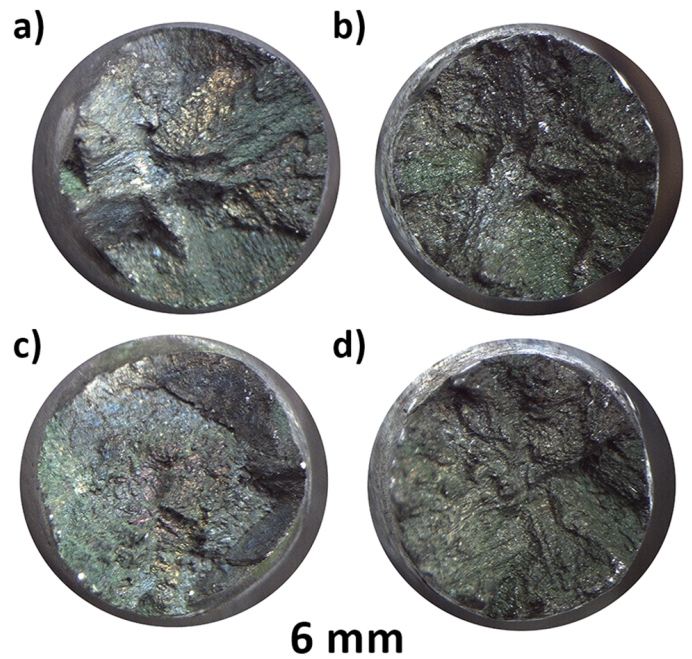

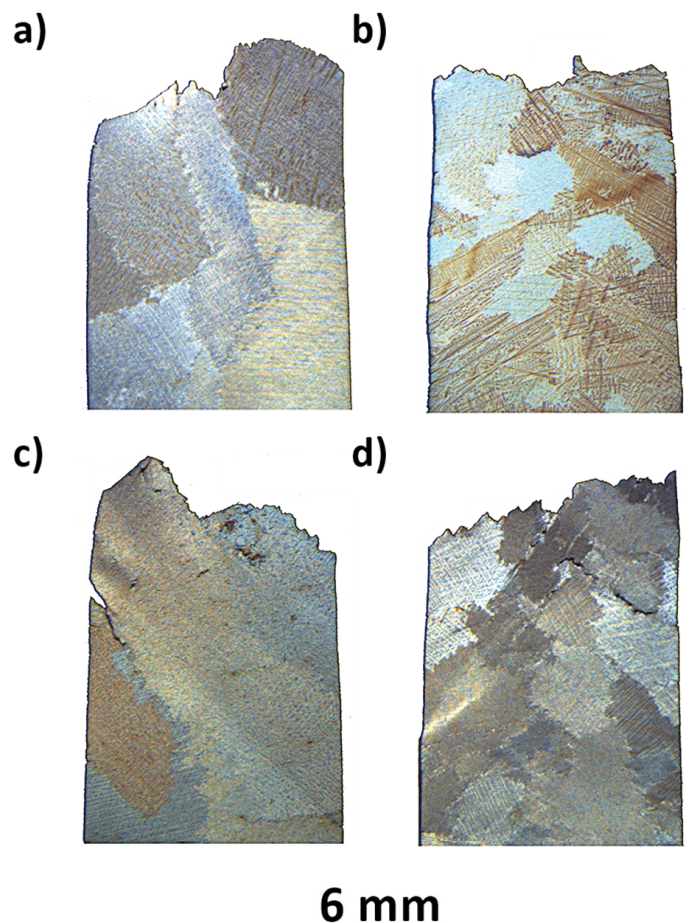Fig. 9. Fractures of crept samples: a) N1; b) M1; c) N2; d) M2

Fig. 10. Cross sections of crept samples: a) N1; b) M1; c) N2; d) M2

and also some which develop inwards from external areas. No cracks inside grains have been observed. The obtain results for all tested specimens reveal that time to rupture is longer than 30 h (average t = 39.6 h). Values meet the requirements of the industrial standards [17].

TABLE 6

Vickers hardness results

Description	N1	N2	M1	M2
Number of indent				
1	394.1	406.8	400.0	395.6
2	391.2	389.8	428.2	396.9
3	392.7	393.8	404.5	415.3
4	381.0	417.7	422.9	412.3
5	390.1	410.2	407.1	406.0
Mean value	389.8	403.7	412.5	405.2
Standard deviation	5.2	11.6	12.3	8.9
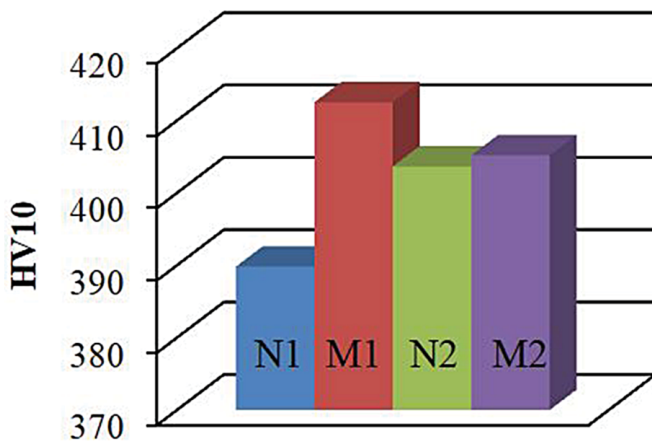
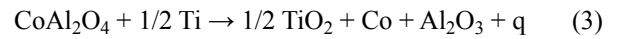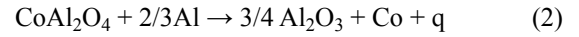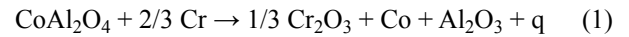Fig. 11. Average Vickers hardness values for all investigated variants

Vickers hardness test results with calculated mean values and standard deviations are shown in Table 5. The average values of the 5 measurements for each variant are graphically presented in Fig. 11. For both melt-pouring temperatures, the hardness average values in the modified samples were observed to increase. For lower temperature, the increase was almost 6%, while for the higher temperature for the unmodified and modified sample, the difference was only 1.5 HV, so it can be assumed that these values are very close (difference is within the measurement error limit).

4. Discussion

4.1. Macro and microstructure

Grain size depends primarily on velocity of growth and nucleation rate. In this work are considered two variants where preheat and melt-pouring temperature remain unchanged and so grain growth is constant. Refinement of the grains can be obtained via increment of the heterogeneous nucleation rate.

The fine-grained structure is related to a reaction between the alloying elements consisted in base metal and the inoculant. OES analysis reveals that IN-713C consists of highly reactive alloying elements like titanium, aluminum, as well as chromium. The oxide is reduced and metallic cobalt is formed according to the equations [18]:

$$CoAl_2O_4 + 2/3\ Cr \rightarrow 1/3\ Cr_2O_3 + Co + Al_2O_3 + q \quad (1)$$

$$CoAl_2O_4 + 2/3Al \rightarrow 3/4\ Al_2O_3 + Co + q \quad (2)$$

$$CoAl_2O_4 + 1/2\ Ti \rightarrow 1/2\ TiO_2 + Co + Al_2O_3 + q \quad (3)$$

These reactions are initiated by oxygen affinity of the aforementioned alloying elements. Cobalt in compound would be displaced by these elements to form Co fine particles, which are considered to be the relevant nucleants for surface grain refinement. Particles exist in melt-pouring temperature, Co is similar to Ni-rich γ phase both in crystallographic structure and lattice parameter. Cobalt and nickel have the same Face Centered Cubic system with a_{Co} = 3.5547 Å and a_{Ni} = 3.5805 Å. Cobalt particles due to low lattice misfit with matrix can act as the nucleation substrata. Macrostructure observations did not revealed chill zones, which indicates that modification with the use of $CoAl_2O_4$ gives an exothermic reaction during pouring. Start of γ-matrix dendrite creation is pointed as 1342°C in turn solidification is finished at 1263°C. Inconel 713C has a wide range between liquidus and solidus (79°C) and so porosity is likely to form in its castings. Primary MC-type carbides that are responsible for increase of creep strength start to precipitate directly from liquid phase at 1305°C with a maximum at 1299°C. The main strengthening phase γ' is obtained as a product of transformation $\gamma \rightarrow \gamma'$ that occurs in a solid state in the temperature range 1169°C-929°C. Precipitation of the γ'-phase from the γ solid solution starts near the eutectic areas and then occurs towards the dendrite cores during cooling. Near cubic shape of gamma prime particles indicates that the misfit coefficient is below ±1%. Similar lattice parameters of γ and γ' makes that γ' nucleation energy is low and nucleating takes place under little supercooling. Hence, we observe a significant volume fraction of the γ' phase and consequent high mechanical properties in the as cast condition [15,19].

4.2. Influence of grain size on strength at ambient temperature

The size of the grains in a superalloy influences the strength because adjoining grains normally have different crystallographic orientations. The grain boundaries act as a barrier to dislocation movement for two reasons. Due to different orientation of two grains, a dislocation passing from one into the second grain will have to change its direction of motion. Secondly the atomic disorder within a grain boundary region will result in a discontinuity of slip planes from one grain into the other. A fine-grained alloy is harder and stronger than one that is coarse-grained, because has a greater grain boundaries area to hinder dislocation move-

ment. High strength also results from the high volume fraction of the coherent γ' particles, small width of the γ phase channels and the solid solution strengthening of γ and γ' phase [20]. Phase deformation of γ' occurs by slip on systems $\{111\}$ $<110>$. The dislocation in γ' phase has a Burger vector of length $a\sqrt{2}$, which is twice as long as in γ-matrix. Slip of a dislocation in the γ' phase by one length of the Burgers vector disrupts ordering of the crystal lattice. This creates an interface, which is a defect of high energy, so the dislocation movement in the γ' phase is much more difficult [21].

4.3. Influence of grain size on creep properties of Ni-based superalloy

Depending on the temperature and stress, there are three ranges in which creep mechanisms predominate. At high temperature/low stress (e.g. 982°C /151.8 MPa) creep curve reveals a short primary stage and steady state represented by a plateau and pronounced strain appearing at the tertiary stage. In the case of superalloys and other alloys, two creep mechanisms are distinguished: dislocation creep (dislocation movement and climb) and diffusion creep [22]. The creep rate in both cases is dependent on the diffusion rate, so it fulfill the requirements of the Arrhenius equation. Taking into account the influence of grain size, the creep mechanisms can be divided into dependent and independent of its size. Dislocation creep that occurs inside the grains is independent of their size, while creep diffusion depends on the grain size, as vacancies form and disappear at the boundaries. With constant stress and temperature (as in this work) as the grain size increases, the contribution of dislocation creep goes down rapidly and decreases the creep rate via a diffusion mechanism. At a homologous temperature above 0.7 (in this paper 0.82), Nabarro-Herring creep prevails and occurs by migrating of vacancies inside grains from the stretched to the compressed regions and by the volume diffusion in the opposite direction. Below these temperatures, at a homologous temperature of 0.4-0.7 Coble creep that occurs through diffusion along grain boundaries prevails [20,23]. Creep rate via Nabarro-Herring mechanism is equal $1/d^2$, whereas via Coble is $1/d^3$. These relationships indicate that Coble creep is more strongly dependent on grain size than Nabarro-Herring creep, so that the contribution of the second mechanism will be much inconsiderable in fine-grained materials. Therefore, coarse grained nickel-alloys are characterized by higher creep resistance. Improvement of creep resistance can be achieved by solid solution and precipitation strengthening and also by grain boundary reduction or elimination.

5. Summary

Control of grain size in lost-wax casting is attained by control of manufacturing parameters like preheat and pouring temperature, together with the use of nucleants in prime coat of the mould. The present research combines variants without and with addition of 5% cobalt aluminate and also two pouring temperatures namely 1480°C and 1520°C. The grains of superalloy castings can be refined to a considerable range by addition of the inoculant $CoAl_2O_4$ to the prime coat of moulds. The aim of inoculants is to produce during solidification of casting a large number of heterogeneous nucleation sites, which leads to an increase in the number of nucleating areas, so a numerous of crystals is created, which soon impinge on each other and preclude further growth. The influence of grain refinement on mechanical properties at elevated temperature and ambient temperature of Inconel 713C superalloy is analyzed. The research outcomes can be concluded as follows:

1) The highest refinement was observed in the modified sample poured at lower temperature (1480°C). The average surface of grain in specimen N1 with the prime coat that consisted zircon filler and colloidal silica binder is 6.42 mm^2 while the addition of $CoAl_2O_4$ decreases the average surface area above 2.5 times.

2) Grain refinement by addition of cobalt aluminate for specimens poured from both temperatures increase yield strength and hardness. Fine grain microstructure with high mechanical properties were obtained in as cast state. It is beneficial for elements like aerospace vanes clusters since they are mainly exposed to low cycle fatigue.

3) The creep resistance test indicated that all variants have favourable properties at 982°C with a mean time to fracture of nearly 40 h. Creep rate in the steady state depends strictly on grain size in both melt-pouring temperatures. In modified sample poured at 1480°C creep rate increases by more than 40% relative to non-modified sample, from 0.035% per hour to 0.050% per hour. In contrast, in specimens N2 and M2 creep rate slightly increases from 0.022 %/h to 0.025 %/h. Testing temperature was 0.82 of homologous temperature and so according to literature data Nabarro-Herring creep mechanism prevailed during testing.

Conflicts of Interest

The authors declare no conflict of interest.

REFERENCES

[1] R. Reed, The Superalloys: Fundamentals and applications, Cambridge University Press, Cambridge (2006).

[2] Ł. Rakoczy et al., Adv. in Mat. Sci. **17** (2), 55-63 (2017) DOI: 10.1515/adms-2017-0011.

[3] A. Chamanfar et al., Mat. Sci. and Eng. A **642**, 230-400 (2015) http://dx.doi.org/10.1016/j.msea.2015.06.087.

[4] D. Laughlin, K. Hono, Physical Metallurgy, Elsevier (2014) http://dx.doi.org/10.1016/B978-0-444-53770-6.00022-8 .

[5] R. Ramesh et al., J. Mat. Sci. **27**, 270-278 (1992).

[6] A. Royer et al., Scr. Mat. **40** (8), 955-961 (1991).

[7] A. Szczotok, H. Matysiak, J. of Mat. Eng. and Perform. **23**, 2749-2759 (2014).

[8] S. Roskosz, R. Cygan, Inż. Mat. **37** (2), 59-64 (2016).

[9] P.Willemin, M. Durrand-Charre, J. of Mat. Sci. **25**, 168-174 (1990).

[10] H. Matysiak et al., JOM. **68** (1), 185-197 (2015) https://doi.org/10.1007/s11665-014-1123-4

[11] M. Zielińska, J. Sieniawski, Arch. of Met. and. Mat. **58** (1), 95-98 (2013) https://doi.org/10.2478/v10172-012-0157-6 .

[12] T. Murakumo at el., "Superalloys" 155-62 (2004).

[13] W. Jin, F. Bai, T. Li, G. Yin, Mat. Let. **62** 1585-1588 (2008) http://dx.doi.org/10.1016/j.matlet.2007.09.028.

[14] Ł. Rakoczy, R. Cygan, Analysis of temperature distribution in shell mould during thin-wall superalloy casting and its effect on the resultant microstructure, Arch. of Civ. and Mech. Eng. **18**, 1441-1450 (2018). https://doi.org/10.1016/j.acme.2018.05.008.

[15] H. Matysiak et al., J. of Mat. Eng. and Perform. **23** (9), 3305-3013 (2014). https://doi.org/10.1007/s11665-014-1123-4.

[16] M. Azadi, M. Azadi, Mat. Sci. and Eng. 689 (24), 298-305 (2017).

[17] https://www.nickelinstitute.org/~/media/Files/TechnicalLiterature/Alloy713C_337_.ashx.

[18] F. Jian, Y. Bin, High Temperature Alloys for Gas Turbines: Investigation of the Surface Grain Refinement for Superalloys Castings, Springer, Dordrecht (1982). https://doi.org/10.1007/978-94-009-7907-9_50.

[19] F. Zupanic et al., J. Alloy. Compd. **329**, 290-297 (2001).

[20] W.D. Callister, Materials Science and Engineering, John Wiley & Sons, New York (2007).

[21] C.T. Liu, Ordered Intermetallics: Physical Metallurgy and Mechanical Behaviour, Springer Netherlands, Dordrecht (1992)

[22] F. Nabarro, The Physics of Creep, Taylor and Francis, London (1995).

[23] B. Burton, J. of. Mat. Sci. 4900-4903, (28) 1993.

Influence of Melt-Pouring Temperature and Composition of Primary Coating of Shell Mold on Tensile Strength and Creep Resistance of Ni-Based Superalloy

Łukasz Rakoczy, Małgorzata Grudzień, and Rafał Cygan

Eight investment castings of Inconel 713C superalloy were fabricated, varying in the melt-pouring temperature, from 1400 to 1520 °C, and $CoAl_2O_4$ inoculant content, 0 or 5 wt.%, in the primary coat. Their influence on grain size on tensile and creep properties was investigated. The best combination of yield stress (815 MPa) and elongation ($A_4 = 7.65\%$) at ambient temperature was obtained in surface-modified castings poured from 1520 °C. The longest time to rupture was for the unmodified castings (76.8 h) poured from 1520 °C, while for the modified variant, the time to rupture was lower around, 7.4 h, which was still a satisfactory value. During tensile testing, microcracks were formed in large eutectic γ', carbides and borides, due to the accumulation of stress at interfaces with the matrix. During creep, N-type rafting of γ' precipitates and phase transformation $MC + \gamma \rightarrow \gamma' + M_{23}C_6$ took place.

1. Introduction

Precipitation-strengthened nickel-based superalloys are widely used in the manufacturing of turbine blades and vanes, which operate in hot sections, both in turbochargers of combustion engines and turbofan jet engines (Ref 1, 2). One of the most important representatives of this group is Inconel 713C. This alloy is also extensively used in the automotive, power and oil and gas industries due to a unique combination of strength at operating temperature and excellent hot corrosion resistance. The very good castability, low-cycle fatigue resistance (LCF) and microstructural stability determine the wide use of the Inconel 713C for low-pressure turbine (LPT) guide vanes in GP7200 engines (Ref 3-6). Usually, superalloys are heat-treated (solution + aging); however, Inconel 713C achieves sufficiently high properties in the as-cast condition, and so increase in mechanical properties is by optimization of investment casting parameters and composition of the shell mold (Ref 7). Major features of investment castings are macrostructural coarseness and non-uniformity of grain size,

which may reduce the fatigue life and reliability of turbine vanes in the intermediate temperature range. The microstructure improvement of cast superalloys may be obtained by more uniform equiaxed grain size (Ref 8-10). Desired grain size can be achieved by selection of melt-pouring temperature, preheat of ceramic shell mold, and/or introduction of an inoculant into the primary coat (Ref 11, 12). Grain refinement through the addition of inoculants is an important way to increase the strength of cast polycrystalline superalloys. At a relatively low temperature, the strength of the grain boundary is higher than that of the grain interior and so increasing the area of grain boundaries can increase the strength of superalloys. However, with the increase in operating temperature, the strength of grain boundary decreases more quickly than the grain interior strength. Increasing the grain boundary area can, therefore, lead to a significant reduction in strength. Grain refinement by the addition of inoculants has several benefits, namely a substantially easy operation, no change in production equipment and a very good refining effect (Ref 13, 14). It has been reported (Ref 13, 15-18) that inoculants have a favorable influence on grain refinement and thus low-temperature mechanical properties. The main aim of this research was to determine the influence of the melt-pouring temperature and the $CoAl_2O_4$ inoculant in the prime coat of the shell mold on the structure and mechanical properties of IN713C superalloy castings.

Łukasz Rakoczy, Faculty of Metals Engineering and Industrial Computer Science, AGH University of Science and Technology, av. Mickiewicza 30, 30-059 Kraków, Poland; **Małgorzata Grudzień**, Foundry Research Institute, ul. Zakopianska 73, 30-418 Kraków, Poland; and **Rafał Cygan**, Consolidated Precision Products, Investment Casting Division, ul. Hetmanska 120, 35-078 Rzeszow, Poland. Contact e-mail: lrakoczy@agh.edu.pl.

2. Material and Experimental Procedure

Ni-based superalloy Inconel 713C was used as the casting and the gating system. Result of chemical composition analysis obtained by optical emission spectroscopy is shown in Table 1.

The eight shell molds were fabricated in the Investment Casting Division of Consolidated Precision Products Corp. Each of the disposable wax assemblies consisted of a "carrot"-type shape specimens with dimensions: bottom diameter 23 mm, upper diameter 12 mm and height 90 mm. Four vents

Table 1 Chemical composition of Ni-based superalloy Inconel 713C

Element	Cr	Al	Mo	Nb	Ti	C	Zr	B	Ni
wt.%	14.14	5.78	4.38	2.16	0.87	0.10	0.07	0.012	Bal.

were prepared in order to stabilize and strengthen the wax models and also for better wax melting. The wax patterns were injection molded, and then, the ceramic monolithic mold was built up around these patterns by a series of dip coatings (8 layers). Alumina grit was used as the primary stucco. One of the prepared shell molds is shown in Fig. 1. Two prime coats were produced for the casting:

(a) Shell molds no. 1, 3, 5, 7: zircon filler and colloidal silica binder,
(b) Shell molds no. 2, 4, 6, 8: zircon filler and colloidal silica binder plus 5 wt.% of $CoAl_2O_4$ inoculant.

The wax patterns were removed from the shell molds in boilerclave and then covered with alumina silicate Fiberfrax® insulation. All molds were then fired to increase the strength and remove the wax residue. Directly before melt-pouring, the molds were placed in a heating chamber preheated to 1000 °C for 100 min. The temperature was controlled by Pt/Pt-Rh thermocouples. The raw ingots were melted in a zirconia crucible placed in a vacuum induction furnace. The Inconel 713C superalloy was inductively melted in a vacuum of 2.9×10^{-3} Pa. The liquid superalloy was poured into molds at four different temperatures: 1400, 1450, 1480 and 1520 °C. A total of 40 specimens were machined for microstructural and mechanical properties investigations. Those for macroscopic and microscopic examinations were mounted in resin, metallographically prepared (grinding and polishing) and finally chemically etched in 50 mL lactic acid, 30 mL nitric acid, 2 mL hydrofluoric acid (macro) and electrochemically (micro) in 10% CrO_3. Tensile tests were carried out at ambient temperature according to ASTM E8M-13a standard (Ref 19) using INSTRON 3382 tester, and yield strength and elongation A_4 were determined. The geometry of the sample is presented in Fig. 2.

Creep tests were performed on a Walter + Bai AG LFMZ-30 machine in accordance with the requirements of ASTM E139-11 standard (Ref 20). The samples were preheated to 982 °C, annealed for 60 min, and then loaded with an axial force, which produced in their cross sections an initial tensile stress of 151.8 MPa. Two specimens were prepared for creep and two for the tensile testing (for each variant presented in Table 2), and finally, average values were calculated. The solidus temperature of Inconel 713C is 1263 °C (Ref 11), so creep testing was at a high homologous temperature, 0.82.
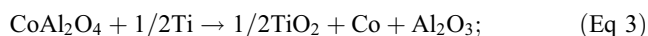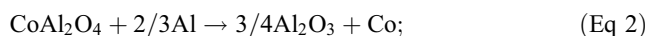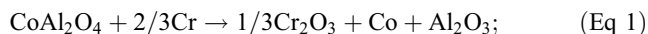
3. Results and Discussion

3.1 Microstructure of Castings

The microstructures of castings did not reveal casting defects like cracks, porosity and misruns (Fig. 3). The increase in melt-pouring temperature induced a decrease in cooling rate which led to grain growth. The microstructure showed that

Fig. 1 Shell mold fabricated through the "dip and stucco" technique

cobalt aluminate ($CoAl_2O_4$) was an effective modifier for Inconel 713C in the whole range of melt-pouring temperatures, especially at 1450 and 1520 °C. Differential thermal analysis of IN713C indicated that the creation of the first γ primary dendrites started at 1342 °C (liquidus) (Ref 11). The solidification finished at 1263 °C, and so liquidus–solidus range is relatively wide, 79 °C. Table 1 indicates that IN713C consists of highly reactive alloying elements like chromium, aluminum, as well as titanium, characterized by high oxygen affinity. During the contact of the primary coat with the liquid alloy, cobalt aluminate was reduced and metallic cobalt was created in accordance with the reactions (Ref 13):

$$CoAl_2O_4 + 2/3Cr \rightarrow 1/3Cr_2O_3 + Co + Al_2O_3; \quad (Eq\ 1)$$

$$CoAl_2O_4 + 2/3Al \rightarrow 3/4Al_2O_3 + Co; \quad (Eq\ 2)$$

$$CoAl_2O_4 + 1/2Ti \rightarrow 1/2TiO_2 + Co + Al_2O_3; \quad (Eq\ 3)$$

Cobalt from the inoculant was superseded by Al, Cr and Ti, and then, Co fine particles were formed on the internal surfaces of shell molds. Above 450 °C, cobalt and γ (Ni) phase have the same crystallographic structure (face-centered cubic). The lattice constants are $a_{Co} = 3.5480$ Å and $a_{Ni} = 3.5805$ Å, respectively, which gives a low lattice misfit (Ref 21, 22). In accordance with the equation $f = \frac{a_{Ni} - a_{Co}}{a_{Co}} \times 100\%$, misfit is only
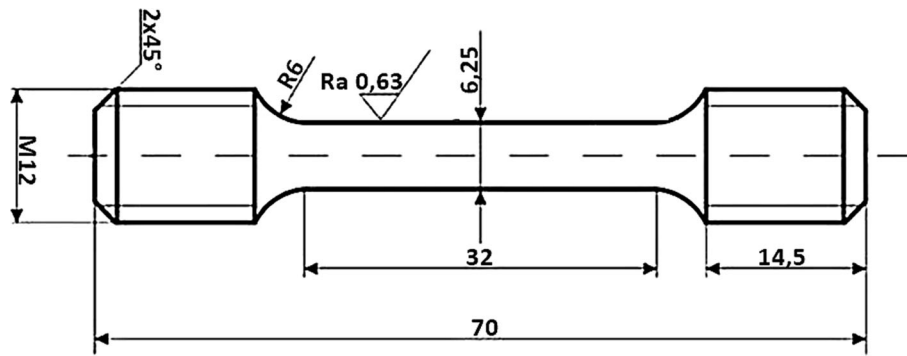
Fig. 2 Geometry of specimen for tensile and creep tests

Table 2 Designation of shell molds

Shell mold, No.	Content of inoculant in prime coat, wt.%	Melt-pouring temperature, °C
1	0	1400
2	5	1400
3	0	1450
4	5	1450
5	0	1480
6	5	1480
7	0	1520
8	5	1520

Fig. 3 Macrostructure of castings
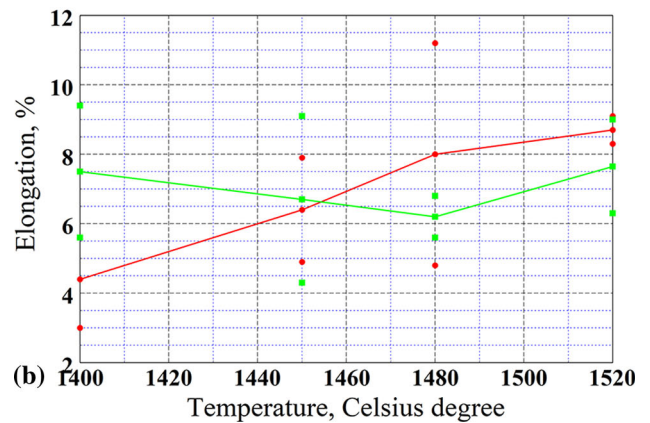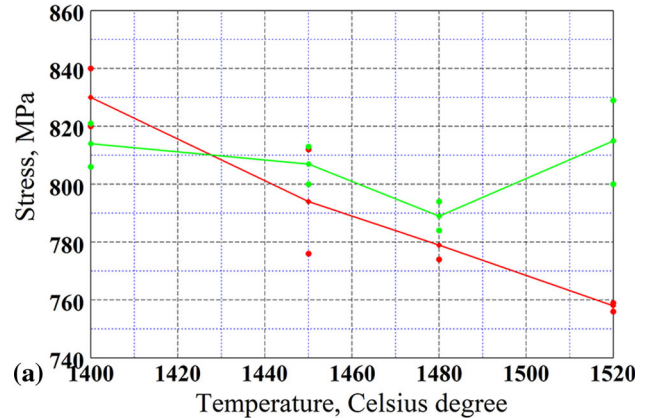
Fig. 4 Influence of pouring temperature on: (a) yield strength; (b) elongation A_4

3.2 Tensile Tests Results and Changes of Microstructure

The results of the tensile tests are shown in Fig. 4. The averaged values calculated are joined by the green line for the modified samples and by the red line for the unmodified. According to the AMS 5391 standard (Ref 23), Inconel 713C castings should be characterized by the following properties: yield strength 689.5 MPa (100 psi) and elongation A_4 min. 3%. Yield stress in all samples significantly exceeded the required minimum (Fig. 4a). With the exception of the melt-pouring temperature of 1400 °C, higher average values were obtained for the modified samples. The difference between the highest (830 MPa) and the lowest mean value was around 76 MPa. For unmodified samples, yield stress decreased as the casting
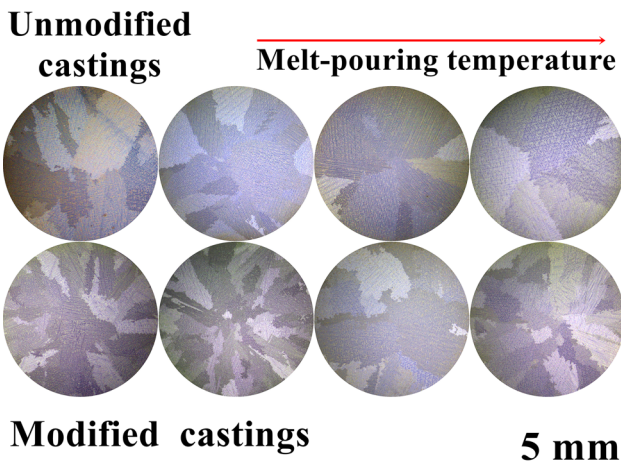
0.9% and Co can act as a good nucleation substrate. The heterogeneous nucleation rate of the cast surface was increased. The modification gave an exothermic reaction during pouring, which prevented the formation of a chill zone structure. It is also important to mention that some other variables have also an influence on the microstructure of superalloys, and consequently on mechanical properties. An increase in the melt-pouring temperature influences strongly the reactivity of the molten alloy with the crucible and filter. Alloys poured from higher temperatures have also a higher concentration of vacancies, which is important for mechanical properties at high homologous temperatures (Ref 1, 2).

temperature increased. The elongation A_4 is presented in Fig. 4(b). Relatively low values were measured in unmodified samples poured from 1400 °C. The highest A_4 values for both modified and unmodified samples were obtained for 1520 °C pouring temperature. The results of single measurements for melt-pouring temperatures of 1450 and 1480 °C were close to 4% minimum.

Macrostructures of cross-sectioned specimens after the tensile test are shown in Fig. 5. The complex character of cracking indicated structural heterogeneity of the castings. Conventionally, higher yield strength was associated with finer grain size. High strength also results from a high volume fraction of the γ' precipitates, narrow matrix channels and the solid solution strengthening effect in both matrix and γ' phases. The total content of γ' formers exceeded 6.6 wt.%, which is a relatively high value in comparison with other equiaxed superalloys widely used in aircraft engines (Ref 24). Plastic deformation of the superalloys occurs through dislocations slip in the matrix channels. A high volume fraction of the γ' phase and the substantial local grain-boundary curvature in castings effectively block their movement.

The microstructural changes, the location of EDS points and results of the analysis are presented in Fig. 6 and Table 3. Numerous cracks have been observed inside many large precipitates. The results of analysis no. 1 and 2 revealed the increased concentration of Ni and Al which confirmed the presence of eutectic γ'. Precipitates strongly enriched in Nb, Ti and Mo were MC-type carbides (points 3 and 4), while the precipitates with a total concentration of around 75 at.% of Mo and Cr were M_3B_2 borides (points 5 and 6). The uncracked precipitates along interdendritic spaces were Ni_7Zr_2 intermetallic compounds formed from the residual liquid phase through the eutectic transformation. The deformation of γ' phase takes place by slip on systems $\{111\} <110>$. The dislocation in γ' phase has a length of Burger vector $a\sqrt{2}$, which is twice as long as in γ. Dislocation slip in the γ' by one length of the Burgers vector disturbs the lattice order. This leads to the formation of a high energy defect, so dislocation movement in the γ' is more difficult (Ref 25). The microstructural observations and tensile tests results indicated that the deformation of IN713C was dominated by the type of primary precipitates and dislocation movement in the matrix. Due to the high stiffness of eutectic γ' phase, carbides and borides, accumulation of created dislocations occurred in the γ matrix and interfaces. Microcracks of large precipitates confirmed the stress concentration along interfaces with the matrix. In the Ni-based superalloys, interfaces γ/MC-type carbides and γ/eutectic γ' are areas of increased stress concentration (Ref 26, 27).

3.3 Creep Tests Results and Changes of Microstructure

The AMS5391 (Ref 23) standard indicates that with the assumed test parameters the time to rupture should be at least 30 h. The creep properties of castings tested at 982 °C and 151.8 MPa as a function of melt-pouring temperature are presented in Fig. 7(a) and (b). The creep life was improved with increasing pouring temperature, and in addition, the mean time to rupture for each melt-pouring temperature was higher for the unmodified samples (Fig. 7a). The mean time to rupture for unmodified and modified castings poured from 1400 °C was 48.1 and 46.0 h, respectively. Increasing the pouring temperature by 120 °C contributed to the increase in these values by more than 50%, namely to 76.8 h and 69.4 h. The minimum value defined by the standard has been exceeded twice. The effect of cobalt aluminate was most pronounced at 1480 °C, with a difference in mean time to rupture over 11 h. Depending on the temperature and the load, three creep ranges were observed. At high temperature and low stress (982 °C/ 151.8 MPa), curves showed a short primary stage and steady state characterized by a plateau and pronounced strain at the tertiary stage.

The steady-state creep rate decreased with an increase in the melt-pouring temperature, both for the unmodified and the modified castings (Fig. 7b). The highest creep rate for the modified variant was 0.035%/h (1450 °C), while the lowest 0.0245%/h (1520 °C). In the unmodified castings, the difference between the highest 0.0306%/h (1400 °C) and the lowest creep rate (1520 °C) was 0.0093%/h. The creep rate of modified samples was higher for each melt-pouring temperature, although the value calculated for the 1520 °C variant was the second lowest in the entire study. The comparison of creep curves which represents variants with the highest (modified at 1450 °C) and the lowest (unmodified at 1520 °C) steady-state creep rate is presented in Fig. 7(c). Generally, the creep mechanisms can be divided into dependent and independent of the grain size (Ref 1, 8, 28). In both cases, the creep rate is related to the diffusion rate. Creep diffusion via formation and disappearance of vacancies at the boundaries depends strongly on grain size, but dislocation creep which occurs inside the grains is independent of their size. Under constant stress and temperature, as the grain size increases, the contribution of
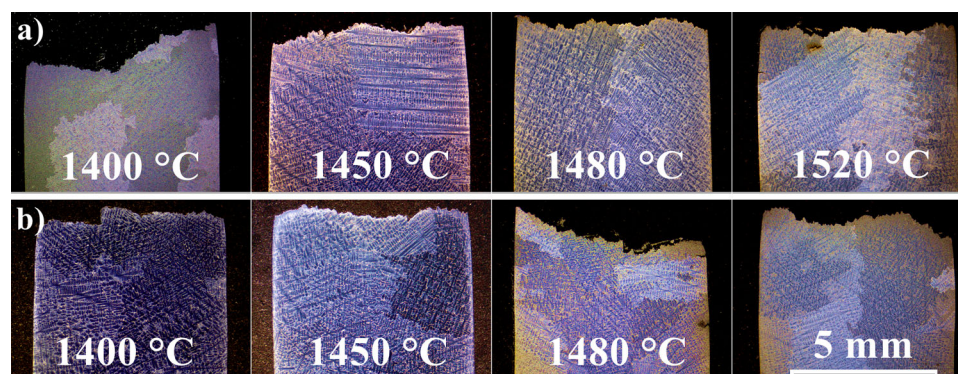

Fig. 5 Cross sections after tensile testing: (a) unmodified castings; (b) modified castings
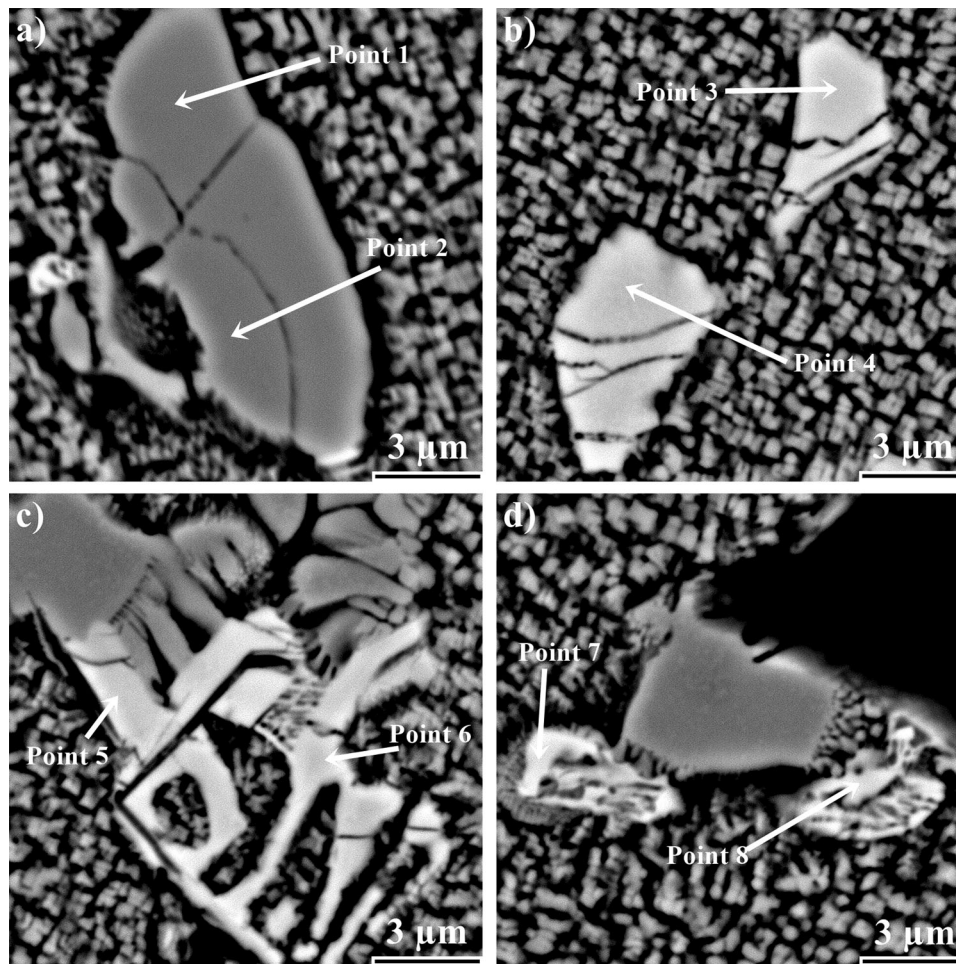
Fig. 6 Microcracks of precipitates: (a) eutectic γ'; (b) MC-type carbides; (c) M_3B_2 boride; (d) intermetallic compound Ni_7Zr_2

Table 3 Concentration of alloying elements in selected points (at.%)

Point/element	Al	Cr	Nb	Ti	Mo	Zr	Ni
1	16.1	4.3	3.3	2.4	1.3	1.0	71.6
2	15.9	4.2	3.4	2.3	1.3	1.0	71.9
3	0.9	1.5	59.5	11.8	13.9	7.4	5.0
4	3.1	1.6	56.1	9.4	9.9	10.8	9.1
5	1.7	26.9	8.1	0.8	50.0	3.2	9.3
6	1.8	30.6	8.5	0.9	44.7	2.3	11.2
7	6.0	2.6	3.5	0.8	1.2	17.4	68.5
8	5.1	2.5	3.7	0.7	0.8	17.4	69.8

dislocation creep drops rapidly, while creep rate through a diffusion mechanism decreases. The microstructure of crept Inconel 713C is shown in Fig. 8. Intergranular cracks with numerous secondary cracks and voids were observed. The main microstructural change in the dendrite cores was directional growth (rafting) of γ' precipitates (Fig. 9). The rafting process of γ' phase in Ni-based superalloys is induced by several factors, namely the value and direction of the external stress, the value of misfit coefficient and the elastic constant of γ' and γ phases (Ref 29).

The morphology change in γ' phase was N-type rafting, in which the lamellae of γ' phase were perpendicular to the applied tensile stress direction. Lattice misfit is defined as $\delta = 2(a_{\gamma'} - a_\gamma)/(a_{\gamma'} + a_\gamma)$, where $a_{\gamma'}$ and a_γ are lattice constants (Ref 31). When lattice misfit is negative, it can be concluded that the rafting is a sequential process (Ref 32, 33). At the beginning, plastic deformation of the matrix takes place, which leads to a loss of coherency at the γ/γ' interface and decrease in the misfit stress. Tensile stresses act in the γ' precipitates parallel to the matrix channels. Compressive stresses in the surfaces of matrix channels balance these forces, and moreover, they are much higher than the tensile stress components perpendicular to the channels. The combination of internal stresses yields a specific value for the hydrostatic stress, which is well known to directly affect the chemical potential of atoms (Ref 30). If the superalloy is not loaded ($\sigma = 0$), the tendency to reduce the overall γ/γ' interface energy leads to non-directional coarsening of cubic precipitates (Fig. 10a). In this case, the chemical potentials of the γ' phase at points 1 and 2 are equal. When the external stress is applied, the stress components at positions 1 and 2 are not the same (Fig. 10b). The local stresses inside material are modified in the direction of the applied external stress. The internal stresses change to perpendicular to the external stress axis because of the difference in values of Poisson's ratio of the matrix and the
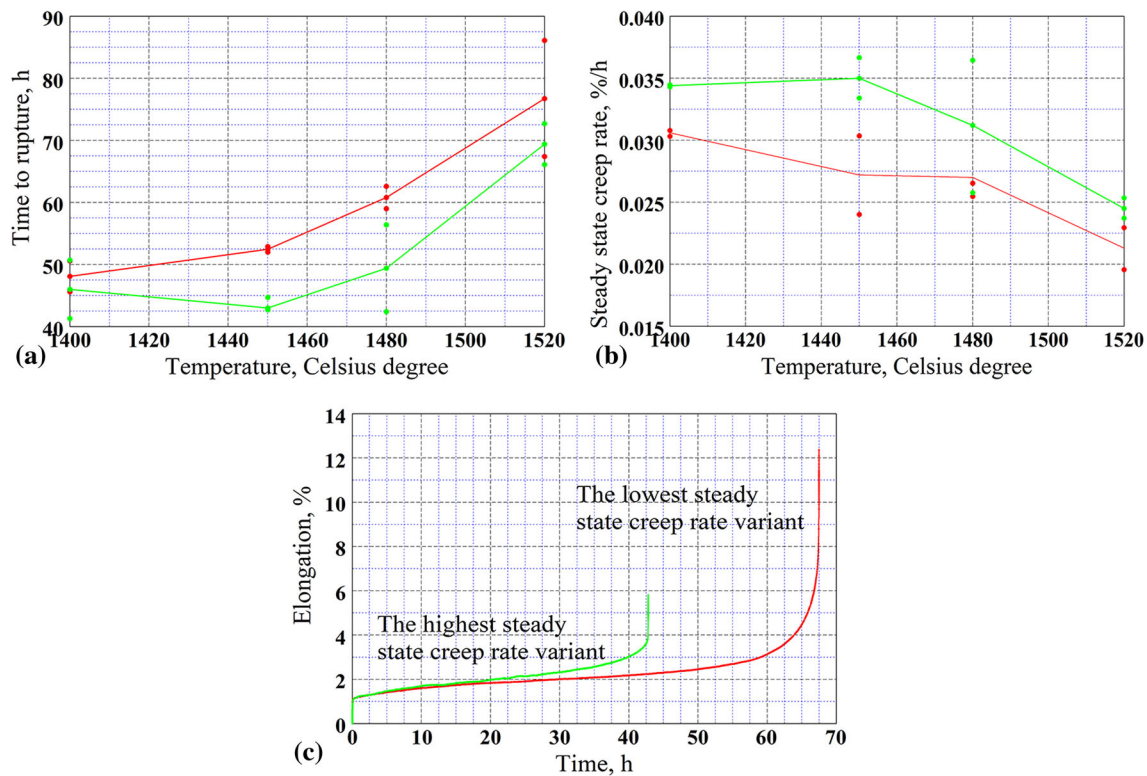
Fig. 7 Results of creep tests: (a) time to rupture; (b) steady-state creep rate: (c) comparison of creep curves for variants characterized by the highest and the lowest steady-state creep rate
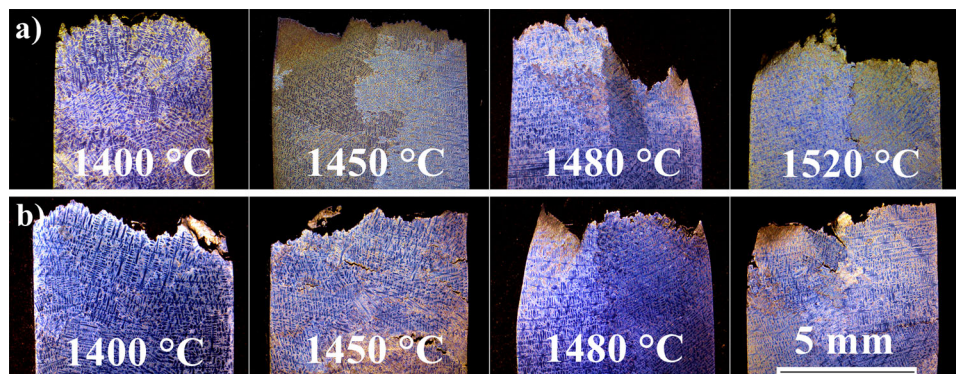

Fig. 8 Microstructure of cross sections after creep: (a) unmodified castings; (b) modified castings

precipitates. The effective stress in the perpendicular channels of the matrix is greater than in the parallel channels, which favors diffusion processes and dislocation movement in the perpendicular channels. The result is rafting of γ' perpendicularly to the external tensile direction.

Morphology of constituents and location of EDS lines are shown in Fig. 11 and 12. Microstructural observations in interdendritic spaces revealed much more complex changes, and so selected regions were subjected to EDS analysis. In Fig. 12(a), the enrichment in Nb and Ti was observed, which suggests that it was a primary Nb-rich carbide surrounded by

the coarse-grained γ'. M_3B_2 boride enriched in Mo and Cr (Fig. 12b) did not transform during creep. Intermetallic compound Ni_7Zr_2 (Fig. 12c) was also stable during exposure to 982 °C. Inside interdendritic γ' phase, near the MC-type carbides, precipitates strongly enriched in Cr were observed (Fig. 12d). These precipitates were not present in the as-cast state. In Ni-based superalloys, MC-type carbides can decompose during exposure to high temperature by one of the transformations: $MC + \gamma \rightarrow M_{23}C_6 + \gamma'$, $MC + \gamma \rightarrow M_6C + \gamma'$ and/or $MC + \gamma \rightarrow M_{23}C_6 + \eta$. Despite intensive observation, M_6C carbide and intermetallic η phase

were not observed in IN713C, which was earlier reported by (Ref 6).

4. Conclusions

Melt-pouring temperature and the composition of the primary coat in the shell mold influenced grain size of IN713C castings and consequently their mechanical properties both at ambient temperature and 982 °C. This work combines
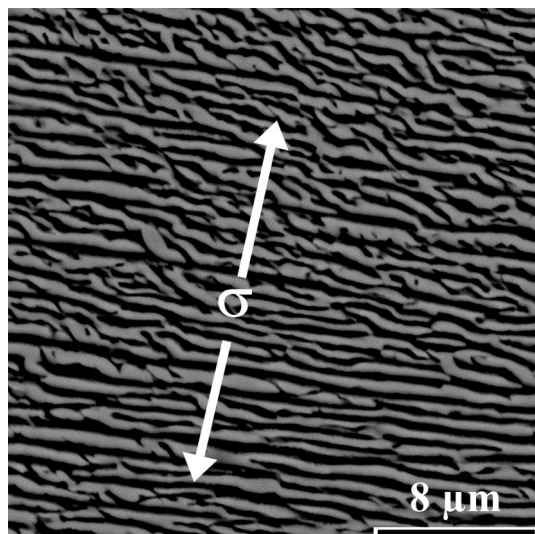

Fig. 9 Morphology of rafted γ'

two variants of the primary coat, without and with the addition of 5% $CoAl_2O_4$ inoculant, and also four pouring temperatures from 1400 to 1520 °C. The main conclusions of the research are:

(a) The compound $CoAl_2O_4$ is suitable for surface modification of IN713C castings. The highest grain refinement was obtained in castings poured between 1450 and 1520 °C,

(b) The mean yield strength in unmodified samples decreased with the increase in melt-pouring temperature, while elongation A_4 had the opposite relation. The highest mean yield strength (815 MPa) was obtained in modified samples poured from 1520 °C,

(c) The time to rupture increased with the increase in melt-pouring temperature both for unmodified and modified castings. The difference between the lowest and the highest time to rupture (72.8 h) for unmodified castings was 28.7 h. Modified castings were characterized by a similar difference between the lowest and highest time to rupture (69.4 h) at 1520 °C, equal to 26.4 h,

(d) The changes in microstructure during tensile testing included microcracking of large strengthening phases,

(e) During creep, N-type rafting of γ' and transformation of MC carbides to $M_{23}C_6$ carbides in interdendritic spaces ($MC + \gamma \rightarrow M_{23}C_6 + \gamma'$) were observed,

(f) The best combination of mechanical properties, for application in intermediate service temperature (LPT section) in jet engines, was for modified IN713C with 1520 °C pouring temperature. The temperature is below the creep range, where stresses originating from centrifugal loads are high. In this case, the best combination of tensile strength and creep resistance is required.
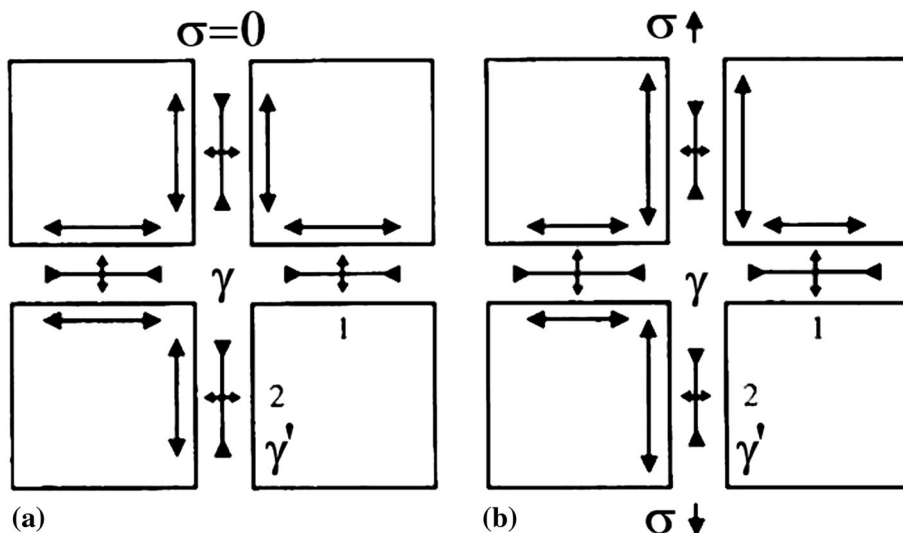

Fig. 10 Representation of internal stress components in the γ and γ' phases: (a) $\sigma = 0$; (b) $\sigma > 0$ (Ref 30)
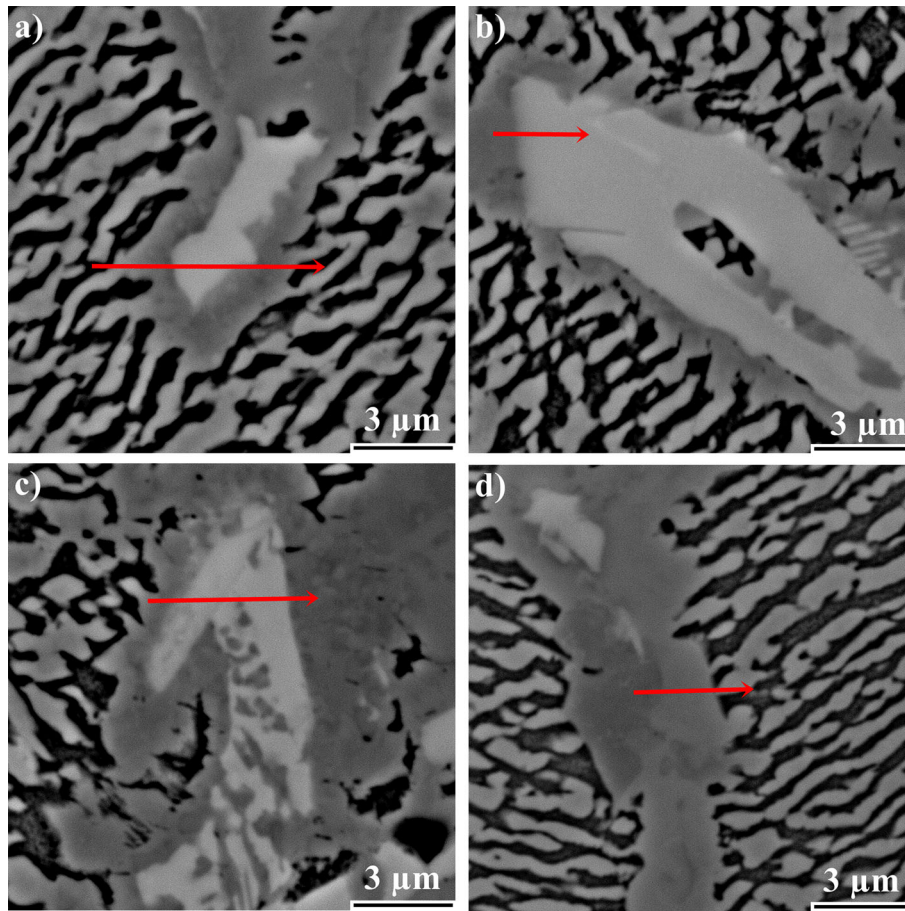
Fig. 11 Morphology of phases after creep and location of EDS lines: (a) MC-type carbide; (b) M_3B_2 boride; (c) intermetallic compound Ni_7Zr_2; (d) $M_{23}C_6$ Cr-rich carbides
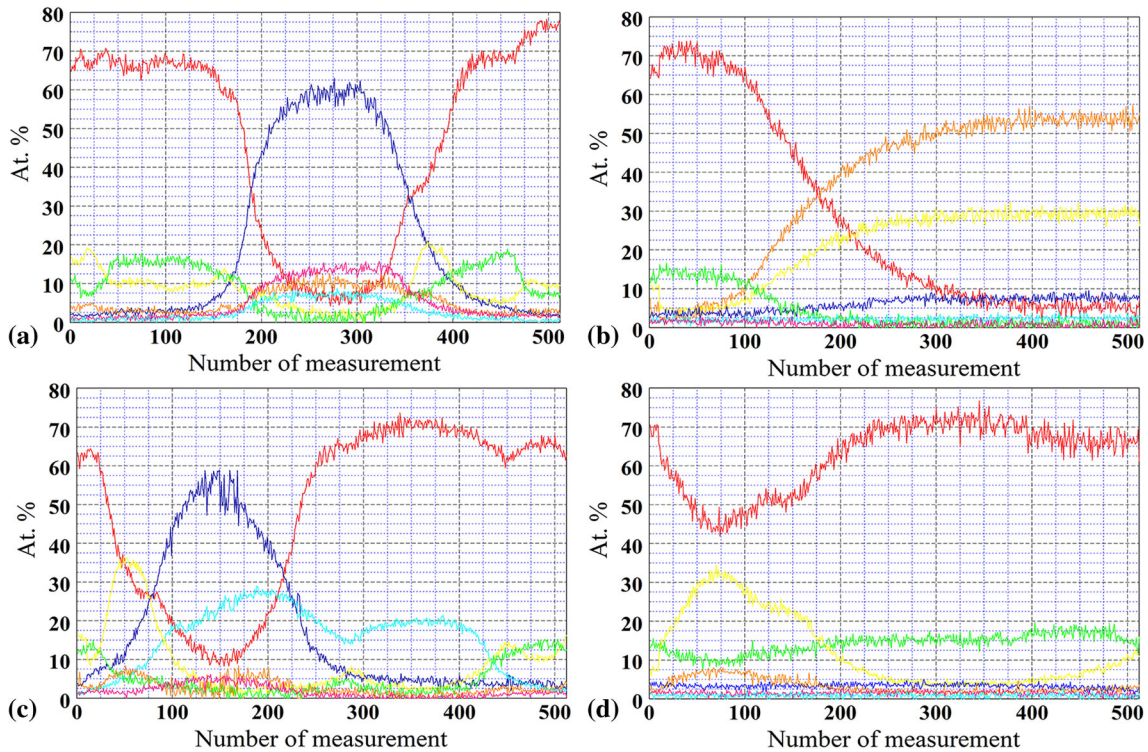

Fig. 12 Distribution of alloying elements (at.%): (a) MC carbide and γ'; (b) M_3B_2 boride and γ'; (c) Ni_7Zr_2 and MC carbide; (d) $M_{23}C_6$ Cr-rich carbides and γ'. Colors: Ni—red, Mo—orange, Cr—yellow, Al—green, Nb—blue, Zr—turquoise, Ti—pink (Color figure online)

Acknowledgments

Open Access

References

1. R. Reed, *The Superalloys: Fundamentals and Applications*, Cambridge University Press, Cambridge, 2006
2. H. Long et al., Microstructural and Compositional Design of Ni-Based Single Crystalline Superalloys—A Review, *J. Alloys Compd.*, 2018, **743**, p 203–220. https://doi.org/10.1016/j.jallcom.2018.01.224
3. Ł. Rakoczy and R. Cygan, Analysis of Temperature Distribution in Shell Mould During Thin-Wall Superalloy Casting and its Effect on the Resultant Microstructure, *Arch. Civ. Mech. Eng.*, 2018, **18**, p 1441–1450. https://doi.org/10.1016/j.acme.2018.05.008
4. F. Zupanic et al., Structure of Continuously Cast Ni-Based Superalloy Inconel 713, *J. Alloys Compd.*, 2001, **329**, p 290–297. https://doi.org/10.1016/S0925-8388(01)01676-0
5. M. Azadi et al., Effects of Solutioning and Ageing Treatments on Properties of Inconel-713C Nickel-Based Superalloy Under Creep Loading, *Mater. Sci. Eng. A*, 2018, **711**, p 195–204
6. H. Matysiak et al., The Microstructure Degradation of the IN 713C Nickel-Based Superalloy After the Stress Rupture Tests, *J. Mater. Eng. Perform.*, 2014, **23**(9), p 3305–3313. https://doi.org/10.1007/s11665-014-1123-4
7. A. Szczotok and H. Matysiak, Influence of Constituents of Shell Mold on the Morphology and Chemical Composition of Carbides Occurring in IN 713C Superalloy Castings, *J. Mater. Eng. Perform.*, 2014, **23**(8), p 2748–2759. https://doi.org/10.1007/s11665-014-1035-3
8. L. Thébaud et al., Is There an Optimal Grain Size for Creep Resistance in Ni-Based Disk Superalloys?, *Mater. Sci. Eng. A*, 2018, **716**, p 274–283. https://doi.org/10.1016/j.msea.2017.12.104
9. J. Salvant Canto et al., A Study of Low Cycle Fatigue Life and Its Correlation with Microstructural Parameters in IN713C Nickel Based Superalloy, *Mater. Sci. Eng. A*, 2018, **718**, p 19–32. https://doi.org/10.1016/j.msea.2018.01.083
10. K. Young-Wang et al., A Numerical Model to Predict Mechanical Properties of Ni-Base Disk Superalloys, *Int. J. Plast.*, 2018, **110**, p 123–144. https://doi.org/10.1016/j.ijplas.2018.06.011
11. H. Matysiak et al., The Influence of the Melt-Pouring Temperature and Inoculant Content on the Macro and Microstructure of the IN713C Ni-Based Superalloy, *J. Miner.*, 2016, **68**(1), p 185–197. https://doi.org/10.1007/s11837-015-1672-5
12. C.H. Konrad et al., Determination of Heat Transfer Coefficient and Ceramic Mold Material Parameters for alloy IN738LC Investment Castings, *J. Mater. Proc. Technol.*, 2011, **211**, p 181–186. https://doi.org/10.1016/j.jmatprotec.2010.08.031
13. W. Jin et al., Grain Refinement of Superalloy IN100 Under the Action of Rotary Magnetic Fields and Inoculants, *Mat. Let.*, 2008, **62**, p 1585–1588. https://doi.org/10.1016/j.matlet.2007.09.028
14. F. Wang et al., Preparation of Inoculants Used in Superalloy and Analysis of the Atomic Matching Models, *J. Mater. Sci. Technol.*, 2013, **29**(4), p 387–392. https://doi.org/10.1016/j.jmst.2013.02.007
15. L. Liu et al., Grain Refinement of Superalloy K4169 by Addition of Refiners: Cast Structure and Refinement Mechanisms, *Mater. Sci. Eng. A*, 2005, **394**, p 1–8. https://doi.org/10.1016/j.msea.2004.10.005
16. B. Du et al., Effects of Grain Refinement on the Microstructure and Tensile Behavior of K417G Superalloy, *Mater. Sci. Eng. A*, 2015, **623**, p 59–67. https://doi.org/10.1016/j.msea.2014.11.041
17. C.N. Wei et al., A Study of IN-713LC Superalloy Grain Refinement Effects on Microstructure and Tensile Properties, *Mater. Chem. Phys.*, 2003, **80**, p 89–93
18. B. Du et al., Effects of grain size on the high-cycle fatigue behavior of IN792 superalloy, *Mater. Des.*, 2015, **65**, p 57–64. https://doi.org/10.1016/j.matdes.2014.08.059
19. ASTM E8M-13a Standard—Standard Test Methods for Tension Testing of Metallic Materials
20. ASTM E139-11—Standard Test Methods for Conducting Creep, Creep-Rupture, and Stress-Rupture Tests of Metallic Materials
21. R.W.G. Wyckoff, *Crystal Structures: Cubic Closest Packed*, Interscience, New York, 1963
22. S. Ackerbauer et al., The Constitution of the Ternary System Fe-Ni-Si, *Intermet*, 2009, **17**(6), p 414–420. https://doi.org/10.1016/j.intermet.2008.11.016
23. AMS 5391 standard—Nickel Alloy, Corrosion and Heat Resistant, Investment Castings, 73Ni 13Cr 4.5Mo 2.3Cb 0.75Ti 6.0Al 0.010B 0.10Zr Vacuum Cast, As-Cast
24. R. Reed and C.M.F. Rae, *Physical Metallurgy of the Nickel-Based Superalloys, Physical Metallurgy (Fifth Edition)*, 2014, p 2215–2290. https://doi.org/10.1016/B978-0-444-53770-6.00022-8
25. A. Epishin and T. Link, Mechanisms of High Temperature Creep of Nickel-Base Superalloys Under Low Applied Stress, *Phil. Mag.*, 2004, **84**(19), p 1979–2000. https://doi.org/10.1080/14786430410001663240
26. X.Z. Qin et al., Decomposition of Primary MC Carbide and its Effects on the Fracture Behaviors of a Cast Ni-Base Superalloy, *Mater. Sci. Eng. A*, 2008, **485**(1–2), p 74–79. https://doi.org/10.1016/j.msea.2007.07.055
27. J. Yang et al., Effects of Different C Contents on the Microstructure, Tensile Properties and Stress-Rupture Properties of IN792 Alloy, *Mater. Sci. Eng. A*, 2011, **528**(3), p 1534–1539. https://doi.org/10.1016/j.msea.2010.11.003
28. F. Nabarro, *The Physics of Creep*, Taylor and Francis, London, 1995
29. P. Nörtershäuser et al., The Effect of Cast Microstructure and Crystallography on Rafting, Dislocation Plasticity and Creep Anisotropy of Single Crystal Ni-Base Superalloys, *Mater. Sci. Eng. A*, 2015, **626**, p 305–312. https://doi.org/10.1016/j.msea.2014.12.030
30. M. Kamaraj et al., On the Influence of Stress State on Rafting in the Single Crystal Superalloy CMSX-6 Under Conditions of High Temperature and Low Stress Creep, *A. Metall.*, 1998, **38**(4), p 589–594
31. A. Royer et al., In Situ Determination of γ' Phase Volume Fraction and of Relations Between Lattice Parameters and Precipitate Morphology in Ni-Based Single Crystal Superalloy, *Acta Mater.*, 1998, **46**(15), p 5357–5368. https://doi.org/10.1016/S1359-6454(98)00206-7
32. W. Huang et al., Experimental Investigation and Modelling of Microstructure Degradation in a DS Ni-Based Superalloy Using a Quantitative Cross Correlation Analysis Method, *J. Alloys Compd.*, 2018, **762**, p 488–499. https://doi.org/10.1016/j.jallcom.2018.05.131
33. V. Caccuri et al., γ'-Rafting Mechanisms Under Complex Mechanical Stress State in Ni-Based Single Crystalline Superalloy, *Mater. Des.*, 2017, **131**, p 487–497. https://doi.org/10.1016/j.matdes.2017.06.018

The Influence of Shell Mold Composition on the As-cast Macro- and Micro-structure of Thin-Walled IN713C Superalloy Castings

Łukasz Rakoczy, Małgorzata Grudzień-Rakoczy, and Rafał Cygan

In the investment casting process, the building of ceramic layers around the wax pattern is the main time-consuming stage. Increasing their number ensures sufficient mechanical properties, but also lengthens the whole process, including drying time and preheating of the mold. Four molds for casting Ni-based superalloy IN713C were strengthened by glass fibers, included in the slurry, and metal powder, of Al, Cu, Fe or Ni, in the coverage. Castings were subjected to microstructural investigations in order to find out if the new design can be promising for the manufacture of jet engine components. Bend tests revealed that the green strengths of all new molds were higher, at least 3.65 MPa, than that of the unmodified molds, 3.0 MPa. Optical microscopy revealed that the composition of a mold had a strong influence on stereological parameters of equiaxed IN713C grains. Microstructural observation and hardness measurements of castings revealed differences in the volume fraction of strengthening phases, porosity and hardness. The microstructure due to the complex chemical composition of IN713C consisted of several phases including ternary eutectics as a consequence of L $\rightarrow$ γ + Ni_7Zr_2 + (Nb, Zr)C.

1. Introduction

Ni-based superalloys are characterized by high mechanical strength and resistance to creep at high temperatures, which is ensured by their complex chemical composition, microstructure and technological process. One of these alloys is precipitation-strengthened Inconel 713C which possesses excellent strength up to 980 °C (Ref 1-4). It is widely used for rotating and nonrotating components, namely low-pressure turbine blades and vane clusters in the new generation aircraft jet engines GP7200 (Ref 5, 6). The complex geometry of these components effectively does not allow machining. Investment casting (IC) is an extremely important technique for such fabrication because of its ability to obtain complex geometries, dimensionally very accurate, with an excellent surface finish. Taking

Łukasz Rakoczy, Department of Physical and Powder Metallurgy, Faculty of Metals Engineering and Industrial Computer Science, AGH University of Science and Technology, Av. Mickiewicza 30, 30-059 Cracow, Poland; **Małgorzata Grudzień-Rakoczy**, Lukasiewicz Research Network-Foundry Research Institute, ul. Zakopianska 73, 30-418 Cracow, Poland; and **Rafał Cygan**, Investment Casting Division CPP-Poland, Consolidated Precision Products Corp. (CPP), ul. Hetmanska 120, 35-078 Rzeszow, Poland. Contact e-mails: lrakoczy@agh.edu.pl, rafal.cygan@cppcorp.com

into account the aviation safety requirement, these complicated castings must meet all quality standards, which in this case are highly strict (Ref 7-9). The various stages involved in the IC process are the creation of a disposable wax pattern, construction of several ceramic layers around the wax pattern, dewaxing and firing the mold and metal pouring into the mold under vacuum protection (Fig. 1).

The layers are usually made from the following basic ingredients: binder, refractory filler, additives (e.g., for stabilizing pH) and stucco powders. In the forming process, binders perform particularly important functions, which include: ensuring appropriate strength before firing, regulating the properties of slurries and preventing the sedimentation of solid particles (Ref 10, 11). The dimensional changes of the molds during dewaxing, melt pouring and solidifying strongly depend on the green strength and elevated temperature strength. The high strength of ceramic molds for complex and large jet engines components is usually achieved by increasing thickness. On the other hand, low permeability, cooling rate and collapsibility of molds result mainly from the excessively large thickness of the layers (Ref 12). Additionally, the high number of layers prolong the drying, dewaxing, firing and preheating time, which is undesirable. Molds should be adequately porous and gas permeable, required to evacuate air and other entrapped gases promptly during melt pouring. For these reasons, some research has been undertaken to develop a fabrication method for reinforcing thin molds (Ref 13-15). One trend in the development of binders in investment casting is the introduction of ceramic or polymer fibers in the slurry for increasing mold strength (Ref 13). The literature data indicate that the ceramic fibers can significantly improve also the gas permeability of molds (Ref 16). Alumino-silicate fibers in the slurry were tested by Maity and Maity (Ref 17) up to a concentration of 0.66 wt.%. Their research indicated a strong increase in modulus of rupture for the specimens as the concentration of fibers increased. An important stage in the investment casting

process is also preheating the ceramic molds. For a typical mold consisting of nine layers, the time of heating up to a design preheat temperature is 100 min (Ref 18). Therefore, it seems reasonable to initiate research aimed to shorten this time. One way to shorten this time is to reduce the number of layers; however, this is not always possible due to the lowering of the mechanical properties of the mold. Therefore, a different solution was proposed, the addition of metal powders to the backup coat to increase the thermal conductivity of the molds. At the same time, it should be noted that the open literature lacks information on the influence of such molds on the primary microstructure of the superalloys used in aircraft components. In this work, new ceramic molds strengthened by glass fibers and metal powders (Ref 19) were fabricated and utilized in the investment casting of Inconel 713C. The main aim was to investigate the influence of selected mold variant on the stereological parameters of equiaxed grains, segregation of alloying elements and the morphology of primary constituents.

2. Experimental Procedure

The Inconel 713C nickel-based superalloy "master heat" was used as the casting and the gating system. Chemical composition designated by optical emission spectroscopy (OES) is presented in Table 1.

The molds were fabricated in the Investment Casting Division of Consolidated Precision Products Corp., and all technological conditions were as similar as possible to internal standards accepted by aerospace customers. Wax pattern plates with dimensions 105 mm × 65 mm × 4 mm with H-type gating system were combined into a set. Four vents were prepared in order to stabilize and strengthen the wax model and also for better wax melting. Five molds were fabricated by the "dip and stucco" technique in accordance with data in Table 2. Every layer was created by dipping the wax pattern into a slurry (binder and filler) and then covered by a coarse dry backup. The prime layer of every mold was the same in all variants, namely colloidal silica, polymeric acrylic emulsion and fillers. Layers 2-7 had a different composition in the modified mold (acrylic polymer emulsion containing additionally randomly distributed glass fibers). The geometry of raw wax assembly and after coating is shown in Fig. 2. The castings are marked in accordance with letters Al to Ni, Table 2, according to the type of metal powder added to the coverage (unmodified casting is marked as B). Commercially available metal powders were used.

The molds after drying (48 h) were subjected to dewaxing in a boiler clave, burning out to remove residual wax, and finally were covered by alumina silicate Fiberfrax® heat insulation. In order to compare the influence of glass fibers and metal powder on the green strength (after dewaxing) of ceramic molds, additional sets were made from which bend test samples were
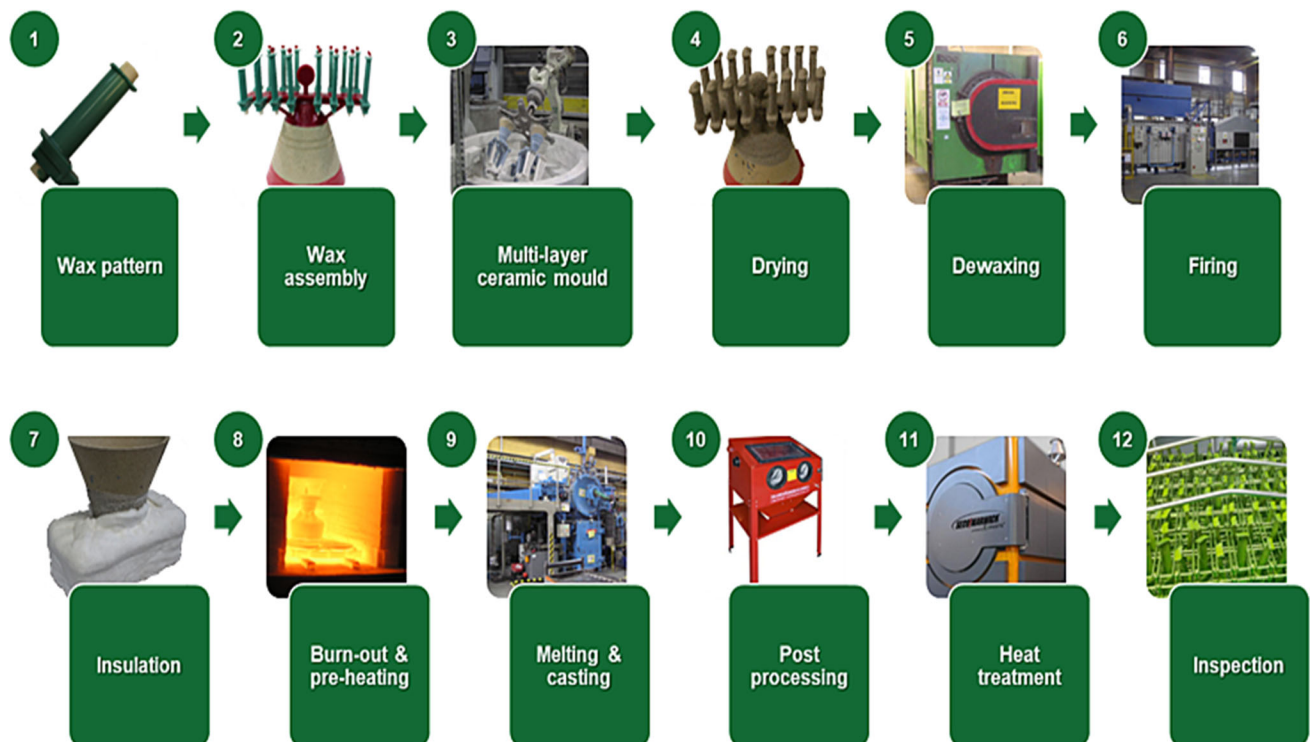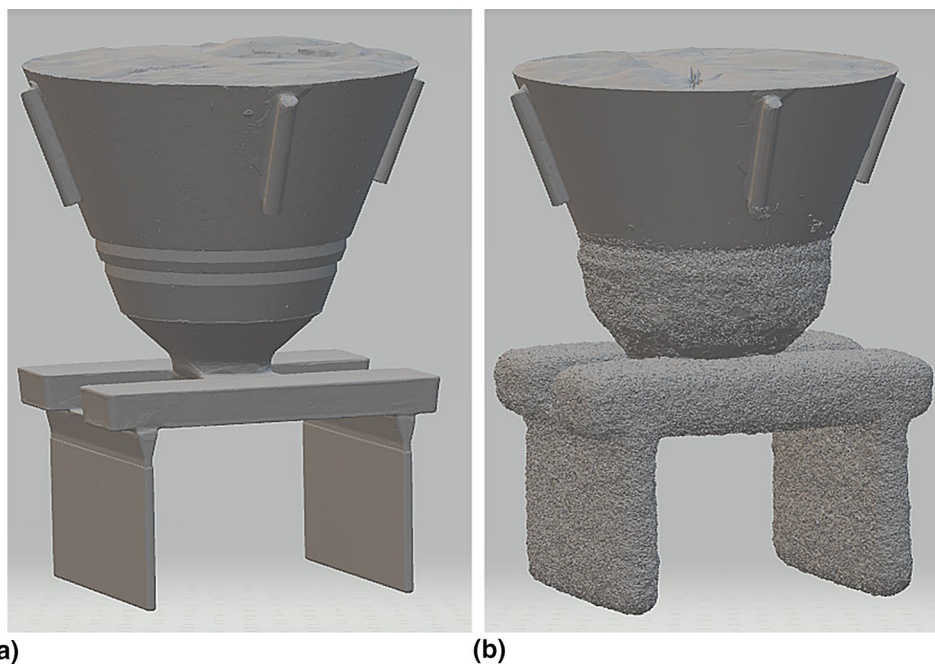

Fig. 1 Scheme of the investment casting process of the aircraft engines components

Table 1 Chemical composition of Inconel 713C

Element	Cr	Al	Mo	Nb	Ti	C	Zr	Co	B	Ni
wt.%	14.24	5.93	4.29	2.45	0.92	0.11	0.08	0.04	0.012	Bal.

Table 2 Composition of layers 2-7

Mold	Binder	Calcium aluminate glass fiber	Fillers		Backup layers + 5 wt.% metal powder
"B"	Colloidal silica + Acrylic polymer emulsion	0	$3Al_2O_3 2SiO_2$ (mullite)	Alumina silicate	Without metal powder
"Al"		1.5 wt.%	Al_2O_3		Al
"Cu"			SiO_2		Cu
"Fe"					Fe
"Ni"					Ni

Fig. 2 Geometry of wax model: (a) before coating; (b) after coating

taken. The strength of mold samples was determined in a three-point bend test (minimum of 20 samples for each variant). The measurements were carried out using Q TEST testing machine with a span L equal to five times the average thickness (approx. 7 mm) of the samples, i.e., $L = 35$ mm. The samples were loaded at a speed of 1000 mm/min up to fracture. The pouring process of Inconel 713C was carried out in the Research and Development Laboratory for Aerospace Materials at the Rzeszow University of Technology in a double-chamber vacuum oven VIMIC2E—DS/SC produced by ALD Vacuum Technology. Each ceramic mold was placed in the chamber of the furnace and preheated at 1250 °C for 100 min. The 4-kg ingot of the Inconel 713C superalloy was inductively melted in a vacuum of 2.9×10^{-3} Pa. The liquid superalloy was poured into molds at 1520 °C and subsequently displaced to the cooling zone of the furnace (in about 10 s). It should be mentioned that differential scanning calorimetry (DSC) of fibers which was isolated from the binder indicated strong exothermic peak at 885 °C. During solidification of castings, the cooling chamber was ventilated and the next mold was mounted inside the furnace. After solidification, the products were cooled to room temperature, the molds were broken, and cast plates were cut off. The surfaces of all plates were sand-blasted and etched in the solution of 0.75 g molybdic acid,

25 mL nitric acid and 25 mL hydrochloric acid in 25 mL water. Macrostructures of the castings recorded on an Optimus device were subjected to analysis by ImageJ commercial software (five images for one casting). The mean area, perimeter, size of grain (diameter of a circle with the same surface area) and number of grains per cm^2 were calculated. Further microstructural observations were carried out on an optical microscope and scanning electron microscope equipped with (EDS) energy-dispersive x-ray spectrometer (accelerating voltage 20 kV). Microstructure images recorded on (LM) Leica DM4500 and SEM Phenom XL were subjected to threshold and binarization by ImageJ, and then, the area fraction of porosity, area fraction of carbides and volume fraction of γ' both in dendrite arms and interdendritic spaces were calculated. Minimum five images for each casting were used to calculate the stereological parameters. Samples were electrochemically etched in 10% CrO_3 solution. Segregation coefficient $k = \frac{C_D^i}{C_{ID}^i}$ (concentration of alloying element in the centerline of dendrite divided by concentration in the interdendritic space) was calculated based on the 20 measurements in different locations. Each EDS linear distribution of alloying elements included 512 measurements on the selected line. Vickers hardness (HV10) measurements (10 for each casting) were carried out on Zwick/Roell device.

3. Results and Discussion

3.1 Green Strength of Molds

Bend strengths of the unmodified and fiber- and metal-reinforced molds are shown in Table 3. There is a clear indication that the fiber- and metal-free mold has a lower green strength than all the reinforced molds. For mold Ni, the strength, 3.94 MPa, was higher by more than 30% from unmodified mold B. Addition of glass fibers and metal powders also led to more uniform bend strengths of the modified molds. Obtaining more repeatable results is very beneficial to the production of castings.

According to the Maity and Maity (Ref 17), the reason for the increased strength was crack growth resistance ensured by the fibers, located mostly parallel to the layers, perpendicular to the direction of cracking propagation. Based on the results of Wang (Ref 20), the exothermic peak at 885 °C obtained during DSC corresponded to the crystallization of fibers. During firing of mold and subsequent melt pouring, the phase transformation solid state (metal powders) → liquid also occurred. Designed melt-pouring temperature was 1520 °C and so higher than the melting point of Al (660 °C), Cu (1085 °C) and Ni (1455 °C), whereas slightly lower than for Fe (1538 °C) (Ref 21). A previous investigation (Ref 18) showed that the maximum temperature in the second layer during investment casting process can be lower approximately 150 °C than the pouring temperature. This indicates that the Fe and Ni existed as solid particles.

3.2 Stereological Parameters of Castings Structure

The macrostructure of the castings produced using molds reinforced with glass fibers and metal powders is shown in Fig. 3. The thin-walled plates were of very high quality, so the lost-wax casting process was conducted correctly. Casting defects as cracks or misruns were not observed. It supposed that the presence of metal powders in the ceramic molds increased the thermal conductivity, and thus the cooling times of the molds could be shorter. Very high heat dissipation during pouring and solidification of castings favors undercooling and so consequently, the formation of a chill zone structure. These columnar grains were not revealed, so appropriate heat transfer after pouring was obtained. To compare the stereological parameters of the macrostructure of castings, image analysis was performed and the results are recorded in Table 4. The addition of Ni or Cu to the coverage led to slight grain refinement. The largest mean grain area was obtained in the casting Al; however, the large standard deviation indicates that the structure was not uniform. Among the large grains, very small ones were present. The most uniform mean area and mean perimeter of the grains were observed in the Ni casting. The standard deviation for the mean area 23.72 mm^2 was 19.49 mm^2, while for the mean perimeter 24.07 mm, it was 11.56 mm. The difference of mean grain size between the

Table 3 Green strength of molds

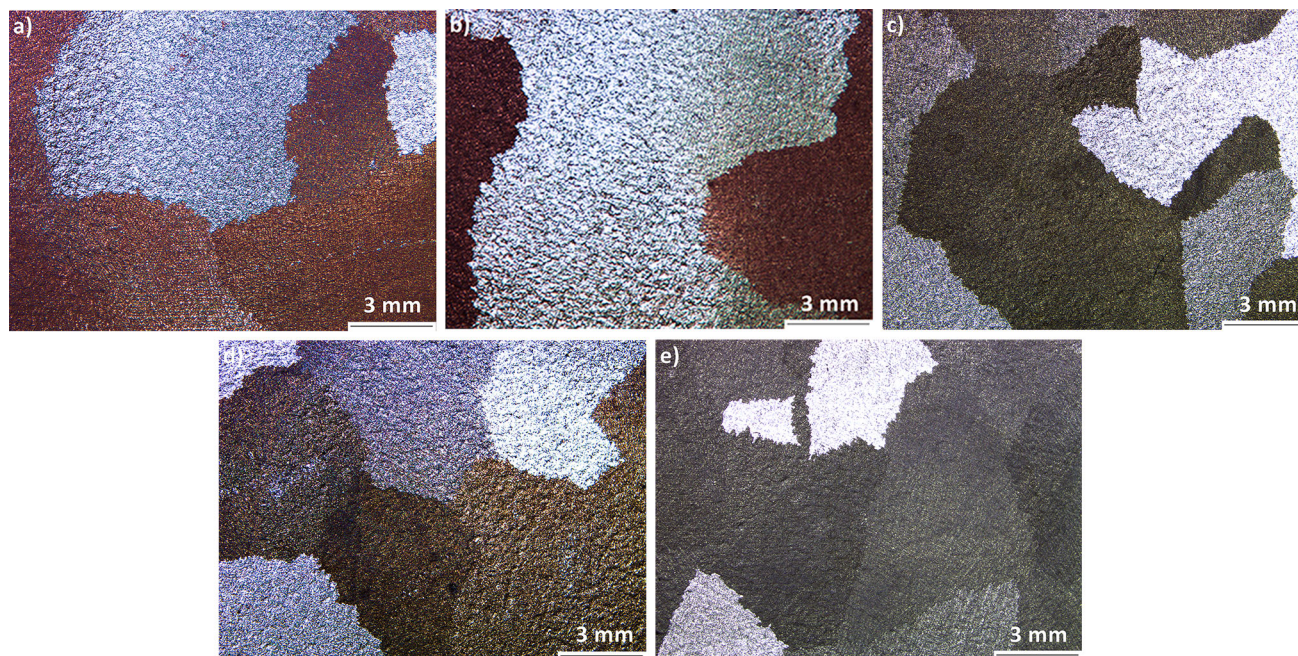| Shell mold	B	Al	Cu	Fe	Ni
Strength, MPa	3.0 (± 1.5)	3.65 (± 0.89)	3.74 (± 0.91)	3.66 (± 0.85)	3.94 (± 1.0)

Fig. 3   Selected macrostructure of casting produced in mold: (a) B; (b) Al; (c) Cu; (d) Fe; (e) Ni

Table 4 Results of macrostructure analysis

Mold	Mean area, mm²	Mean perimeter, mm	Mean grain size, mm	Range of grain size, mm	Number of grains per cm²
B	31.96 (± 29.63)	25.81 (± 13.68)	5.60 (± 3.04)	10.09	3.19 (± 0.53)
Al	54.01 (± 55.81)	34.61 (± 20.66)	7.26 (± 4.14)	11.51	1.85 (± 0.30)
Cu	23.54 (± 24.85)	23.71 (± 16.95)	4.76 (± 2.76)	9.83	4.25 (± 0.93)
Fe	29.03 (± 33.21)	24.19 (± 14.04)	5.30 (± 3.06)	12.13	3.45 (± 0.70)
Ni	23.72 (± 19.49)	24.07 (± 11.56)	5.04 (± 2.26)	8.27	4.21 (± 1.35)

Table 5 Secondary dendrite arm spacing in the molds

Mold	B	Al	Cu	Fe	Ni
Mean value, µm	82 (± 10)	74 (± 8)	63 (± 5)	74 (± 7)	80 (± 5)
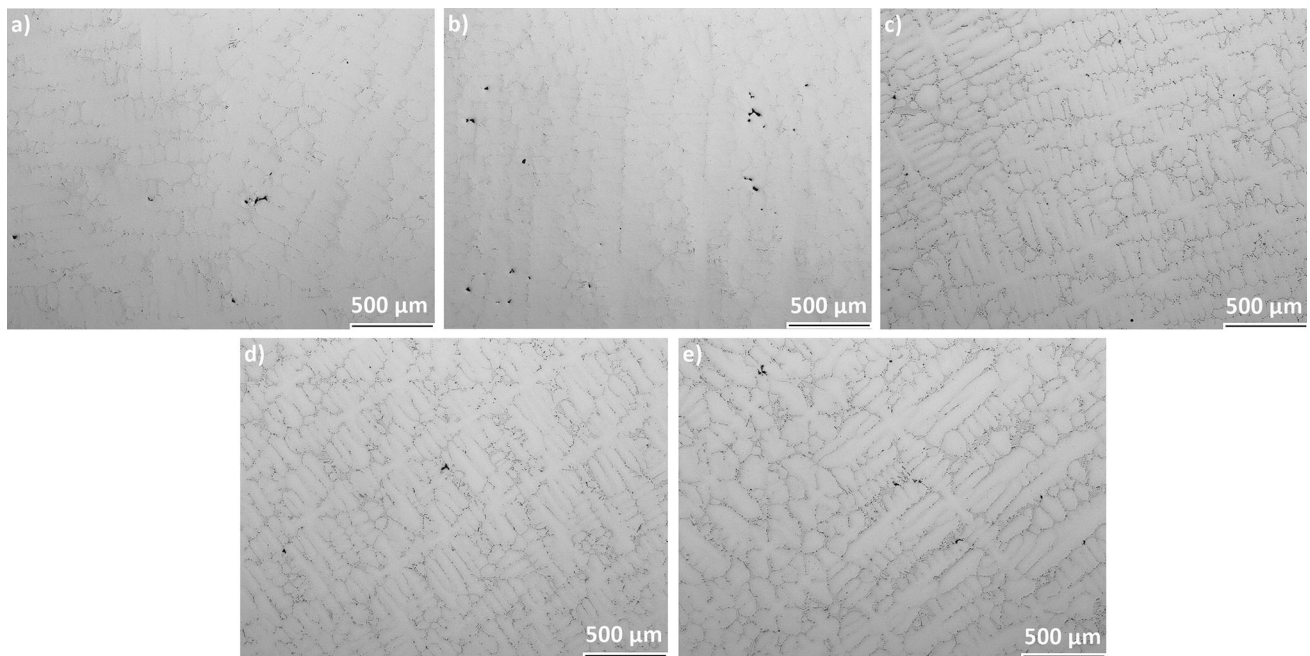
Fig. 4 Porosity of casting produced in mold: (a) B; (b) Al; (c) Cu; (d) Fe; (e) Ni

casting Al and the casting Cu, characterized by a more refined structure, was less than 2.5 mm.

Secondary dendrite arm spacing (SDAS) was measured, and the results are shown in Table 5. Strong correlation between SDAS and the variant of mold used was not found. The casting from unmodified mold was characterized by the largest mean SDAS. The average distance between the dendrite arms in the modified castings was in the range of 63-80 µm. The lowest average value was achieved in the Cu castings, whereas the highest in the casting Ni. The unmodified casting was characterized by the largest standard deviation of SDAS.

3.3 Optical Microscopic and SEM Observations

Microscopic examination of all specimens indicated the presence of irregularly distributed shrinkage porosity (Fig. 4), predominantly in the interdendritic regions. Their location indicated that porosity formed during the last stages of

solidification, when capillary feeding becomes insufficient. Based on the unetched microstructures, the area fraction of porosity was calculated and results are shown in Fig. 5.

In the casting B, the porosity was 0.095%. Only in casting Al, the porosity was higher 0.107%. In the other modified castings, namely Cu, Fe and Ni, the porosity was much lower 0.044, 0.029 and 0.061%, respectively. The investment casting of IN713C in the mold with the addition of glass fibers and Fe powder led to a threefold reduction in porosity. Subsequent reduction in porosity can be obtained by using hot isostatic pressing (HIP) treatment. According to the investigation focusing on the healing mechanism of K452 superalloy, porosity can be reduced through HIP even 82% (Ref 22). At least two factors have been proposed, which can control microporosity formation in superalloys: the volume fraction of residual liquid at the end of solidification, and the so-called cork effect associated with carbides formed near the liquidus

temperature (Ref 23). In order to compare the fraction of porosity with the fraction of primary carbides in the castings, SEM observation of unetched specimens was carried out (Fig. 6). The largest volume fraction of carbides was calculated for casting Al, 1.05%, which was characterized by the highest porosity (Fig. 7). The lowest volume of carbides was in casting Fe (0.72%) with the lowest porosity. For castings B, Cu and Fe, no such a clear relationship was recorded. Baldan (Ref 23) observed that the porosity level in DS200 + Hf alloy decreases with the increasing fraction of carbides, whereas the carbon content of IN100 was found to impair the soundness (Ref 23).
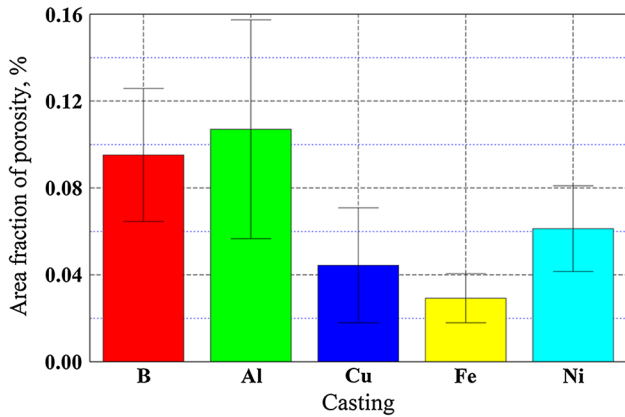
The contradictory relations indicate that the influence of one specific factor on microporosity incidence in Ni-based super-alloy depends not only on the nature of this factor, but also on the whole chemical composition and segregation of alloying elements during solidification.

SEM examination of etched specimens indicated the presence of a dendritic microstructure typical of the as-cast state (Fig. 8). The microstructure of interdendritic regions in all castings was complex due to the presence of numerous constituents, which has been analyzed in detail (Sect. 3.5). The near-cubic-shaped precipitates of intermetallic γ' phase

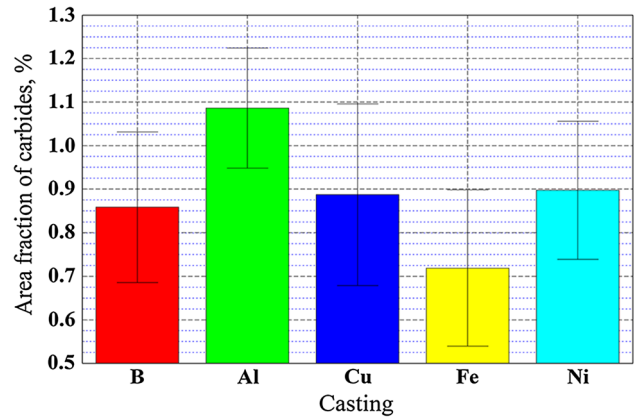Fig. 5   Area fraction of porosity in castings

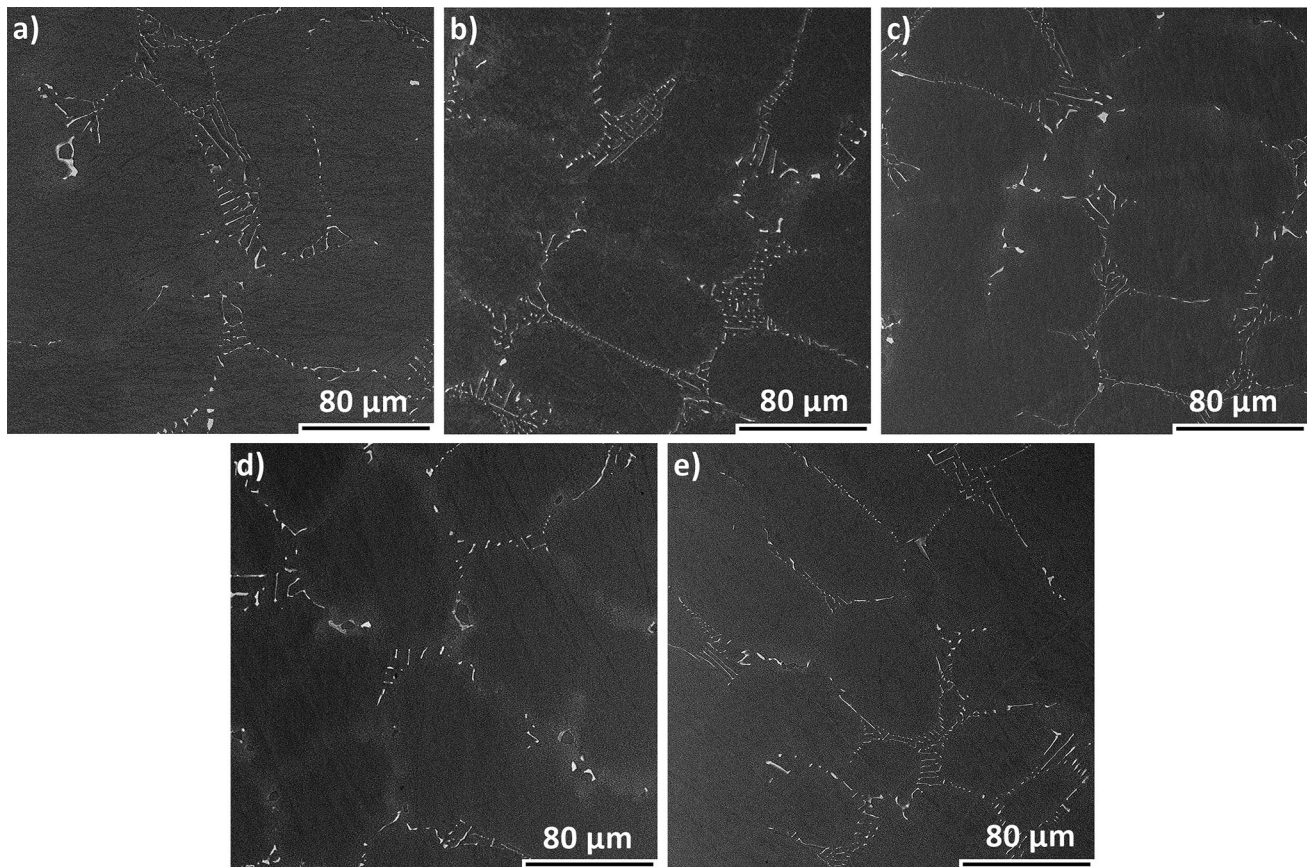Fig. 7   Area fraction of carbides in castings

Fig. 6   Morphology of primary carbides in casting: (a) B; (b) Al; (c) Cu; (d) Fe; (e) Ni

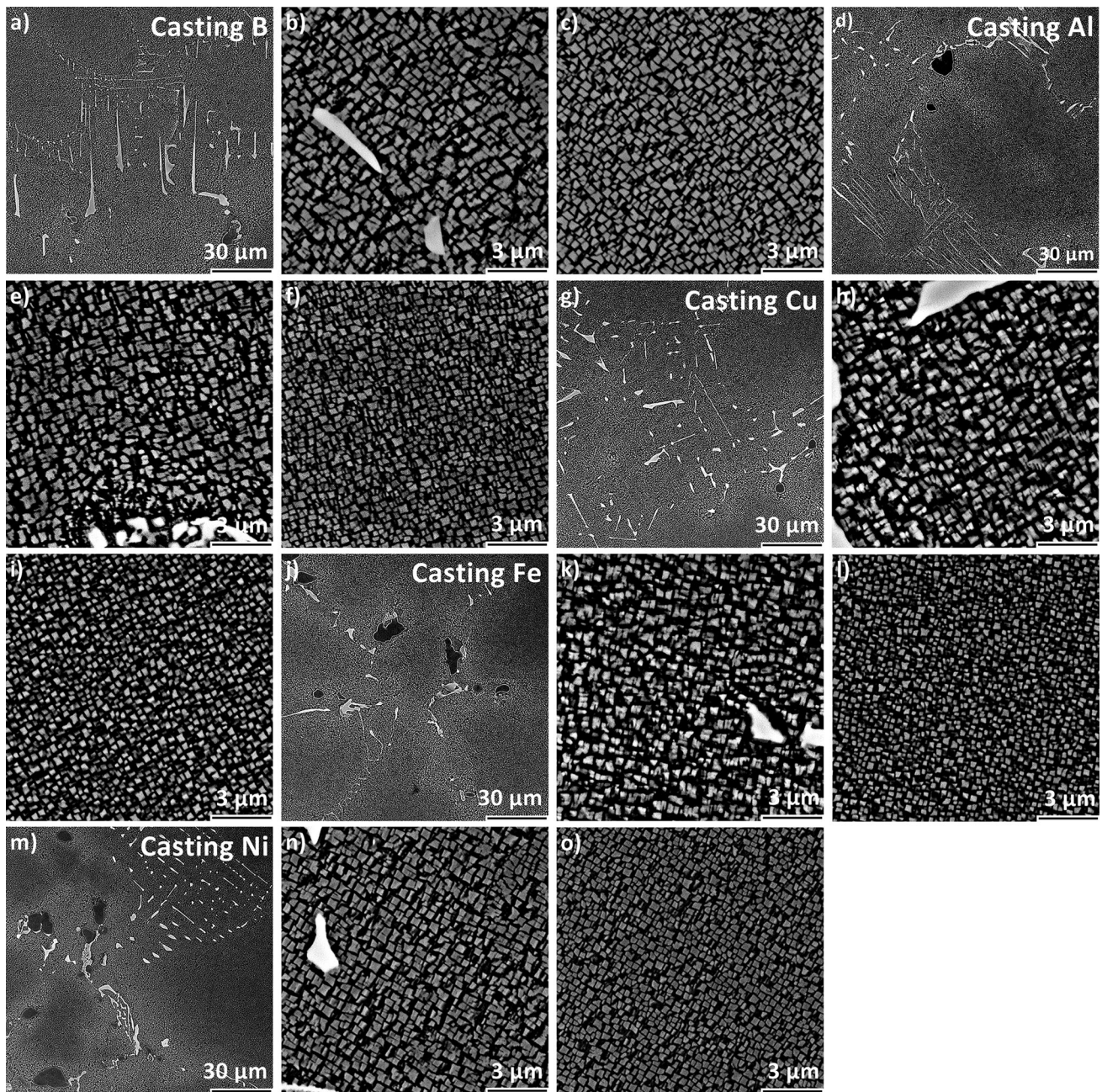**Fig. 8** Microstructure of Inconel 713C castings: (a, d, g, j, m) interdendritic spaces; (b, e, h, k, n) γ' in interdendritic space (c, f, i, l, o) γ' precipitates in dendrite arm

were surrounded by the γ phase, while their size and morphology were different in dendrite arms and between them. This difference is related to the irregular distribution of alloying elements in the volume of castings, which affected the size of the γ' phase precipitates. The volume fraction of γ' phase also differed between the castings. Measurements were carried out in dendrite arms and interdendritic spaces, and the results are shown in Fig. 9. In each casting, the volume fraction of the γ' phase reached a higher value in the dendrite arms. The volume fraction of γ' phase in the dendrite arms of casting B was 49%, while a lower value was only in the casting Cu, 46.5%. The highest volume fraction of the γ' phase in the dendrite arms was obtained in the casting Al: 53.7%. Thus, an increase of over 9% was reached in comparison with the casting B. Taking into

account interdendritic spaces, the highest volume fraction of γ' phase was also obtained in the casting Al (48.5%). Similar to the measurements in dendrite arms, the volume fractions of precipitates in castings Fe and Ni were higher than in the casting B.

3.4 Segregation Coefficient

The average concentration of the main alloying elements in the dual-phase area ($\gamma + \gamma'$) in dendrite arms and the interdendritic spaces were measured using energy-dispersive x-ray spectroscometry. Microsegregation of alloying elements during solidification caused their concentrations in different regions to be quite different. In order to show irregular distribution of alloying elements between these regions, the coefficient
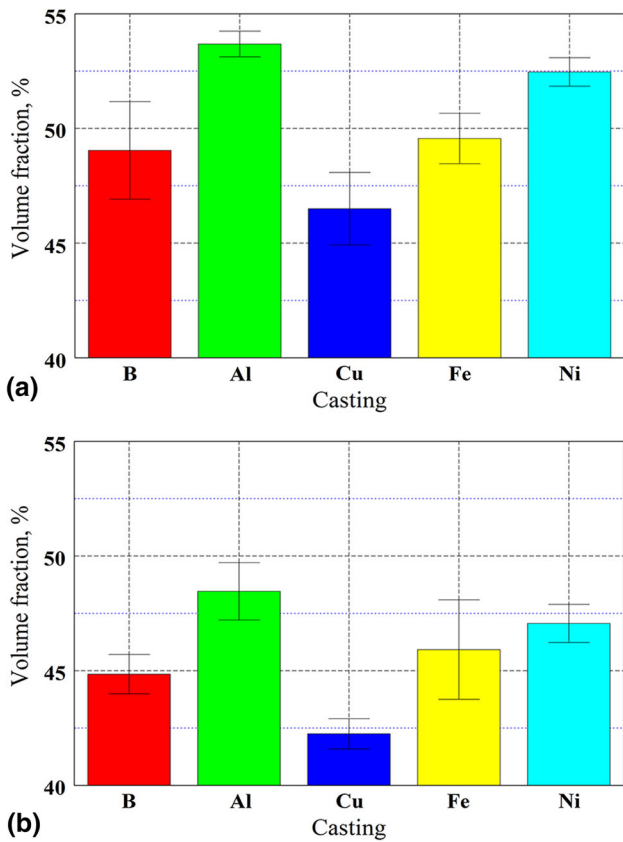
Fig. 9 Volume fraction of γ' in: (a) dendrite arms; (b) interdendritic spaces

$k = \frac{C_D^i}{C_{ID}^i}$, the ratio of the concentration of alloying element in the centerline of dendrites to the concentration in interdendritic spaces, was calculated and is presented in Fig. 10 for all castings.

Aluminum is the main γ' former in Ni-based superalloys. The highest k_{Al} value was observed in the castings from molds designated as B and Ni, namely 1.12 and 1.10, although the standard deviation was also the highest for these variants. The lowest k_{Al} value and also standard deviation were obtained for the casting Cu. Significantly lower segregation coefficients were observed when measuring the Ti contents. In all castings $k < 1$, which indicates a significant enrichment in the interdendritic spaces in this alloying element. The lowest value was recorded for the Fe casting, while the highest for Al casting, and so $0.54 \leq k \leq 0.65$. Analysis of the distribution of Nb in the castings also indicated a significant increase in its concentration in interdendritic spaces. The lowest k_{Nb} was for the Cu casting; the highest for Ni casting, 0.56 and 0.71, respectively. The distribution of Mo in the castings was much more uniform relative to Ti and Nb. The obtained mean k_{Mo} values were in the range of 1.01-1.16. The highest k_{Mo} was for the casting from mold B (the standard deviation was also the highest), while the lowest was for the Al and Ni castings. Measurements of Cr concentration gave all k_{Cr} values higher than 1, so its content was higher in dendrite arms. By far, the highest k_{Cr} was calculated for castings from molds Fe and B, 1.38 and 1.37, respectively. Resulted segregation leads to inhomogeneity of the coherence stresses and inhomogeneity of the thermal contraction during γ'-precipitation. In order to

decrease the irregular distribution of all alloying elements, a solution heat treatment is usually carried out. Segregation of alloying elements causes a misfit inhomogeneity, and hereby, it influences the primary creep of superalloys (Ref 24, 25).

3.5 Morphology and Chemical Composition of the Primary Phases

The segregation of the alloying elements during solidification led to the formation of many phases in interdendritic spaces of castings. Intensive observation and analysis indicated that, independently of casting variant, the same phases occurred in interdendritic spaces. The microstructure of these selected constituents and results of EDS analysis were presented, respectively, in Fig. 11 and 12.

Based on the microstructural features, it can be concluded that in the first stage of solidification, γ phase is formed. During cooling, the solubility of elements like Nb, Mo, Ti and C in the existing matrix decreased, which induces their segregation at the γ phase dendrite–interdendritic liquid interface. These conditions favor the precipitation of carbides which occurs in various forms, from blocky shaped to Chinese script, e.g., those in Fig. 8 and 11. All identified carbides were strongly enriched in Nb, Mo and Ti, which is clearly shown in Fig. 11(a). Nb forms MC-type carbides in superalloys, which are precipitated directly from the liquid according to L $\rightarrow$ MC and L $\rightarrow$ γ + MC reactions (Ref 26). Precipitates formed via the first reaction were moved into interdendritic spaces by solidified γ phase. Eutectic-type reaction also occurred at the final stage of Inconel 713C solidification, the L $\rightarrow$ γ + γ' reaction happened, and the gamma prime precipitates took up an irregular morphology as eutectic islands γ/γ'. Carbide formed through the eutectic reaction, in the close vicinity of constituent with lamellar morphology, is presented in Fig. 11(b). Microanalysis in the main core of this precipitate revealed an increased concentration of Ni and Zr (Fig. 12b). One of the important features of superalloys is the enhancement of creep strength when minute amounts of Zr and also B are added. Both these elements are in the investigated alloy: 0.012 wt.% (B) and 0.08% (Zr). As their solubility in the γ and γ' is very low, favorable conditions for the formation of intermetallic phases and borides exist. Transmission electron microscopy of IN713C (Ref 9) indicated that such lamellar precipitates were Ni_7Zr_2. According to the Ni-Zr (Ref 27) binary diagram, Ni_7Zr_2 (mC36, C2/m) is formed at 1438 °C through congruent reaction L $\rightarrow$ Ni_7Zr_2, and then, two peritectic reactions occur: at 1304 °C, L + Ni_7Zr_2 $\rightarrow$ Ni_5Zr (cF24, F-43 m) and subsequently at 1181 °C L + Ni_7Zr_2 $\rightarrow$ $Ni_{21}Zr_8$. Franke (Ref 27) indicated that only one eutectic reaction occurs with the formation of face-centered cubic FCC-γ, L $\rightarrow$ γ + Ni_5Zr at 1164 °C. Thus, Ni_7Zr_2 phase can be present in the Inconel 713C, but not in the form of eutectic γ/Ni_7Zr_2, and its formation can be complex as the microstructure suggests. Residual liquid is enriched in Zr at the final stage of solidification reaction with the eutectic phase or primary γ' through a peritectic-type transformation L + γ' $\rightarrow$ γ + Ni_7Zr_2 (Ref 28). Due to the complex chemical composition of Ni-based superalloys, at the end of solidification, ternary eutectic transformation can take place. An example of ternary eutectic reaction which produces Ni_7Zr_2 was proposed (Ref 28), namely L $\rightarrow$ γ + Ni_7Zr_2 + Ni_5Zr, but the Ni_5Zr was not detected in IN713C. Similarly, in other Ni-based superalloys (IN100 and IN738), the presence of Ni_7Zr_2 phase was
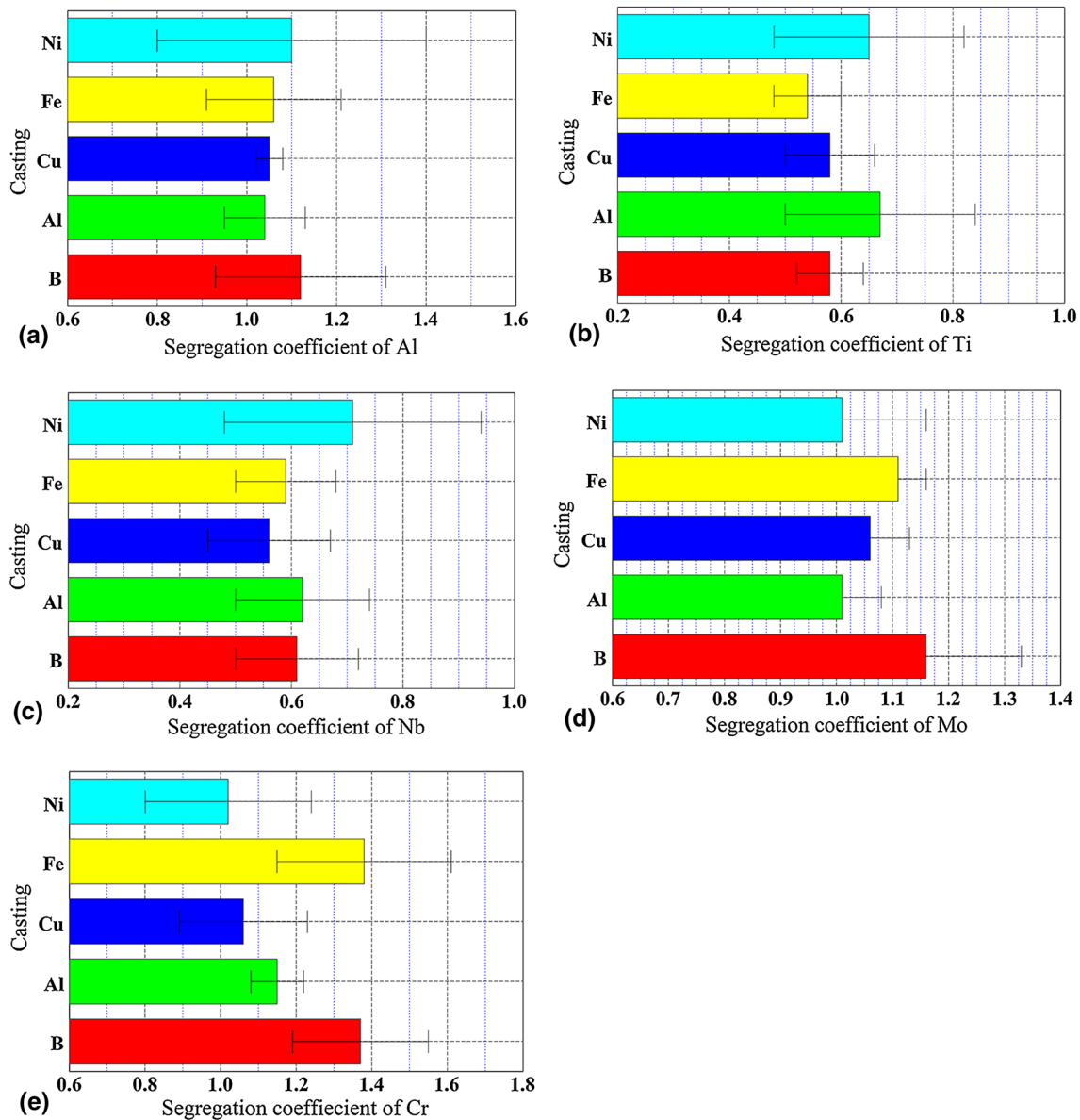
Fig. 10 Segregation coefficient of alloying element in produced castings: (a) Al; (b) Ti; (c) Nb; (d) Mo; (e) Cr

confirmed (Ref 29, 30). Morphology and microanalysis of carbides (MC type) near the compound Ni_7Zr_2 show that they are strongly enriched in Nb and Zr. Such enrichment suggests that during solidification of castings, a ternary eutectic transformation, namely L (residual with high content of Zr and C) $\rightarrow$ γ + Ni_7Zr_2 + (Nb, Zr)C. In Fig. 11(c), the microstructure of the lamellar precipitate formed in the close vicinity of eutectic island is illustrated. EDS analysis of this precipitate showed an increased concentration of Mo and Cr (Fig. 12c). The total content of these elements exceeded even 80 at.%. Similar results were obtained in several Ni-based superalloys and indicated that it is a boride (Ref 31-34), e.g., M_5B_3 and M_3B_2. The difference in microstructure and chemical composition between these borides was investigated on the atomic scale resolution by Hu (Ref 35), who showed that the M_5B_3 borides are strongly enriched in tungsten, while the M_3B_2 in Mo and Cr. Due to lack of W in IN713C, M_5B_3

should not be present and only an M_3B_2 can be formed in IN71C, in accord with TEM observations (Ref 9). Babu (Ref 36) indicated that in chemically complex alloys, eutectic-type reactions can be much more complicated. He suggested that solute enrichment in the last portion of solidifying liquid phase to be inadequate to initiate a typical eutectic reaction due to negligible volume fraction of eutectic γ/γ'. In Fig. 11(d) and 12(d), morphology and alloying elements distribution in M_3B_2 adjacent to the Ni_7Zr_2 and eutectic island γ/γ' are presented. Such multiphase regions indicate that the formation of the γ/γ' eutectic islands can be accompanied by precipitation from the remaining liquid phase of a ternary eutectic in line with L (enriched in Zr and B) $\rightarrow$ γ + Ni_7Zr_2 + M_3B_2. Observations of the morphology of constituents in our IN713C castings were similar to Babu's (Ref 36) interpretation, so can be an explanation of the formation of primary phases in the interdendritic regions.
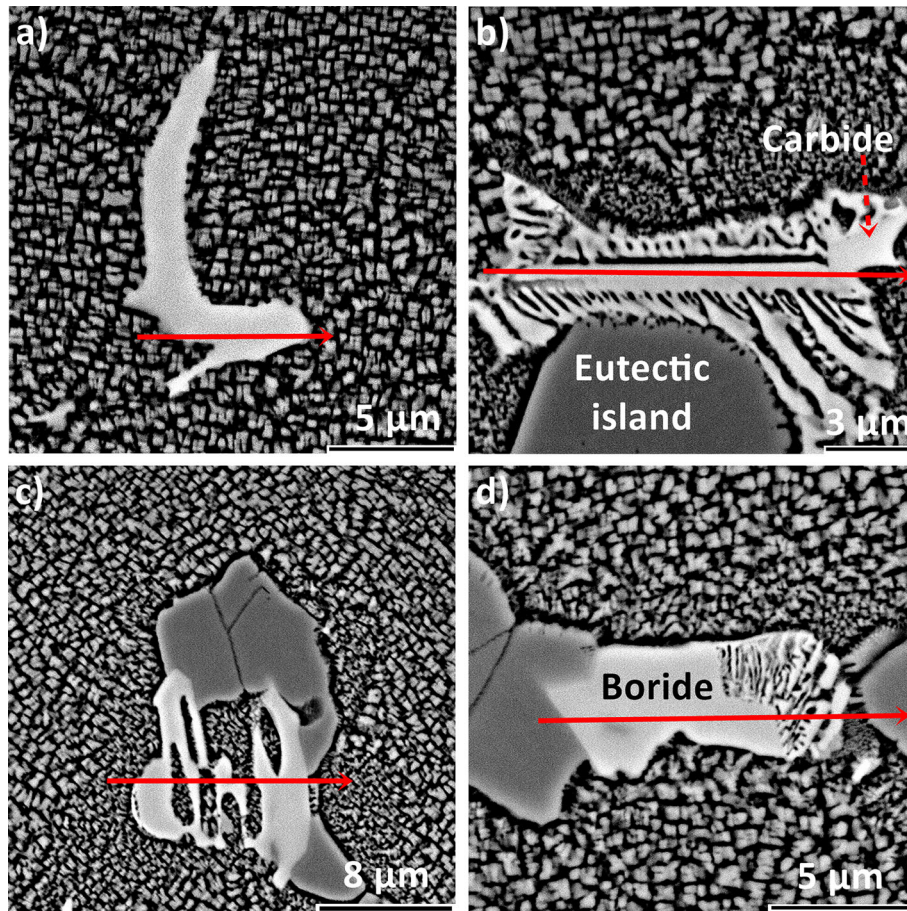
Fig. 11 Morphology of microstructural constituents and location of EDS line: (a) MC carbide; (b) MC carbide and Ni_7Zr_2; (c) boride M_3B_2; (d) eutectic island γ/γ', M_3B_2 and Ni_7Zr_2

3.6 Vickers Hardness Measurements

The average values of Vickers hardness with the standard deviation or all castings are shown in Fig. 13. The casting from the mold not reinforced with fibers, and metal powders had a hardness of 348 HV10. In the remaining castings made in modified molds with the exception of Cu, the hardness was higher. The highest value was achieved in the casting Al: 366 HV10, then in the castings Fe: 361 HV10 and the Ni: 358 HV10. The difference between the highest (Al) and the lowest (Cu) value was 7%, while in comparison with casting B, it was 5%. The highest hardness value was obtained in the casting (Al), strengthened by the highest volume fraction both of the γ' phase and carbides. The reverse dependence was attributed to the casting Cu. The lowest hardness corresponded with the lowest volume fraction of the γ' phase and carbides.

4. Conclusions

Five kinds of mold were used to fabricate thin-walled Ni-based superalloy castings: one was made without strengthening agents, the others contained glass fibers and metal, Al, Cu, Fe, Ni, powder particles.

- An increase in green strength was obtained for all modified molds, while the variant with glass fibers and nickel powder achieved the highest bend strength (3.94 MPa). One of the important goals was obtained, namely it is possible to strengthen molds simultaneously through glass fibers and metal powders,

- The addition of glass fibers and Al powder produced a structure with a very large grain size (7.26 mm). Variants Cu and Ni led to grain refinement in comparison with the casting from unmodified mold, respectively, 4.76 and 5.04 mm. The most uniform grain size distribution was found in the casting Ni,

- Measurements of SDAS suggested that addition of metal powders increased the thermal conductivity of modified molds,

- The highest porosity was in the casting Al, namely 0.107%, while the lowest in casting Fe 0.029%. The casting produced in standard form B had a area fraction of porosity 0.095%,

- The area fraction of the carbides in the casting B was 0.86%, higher in the castings Al: 1.09%,

- Microstructure of castings due to the irregular distribution of alloying elements during solidification also affected the smaller size of the γ' phase precipitates in dendrite arms,

- Volume fraction of γ' precipitates in all castings was higher in dendrite arms. The highest volume fraction of γ' precipitates was in casting Al, 53.7% in dendrite arms and 48.5% in interdendritic spaces. Castings Fe and Ni were also characterized by higher volume fraction of γ' in com-
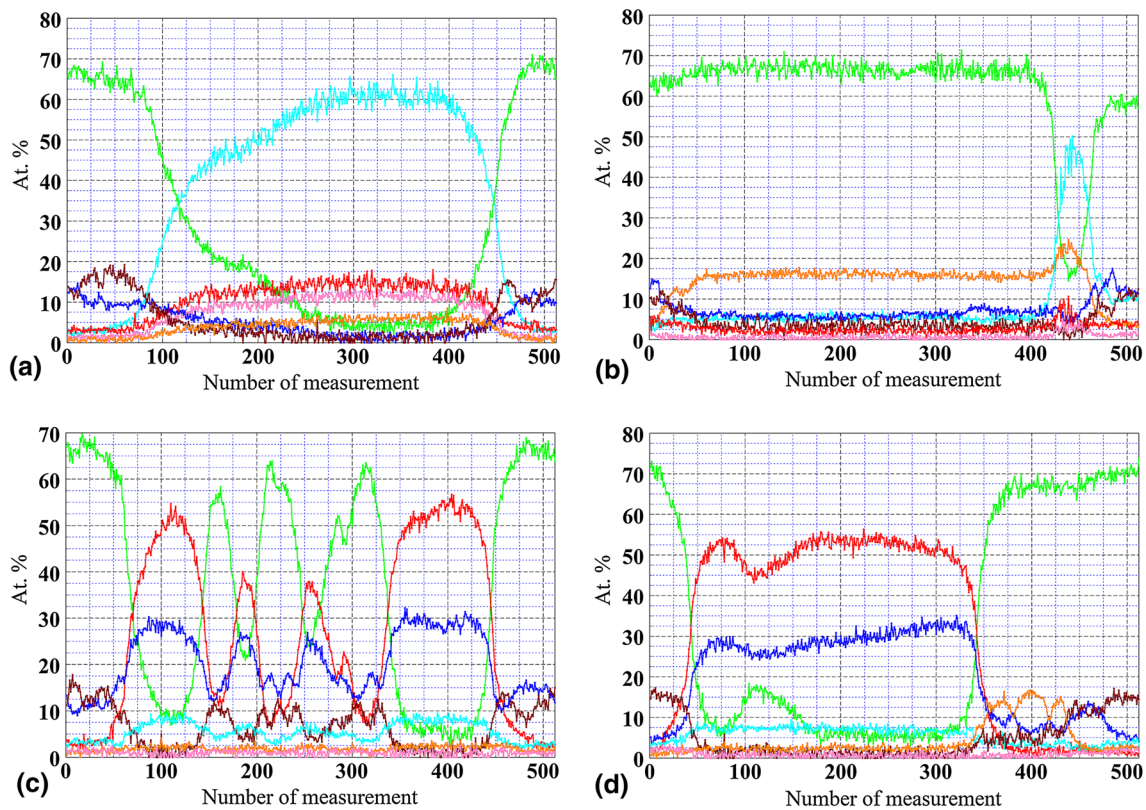
Fig. 12 Results of EDS line analysis: (a) MC carbide; (b) MC carbide and Ni7Zr2; (c) M3B2; (d) eutectic island γ/γ', M3B2 and Ni7Zr2. Colors: bright green—Ni, turquoise—Nb, bronze—Al, blue—Cr, red—Mo, pink—Ti, orange—Zr (Color figure online)
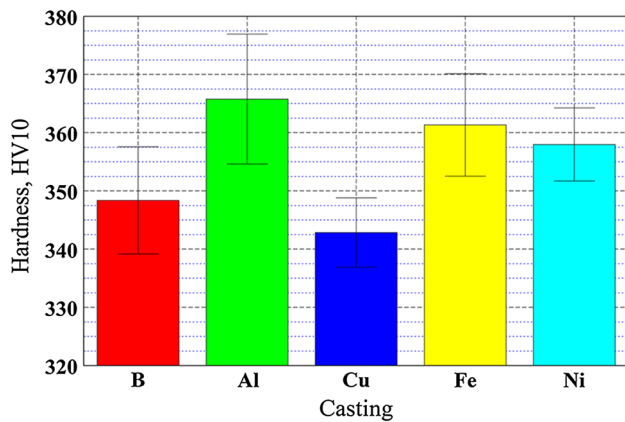

Fig. 13 Hardness of castings

parison with casting from unmodified mold,

- During solidification, of Inconel 713C constituents in interdendritic spaces were created through complex phase transformation. Enrichment of residual interdendritic liquid phase in Al and Ti led to formation of irregular γ' in the form of eutectic islands γ/γ'. Low solubility of Zr and B in the γ and γ' caused the formation of Ni_7Zr_2 and Mo-rich borides M_3B_2.
- The highest hardness, 366 HV10, was obtained in casting with the highest volume fraction of γ' and carbides, namely Al, to be compared with that from the unmodified mold, 348 HV10.
- Results of the microstructural investigation showed that castings produced in the modified molds characterized by the same high quality like in standard mold B,
- Due to the increased strength of molds, the number of layers can be lower; consequently, the drying time during fabrication may be shorter.

Acknowledgments

Open Access

References

1. H. Long et al., Microstructural and Compositional Design of Ni-Based Single Crystalline Superalloys—A Review, *J. Alloys Compd.*, 2018, **743**, p 203–220. https://doi.org/10.1016/j.jallcom.2018.01.224

2. T. Pollock and S. Tin, Nickel-Based Superalloys for Advanced Turbine Engines: Chemistry, Microstructure, and Properties, *J. Propuls. Power*, 2006, **22**(2), p 361–374. https://doi.org/10.2514/1.18239

3. H. Matysiak et al., The Microstructure Degradation of the IN 713C Nickel-Based Superalloy After the Stress Rupture Tests, *J. Matet. Eng. Perform.*, 2014, **23**(9), p 3305–3313. https://doi.org/10.1007/s11665-014-1123-4

4. M. Azadi and M. Azadi, Evaluation of High-Temperature Creep Behavior in Inconel 713C Nickel-Based Superalloy Considering Effects of Stress Levels, *Mater. Sci. Eng., A*, 2017, **689**, p 298–305. https://doi.org/10.1016/j.msea.2017.02.066

5. A. Chamanfar et al., Cracking in Fusion Zone and Heat Affected Zone of Electron Beam Welded Inconel-713LC Gas Turbine Blades, *Mater. Sci. Eng., A*, 2015, **642**, p 230–240. https://doi.org/10.1016/j.msea.2015.06.087

6. M. Coleman et al., Deformation Mechanisms of IN713C Nickel Based Superalloy During Small Punch Testing, *Mater. Sci. Eng., A*, 2016, **650**, p 422–431. https://doi.org/10.1016/j.msea.2015.10.056

7. A. Szczotok and H. Matysiak, Influence of Constituents of Shell Mold on the Morphology and Chemical Composition of Carbides Occurring in IN 713C Superalloy Castings, *J. Mater. Eng. Perform.*, 2014, **23**(8), p 2748–2759. https://doi.org/10.1007/s11665-014-1035-3

8. S. Pattnaik and M. Sutar, A Review on Investment Casting Ceramic Shell Building Process, *Int. J. Electr. Electron. Comput. Syst.*, 2017, **6**(8), p 399–405

9. H. Matysiak et al., The Influence of the Melt-Pouring Temperature and Inoculant Content on the Macro and Microstructure of the IN713C Ni-Based Superalloy, *J. Miner.*, 2016, **68**(1), p 185–197. https://doi.org/10.1007/s11837-015-1672-5

10. Y. Venkat et al., Effect of Fine Alumina in Improving Refractoriness of Ceramic Shell Moulds Used for Aeronautical Grade Ni-Base Superalloy Castings, *Ceram. Int.*, 2018, **44**, p 12030–12035. https://doi.org/10.1016/j.ceramint.2018.03.197

11. D. Szeliga et al., Investigation of Casting-Ceramic Shell Mold Interface Thermal Resistance During Solidification Process of Nickel Based Superalloy, *Exp. Therm. Fluid Sci.*, 2017, **87**, p 149–160. https://doi.org/10.1016/j.expthermflusci.2017.04.024

12. S. Jones and C. Yuan, Advances in Shell Moulding for Investment Casting, *J. Mater. Process. Technol.*, 2003, **135**, p 258–265. https://doi.org/10.1016/S0924-0136(02)00907-X

13. K. Lü et al., The Interfacial Characteristics and Action Mechanism of Fibre-Reinforced Shell for Investment Casting, *Int. J. Adv. Manuf. Technol.*, 2017, **93**, p 2895–2902. https://doi.org/10.1007/s00170-017-0735-x

14. K. Lü et al., Properties of Hybrid Fibre Reinforced Shell for Investment Casting, *Ceram. Int.*, 2016, **42**, p 15397–15404. https://doi.org/10.1016/j.ceramint.2016.06.188

15. K. Lü et al., Bending Strength and Fracture Surface Topography of Natural Fiber-Reinforced Shell For Investment Casting Process, *China Found.*, 2016, **13**, p 211–216. https://doi.org/10.1007/s41230-016-5100-4

16. F. Wang et al., Microstructure and Strength of Needle Coke Modified Ceramic Casting Molds, *Ceram. Int.*, 2016, **40**, p 479–486. https://doi.org/10.1016/j.ceramint.2013.06.027

17. P. Maity and J. Maity, Development of High Strength Ceramic Shell for Investment Casting, *Indian Found. J.*, 2001, **47**(7), p 23–26

18. Ł. Rakoczy and R. Cygan, Analysis of Temperature Distribution in Shell Mould During Thin-Wall Superalloy Casting and its Effect on the Resultant Microstructure, *Arch. Civ. Mech. Eng.*, 2018, **18**, p 1441–1450. https://doi.org/10.1016/j.acme.2018.05.008

19. R. Cygan, Patent Application, Self-Supporting Multi-Layered Ceramic Moulds with the Addition of Metals to Production of Precision Castings. Number P.421560. Warsaw 2017 (in Polish)

20. Y. Wang, Crystallization Kinetics of Calcium Aluminate Glasses Studied by Non-Isothermal Techniques, *J. Wuhan Univ. Technol. Mater. Sci. Ed.*, 2013, **28**, p 907–911. https://doi.org/10.1007/s11595-013-0791-5

21. D.L. Ride, *CRC Handbook of Chemistry and Physics*, 95th ed., CRC Press, Boca Raton, 2009

22. C. Yuan et al., On Healing Mechanism of Cast Porosities in Cast Ni-based Superalloy by Hot Isostatic Pressing, Energy Materials, *The Minerals, Metals and Materials Series*, Springer, 2017 https://doi.org/10.1007/978-3-319-52333-0_24

23. A. Baldan, Effects of Growth Rate on Carbides and Microporosity in DS200 + Hf Superalloy, *J. Mater. Sci.*, 1991, **26**, p 3879–3890. https://doi.org/10.1007/BF01184986

24. A. Epishin et al., Effects of Segregation in Nickel-Base Superalloys: Dendritic stresses, *Superalloys*, 2004, **2004**, p 537–543. https://doi.org/10.7449/2004/Superalloys_2004_537_543

25. Ł. Rakoczy et al., Evolution of γ' Morphology and γ/γ' Lattice Misfit in a Nickel-Based Superalloy During Non-Equilibrium Cooling, *Int. J. Mater. Res.*, 2019, **110**(1), p 66–69. https://doi.org/10.3139/146.111729

26. F. Zupanic et al., Structure of Continuously Cast Ni-Based Superalloy Inconel 713, *J. Alloys Compd.*, 2001, **329**, p 290–297. https://doi.org/10.1016/S0925-8388(01)01676-0

27. P. Franke, D. Neuschutz, Binary Systems. Part 4: Binary Systems From Mn-Mo to Y-Zr. Landolt-Börnstein–Group IV Physical Chemistry, *Numerical Data and Functional Relationships in Science and Technology*, vol. 19B4, Springer, Berlin, Heidelberg, 2006

28. H.B. Motejadded et al., Dissolution Mechanism of a Zr Rich Structure in a Ni_3Al Base Alloy, *J. Mater. Sci. Technol.*, 2011, **27**(10), p 885–892. https://doi.org/10.1016/S1005-0302(11)60160-6

29. Y. Murata and N. Yukawa, Solid-State Reaction for ZrC Formation in a Zr-Doped Nickel-Based Superalloy, *Scr. Metal.*, 1986, **20**(5), p 93–696. https://doi.org/10.1016/0036-9748(86)90493-X

30. O. Ojo et al., Microstructural Study of Weld Fusion Zone of TIG Welded IN 738LC Nickel-Based Superalloy, *Scr. Mater.*, 2004, **51**, p 683–688. https://doi.org/10.1016/j.scriptamat.2004.06.013

31. A. Shulga, Boron and Carbon Behavior in the Cast Ni-Base Superalloy EP962, *J. Alloys Compd.*, 2007, **436**, p 155–160. https://doi.org/10.1016/j.jallcom.2006.07.051

32. J. Wei et al., The Effects of Borides on the Mechanical Properties of TLPB Repaired Inconel 738 superalloy, *Metall. Trans. A*, 2017, **48**(10), p 4622–4631

33. X.B. Hu et al., The Wyckoff Positional Order and Polyhedral Intergrowth in the M3B2- and M5B3-Type Boride Precipitated in the Ni-Based Superalloy, *Sci. Rep.*, 2014, **4**, p 1–9

34. B. Zhang et al., Precipitation and Evolution of Boride in Diffusion Affected Zone of TLP Joint of MAR-M247 Superalloy, *J. Alloys Compd.*, 2017, **695**, p 3202–3210

35. X.B. Hu et al., Atomic-Scale Observation and Analysis of Chemical Ordering in M3B2 and M5B3 Borides, *Scr. Mater.*, 2018, **149**, p 274–284

36. S. Babu et al., Atom-Probe Field-Ion Microscopy Investigation of CMSX-4 Ni-Base Superalloy Laser Beam Welds, *International Field Emission Society IFES'96 Proceedings of the 43rd International Field Emission Symposium*, 1996

Article

The Effect of CoAl$_2$O$_4$ as a Nucleating Agent and Pouring Temperature on the Microstructure and Properties of Inconel 713C® Nickel-Based Superalloy Castings

Rafał Cygan [1],* and Łukasz Rakoczy [2]

[1] Consolidated Precision Products Corporation, Investment Casting Division, Hetmańska 120, 35-078 Rzeszow, Poland

[2] Faculty of Metals Engineering and Industrial Computer Science, AGH University of Krakow, Mickiewicza 30, 30-059 Krakow, Poland; lrakoczy@agh.edu.pl

* Correspondence: rafal.cygan@cppcorp.com

Abstract: In this work, three melt-pouring temperatures (1450 °C, 1480 °C, 1520 °C) and CoAl$_2$O$_4$ inoculant contents in the shell mold's primary coating (0 wt%, 5 wt%, and 10 wt%) were selected to study microstructural and mechanical property changes of the Inconel 713C® nickel-based superalloy. The castings' phase transformation temperatures, phase constitution, microstructure, and mechanical properties at room and elevated temperatures were investigated via thermodynamical simulations, differential thermal analysis, light and scanning electron microscopy, energy-dispersive X-ray spectroscopy, and tensile and stress-rupture tests. The pouring temperature and inoculant content strongly influenced the mean equiaxed grain size, which ranged between 2.36 and 6.55 mm. The primary microstructure of Inconel 713C® castings, owing to its complex chemical composition, comprised multiple phases, including γ, γ', MC, M$_3$B$_2$, and Ni$_7$Zr$_2$. The mean size of γ' was in the 0.446–0.613 µm range, depending on the casting variant. Grain refinement with CoAl$_2$O$_4$ at ambient temperature for each melt-pouring temperature led to increased yield strength (YS) and ultimate tensile strength (UTS). YS was in the range of 775–835 MPa, while UTS was in the range of 868–1010 MPa. A reverse trend was observed in samples that crept in 982 °C/152 MPa, while for each variant, the time to rupture exceeded 30 h. The maximum time to rupture was 46.1 h obtained in the unmodified casting poured at 1480 °C.

Keywords: superalloy; inoculant; Inconel; shell mold; aerospace

1. Introduction

Inconel 713C® is classified as a nickel-based superalloy known for its exceptional properties at elevated temperatures [1]. It exhibits high mechanical strength and excellent resistance to oxidation and hot corrosion, making it suitable for manufacturing components for aerospace engines and industrial gas turbines [2]. Several physical factors contribute to the usefulness of Ni-based superalloys in harsh service environments. The face-centered cubic (FCC) structure of the γ matrix is characterized by low rates of thermally activated processes, resulting in lower creep deformation. The FCC crystal structure also remains thermodynamically stable from the temperature of liquid nitrogen to the melting point. The γ matrix is strengthened by coherent γ' precipitates, characterized by an ordered L1$_2$ structure [3]. This leads to a yield stress anomaly, where the flow stress increases with temperature, making it advantageous for high-temperature components [4]. Due to the high costs associated with superalloy machining, investment casting is crucial for fabricating elements with complex geometries [5]. The lost-wax process is particularly effective, offering high dimensional accuracy by using monolithic ceramic molds [6]. The cost difference between investment casting and other casting methods arises from the need to create disposable patterns and construct individual molds. Investment casting of Inconel

713C® primarily focuses on producing blades and vane clusters, typically for low-pressure turbine (LPT) sections [7]. Over the years, advancements in the complexity and integrity of lost-wax castings have led to continuous improvements in the manufacturing process. The superior mechanical properties of nickel-based superalloys mainly stem from the alloying elements found in their matrix, casting parameters, and heat treatment consisting of solution treatment and aging [8]. Notably, sufficiently high resistance to creep and low-cycle fatigue of the Inconel 713C® alloy can be achieved in as-cast conditions, eliminating the need for expensive heat treatment.

The continuous improvement of engines has made the LPT sections more structurally complex. Turbine components must possess an appropriate microstructure and be free of casting defects that could lead to catastrophic failure [9]. Operating temperatures can reach up to 700 °C, necessitating a fine-grained microstructure with high resistance to low-cycle fatigue (LCF) [10] and sufficiently good creep resistance [11]. Cast aerospace engine components produced by conventional lost-wax casting often have a coarse and inhomogeneous grain structure. However, these features can be controlled by adjusting the melt-pouring temperature and the composition of the prime coating in the shell mold [12]. Increasing the pouring temperature can enhance the filling ability of thin-walled blades and vanes but can also lead to grain coarsening due to decreased cooling rates [13]. The operating temperature in the LPT section is typically below the intensive creep range [14]. To address this issue, castings generally are modified by adding refiners, which contain highly stable particles, or by introducing an inoculant to the prime coat of the ceramic mold [15,16]. Grain refinement in the primary microstructure is directly related to increased heterogeneous nucleation sites during solidification [17]. Introducing inoculants can make the microstructure more uniform. Cobalt aluminate ($CoAl_2O_4$) is the most frequently utilized inoculant in the lost-wax casting process of nickel-based superalloys [18]. This compound is one of the representatives of complex oxides with a common formula AB_2O_4 in which "A" ions are divalent cations filling tetrahedral sites and "B" ions are trivalent cations in octahedral sites [19]. Cobalt aluminate is usually fabricated by firing cobalt (II, III) oxide ($CoO \cdot Co_2O_3$) and aluminum hydroxide ($Al(OH)_3$) at 1200–1300 °C. The solid-state reaction between cobalt oxide and aluminum hydroxide results in the formation of the $CoAl_2O_4$ spinel-structured compound [20]. The amount of cobalt aluminate added to the primary slurry can vary, usually between 1.0 and 10.0 wt% or more, and is determined by the superalloy grade, casting geometry, airfoil thickness, and aerospace customer specification. Too high concentrations do not significantly influence grain size or, in turn, the mechanical properties. However, they may lead to higher manufacturing costs or the presence of non-metallic inclusions. With this in mind, the aim is to determine the influence of $CoAl_2O_4$ content in the prime coat and melt-pouring temperature on the macrostructure, microstructure, and mechanical properties of Inconel 713C® superalloy at room and elevated temperatures.

2. Materials and Methods

The Inconel 713C® nickel-based superalloy was used for the castings and gating systems. Its chemical composition obtained via spark optical emission spectroscopy was the following (wt%): Cr—14.24, Al—5.93, Mo—4.29, Nb—2.45, Ti—0.92, C—0.11, Zr—0.08, Co—0.04, B—0.012, Ni—Bal. The wax patterns were injection molded, and then monolithic ceramic molds were built up around these patterns through several dipping–drying–sieving cycles until the desired shell thickness was obtained. Alumina grit was applied as the primary stucco, while backup coats were made of alumina silicate powder and colloidal silica binder-based ceramic slurries, with alumina silicate grit serving as the backup stucco. Three different shell mold prime coatings were prepared: (a) zircon filler and colloidal silica binder (molds 1–3), (b) addition of 5 wt% of $CoAl_2O_4$ inoculant (molds 4–6), and (c) addition of 10 wt% of $CoAl_2O_4$ inoculant (molds 7–9). The wax was removed from the inside of the molds within a high-pressure boiler clave. Next, each mold was covered with a layer of alumina silicate Fiberfrax® (UNIFRAX I LLC, Tonawanda, NY, USA)

insulation. Pre-annealing was conducted at 600 °C for 2 h to strengthen the entire assembly and remove any remaining wax residue. The 4 kg ingots were melted using an induction furnace with zirconia crucibles in a VIM IC Consarc furnace under a 2×10^{-3} Torr vacuum. Each ceramic mold was placed in the heating chamber, preheated to 1150 °C, and held for 2 h. The liquid metal was poured at three temperatures T_0 (monitored using Pt/Pt-Rh thermocouples): 1450 °C (L—low), 1480 °C (M—medium), and 1520 °C (H—high). After pouring, the mold was transferred from the heating zone to the cooling zone of the furnace within 10 s, followed by 60 s of ventilation in the cooling chamber. Once the castings had cooled to room temperature, the molds were removed and 9 casting variants were subjected to analysis (Table 1). The shell mold, single casting, and machined sample are presented in Figure 1.

Table 1. Technological parameters used to prepare the Inconel 713C® castings.

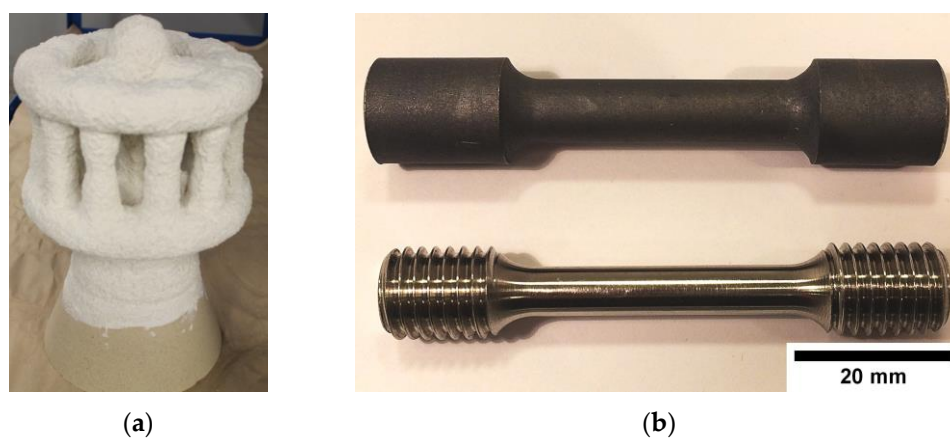| Casting	Pouring Temperature, °C	Inoculant Content, wt%	Shell Mold Temperature, °C
L0		0	
L5	1450	5	
L10		10	
M0		0	
M5	1480	5	1150
M10		10	
H0		0	
H5	1520	5	
H10		10	

(a)   **(b)**

Figure 1. (**a**) Prepared shell mold; (**b**) casting geometry and machined sample for mechanical property testing.

Thermo-Calc® software ver. 2022 (Thermo-Calc Software AB, Stockholm, Sweden) with the TCNI10 database was used to characterize the solidification path of Inconel 713C® using the Scheil model. The model considers the segregation of solute elements during solidification and assumes the absence of back-diffusion during calculations. Complete solidification is assumed when less than 1% liquid is present in the calculation, and generally, the solidification range is quite broad [21]. Here, the model was used to predict the type of primary phases in the as-cast superalloy. The phases' temperature stability between 700 and 1400 °C under equilibrium was also analyzed. Using a Netzsch STA 449F3 Jupiter (Netzsch, Selb, Germany) thermal analyzer equipped with a rhodium furnace operating up to 1600 °C (microbalance resolution 10^{-6} g, calorimetric sensitivity 0.1 mW), differential thermal analysis (DTA) was performed to obtain phase transformation temperatures during Inconel 713C® superalloy cooling and heating. Prior to measurements, the device was calibrated, and the furnace's vacuum chamber was filled with nitrogen. The samples were

placed in Al_2O_3 crucibles and studied in the temperature range of 1000 °C to 1400 °C (20 °C/min).

For macro- and microscopic observation, the cross-sectioned samples were mounted in resin, metallographically prepared, and electrochemically etched in 10% oxalic reagent for 5 s. The commercial software ImageJ 1.53k (National Institutes of Health and the Laboratory for Optical and Computational Instrumentation, University of Wisconsin, 1.51j8, Madison, WI, USA) was used to quantitatively analyze the macrostructures imaged using a Leica i9 microscope (5 images per casting). The mean area, perimeter, and grain size (diameter of an equivalent circle) were calculated. The samples' microstructures were imaged using a Leica DM light microscope (LM) and a Phenom XL (ThermoFisher Scientific, Lenexa, KS, USA) scanning electron microscope (SEM), equipped with an energy-dispersive X-ray (EDX) spectrometer (accelerating voltage was 15 kV). The obtained SEM backscattered electron (BSE) images (magnification ×20k) were subjected to binarization and de-spackling to remove noise without blurring any feature edges.

Considering that γ' precipitates in superalloys usually take on a cubic-like morphology, their mean size was taken as the square side of the precipitates (square root of the precipitates' area). Measurements were performed in 10 regions within the dendritic regions. Only γ' precipitates characterized by an area within the 0.02–4.0 μm^2 range were chosen.

Tensile testing was performed on an INSTRON 3382 (INSTRON Deutschland GmbH, Darmstadt, Germany) at room temperature, following the requirements of ASTM standard E8M-13a [22]. From there, the ultimate tensile strength (UTS), yield strength (YS), and elongation were estimated. Creep rupture tests were performed on a Walter + Bai AG LFMZ-30 (Walter + Bai AG, Löhningen, Switzerland) machine, in line with ASTM standard E139-11 [23]. The specimens (M12) were preheated to 982 °C, annealed for 1 h, and loaded with an axial force, which induced tensile stresses of 152 MPa in cross-sections.

3. Results

3.1. Analysis of the Solidification Path and Phase Stability in Inconel 713C®

Based on the Inconel 713C® nickel-based superalloy's chemical composition, a thermodynamic simulation of the solidification path (Scheil method) was performed (Figure 2a). Superalloy crystallization (γ phase formation) began at 1382 °C. After reaching a γ phase fraction of 0.002 at 1347 °C, MC carbide precipitation from the liquid occurred, which is most favorable in interdendritic spaces (following typical reactions L→MC or L→γ + MC). The formation of MC carbides in the interdendritic liquid induces a depletion in strong carbide-formers, such as Nb and Ti [24]. With decreasing temperatures, the solubility of B in the matrix is reduced, inducing its segregation at the γ phase dendrite–interdendritic liquid interface and leading to M_3B_2 precipitation from the liquid at 1234 °C. According to the Scheil simulation, the equilibrium solidus temperature is 1276 °C. Secondary γ' precipitates are not included in the results as they start precipitating in a solid state from a supersaturated matrix.

Under equilibrium conditions, the main strengthening phase is the γ' phase, which dominates the structure up to 985 °C (Figure 2b). With further temperature increase, the γ takes over as the dominant phase. The solvus temperature of the γ' phase is 1140 °C. The simulation indicates that $M_{23}C_6$ carbides are more stable than MC in the intermediate temperature range, suggesting the possibility of an MC + γ→γ' + $M_{23}C_6$ phase transformation during service or heat treatment [25]. At high temperatures (exceeding 975 °C), MC carbides are more stable than $M_{23}C_6$ ones. The solvus temperature of $M_{23}C_6$ carbides is 980 °C. M_3B_2 borides are very stable up to the temperature of 1290 °C. After exceeding this temperature, they rapidly dissolve, with the possible appearance of a liquid phase caused by matrix enrichment in B. The liquidus temperature is 1340 °C, whereas MC carbides dissolve completely at 1348 °C.
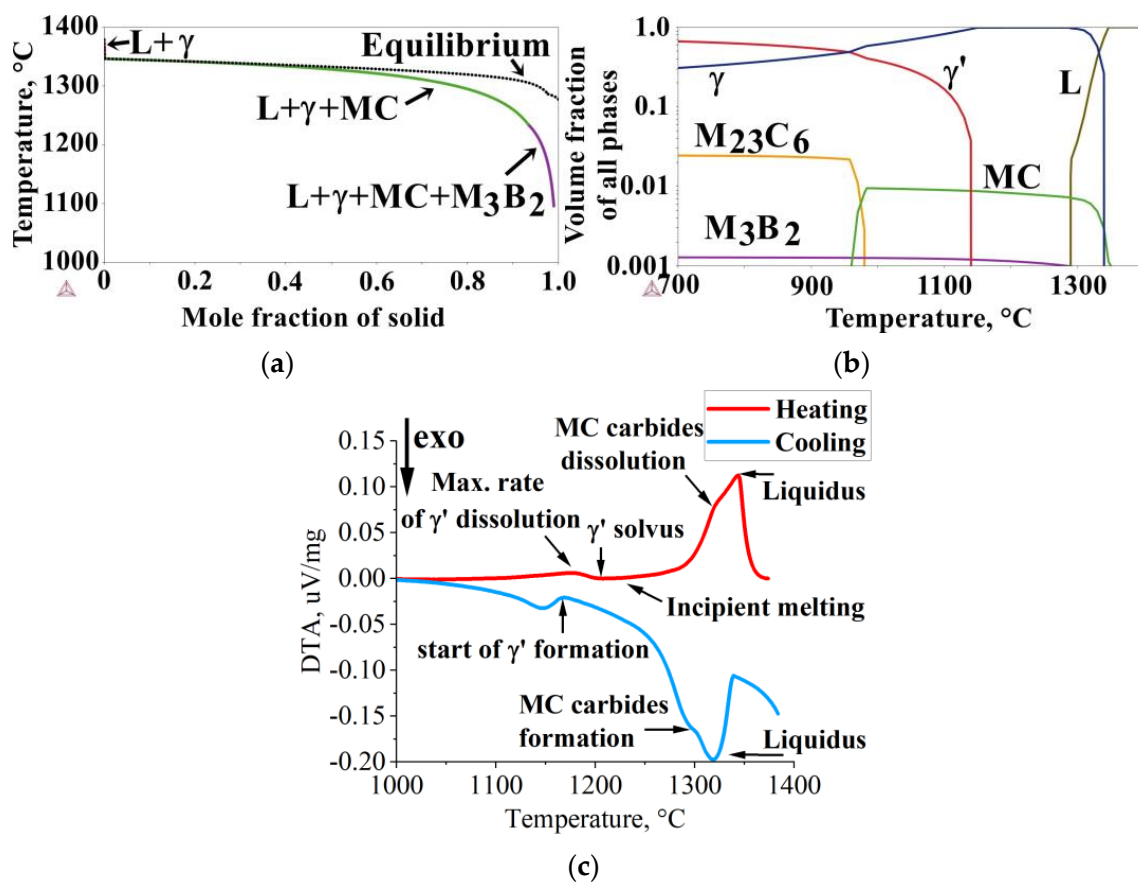
Figure 2. (**a**) Inconel 713C® solidification path calculated via the Scheil model; (**b**) phase stability with increasing temperature under equilibrium conditions; (**c**) DTA curves registered during cooling and heating.

DTA curves registered during specimen cooling and heating are shown in Figure 2c. During cooling, crystallization began at 1319 °C, followed by the precipitation of MC carbides at 1294 °C. Subsequently, a γ-γ' eutectic and minor phases may form over a wide temperature range. A peak onset around 1168 °C suggests that after crystallization concludes, the formation of secondary γ' precipitates from the γ solid solution commences. On the DTA heating curve, a peak is recorded at approximately 1176 °C, which probably corresponds to the maximum dissolution rate of γ' intermetallic phase precipitates. Shortly after exceeding this temperature (at 1201 °C), the solvus temperature of γ' is observed. Heating beyond 1244 °C causes sample melting, and the liquidus temperature was reached at 1344 °C.

3.2. Macro- and Microstructure of the as-Cast Inconel 713C® Castings

The macrostructures of all casting variants are shown in Figure 3. Equiaxed grains of various sizes and distribution are visible. Casting defects, like chill zone structures, hot cracks, or misruns, were not observed. The relationship between surface grain size, melt-pouring temperature, and cobalt aluminate content in the primary coating is presented in Table 2. Increasing the $CoAl_2O_4$ content led to a decrease in grain size for each melt-pouring temperature. For the lowest temperature (1450 °C), the mean grain size changed from 4.40 mm to 2.44 mm when 10 wt% inoculant was applied. The greatest refining effect was obtained at T_0 = 1520 °C, in which the grain size decreased from 6.55 mm (unmodified variant) to 2.36 mm (10 wt% of $CoAl_2O_4$). The relatively high grain size standard deviation values are due to the presence of both large and fine grains.
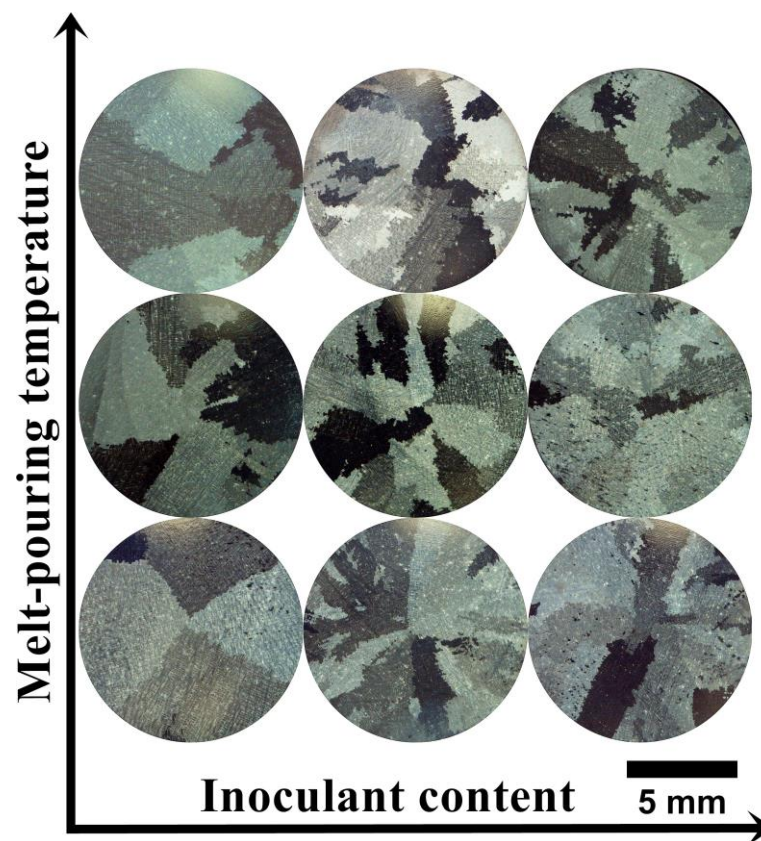
Figure 3. Macrostructure of the as-cast Inconel 713C® castings.

Table 2. Mean grain size of Inconel 713C® castings.

Pouring Temperature, °C	CoAl$_2$O$_4$, wt%	Grain Size, mm	SDAS, μm
1450	0	4.40 (±3.56)	63 (±7)
	5	3.77 (±4.75)	63 (±5)
	10	2.44 (±2.41)	66 (±4)
1480	0	3.18 (±3.34)	69 (±5)
	5	2.68 (±2.57)	69 (±5)
	10	2.40 (±2.07)	72 (±5)
1520	0	6.55 (±3.73)	72 (±8)
	5	2.45 (±2.62)	77 (±7)
	10	2.36 (±2.32)	77 (±6)

The casting microstructures reveal typical dendritic structures, with features of the primary dendrite cores clearly visible (Figure 4). The dendritic areas (primary cores and secondary arms) are characterized by a relatively homogeneous microstructure. Within the interdendritic regions, γ-γ′ eutectic islands and fine carbide-looking precipitates can be found. The secondary dendrite arm spacings (SDASs, λ_2) were measured (Table 2) and the results indicate that the pouring temperature had a stronger effect on the obtained values. The average distance in the castings was in the range of 63–66 μm, 69–72 μm, and 72–77 μm for 0 wt%, 5 wt%, and 10 wt% of CoAl$_2$O$_4$, respectively. According to the equation for $\lambda_2 \sim (t_s)^{1/3} \sim (1/G_v)^{1/3}$, the temperature gradient (G), local solidification time (t_s), and cooling rate (v) influence the SDAS [26]. Values strictly depend on the casting parameters (e.g., shell mold thickness, preheating and pouring temperature, cooling rate after solidification) and heat transfer between the nickel-based superalloy and the ceramic shell mold, originating from their thermophysical features. In general, the investment casting of Ni-based superalloys is characterized by low cooling rates due to the very low thermal conductivity of the shell molds. Matysiak [27] suggested that the cooling

rate of the Inconel 713C® nickel-based superalloy at 1263–650 °C after casting is approx. 10–12 °C/min. The thermal conductivity of the shell mold, which consisted of a zircon filler, colloidal silica binder, and alumina silicate powders as a backup material, was 1.09 W/(m·K) at 1200 °C and 0.77 W/(m·K) at 600 °C [27].
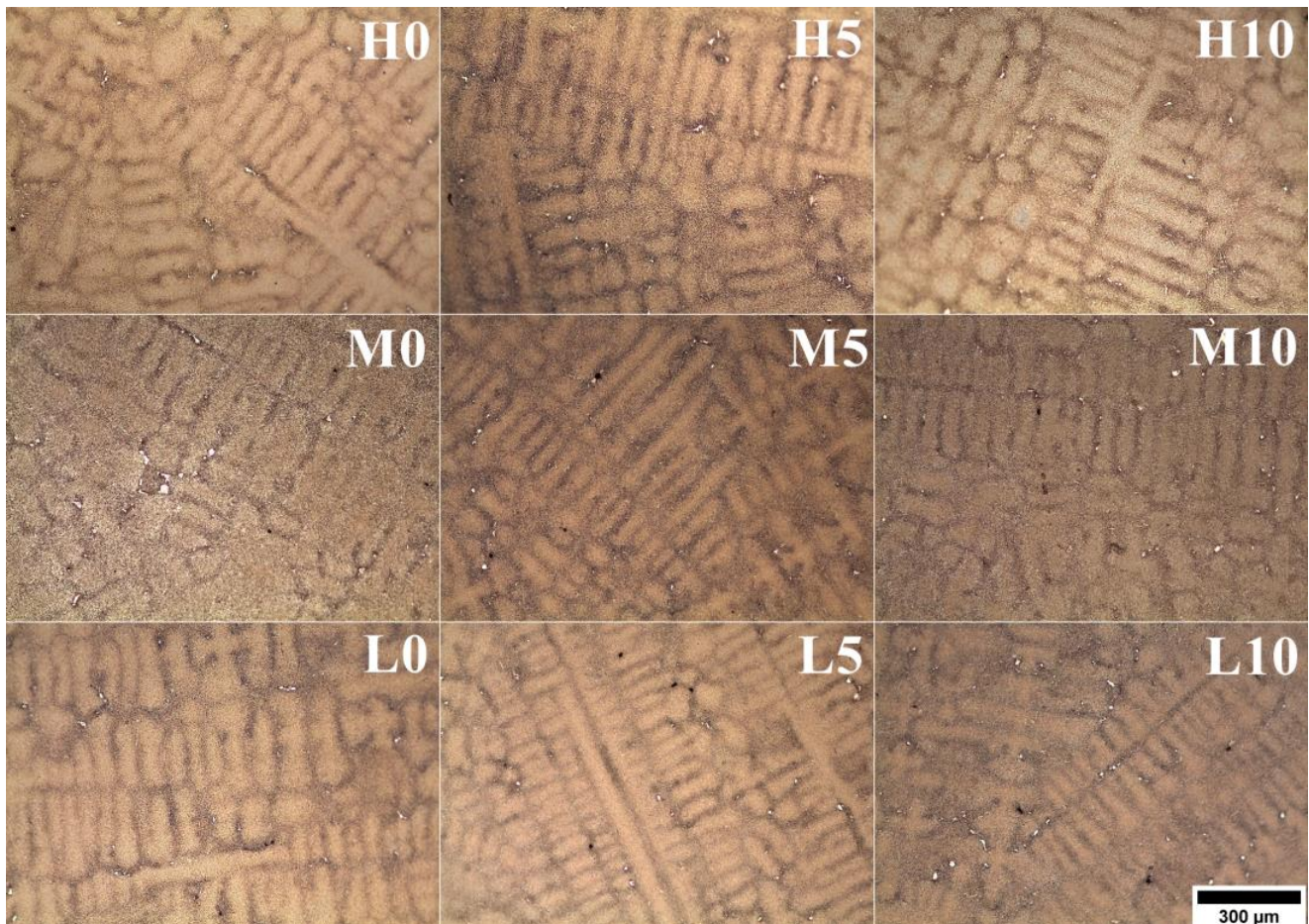

Figure 4. Dendritic microstructure of the as-cast Inconel 713C® castings, LM.

Based on ThermoCalc® simulations and microstructural characteristics, it can be stated that the formation of the γ matrix phase occurs in the initial solidification stage. As the temperature decreases, the solubility of strong carbide-formers, such as Nb, Ti, and C, in the formed matrix decreases, leading to their segregation at the interface between the matrix dendrite and the interdendritic liquid [24]. Notably, $k^i = 1$ indicates a uniform distribution of alloying elements. These conditions promote carbide precipitation, which can appear in various forms ranging from blocky shapes to Chinese script-like structures, as shown in Figure 5. Bhambri [28] observed that carbide morphology transforms with increasing cooling rates. Initially, carbides appear octahedron-shaped, resembling blocks in a two-dimensional image. In this work, carbide growth conditions were closer to an equilibrium state, with slower cooling rates. However, with higher cooling rates, the shape of the carbides changed to a more arrow-like structure and eventually evolved into shapes reminiscent of Chinese script. At these higher cooling rates, the carbide growth rate increased, accompanied by the sufficient diffusion of carbide-forming elements. The formation of equilibrium shapes becomes increasingly challenging, being affected by the heat flow direction and the distribution of carbide-formers.
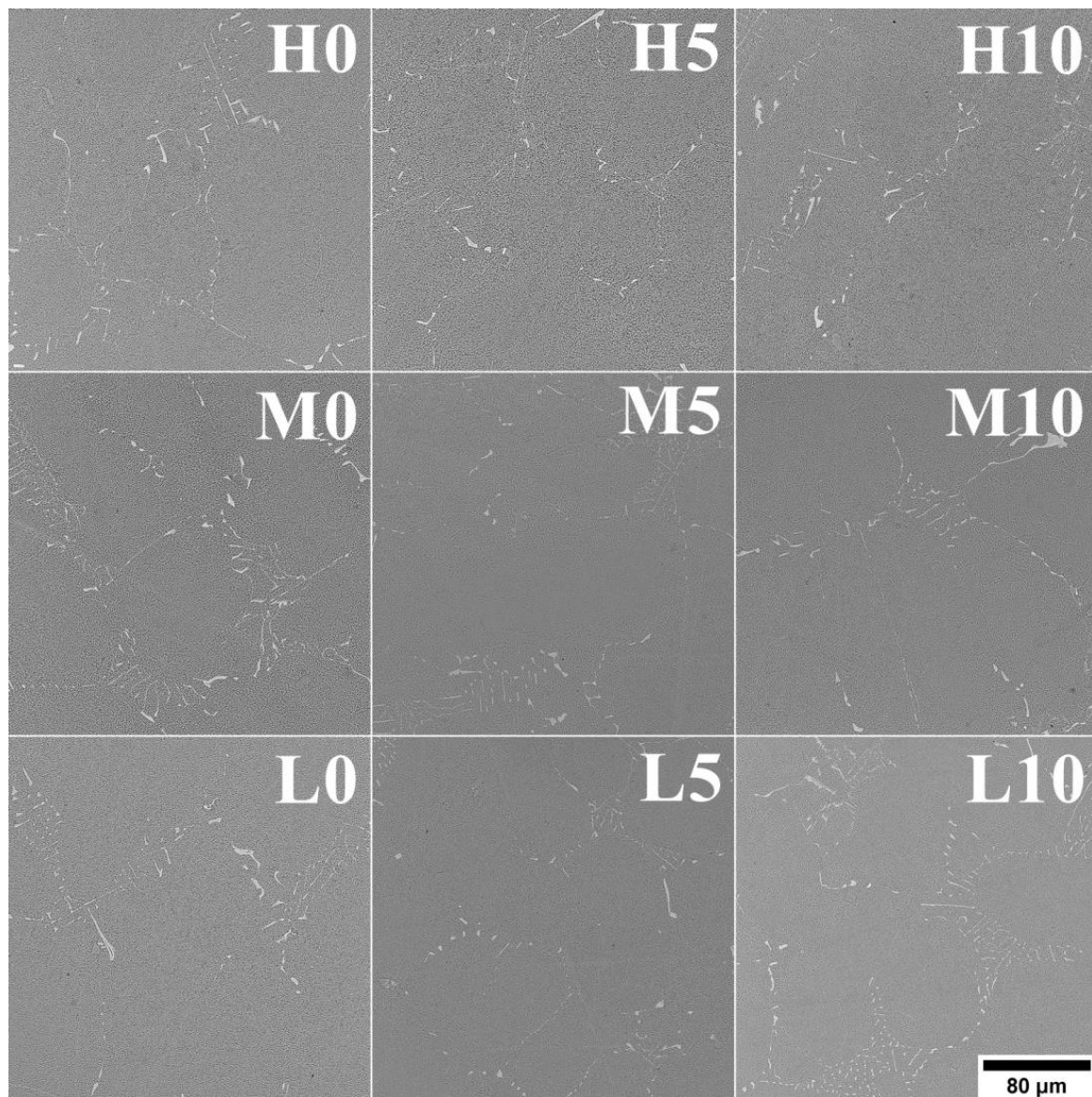
Figure 5. The distribution, morphology, and size of MC carbides in the as-cast Inconel 713C® castings, SEM-BSE.

The morphology of the secondary γ′ precipitates in the dendritic regions is close to cubic (Figure 6). The local thermodynamic conditions influencing the morphology are determined by the chemical composition, state of elastic stresses, and the mutual interaction between precipitates [29]. These factors change as a function of temperature and are conditioned by the system's attempt to achieve thermodynamic equilibrium. The mean size of secondary γ′ precipitates expressed as the equivalent side of the square was calculated to quantitatively analyze the differences originating from the various melt-pouring temperatures and inoculant contents (Figure 7). For castings produced within the unmodified shell mold, the mean size of secondary γ′ precipitates increased from 0.446 μm to 0.559 μm with increasing pouring temperature. With the addition of inoculant to the primary coating, the mean size of secondary γ′ precipitates tended to be greater. For T_0 = 1450 °C, the mean size was 0.508 μm and 0.539 μm for 5 wt% and 10 wt% $CoAl_2O_4$, respectively; for T_0 = 1480 °C, it was 0.526 μm and 0.548 μm; and for T_0 = 1520 °C, it was 0.562 μm and 0.613 μm. Sims [2] observed that slower cooling rates during the directional solidification process could result in a coarser solid-state cuboidal γ′ directly in the as-cast state, which is in line with our observations. The higher preheating

mold temperature caused a decrease in casting cooling, giving more time for nuclei to re-precipitate and for the γ' nucleus to grow. The influence of the γ' phase's size on superalloys' strength is complex, especially since they have various chemical compositions and most are subjected to heat treatment [30]. Simultaneously, Inconel 713C® can be serviced without such treatment. However, there is a possibility of having precipitates finer than the critical value, meaning that they are small enough for dislocations to cut through them. This critical mean size can range depending on the superalloy type. If this value is crossed, the Orowan mechanism occurs [31]. Additionally, γ' precipitates have an ordered $L1_2$ crystal structure, so dislocations can cut or bypass them in various complex forms, depending on the stress and service temperature [32]. Nathal [33] observed in single-crystal nickel-base superalloys that the cube-like morphology exhibits the best creep properties among all morphologies, while the optimal initial size of the precipitates is around 0.50 µm.
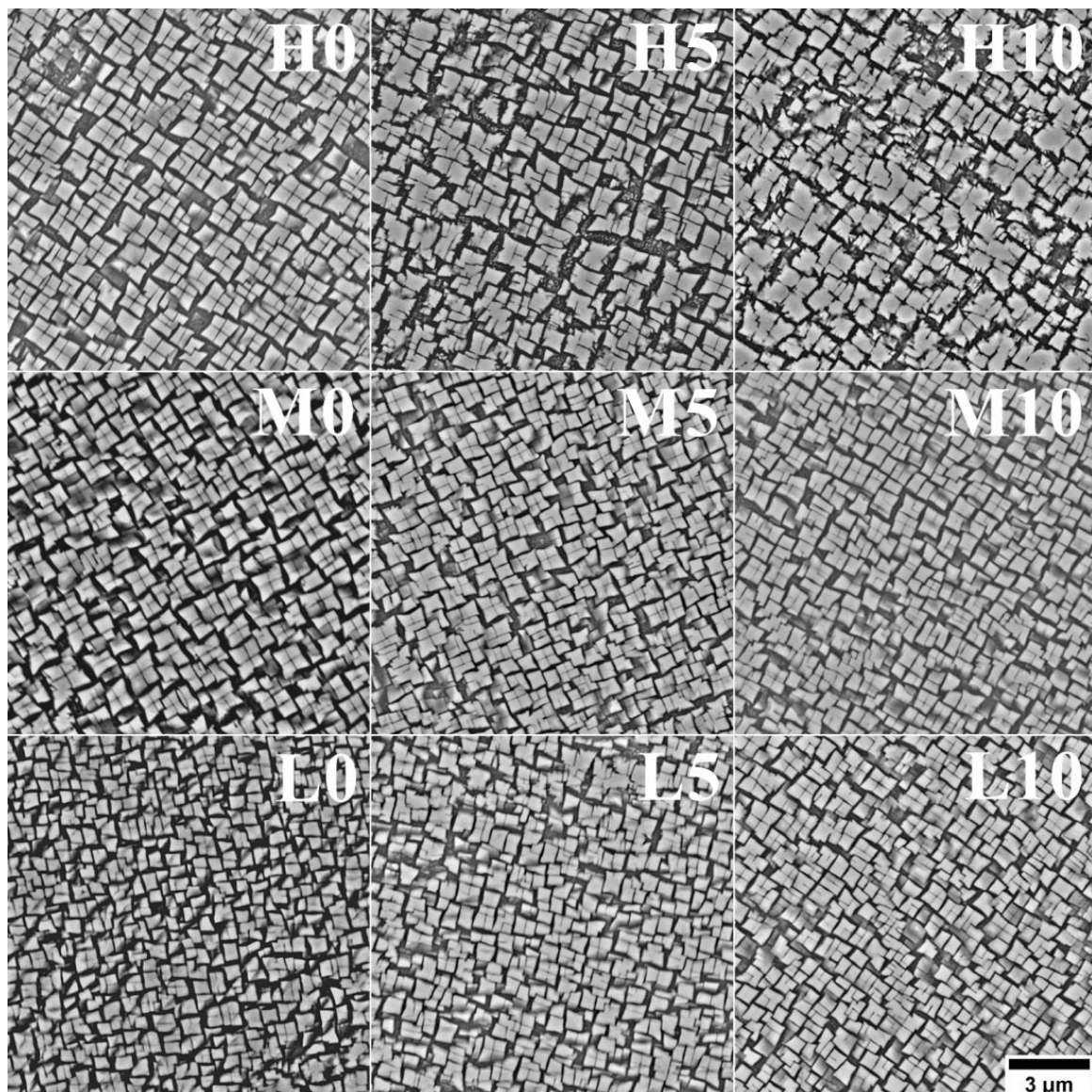

Figure 6. Morphology of secondary γ' precipitates in dendritic regions in the as-cast Inconel 713C® castings, SEM-BSE.
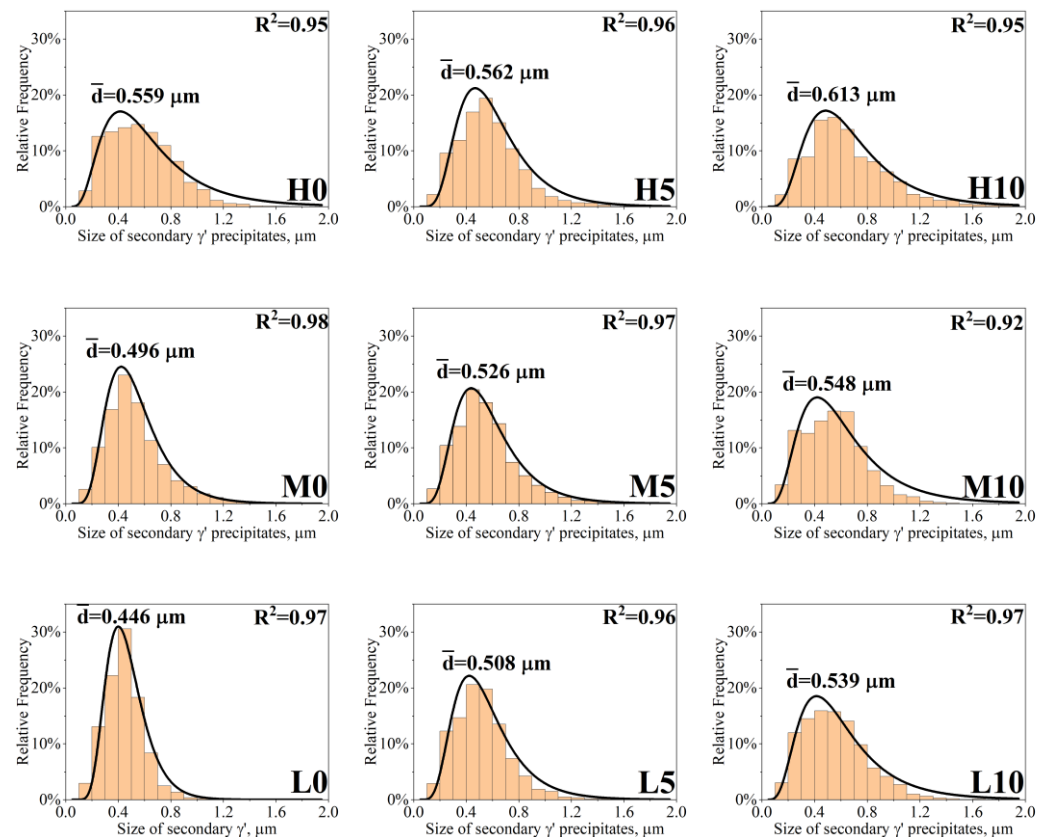
Figure 7. Size of secondary γ′ precipitates in dendritic regions in the as-cast Inconel 713C® castings.

Numerous phases formed in the castings' interdendritic spaces due to alloying element segregation during solidification. Based on SEM-EDX, it was possible to determine that the same phases are present in all castings, regardless of the selected pouring temperature or inoculant content. Morphology images and corresponding qualitative spectra are presented in Figures 8 and 9, respectively. A diversified distribution and complex morphology characterize primary γ′ precipitates, which formed via the L→γ + γ′ eutectic phase transformation. Eutectic γ-γ′ indicates a strong Al enrichment in the residual liquid during casting solidification. The γ-γ′ is an undesirable constituent, and heat treatment can lead to its decrease. Its amount is relatively low compared to that in other superalloys with similarly high Al concentrations, like MAR-M247 [34] or Renè 108 [35]. In the near-eutectic, the carbides are significantly enriched in Nb, Mo, and Ti.

The SEM-EDX analysis of the gray-phase contrast precipitate revealed an increased concentration of Mo and Cr (Figures 8 and 9). The size of some of these precipitates locally exceeded 5–10 μm. Similar findings were obtained for various Ni-based superalloys, indicating the presence of borides, such as M_3B_2 and M_5B_3 [36]. M_5B_3 borides are strongly enriched in W and Cr, while M_3B_2 borides are strongly enriched in Mo and Cr. Since Inconel 713C® lacks tungsten, M_5B_3 is not expected to be present, and only M_3B_2 is likely to form (which was also confirmed by ThermoCalc® simulations). Boron is added to Ni-based superalloys to increase creep strength, and its nominal concentration in Inconel 713C® is 0.012 wt%. Considering borides' very low solubility in γ and γ′, favorable conditions for their formation exist only at the end of solidification. The presence of such large boride precipitates indicates that the solution heat treatment temperature should be selected carefully so as not to lead to the local melting of B-rich areas. The relationship between size, distribution, boride fraction, and melt-pouring temperature or inoculant content was not observed due to their irregular presence in the interdendritic spaces. Apart from near-eutectic γ-γ′ islands and borides, precipitates with a lamellar-like morphology are also observed. SEM-EDX spectra revealed an increased concentration of Ni and Zr. Matysiak [37] ob-

served with selected area electron diffraction (SAED) that these precipitates are Ni_7Zr_2. On the Ni-Zr binary diagram, the Ni_7Zr_2 phase (mC36, C2/m (12)) precipitates at 1438 °C through a congruent phase transformation, $L \rightarrow Ni_7Zr_2$ [38]. Subsequently, two peritectic transformations occur: at 1304 °C, $L + Ni_7Zr_2 \rightarrow Ni_5Zr$ (cF24, F-43m), and at 1181 °C, $L + Ni_7Zr_2 \rightarrow Ni_{21}Zr_8$ (aP29, P-1). Only one eutectic transformation resulting in the formation of the γ phase (FCC), namely $L \rightarrow \gamma + Ni_5Zr$ at 1164 °C, takes place. Consequently, the Ni_7Zr_2 phase can be present in Inconel 713C® but not in the form of a γ-Ni_7Zr_2 eutectic, indicating that its formation is likely more complex, as suggested by the morphology of the precipitates. During the final stage of solidification, the residual liquid in the nickel-based superalloy becomes enriched in Zr due to a peritectic transformation with the eutectic phase or primary γ' phase, namely $L + \gamma' \rightarrow \gamma + Ni_7Zr_2$ [39]. The superalloy's complex chemical composition allows for a ternary eutectic transformation at the end of casting solidification. One of the ternary eutectic transformations leading to Ni_7Zr_2 formation is $L \rightarrow \gamma + Ni_7Zr_2 + Ni_5Zr$. However, the presence of Ni_5Zr was not detected in Inconel 713C® by other authors [40,41]. Similar findings confirming the Ni_7Zr_2 phase have been reported for Inconel 939® [42] and Inconel 738® [43]. The morphology and microanalysis of carbides (MC-type) located near the Ni_7Zr_2 compound reveal a strong enrichment in Nb and Zr, which can indicate that during casting solidification, a ternary eutectic transformation occurs: L (residual with high Zr and C content) $\rightarrow \gamma + Ni_7Zr_2 + (Nb, Zr)C$. Babu [44] suggested that eutectic-type transformations in chemically complex nickel-based superalloys can be more intricate. The enrichment of solutes in the residual solidifying liquid may be insufficient to initiate a typical eutectic transformation, primarily due to the minimal volume fraction of eutectic γ-γ'. Microstructure investigations show that the M_3B_2 is adjacent to Ni_7Zr_2 and eutectic γ-γ' islands. These multiphase regions indicate that the formation of eutectic γ-γ' islands can coincide with the precipitation of a ternary eutectic from the remaining liquid, following the sequence L (enriched in Zr and B) $\rightarrow \gamma + Ni_7Zr_2 + M_3B_2$. The observed morphology of constituents in our Inconel 713C® castings aligns with Babu's interpretation [44], possibly explaining the formation of primary phases in the interdendritic regions. According to Murata [45], the intermetallic phase $Ni_7(Hf, Zr)_2$ is not stable at the selected intermediate temperature (like heat treatment, creep, or service). It undergoes the phase transformation $MC + (Ni, Co)_7(Hf, Zr)_2 + Cr$ (in the matrix) $\rightarrow (Hf, Zr)C + Cr_{23}C_6 + \gamma$. It should be noted that the Ni_7Hf_2 and Ni_7Zr_2 phases have the same crystallographic structure and can dissolve each other and have similar behavior during thermal exposure.

3.3. Mechanical Properties of Inconel 713C® Castings at Room and Elevated Temperature

Tensile test results are presented in Table 3. The Inconel 713C® superalloy, when poured at 1450 °C, exhibits an average yield strength of 787 MPa. However, when cobalt aluminate is added to the first layer of the ceramic mold, the YS increases to 813 MPa and 835 MPa for 5 wt% and 10 wt%, respectively. At a melt-pouring temperature of 1480 °C, the unmodified casting had an average YS of 783 MPa, while for the modified casting, the measured values were at least 27 MPa higher. When $T_0 = 1520$ °C, the unmodified castings exhibit a YS of 775 MPa. With the addition of $CoAl_2O_4$, the YS increased to 804 MPa (5 wt%) and 819 MPa (10 wt%). These results demonstrate that the yield strength of the unmodified castings remained below 800 MPa for each pouring temperature. Castings L0 (1450-0) and M0 (1480-0) exhibited the highest standard deviation in YS. However, the average YS values exceed 800 MPa when cobalt aluminate was included in the first layer of the ceramic mold. Regarding UTS, the values did not exceed 900 MPa for the unmodified castings. However, selecting the optimal pouring temperature and $CoAl_2O_4$ concentration allowed achieving values exceeding 1000 MPa. These results suggest that adding cobalt aluminate in the first layer has a significantly greater impact on the YS and UTS in comparison to pouring temperature changes. This effect can be attributed to the role of $CoAl_2O_4$, which is aimed at grain refinement. Following the AMS5291 standard [22], the minimum YS of Inconel 713C® castings should be higher than 690 MPa, while UTS should be more than 758 MPa, which is in line with what was achieved in this study.
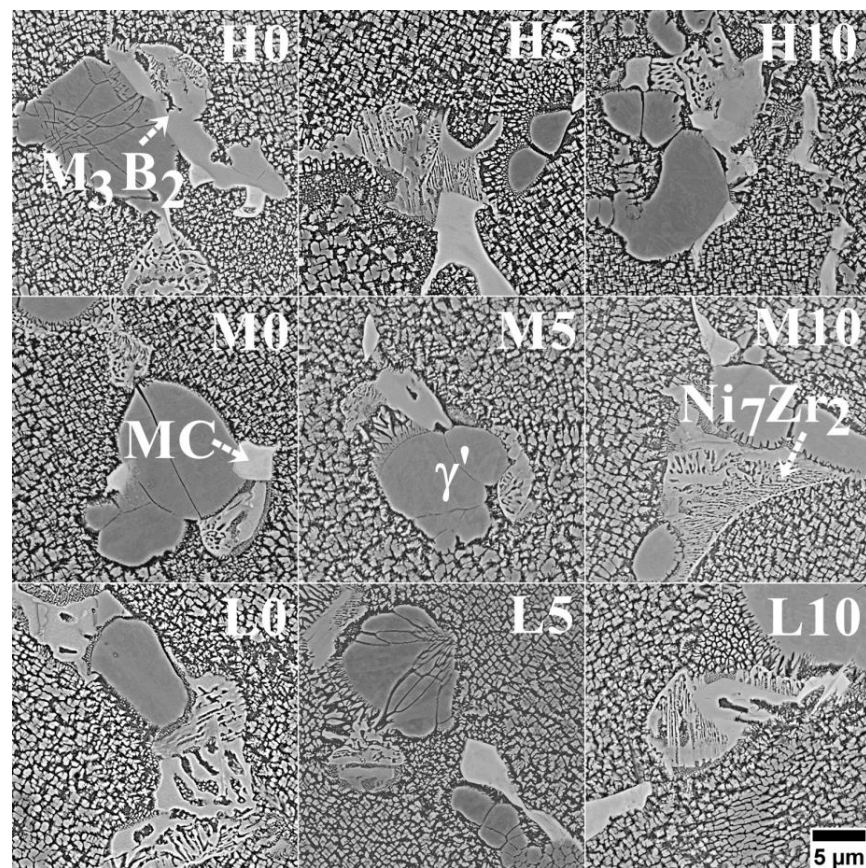
Figure 8. Morphology of the precipitates in the interdendritic spaces of as-cast Inconel 713C® castings, SEM-BSE.
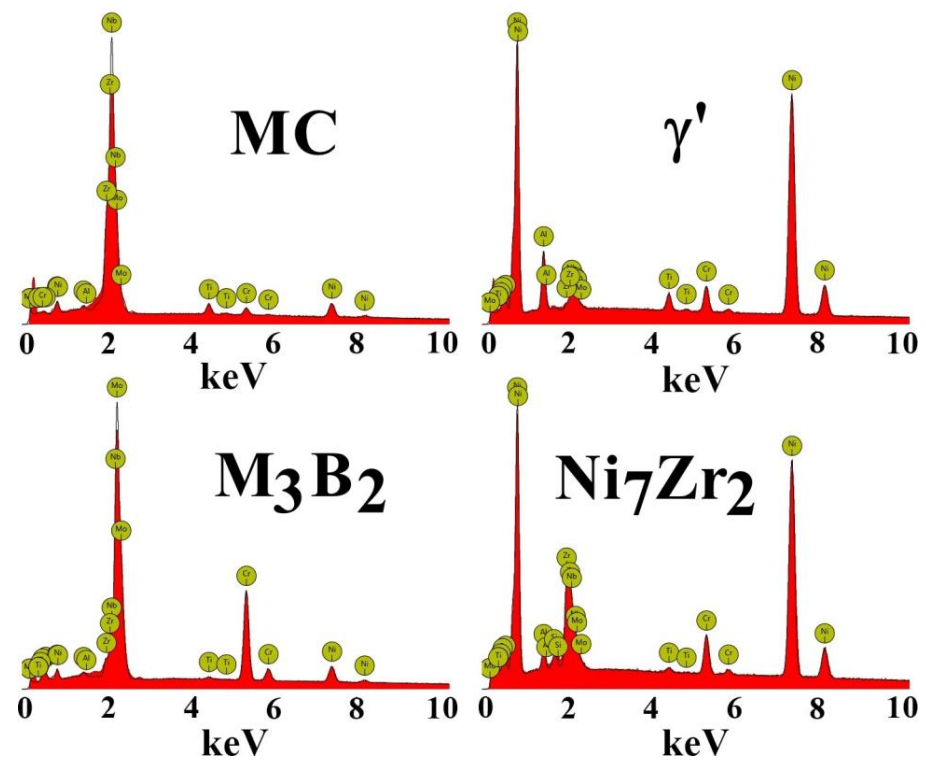

Figure 9. The EDX spectra of the phases detected in as-cast Inconel 713C® castings, SEM-EDX.

Table 3. Tensile strength of as-cast Inconel 713C$^{®}$ castings.

Pouring Temperature, °C	CoAl$_2$O$_4$, wt%	YS, MPa	UTS, MPa
	0	787 ($\pm$21)	879 ($\pm$14)
1450	5	813 ($\pm$2)	1010 ($\pm$7)
	10	835 ($\pm$6)	994 ($\pm$28)
	0	783 ($\pm$23)	877 ($\pm$5)
1480	5	828 ($\pm$1)	984 ($\pm$6)
	10	814 ($\pm$2)	970 ($\pm$21)
	0	775 ($\pm$8)	868 ($\pm$18)
1520	5	804 ($\pm$14)	947 ($\pm$46)
	10	819 ($\pm$8)	967 ($\pm$14)

Figure 10 presents the creep curves of the as-cast Inconel 713C$^{®}$ castings (982 °C/152 MPa), with one representative curve selected for each variant. The recorded curves consist of three characteristic stages. Stage I corresponds to the initial deformation, where the creep rate is the highest, followed by stage II, i.e., steady-state creep, and stage III, where the sample is fractured. The sample poured at 1450 °C into the mold without CoAl$_2$O$_4$ exhibited a time to rupture of approx. 40.7 h. However, with the addition of the modifier, the time to rupture dropped to 39.8 h for 5 wt% CoAl$_2$O$_4$ and 36.0 h for 10 wt% CoAl$_2$O$_4$. At the pouring temperature of 1480 °C, the unmodified casting had a time to rupture of about 46.1 h. The presence of cobalt aluminate in the amount of 5 wt% or 10 wt% reduced this time to 40.4 h and 36.2 h, respectively. For the highest tested pouring temperature, the unmodified superalloy sample's time to rupture was 42.7 h, whereas for the modified sample, it was 40.2 h for 5 wt% addition and 37.3 h for 10 wt%. Notably, the casting with the longest time to rupture also exhibited the lowest steady-state creep rate. This characteristic is highly beneficial during service, as it indicates improved resistance to deformation over time. Under typical stresses in service, the steady-state creep rate decreases with increasing grain size, while YS and UTS usually decrease, which is visible in the performed experiments. According to the AMS5391 standard [23], the expected minimum time to rupture is 30 h under the assumed test parameters, which states that the selected manufacturing parameters and composition of the primary coat in the shell mold guarantee sufficient creep properties.

Figure 11a displays the microstructures of cross-sectioned specimens following the tensile test, revealing the nature of cracking and their development along the grain boundaries. The grain size influences the strength primarily due to the different crystallographic orientations present in adjacent grains. Grain boundaries play a crucial role in impeding the movement of dislocations, which can be attributed to two main factors [46]. Firstly, when a dislocation transitions from one grain to another, it encounters a change in its direction of motion due to the distinct orientations of the two equiaxed grains. This alteration in direction acts as a barrier to dislocation movement. Secondly, within the region of a grain boundary, atomic disorder exists, resulting in a discontinuity of slip planes from one grain to the next one. This discontinuity further obstructs the easy progression of dislocations between adjacent grains. Figure 11b illustrates the microstructure of crept Inconel 713C$^{®}$, revealing the presence of intergranular cracks along with numerous secondary cracks and local voids. Creep mechanisms can be categorized into two groups: those influenced by grain size and those not [47]. In both cases, the creep rate is connected to the diffusion rate. The process of diffusion creep, involving the creation and disappearance of vacancies at boundaries, is highly dependent on grain size. Dislocation creep occurs within the grains and is not influenced by grain size. When subjected to constant stress and temperature, an increase in grain size leads to a significant decrease in the contribution of dislocation creep. Simultaneously, the rate of diffusion creep also decreases. When the homologous temperature (ratio of test temperature and solidus temperature) exceeds 0.7, the dominant creep mechanism is Nabarro–Herring creep [48]. This type of creep occurs as vacancies migrate within grains, moving from regions under tension to compressed

regions and through volume diffusion in the opposite direction. In contrast, at homologous temperatures ranging from 0.4 to 0.7, Coble creep becomes more prevalent, which operates through diffusion along grain boundaries [49]. This means that the creep rate via the Nabarro–Herring mechanism is proportional to $1/d^2$ (d—grain size), while Coble creep is proportional to $1/d^3$. Coble creep is more strongly influenced by grain size compared to Nabarro–Herring creep. As a result, the contribution of Coble creep is considered negligible in fine-grained materials. Consequently, coarse-grained materials exhibit higher resistance to creep.
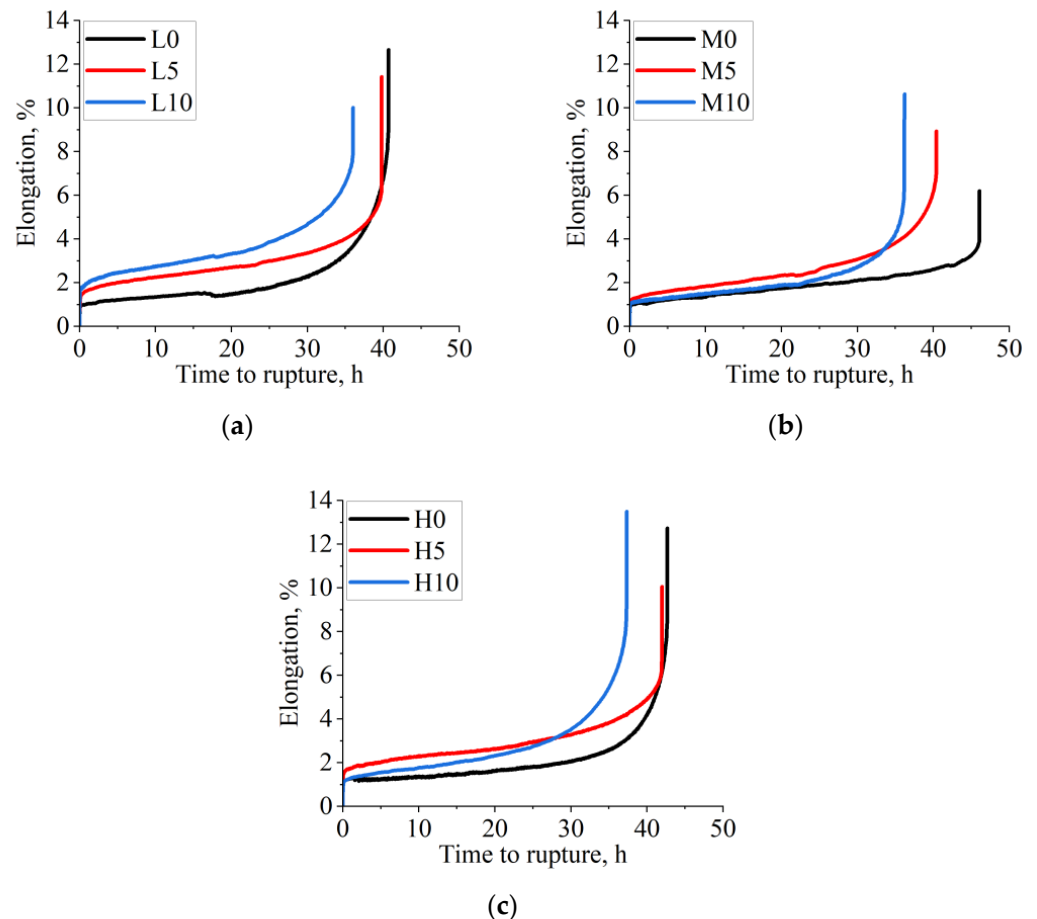

Figure 10. Creep curves of as-cast Inconel 713C® castings: (**a**) L0-L10; (**b**) M0-M10; (**c**) H0-H10.

Apart from grain size, the mechanical properties are influenced by a high volume fraction of γ′ precipitates and the presence of other strengthening phases, narrow γ matrix channels, and the strengthening effect of solid solution in both the matrix and γ′ phases. The total content of γ′-formers in the material exceeds 6 wt%, which is relatively high compared to that in other superalloys commonly used in aerospace engines [2]. The γ′ phase undergoes deformation primarily through slip-on systems characterized by {111} <110> planes. Dislocations in the γ′ phase have a Burger vector with a length of a$\sqrt{2}$, which is twice as long as that in the matrix. When a dislocation in the γ′ precipitate slips by a distance equal to the length of the Burger vector, it disrupts the ordering of the crystal lattice. This disruption leads to the creation of interfaces, which are defects characterized by high energy. The dislocation movement within γ′ precipitates becomes significantly more challenging due to these high-energy interface defects [50–52].
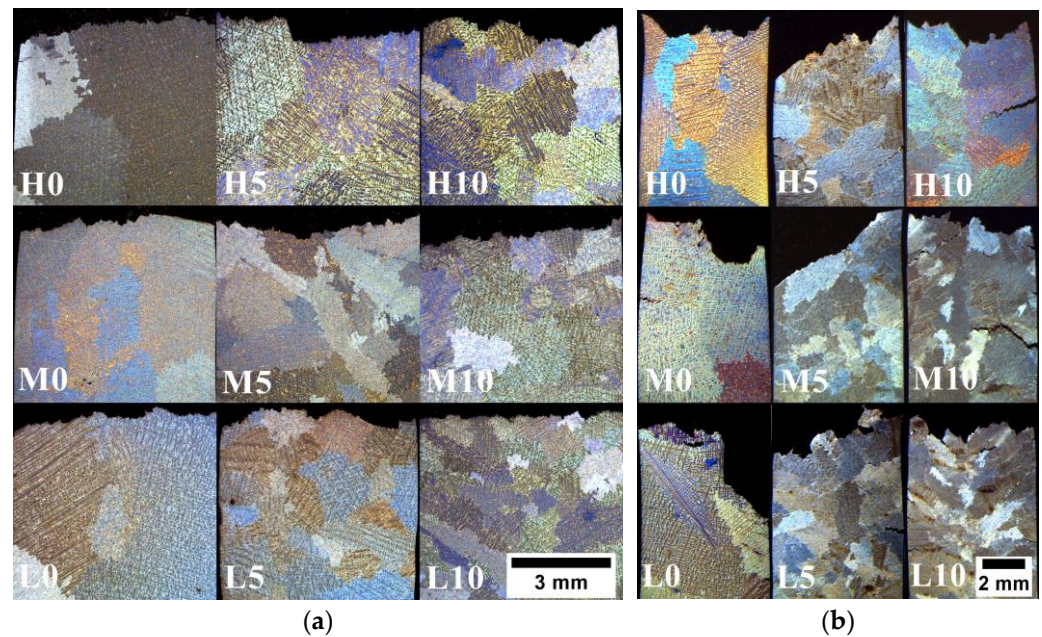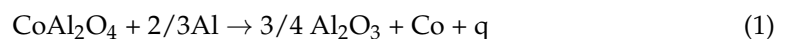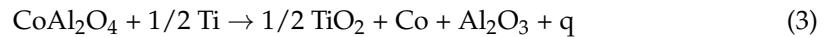
Figure 11. Microstructure of the cross-sectioned specimens after (**a**) tensile tests and (**b**) stress-rupture tests.

4. Grain Refinement Mechanism via $CoAl_2O_4$ Inoculant Incorporation

A fine-grained and more uniform structure can be obtained via the chemical reaction of the inoculant, included in the primary coating of the shell mold, with selected alloying elements in the superalloy [53,54]. Feagin [55] indicated that the use of more stable $CoAl_2O_4$ or Co_2SiO_4 compounds as the nucleus does not exclude the possibility of their decomposition into, among others, pure nanoparticles of Co when in contact with a reducing atmosphere or the liquid alloy. To investigate the mechanism of Co particle formation and morphology during casting, Jian [20] examined several shell molds with $CoAl_2O_4$ as the primary layer. Upon observing the molds after contact with a liquid superalloy, they discovered three distinct layers: white, blue, and black (corresponding to the colder to hotter sections). The unmelted portion of the molds, known as the backup part, consisted of Al_2O_3 and SiO_2 in cristobalite and an amorphous phase. The transitional region (blue) was predominantly composed of cobalt aluminate, amorphous silicate, and fine metallic cobalt particles measuring up to a maximum diameter of 4 μm. The amount of amorphous phase and metallic cobalt steadily increased as the shell mold became hotter. In the final black region (0.02 mm) of the primary layer, the major constituents were Co, Al_2O_3 (some of which formed solid solutions with chromium or cobalt), and a small quantity of cristobalite. These constituents also exhibited a gradual change. Notably, the number of cobalt particles in the black layer exceeded the amount in the blue layer. $CoAl_2O_4$ and silicates transformed into mineral phases primarily composed of Al_2O_3 solid-solution, with Cr and Co as solutes. To determine which of the elements could reduce cobalt aluminate to its metallic form and identify the remaining products, an experiment involving the annealing of metal powders (Al, Cr, Ti) with $CoAl_2O_4$ was conducted. The mixtures were subjected to heat treatment at 1200 °C for 2 h under vacuum and subsequently analyzed using X-ray diffraction. During the pouring of liquid metal into the shell mold cavity, the $CoAl_2O_4$ present in the primary layer underwent reduction. As a result, pure Co particles were formed according to the following reactions (Equations (1)–(3)):

$$CoAl_2O_4 + 2/3Al \rightarrow 3/4\ Al_2O_3 + Co + q \tag{1}$$

$$CoAl_2O_4 + 2/3\ Cr \rightarrow 1/3\ Cr_2O_3 + Co + Al_2O_3 + q \tag{2}$$

$$CoAl_2O_4 + 1/2 \, Ti \rightarrow 1/2 \, TiO_2 + Co + Al_2O_3 + q \tag{3}$$

The reduction capacities of the selected metals vary. The highest amount of obtained Co particles occurred after the reaction with Al and then decreased in sequence when reacting with Cr and Ti. The residual amount of cobalt aluminate increased in the same order. Reactions with Al and Cr allowed for decomposing 95 wt% and 70 wt% of cobalt aluminate, respectively. Crystallographic matching at the inoculant–matrix interface has typically served as a good indicator for the potency of nucleating substrates in terms of the low ΔT_n (nucleation undercooling) required to nucleate grains, and the formation of solid Co particles is ideal as they possess an FCC lattice structure with a small lattice mismatch with the γ phase. From microstructural observations of the Inconel 713C® castings and described experiments conducted by Jian [20], it can be concluded that during the melt-pouring process, the cobalt aluminate compound reacted with Al, Cr, and Ti alloying elements (total concentration exceeds 20 wt%). Grain refinement occurred through the increase in the heterogeneous nucleation rate.

5. Conclusions

In this work, the influence of melt-pouring temperature (L—low; M—medium, H—high) and the concentration of $CoAl_2O_4$ (0 wt%, 5 wt%, 10 wt%) in the primary coating of the shell mold on Inconel 713C® castings' grain size, microstructure, and strength at room temperature and 982 °C was shown. The main conclusions are as follows:

1. Grain size control in lost-wax Inconel 713C® castings can be performed by changing the melt-pouring temperature and $CoAl_2O_4$ contents in the prime coating of the shell mold. The most significant grain refinement was achieved in casting H10, where the grain size was reduced from 6.55 mm to 2.36 mm.
2. The melt-pouring temperature had a greater influence on the SDAS than the inoculant content. The lowest average SDAS (63 µm) was achieved in the L0 casting, whereas the highest was achieved in the H10 casting (77 µm).
3. The size of secondary γ' in the dendritic regions exhibited a log-normal distribution with increasing melt-pouring temperature, whereas the mean size increased with increasing inoculant contents. The finest mean precipitate size was in casting L0 (0.446 µm), while the coarsest was in casting H10 (0.613 µm).
4. Primary and secondary γ', MC carbides, M_3B_2 borides, and the intermetallic Ni_7Zr_2 phase were found in the interdendritic regions of all castings, regardless of the applied melt-pouring temperature or $CoAl_2O_4$ concentration.
5. Grain refinement influenced the mechanical properties of the Inconel 713C® superalloy at ambient and elevated temperatures. In unmodified variants, the average YS decreased with increasing melt-pouring temperature from 787 MPa (L0–1450 °C) to 775 MPa (H0–1520 °C). Among the $CoAl_2O_4$-modified variants, the highest average YS of 835 MPa was achieved in casting L10.
6. With increasing inoculant content and, in turn, grain size refinement, the creep resistance tended to be lower, while all samples exceeded the required minimum time to rupture of 30 h (max. 46.1 h for casting M0).

Author Contributions: Conceptualization, R.C. and Ł.R.; methodology, R.C. and Ł.R.; software, R.C. and Ł.R.; validation, R.C. and Ł.R.; formal analysis, R.C.; investigation, R.C. and Ł.R.; resources, R.C. and Ł.R.; data curation, R.C. and Ł.R.; writing—original draft preparation, R.C. and Ł.R.; writing—review and editing, R.C. and Ł.R.; supervision, R.C.; project administration, R.C.; funding acquisition, R.C. All authors have read and agreed to the published version of the manuscript.

Institutional Review Board Statement: Not applicable.

Informed Consent Statement: Not applicable.

Data Availability Statement: Not applicable.

Conflicts of Interest: The authors declare no conflict of interest.

References

1. Liu, G.; Salvat Canto, J.; Winwood, S.; Rhodes, K.; Birosca, S. The Effects of Microstructure and Microtexture Generated During Solidification on Deformation Micromechanism in IN713C Nickel-based Superalloy. *Acta Mater.* **2018**, *148*, 391–406. [CrossRef]
2. Superalloys, I.I. *High-Temperature Materials for Aerospace and Industrial Power*; Sims, C.T., Stoloff, N.S., Hagel, W.C., Eds.; John Wiley & Sons: New York, NY, USA, 1987.
3. Reed, R.C. *The Superalloys Fundaments and Applications*; Cambridge University Press: Cambridge, UK, 2006.
4. Hou, K.; Wang, M.; Zhao, P.; Ou, M.; Li, H.; Ma, Y.; Liu, K. Temperature-Dependent Yield Strength and Deformation Mechanism of a Casting Ni-based Superalloy Containing Low Volume-Fraction γ' phase. *J. Alloys Compd.* **2022**, *905*, 164187. [CrossRef]
5. Grudzień-Rakoczy, M.; Rakoczy, Ł.; Cygan, R.; Chrzan, K.; Milkovič, O.; Pirowski, Z. Influence of Al/Ti Ratio and Ta Concentration on the As-Cast Microstructure, Phase Composition, and Phase Transformation Temperatures of Lost-Wax Ni-Based Superalloy Castings. *Materials* **2022**, *15*, 3296. [CrossRef]
6. Kanyo, J.; Schafföner, S.; Sharon Uwanyuze, R.; Leary, K. An Overview of Ceramic Molds for Investment Casting of Nickel Superalloys. *J. Eur. Ceram. Soc.* **2020**, *40*, 4955–4973. [CrossRef]
7. Szczotok, A.; Matysiak, H. Influence of Constituents of Shell Mold on the Morphology and Chemical Composition of Carbides Occurring in IN 713C Superalloy Castings. *J. Mater. Eng. Perform.* **2014**, *23*, 2748–2759. [CrossRef]
8. Szczotok, A.; Chmiela, B. Effect of Heat Treatment on Chemical Segregation in CMSX-4 Nickel-Base Superalloy. *J. Mater. Eng. Perform.* **2014**, *23*, 2739–2747. [CrossRef]
9. Matysiak, H.; Michalski, J.; Balkowiec, A.; Sikorski, K.; Kurzydłowski, K.J. Surface Defects of Investment Castings of turbofan engine components made of IN713C nickel Superalloy. *Mater. Sci.-Pol.* **2009**, *27*, 1103–1110.
10. Liu, G.; Winwood, S.; Rhodes, K.; Birosca, S. The Effects of Grain Size, Dendritic Structure and Crystallographic Orientation on Fatigue Crack Propagation in IN713C Nickel-based Superalloy. *Int. J. Plast.* **2020**, *125*, 150–168. [CrossRef]
11. Thébauda, L.; Villechaise, P.; Crozet, C.; Devaux, A.; Bécheta, D.; Franchet, J.-M.; Rouffié, A.-L.; Mills, M.; Cormier, J. Is There an Optimal Grain Size for Creep Resistance in Ni-based Disk Superalloys? *Mater. Sci. Eng. A* **2018**, *718*, 274–283. [CrossRef]
12. Rakoczy, Ł.; Grudzień-Rakoczy, M.; Cygan, R. The Influence of Shell Mold Composition on the As-cast Macro- and Micro-structure of Thin-Walled IN713C Superalloy Castings. *J. Mater. Eng. Perform.* **2019**, *28*, 3974–3985. [CrossRef]
13. Nawrocki, J.; Motyka, M.; Szeliga, D.; Ziaja, W.; Cygan, R.; Sieniawski, J. Effect of Cooling Rate on Macro- and Microstructure of Thin-Walled Nickel Superalloy Precision Castings. *J. Manuf. Process.* **2020**, *49*, 153–161. [CrossRef]
14. Utada, S.; Despres, L.; Cormier, J. Ultra-High Temperature Creep of Ni-Based SX Superalloys at 1250 °C. *Metals* **2021**, *11*, 1610. [CrossRef]
15. Gao, F.; Fan, Z. Effect of Nucleant Particle Agglomeration on Grain Size. *Metall. Mater. Trans. A* **2022**, *53*, 810–822. [CrossRef]
16. Venkat, Y.; Choudary, K.R.; Das, D.K.; Pandey, A.K.; Singh, S. Ceramic Shell Moulds for Investment Casting of Low-Pressure Turbine Rotor Blisk. *Ceram. Int.* **2021**, *47*, 5663–5670. [CrossRef]
17. Wittenzellner, T.; Sumarli, S.; Schaar, H.; Wang, F.; Ma, D.; Bührig-Polaczek, A. Microstructural Investigations of Ni-Based Superalloys by Directional Solidification Quenching Technique. *Materials* **2020**, *13*, 4265. [CrossRef] [PubMed]
18. Tiparti, D.; Ho, I.-T.; Chang, K.-H.; Hsu, T.-H.; Yeh, A.-C.; Tin, S. Understanding the Effects of $CoAl_2O_4$ Inoculant Additions on Microstructure in Additively Manufactured Inconel 718 Processed Via Selective Laser Melting. *Metall. Mater. Trans. A* **2021**, *52*, 2630–2641. [CrossRef]
19. Chueachot, R.; Nakhowong, R. Synthesis and Optical Properties of Blue Pigment $CoAl_2O_4$ Nanofibers by Electrospinning. *Mater. Lett.* **2020**, *259*, 126904. [CrossRef]
20. Jian, F.; Bin, Y. Investigation of the Surface Grain Refinement for Superalloys Castings. In *High Temperature Alloys for Gas Turbines*; Brunetaud, R., Coutsouradis, D., Gibbons, T.B., Lindblom, Y., Meadowcroft, D.B., Stickler, R., Eds.; Springer: Dordrecht, The Netherlands, 1982; pp. 987–997. [CrossRef]
21. Walter, C.; Hallstedt, B.; Warnken, N. Simulation of the Solidification of CMSX-4. *Mater. Sci. Eng. A* **2005**, *397*, 385–390. [CrossRef]
22. *ASTM E8/E8M-13*; Standard Test Methods for Tension Testing of Metallic Materials. ASTM: West Conshohocken, PA, USA, 2013.
23. *ASTM E139-11*; Standard Test Methods for Conducting Creep, Creep-Rupture, and Stress-Rupture Tests of Metallic Materials. ASTM: West Conshohocken, PA, USA, 2018.
24. Grudzień-Rakoczy, M.; Rakoczy, Ł.; Cygan, R.; Kromka, F.; Pirowski, Z.; Milkovič, O. Fabrication and Characterization of the Newly Developed Superalloys Based on Inconel 740. *Materials* **2020**, *13*, 2362. [CrossRef]
25. Rakoczy, Ł.; Rutkowski, B.; Grudzień-Rakoczy, M.; Cygan, R.; Ratuszek, W.; Zielińska-Lipiec, A. Analysis of γ' Precipitates, Carbides and Nano-Borides in Heat-Treated Ni-Based Superalloy Using SEM, STEM-EDX, and HRSTEM. *Materials* **2020**, *13*, 4452. [CrossRef]
26. Franke, M.M.; Hilbinger, R.M.; Konrad, C.H.; Glatzel, U.; Singer, R.F. Numerical Determination of Secondary Dendrite Arm Spacing for IN738LC Investment Castings. *Metall. Mater. Trans. A* **2011**, *42*, 1847–1853. [CrossRef]

27. Matysiak, H.; Zagorska, M.; Balkowiec, A.; Adamczyk-Cieslak, B.; Dobkowski, K.; Koralnik, M.; Cygan, R.; Nawrocki, J.; Cwajna, J.; Kurzydlowski, K.J. The Influence of the Melt-Pouring Temperature and Inoculant Content on the Macro and Microstructure of the IN713C Ni-Based Superalloy. *JOM* **2016**, *68*, 185–197. [CrossRef]

28. Bhambri, A.; Kattamis, T.; Morral, J. Cast Microstructure of Inconel 713C and its Dependence on Solidification Variables. *Metall. Trans. B* **1975**, *6*, 523–537. [CrossRef]

29. Grosdidier, T.; Hazotte, A.; Simon, A. Precipitation and Dissolution Processes in γ/γ' Single Crystal Nickel-Based Superalloys. *Mater. Sci. Eng. A* **1998**, *256*, 183–196. [CrossRef]

30. Long, H.; Mao, S.; Liu, Y.; Zhang, Z.; Han, X. Microstructural and Compositional Design of Ni-based Single Crystalline Superalloys—A Review. *J. Alloys Compd.* **2018**, *743*, 203–220. [CrossRef]

31. Chen, Y.; Kong, W.; Yuan, C.; Liu, S.; Cai, Y.; Wang, Y.; Gao, X. The Effects of Temperature and Stress on the High-Cycle Fatigue Properties of a Ni-based Wrought Superalloy. *Int. J. Fatigue* **2023**, *172*, 107669. [CrossRef]

32. Chatterjee, S.; Li, Y.; Po, G. A Discrete Dislocation Dynamics Study of Precipitate Bypass Mechanisms in Nickel-based Superalloys. *Int. J. Plast.* **2021**, *145*, 103062. [CrossRef]

33. Nathal, M.V. Effect of Initial Gamma Prime Size on the Elevated Temperature Creep Properties of Single Crystal Nickel Base Superalloys. *Metall. Mater. Trans.* **1987**, *18*, 1961–1970. [CrossRef]

34. Rakoczy, Ł.; Grudzień, M.; Zielińska-Lipiec, A. Contribution of Microstructural Constituents on Hot Cracking of MAR-M247 Nickel Based Superalloy. *Arch. Metall. Mater.* **2018**, *63*, 181–189. [CrossRef]

35. Rakoczy, Ł.; Milkovič, O.; Rutkowski, B.; Cygan, R.; Grudzień-Rakoczy, M.; Kromka, F.; Zielińska-Lipiec, A. Characterization of γ' Precipitates in Cast Ni-Based Superalloy and Their Behaviour at High-Homologous Temperatures Studied by TEM and in Situ XRD. *Materials* **2020**, *13*, 2397. [CrossRef] [PubMed]

36. Hu, X.B.; Zhu, J.L.; Sheng, N.C.; Ma, X.L. The Wyckoff positional order and polyhedral intergrowth in the M3B2- and M5B3-type boride precipitated in the Ni-based superalloys. *Sci. Rep.* **2014**, *4*, 7367. [CrossRef] [PubMed]

37. Matysiak, H.; Zagorska, M.; Balkowiec, A.; Adamczyk-Cieslak, B.; Cygan, R.; Cwajna, J.; Nawrocki, J.; Kurzydłowski, K.J. The Microstructure Degradation of the IN 713C Nickel-Based Superalloy After the Stress Rupture Tests. *J. Mater. Eng. Perform.* **2014**, *23*, 3305–3313. [CrossRef]

38. Franke, P.; Neuschutz, D. Binary Systems. Part 4: Binary Systems From Mn-Mo to Y-Zr. In *Landolt-Bornstein–Group IV Physical Chemistry, Numerical Data and Functional Relationships in Science and Technology*; Springer: Berlin/Heidelberg, Germany, 2006; p. 19B4.

39. Motejadded, H.B.; Soltanieh, M.; Rastegari, S. Dissolution Mechanism of a Zr Rich Structure in a Ni₃Al Base Alloy. *J. Mater. Sci. Technol.* **2011**, *27*, 885–892. [CrossRef]

40. Moreira, M.F.; Fantin, L.B.; Beneduce Neto, F.; Azevedo, C.R.F. Microstructural and Mechanical Characterization of As-Cast Nickel-Based Superalloy (IN-713C). *Int. J. Met.* **2021**, *15*, 1129–1148. [CrossRef]

41. Keshavarz, M.K.; Turenne, S.; Bonakdar, A. Solidification Behavior of Inconel 713LC Gas Turbine Blades During Electron Beam Welding. *J. Manuf. Process.* **2018**, *31*, 232–239. [CrossRef]

42. Kazempour-Liasi, H.; Tajally, M.; Abdollah-Pour, H. Liquation Cracking in the Heat-Affected Zone of IN939 Superalloy Tungsten Inert Gas Weldments. *Int. J. Miner. Metall. Mater.* **2020**, *27*, 764–773. [CrossRef]

43. Chen, K.-C.; Chen, T.C.; Shiue, R.-K.; Tsay, L.-W. Liquation Cracking in the Heat-Affected Zone of IN738 Superalloy Weld. *Metals* **2018**, *8*, 387. [CrossRef]

44. Babu, S.; David, S.A.; Vitek, J.M.; Miller, M.K. Atom-Probe Field-Ion Microscopy Investigation of CMSX-4 Ni-Base Superalloy Laser Beam Welds. *J. Phys. IV Fr.* **1996**, *C5*, 253–258. [CrossRef]

45. Murata, Y.; Yukawa, N. Solid-State Reaction for ZrC Formation in a Zr-Doped Nickel-Based Superalloy. *Scr. Metall.* **1986**, *20*, 93–696. [CrossRef]

46. Tang, Y.T.; Wilkinson, A.J.; Reed, R.C. Grain Boundary Serration in Nickel-Based Superalloy Inconel 600: Generation and Effects on Mechanical Behavior. *Metall. Mater. Trans. A* **2018**, *49*, 4324–4342. [CrossRef]

47. Frost, H.J.; Ashby, M.F. *Deformation-Mechanism Maps. The Plasticity and Creep of Metals and Ceramics*; Pergamon Press: Oxford, UK, 1982.

48. Nabarro, F.R.N.; de Villiers, F. *Physics Of Creep And Creep-Resistant Alloys*, 1st ed.; CRC Press: Boca Raton, FL, USA, 1995. [CrossRef]

49. Coble, R.L. A Model for Boundary Diffusion Controlled Creep in Polycrystalline Materials. *J. Appl. Phys.* **1963**, *34*, 1679–1682. [CrossRef]

50. Vamsi, K.V.; Karthikeyan, S. Modeling APB Energies in Multicomponent Ni-base Superalloys. *Intermetallics* **2021**, *132*, 107124. [CrossRef]

51. Thornton, P.H.; Davies, R.G.; Johnston, T.L. The Temperature Dependence of the Flow Stress of the γ' Phase Based Upon Ni₃Al. *Metall. Trans.* **1970**, *1*, 207–218. [CrossRef]

52. Rakoczy, Ł.; Cempura, G.; Kruk, A.; Czyrska-Filemonowicz, A.; Zielińska-Lipiec, A. Evolution of γ' Morphology and γ/γ' Lattice Parameter Misfit in a Nickel-based Superalloy During Non-Equilibrium Cooling. *Int. J. Mater. Res.* **2019**, *110*, 66–69. [CrossRef]

53. Jin, W.; Bai, F.; Li, T.; Yin, G. Grain Refinement of Superalloy IN100 under the Action of Rotary Magnetic Fields and Inoculants. *Mater. Lett.* **2008**, *62*, 1585–1588. [CrossRef]

54. Liu, L.; Huang, T.; Xiong, Y.; Yang, A.; Zhao, Z.; Zhang, R.; Li, J. Grain Refinement of Superalloy K4169 by Addition of Refiners: Cast Structure and Refinement Mechanisms. *Mater. Sci. Eng. A* **2005**, *394*, 1–8. [CrossRef]
55. Feagin, R.C. Dipcoat Nucleation. In *European Investment Caster's Federation Proceedings of the 12th Conference*; ASM: Eindhoven, The Netherlands, 1967.

Ceramic cores for turbine blades via injection moulding

Magdalena Gromada [a,*], Adam Świeca [a], Marek Kostecki [b], Andrzej Olszyna [b], Rafał Cygan [c]

[a] Institute of Power Engineering Ceramic Department CEREL, Research Institute, 1 Techniczna St., 36-040 Boguchwała, Poland
[b] Warsaw University of Technology, Faculty of Materials Science and Engineering, 141 Wołoska St., 02-507 Warsaw, Poland
[c] WSK "PZL – Rzeszów" S.A., 120 Hetmańska St., 35-078 Rzeszów, Poland

ARTICLE INFO

ABSTRACT

The proposed injection moulding method to produce ceramic cores of turbine blades required the selection of raw materials and the thermoplasticiser as well as the determination of the optimal processing conditions. The selected material enabled the formation of cores with a small cross-section area and was characterised by low shrinkage as well as a relatively low coefficient of thermal expansion. The high mechanical strength of the material allowed for the cores to be formed in a wax model and their assembly in a foundry mould; in addition, the appropriate porosity of the cores ensured their easy etching by means of a water solution of bases. The cores were characterised by high dimensional precision and negligibly small shape deformation. The usability of the cores was positively verified in the process of turbine blades casting in production conditions.

© 2015 Elsevier B.V. All rights reserved.

1. Introduction

Ceramic cores are utilised for shaping internal cooling canals in the process of turbine blade casting, which positively influences the turbine engine efficiency. The aim of the hollow spaces inside of the blades is to provide cooling during turbine engine operation, allowing for the temperature increase of the working gases; in addition, the hollow spaces decrease the weight of the blades, which reduces the load of the drive shaft. Obtaining such precise shapes inside the blades during the casting process is only possible by using special 'near net shape' ceramic cores. To satisfy these requirements, the material for the cores should be characterised by the following properties: possibility of the complex shape forming, low shrinkage during forming and sintering, small surface roughness (enabling good mapping of internal blades canal after their casting), and low coefficient of thermal expansion (ensuring resistance to thermal shocks and dimension stability of the cores at the temperature of their casting in liquid alloys). Moreover, the developed material must often satisfy contrasting requirements, for example, a high mechanical strength (that allows the cores to form in the wax model and their assembly in foundry moulds) with the apparent porosity of the cores reaching 35% (allowing for their relatively easy etching by means of a basic water solution). To satisfy these requirements, in this paper, the high pressure injection moulding method was

applied, which enables the formation of cores of very complicated shapes and high dimensional precision.

Soykan and Karakas (2001) stressed that the ceramic powder injection moulding method is used to form complicated elements with shapes that are very close to actual products in mass production at a competitive cost. As was stated by Karatas et al. (2004), this technique is mostly utilised for producing fine shaped pieces with a relatively small cross-section. Park et al. (2001) consider this method as competitive in comparison with casting and mechanical machining. However, according to Zauner (2006), this technique is quite demanding because it generates a wide range of defects, beginning from cavity filling to binder removal and sintering. Krug et al. (2001) confirmed that the wider industrial implementation of the injection moulding method requires high quality standards and low rejection rates.

Thomas and Marple (1998) indicated that the process of ceramic powder injection moulding that has been developed from the injection moulding approach used for the shaping of plastics is quite complicated because of the presence of additional steps after forming. They confirmed that to remove the thermoplasticiser and to densify and strengthen the shaped pieces, the process of heat treatment is applied alone or in combination with other processes.

Wang and Hon (1995) described the process of the fabrication of ceramic cores for single crystal casting. They emphasised that the application of thin and delicate ceramic cores has an influence on the efficiency of turbine engines. The properties of ceramic cores must be finely balanced to produce acceptable dimensions in the blade cast. Wang and Hon (1995) reduced the list of possible

---

ceramic materials to only a few candidates (fused silica, zirconia, and alumina) due to the required chemical solubility.

Recently, a few papers were published regarding the material composition for ceramic cores fabrication. Kazemi et al. (2014) investigated the effect of the zircon content on the mechanical and chemical behaviours of injection moulded silica-based ceramic cores. Kazemi et al. (2013) presented the results of the crystallisation of fused silica and its effects on the most important properties of injection moulded silica-based ceramic cores, including the flexural strength and leachability. Qin and Pan (2009) prepared a series of alumina-based ceramic core nanocomposites by adding silica-sol to an alumina matrix and using the in situ synthesis method. The microstructure and the effect of silica sol on the properties of alumina-based duplex ceramic cores were discussed.

Also new technologies were applied for the fabrication of ceramic cores used in the casting of blades. Kim et al. (2013) presented a new process that consists of the development of a mixture of an inorganic precursor composed of silicate and metal alkoxide; the prepared ceramic core was found to exhibit reasonable strength without shrinkage and shape deformation. Wu et al. (2009) developed a rapid prototyping process to fabricate complex-shaped alumina-based ceramic cores by combining stereolithography with gelcasting. To decrease the drying shrinkage, the conventional air drying process was substituted by the freeze drying one. In addition, the mineraliser in the form of magnesium oxide power was added, which minimised the sintering shrinkage of the cores to below 0.5%.

The aim of this paper was to develop a manufacturing technology for the entire process of the fabrication of ceramic cores that satisfies all of the above-mentioned requirements to be applied in high precision blades. The developed technology, because of its efficiency, can be applied at industrial scale.

2. Materials and methods

In this paper, for the precise fabrication of cores, the injection moulding method was applied, which consists of four basic stages: preparation of feedstock, element formation, binder removal, and sintering. The powder composition and its particle size distribution were developed to ensure the appropriate density of material after sintering. The particle size distribution of raw materials and input powders were determined using Mastersize 2000 from the Melvern Company. Table 1 presents the composition of eleven materials fabricated for the injection process. The fused silica or quartz glass are the basic raw materials for cores, which are characterised by a low coefficient of thermal expansion, sufficient refractoriness, resistance on thermal shock, very good chemical inertness and very high softening temperature. The difference between the quartz glass and the fused silica (SiO_2) is in the phase composition. The quartz glass has a relatively small content of an amorphous phase in relation with the crystal one, while the fused silica contains almost entirely the amorphous phase. The boron glass serves as an agent allowing for the better sintering of cores. At the sintering temperature, the boron glass passes in liquid phase and attracts grains of other raw materials, which causes the increase of sintering stage of material and in turn increases the mechanical strength. The quartz and boron glasses are added as powders. The particle size distributions of these powders are presented in Fig. 2; the average particle sizes (d_{50}) are equal to 31.1 μm and 27.0 μm for the quartz and boron glasses, respectively. The modifying compounds $ZrSiO_4$ and Al_2O_3 were chosen to decrease the value of sintering shrinkage of ceramic cores and improve the dimension stability during cores casting with liquid alloys. The application of water soluble thermoplasticiser Siliplast HS enables the mould powder elimination in the process of binder removal from cores,

Fig. 1. The two types of ceramic cores for the turbine blade.

which has a positively influence on quality of external surface of cores.

The feedstocks were prepared in a GC-MIX-12/13 heated mixer, where the powder and the thermoplasticiser were kneaded at 160 °C to the moment of reaching the homogenous consistence. Next, for the sake of the worm geometry of the injection moulding machine, the obtained material was crushed to the granule size in the range of 1.5–4 mm.

In the stage of the formation of elements, two moulds were designed and executed. The first mould with two cavities enabled the formation of beams of a diameter of 6 mm and length of 60 mm. After sintering, these beams served to determine the materials shrinkage, the density, the bending strength, the coefficient of thermal expansion, and the roughness of the surface; the beams were also used in tests of material etching in a basic water solution. The second mould with two cavities for two types of experimental core shapes enabled the examination of small cross-section formation. The experimental cores had a length of over 30 mm and a minimal cross-sectional area of only 5 mm². Fig. 1 presents a photo of the two types of ceramic cores for the turbine blade.

The selection of injection parameters contained many variables, including temperature, pressure, velocity, volume and time. The improper setting of even one parameter brought the appearance of defects in elements. The mould temperature and dwell time of semi-products were found to have a significant influence on the deformation of the shaped pieces. The forming process was performed on a BOY XS injection moulding machine with a closing force equal to 100 kN, a maximal volume of injection of 6.1 cm³ and a maximal pressure of injection of 230 MPa.

The last two stages of the injection moulding process include the thermoplasticiser removal from the shaped pieces and their
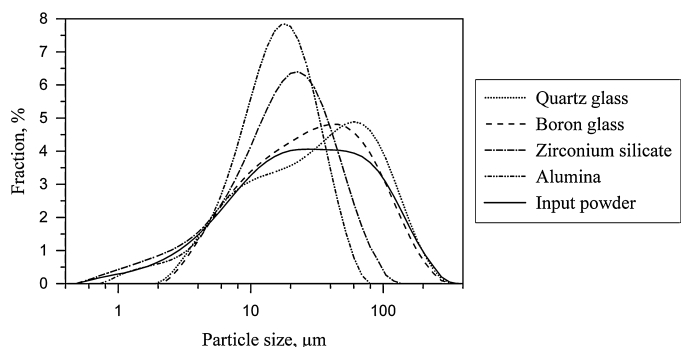

Fig. 2. The particle size distribution of the input powder and the applied raw materials.

Table 1
The composition of the materials fabricated for the injection process.

Materials	Composition of materials, wt%						
	SiO$_2$ (120 mesh), (Precision Electro Minerals)	SiO$_2$ (300 mesh), (Precision Electro Minerals)	Quartz glass, (Juropol)	ZrSiO$_4$ (300 mesh), (Ransom& Randolph)	Al$_2$O$_3$ (325 mesh), (Treibacher)	Boron glass, (TEW)	Siliplast HS, (Zschimmer & Schwarz GmbH & Co. KG)
1	29.1	29.1		10.3	9.5		22.0
2	56.8				19.8	2.4	21.0
3			76.6			2.4	21.0
4	67.1				9.5	2.4	21.0
5	59.2	7.9			9.5	2.4	21.0
6	33.6	33.6			9.5	2.4	21.0
7	57.6				20.0	2.4	20.0
8	34.0	34.0			9.6	2.4	20.0
9			57.3		19.8	1.9	21.0
10			55.0		19.8	4.2	21.0
11			55.0	10.3	9.5	4.2	21.0

sintering. The applied water soluble thermoplasticiser – Siliplast HS (Zschimmer & Schwarz GmbH & Co KG), based on modified polyalcohols, required the execution of two-step debinding. Placing the elements in the water bath at a temperature of 70 °C for 8 h effected the removal approximately 60% of the thermoplasticiser. However, the remaining part was removed in a thermal process combined with the final sintering of goods. To this end, the used electrical furnace was equipped with two fans of pre-heated air blowing and air pull-off from the furnace chamber.

In the process of obtaining the required properties of cores, the sintering stage is of essential significance. The settling of the maximal temperature along with the speed of its increase and decrease influences the production of fracture-free cores with the specified physical and mechanical properties. The maximum temperature in an optimal sintering curve is equal to 1250 °C, with the temperature increasing at the rate of 50 °C/h up to the maximum temperature; the dwell time at the maximum temperature is 1.5 h, followed by cooling at the rate of 100 °C/h.

The basic properties were determined of these eleven materials sintered according to above-presented curve. The parameters characterising the stage of materials sintering, that is, the apparent density, the apparent porosity, and the water absorbability, were estimated using a method that takes advantage of Archimedes law and boiling for the impregnation of the samples with water. The bending strength of the materials was determined using the three-point method on the sintered and unpolished beams of cross-section of 28 mm^2. A home-made strength testing machine was used. The speed of the cross-bar movement was equal to 5 mm/min, and the applied distance of the supports was 50 mm. On the basis of these results, the optimal material for cores fabrication was selected.

The rest of the optimal material properties influencing the usability of the cores were determined and analysed. The distribution of the pores size in the sintered material was determined using

the mercury porosimetry method on a Micromeritics AUTO_PORE 4 model 9500. The microstructure of the material was evaluated using scanning electron microscopy on a HITACHI S-3500N SEM. For determining the coefficient of thermal expansion and the surface roughness, beams were used. The coefficient of linear expansion in the temperature range of 20–600 °C was determined using a high temperature dilatometer from BÄHR-Gerätebau GmbH Company. The test of the roughness profile was performed using a Veeco NT9300 optical profilometer. To ensure light reflection from the sample surface, a layer of gold with a thickness that did not exceed 0.05 µm was deposited. The surface of dimensions of 1 mm × 4 mm was scanned, taking into account that the shape profile follows from the sample geometry. As an effect of the numerical data analysis, the transformation from a cylindrical to a flat surface was made, and then, the calculation of the roughness profile was executed.

The Coordinate Measuring Machine Mitutoyo Crysta Apex C7106 was used for measuring ready cores after sintering in three axes to determine the dimensional accuracy and the stage of deformation of the cores. The machine was equipped with a tilt-rotary head, scanning probe and two measuring modules. The MCOSMOS software enabled measurements to be performed in real-time mode.

The test of core etching was performed under laboratory conditions; therefore, the loss of core weight was determined after 5 h of etching at 110 °C in water solution with potassium hydroxide.

3. Results and discussion

During the selection of the optimal material for the cores, the most important two parameters were considered, i.e., the apparent porosity and the bending strength of the sintered materials. As was mentioned earlier, the material for the fabrication of the cores should be characterised by an apparent porosity close to 35% with

Table 2
The basic properties of the materials after sintering.

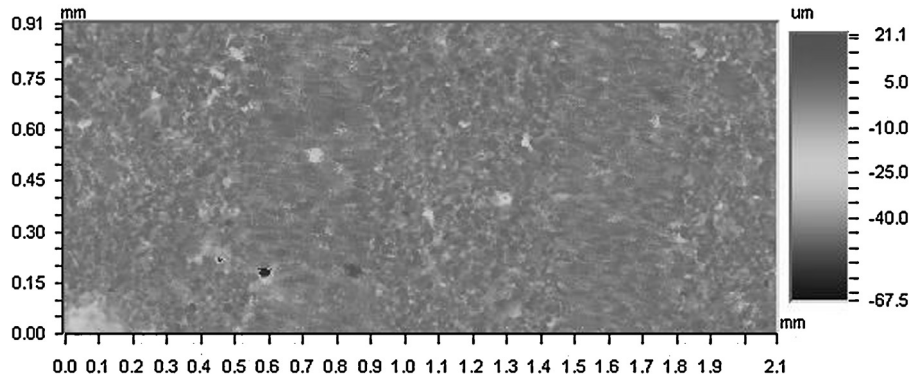| Materials	Water absorbability, %	Apparent density, g/cm^3	Apparent porosity, %	Bending strength, MPa
1	22.38	1.65	36.78	7.0
2	20.02	1.70	34.00	7.9
3	21.32	1.51	32.25	4.2
4	21.06	1.61	33.89	4.4
5	20.80	1.62	33.61	5.8
6	19.88	1.64	32.56	6.1
7	17.22	1.77	30.67	14.4
8	18.23	1.69	30.77	3.3
9	21.07	1.65	34.72	9.2
10	20.32	1.67	33.85	13.8
11	20.44	1.68	34.36	14.7

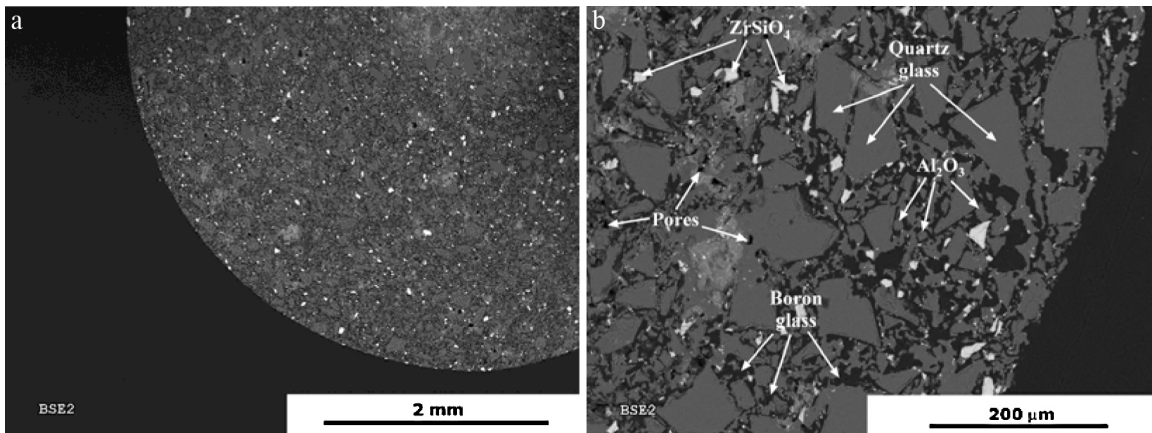**Fig. 3.** The surface profile of the sintered specimen.

Fig. 4. The microstructure of the optimal material.

the highest mechanical strength. From the results summarised in Table 2, the five materials indicated as 1, 2, 9, 10 and 11 possess the appropriate value of the apparent porosity, while for the remaining materials, the apparent porosity is too low. The highest values of the bending strength were found for materials 7, 10 and 11, whereas for the rest of materials, the bending strength is lower than 10 MPa. Therefore, materials 10 and 11 satisfied these two requirements, but finally, material 11, with the higher apparent porosity and bending strength, was chosen as the optimal material in this study. This material is composed of 55.0 wt% quartz glass (Juropol), 4.2 wt% boron glass (TEW), 10.3 wt% zirconium silicate (Ransom & Randolph) and 9.5 wt% alumina (Treibacher) and 21.0 wt% Siliplast HS (Zschimmer & Schwarz GmbH & Co KG). The obtained value of the bending strength (14.7 MPa) will enable the formation of cores in a wax model and their assembly in a foundry mould. Moreover, this result was at least 22.5% higher than the outcome presented by Kim et al. (2013).

In the remaining parts of this paper, the rest of the properties of the optimal material will be determined and investigated. Fig. 2 presents the particle size distribution of the powder used to material for injection fabrication and also the applied raw materials.

As a result of the mass fraction of particular raw materials, the particle size distribution of the input powder is similar to that of the quartz and boron glasses. Moreover, this powder is composed of finer alumina and zirconium silicate. The particle size distribution of the input powder ranges from 0.6 to 250 μm, while the average size of the particles is equal to 26 μm.

To protect the shaped cores from defects and deformation, the optimal injection parameters were selected. The temperature of the cylinder and nozzle was equal to 160 °C, with a tolerance of 5 °C. The pressure of injection was set as 1840 bar, while the velocity of

injection was equal to 15.4 cm^3/s. The temperature of the mould was held at 40 °C, and the time that the cores stay in mould was set to 40 s. As a result of the material composition and set parameters during injection process, the very favourable value of less than 0.1% of material shrinkage during the formation process was observed.

The surface profile of the sintered beam presented in Fig. 3 reveals the smooth, low differential plane, with only few areas of greater level.

The observed value of surface roughness (2.79 μm) allows for good mapping of the internal blades canal after their casting. The relatively low coefficient of thermal expansion ($6.23 \cdot 10^{-6}$ 1/K) ensures resistance to thermal shock and the dimension stability
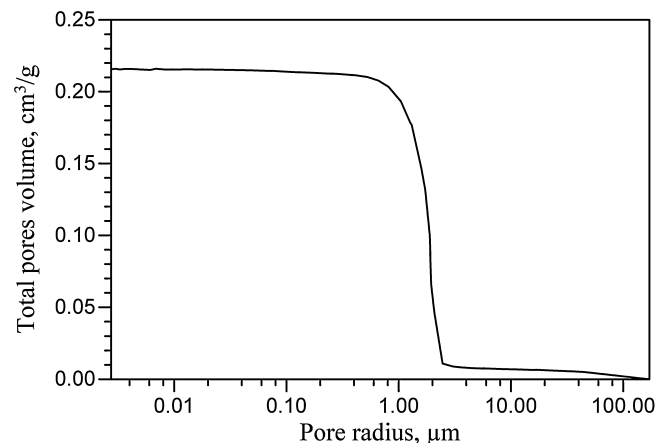

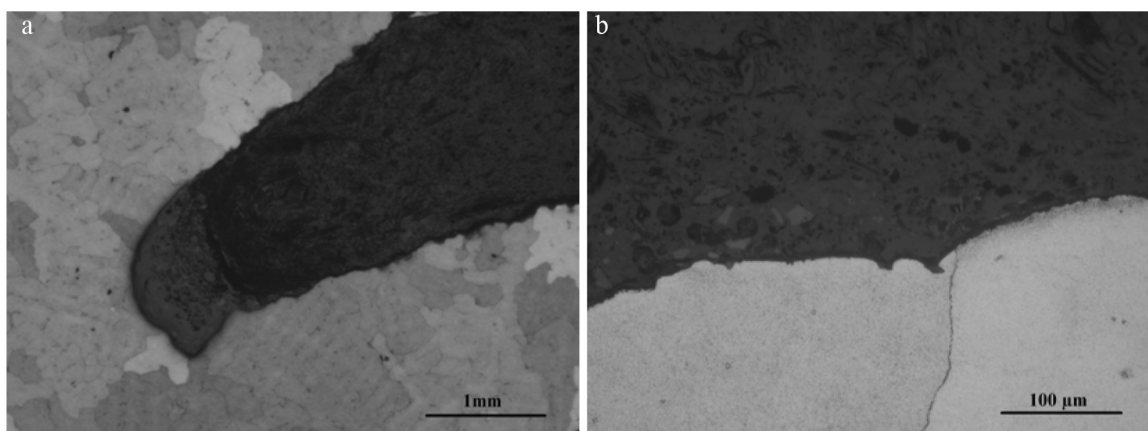**Fig. 5.** The pore size distribution of the optimal material.

Fig. 6. The etched metallographic specimen at magnifications of 50 and 500 times.

of cores at the temperatures of their casting with liquid alloys. Qin and Pan (2009) reported a similar range of the coefficient of thermal expansion for ceramic cores.

The very favourable small value of less than 1.45% of material shrinkage after debinding and sintering is a result of using a homogenous feedstock with a high powder content. The shrinkage of the optimal material developed in this paper is almost three times higher than that reported by Wu et al. (2009), while it is over two times lower than that obtained by Qin and Pan (2009). From the photos of the material microstructures (Fig. 4a), large joint particles were observed with dimensions from 50 to 100 μm and a structure composed of fine particles of dimension of less than a few μm. The distribution of large particles is homogenous, and the visible voids and pores are due to the lack of complete compaction of the material (Fig. 4b). In addition, particles of quartz glass, alumina, zirconium silicate together with pores and melted boron glass are indicated in Fig. 4b.

Fig. 5 shows the pore size distribution. This material is characterised by the presence of small pores with a radius of up to 1 μm and volume of up to 0.23 cm^3/g as well as large pores with a minimal volume dimension of 2–60 μm.

These data are confirmed by the information contained in the microstructure photos (Fig. 4). Therefore, the cores of the obtained microstructure should reveal the ease of etching, which confirms the results of the executed test in laboratory conditions. The loss of the weight of the cores was determined after 5 h of etching at 110 °C in a water solution with potassium hydroxide. For the optimal material, the weight loss was more than 82%.

The results of the measurements of the cores confirmed the high dimensional accuracy of the cores. The highest deviation from the nominal dimension was +0.15 mm, which was still within the range of tolerance.

In the last stage, the verification of the usability of the cores in the process of turbine blade casting was realised. Achieving good mechanical strength and resistance to the thermal shock of the cores were confirmed by the trials of injecting cores in the wax model and the results of mould casting with liquid alloy. The outcomes of the X-ray analysis of the blades revealed the lack of fracture and displacement of the cores in relation to the wall of the casting. Moreover, the cores were characterised by good etching in an autoclave, which indicates the possibility of removing the cores from casts via a chemical method under pressure. In addition, the reactivity of the liquid alloy with the cores was determined by means of metallurgical appraisal of the wall quality. Fig. 6a and b shows an etched metallographic specimen at magnifications of 50 and 500 times, respectively.

The maximal depth of loss of the blade layer was equal to 20 μm. Only in the one case did the loss have a greater value that exceeded the TSL standard for power engineering turbine blades.

4. Conclusions

An injection moulding material was obtained that has the appropriate properties for application in the cores of blades used in gas turbines and turbocompressors. The optimal material parameter was determined to be a composition of coarse-grained quartz and boron glasses as well as finer alumina and zirconium silicate.

The obtained material allowed for the formation of cores of complicated shapes with high dimensional accuracy. The characteristics of material apparent density, water absorbability and apparent porosity, together with the microstructure and etching results (as related to the bending strength), confirm the usability of the cores for casting the internal canal in blades and the ease of their removal from the casts. In addition, a small value of the coefficient of thermal expansion and low surface roughness of developed material ensures good mapping of the internal shape of the canal blades.

References

Karatas, C., Kocer, A., Ünal, H.I., Saritas, S., 2004. Rheological properties of feedstocks prepared with steatite powder and polyethylene-based thermoplastic binders. J. Mater. Process. Technol. 152, 77–83.

Kazemi, A., Faghihi-Sani, M.A., Alizadeh, H.R., 2013. Investigation on cristobalite crystallization in silica-based ceramic cores for investment casting. J. Eur. Ceram. Soc. 33, 3397–3402.

Kazemi, A., Faghihi-Sani, M.A., Nayyeri, M.J., Mohammadi, M., Hajfathalian, M., 2014. Effect of zircon content on chemical and mechanical behavior of silica-based ceramic cores. Ceram. Int. 40, 1093–1098.

Kim, E.-H., Cho, G.-H., Yoo, Y.S., Seo, S.M., Jung, Y.-G., 2013. Development of a new process in high functioning ceramic core without shape deformation. Ceram. Int. 39, 9041–9045.

Krug, S., Evans, J.R.G., ter Maat, J.H.H., 2001. Transient effects during catalytic binder removal in ceramic injection moulding. J. Eur. Ceram. Soc. 21, 2275–2283.

Park, M.S., Kim, J.K., Ahn, S., Sung, H.J., 2001. Water-soluble binder of cellulose acetate butyrate/poly(ethylene glycol) blend for powder injection molding. J. Mater. Sci. 36, 5531–5536.

Qin, Y., Pan, W., 2009. Effect of silica sol on the properties of alumina-based ceramic core composites. Mater. Sci. Eng. A 508, 71–75.

Soykan, H.S., Karakas, Y., 2001. Preparation of homogeneous feedstocks for injection moulding of zirconia-based ceramics. Turk. J. Eng. Environ. Sci. 25, 315–319.

Thomas, Y., Marple, B.R., 1998. Partially water-soluble binder formulation for injection molding submicrometer zirconia. Adv. Perform. Mater. 5, 25–41.

Wang, L.-Y., Hon, M.-H., 1995. The effect of cristobalite seed on the crystallization of fused silica based ceramic core – a kinetic study. Ceram. Int. 21, 187–193.

Wu, H., Li, D., Tang, Y., Sun, B., Xu, D., 2009. Rapid fabrication of alumina-based ceramic cores for gas turbine blades by stereolithography and gelcasting. J. Mater. Process. Technol. 209, 5886–5891.

Zauner, R., 2006. Micro powder injection moulding. Microelectron. Eng. 83, 1442–1444.

CERAMICS INTERNATIONAL

PIETRO VINCENZINI

Check for updates
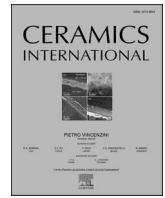
The effect of additives on properties of silica-based ceramic cores utilised in fabrication of multivane clusters for turbofan jet engine

Magdalena Gromada [a,*], Adam Świeca [a], Rafał Cygan [b]

[a] *Institute of Power Engineering – Research Institute, 01–330 Warsaw, Mory 8, Ceramic Department CEREL, Techniczna 1, 36–040, Boguchwała, Poland*
[b] *Consolidated Precision Products Poland Sp. z o.o, 35–078 Rzeszów, Hetmańska, 120, Poland*

ARTICLE INFO

ABSTRACT

Ceramic cores for mapping internal cooling channels in multivane clusters for turbofan jet engine must satisfy rigorous requirements concerning material properties and dimensional precision. The effect of different additives (borosilicate glass, alumina and zirconium silicate) on features of silica-based ceramic cores was investigated. The elaborated in this paper material for cores fabrication composed of 64.0 wt% quartz glass, 11.0 wt% borosilicate glass, 13.0 wt% zirconium silicate and 12.0 wt% alumina reveals mechanical strength equal to 25.8 MPa, coefficient of thermal expansion of $3.52 \cdot 10^{-6}$ $^{1/K}$, surface roughness equal to 2.3 μm, shrinkage less than 1.9% and average pore size diameter of 4.8 μm. The thin-walled long ceramic cores were shaped by the high-pressure injection moulding method, which covered the choice of a thermoplasticizer, feedstock development and determination of the processing parameters protecting the formed cores from imperfection and deformation. The after-shaping process of cores manufacturing included water and thermal debinding, sintering and dimension measurement. The high dimension accuracy of cores was verified by measurement results made on the coordinate measurement machine.

1. Introduction

The internal cooling canals in the multivane clusters for turbofan jet engine are manufactured by the investment casting method with the use of thin-walled long ceramic cores of high precision. The main aim of these hollow spaces inside the multivane clusters is cooling during turbine engine operation, which enables the temperature increase of the working gases. Additionally, the hollow spaces decrease the weight of the multivane clusters, which reduces the load of the drive shaft.

Development of ceramic cores requires elaboration of the new material composition, which satisfies all requirements for cores application in investment casting method of multivane clusters and specific features ensuing from shape and dimension of cores. The elaborated material for such demanding cores should be characterised by the possibility of complex shape formation, low shrinkage during sintering, small surface roughness, low coefficient of thermal expansion, high mechanical strength and high apparent porosity [1–3]. The applied manufacturing technology must ensure possibility of the complex geometries forming with high precision, short cycle of development, low manufacturing cost and level of defects and high cores repeatability. The high accuracy of thin-walled long ceramic cores with complicated shapes has essential

significance, as multivane clusters are composed of six airfoils and application of even one core of dimension exceeding the tolerance field in the casting process will bring to the defective product for multivane cluster. Moreover, such responsible parts as multivane clusters for turbofan jet engine possess very tight tolerance field of wall thickness, which obliges to manufacture cores of high precision. Whole fabrication process of ceramic cores must be carefully inspected beginning from raw materials and input powder characterisation, through feedstock preparation, cores injection, water and thermal debinding as well sintering, ending at measurement of all pieces of ready cores on the coordinate machine.

The material composition for ceramic cores and manufacturing technology for their fabrication were a subjects of many publications. Wang et al. [4] developed the method of ceramic cores manufacturing for single crystal casting. They applied fused silica, zirconia and alumina as the raw materials for cores material due to the required chemical solubility. Kazemi et al. [5] presented the results of the crystallisation of fused silica and its effects on the flexural strength and leachability of injection moulded silica-based ceramic cores. Kazemi et al. [6] studied the influence of the zircon content on the mechanical and chemical properties of injection moulded silica-based ceramic cores. Qin and Pan

---

[7] investigated alumina-based ceramic core by adding silica-sol to an alumina matrix and utilizing the in situ synthesis technique. They considered cores microstructure and studied the influence of silica sol on the features of alumina-based ceramic cores. Kim et al. [8] offered a new procedure for cores fabrication that consists of the elaboration of an inorganic precursor mixture composed of silicate and metal alkoxide. The prepared ceramic core exhibited reasonable mechanical strength without shrinkage and deformation of shape. Wu et al. [9] proposed a rapid prototyping process to manufacture complex-shaped alumina-based cores by joining stereolithography with gelcasting. They applied the freeze drying process and magnesium oxide power as the mineraliser to decrease the cores shrinkage.

One of interesting approaches in ceramic cores fabrication is introduction to ceramic powder the silicone resin. Yu et al. [10] firstly coated silica composite powders by the silicon resin to prepare the ceramic cores by the dry pressing technique. They investigated the phase composition and microstructure of the ceramic cores with the sintering temperatures. Yang et al. [11] fabricated alumina-based ceramic cores with uniform microstructure by sintering ball-shaped alumina powders as the matrix and silicone resin as the precursor and binder in air atmosphere. They investigated effects of silicone resin content and sintering temperature on phase composition, microstructure and properties of the alumina-based ceramic cores. Yang et al. [12] infiltrated the pre-sintered alumina-based ceramic cores by liquid silicone resin in a vacuum. The infiltrated silicone resin was well filled in the gaps among alumina particles by forming big polymer with network structure after curing.

A few papers were published recently in the subject of the material composition for ceramic core manufacturing. Li et al. [13] fabricated the network-structured zirconium silicate by the cristobalite reaction on the surface of particles of fused quartz with nano-sized zirconium oxide. They applied the large alumina ceramic particles to reduce the shrinkage and deformation of ceramic cores during sintering. Pan et al. [14] considered the effect of zircon content, particle size distribution and sintering temperature on performance in high-temperature of silica-based ceramic cores. The results confirmed that zircon is favourable for reducing the shrinkage, improving significantly the creep resistance and flexural strength at high-temperature. Zheng et al. [15] investigated the influence of alumina content on the mechanical properties of silica-based ceramics. They determined mechanical properties at the room-temperature and high-temperature of the as-obtained silica-based ceramics. Yang et al. [16] investigated the influences of the particle size ratio and maximal sintering temperature on the mechanical and chemical leaching properties of calcium zirconate cores materials. Zhao et al. [2] analysed the effects of the sintering parameters on the leaching characteristics and microstructures of barium zirconate cores. Li et al. [1] examined influence of different silica content to alumina ceramics to improve the performance of sintered materials and make use of the low sintering temperature, high open porosity, wide application of silica-based cores and high operating temperature. Lu et al. [17] reinforced silica-based ceramic cores with short carbon fibers. The cores were shaped by injection moulding and sintered in air and nitrogen atmospheres. Kim et al. [18] applied for the ceramic core powders a mixture of fused silica with three particle size distributions, zircon flour and silicon carbide. The mixed ceramic powder was coated with a silica precursor and then dried at high temperature for 1 h.

The new technologies were developed in the manufacturing process of ceramic cores utilised in the blades casting. Li et al. [13] presented experimental results for the ceramic core fabricated by digital light processing three-dimensional printing technology, where nano-sized zirconia oxide reacted with large fused silica particles to create network-structure zirconium silicate in the re-sintering process. Such network structure highly improved the mechanical properties of the cores while keeping a high porosity. Additionally, the stable alumina in the cores increased the high-temperature mechanical strength of the ceramic cores. As the authors underlined, their approach was the first

investigation on designing the ceramic cores microstructure using stereolithography three-dimensional printing technology. Ozkan et al. [19] elaborated photocurable ceramic suspensions composed of fused silica, alumina and zirconium silicate for utilization in visible light photopolymerization. They optimized the binder compositions for the target of LCD-based ceramic 3D printing applications. Tang et al. [20] fabricated photo-curable ceramic pastes of bimodal particle size distributions with high solid loadings and manufactured porous alumina ceramic cores of complex shapes by stereolithography 3D printing method. The obtained results prove that the elaborated materials and applied method is suitable for manufacturing complex-shaped alumina cores utilised in hollow turbine blades for aircraft engines. Huang et al. [21] proposed a decomposable binder utilizing binder-jetting by dispersing various contents of zirconium basic carbonate into inorganic colloidal binder. The authors examined an influence of different zirconium basic carbonate content on the binder printability and the performance characteristics of the cores by binder-jetting.

In our approach, as the basic raw material for a cores structure the quartz glass was applied, which possesses a low thermal expansion coefficient, excellent chemical resistance with molten metal, sufficient refractoriness, resistance on thermal shock and very high softening temperature. The borosilicate glass works as means for improving the stage of cores sintering. It passes in liquid phase and attracts grains of other raw materials, which causes the increase of sintering stage and the mechanical strength of material. Zirconium silicate is an essential component in silica-based ceramic cores, which can improve their high temperature properties. It reveals low thermal expansion coefficient, low coefficient of heat conductivity and high thermal and chemical stability. The alumina in the core can improve the high-temperature strength and reduces shrinkage of the ceramic core [3,6,13,15,22–24].

The 3D printing method is considered to be suitable for fabricating ceramic cores with complex 3D geometries with high precision, short development cycle, low manufacturing cost, less material waste and unlimited design freedom without necessity of mould application. However, the high pressure injection moulding method enables formation of cores of very complicated shapes, high dimensional precision and surface quality without the need for additional finishing processes at a competitive cost in mass production, when the mould cost for one formed cores is very low. The main advantage of the high pressure injection moulding method in comparison with 3D printing is much shorter time of manufacturing cycle for one cores in optimized mass production even for very complicated shape of cores [13,20,25–27].

The aim of this paper was to develop a new material composition based on fused silica, which satisfies all requirements for cores application and a manufacturing technology with the use of the high-pressure injection moulding method for the fabrication of thin-walled long ceramic cores with high dimensional precision to be applied in multivane clusters production for turbofan jet engine.

2. Experimental

The basic raw materials for input powder of ceramic cores, i.e. quartz glass (Juropol) and borosilicate glass (TEW) were separately mechanically activated in the ball mills with the use of alumina balls to the average particle size equal to 31.5 and 20.4 μm, respectively. The alumina (325 mesh, Treibacher) and zirconium silicate (300 mesh, Ransom & Randolph) were added to the input powders without any additional treatment. The particle size analysis was made with the Mastersizer 2000 device (Malvern). Fig. 1 presents the particle size distribution of raw materials utilised for the input powders preparation. The average particle size for alumina was determined as 14.7 μm while for the zirconium silicate – 12.7 μm.

In order to develop the material composition of appropriate properties for ceramic cores fabrication, six powders were prepared of content presented in Table 1. The mass fractions of individual raw materials was chosen in the way which allows to investigate the influence of
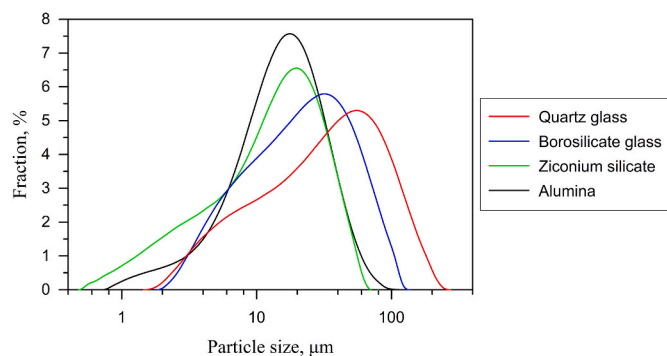
Fig. 1. The particle size distribution of raw materials.

Table 1
The material composition for ceramic cores.

Powder	Composition of powders, wt.%			
	Quartz glass (Juropol)	Borosilicate glass (TEW)	ZrSiO$_4$ (300 mesh), (Ransom & Randolph)	Al$_2$O$_3$ (325 mesh), (Treibacher)
1	70.0	5.0	13.0	12.0
2	67.0	8.0	13.0	12.0
3	64.0	11.0	13.0	12.0
4	73.0	8.0	10.0	9.0
5	70.0	8.0	13.0	9.0
6	70.0	11.0	10.0	9.0

Fig. 2. The debinding and sintering curve for beams and cores.

increasing the borosilicate glass content and decreasing the zirconium silicate and alumina contents in input powders for material strength.

The six feedstocks for injection moulding were carried out with the use of the GC-MIX-12/13 heated mixer (Goceram AB). The thermo-plasticizer Siliplast HS (Zschimmer & Schwarz GmbH & Co KG) was placed into heated stirrer together with separating added input powders 1–6. The fraction of thermoplasticizer in feedstock was equal to 21.0 wt % for all materials. The chosen thermoplasticizer Siliplast HS, based on modified polyalcohol was characterised by the low melting temperature reaching 115 °C and solidification shrinkage equal to 14.3 vol %. The feedstocks were kneaded for approximately 45 min at the temperature of 170 °C. Due to geometry of feeding screw in the high-pressure injection moulding machine, obtained materials 1–6 were broken up with the use of crusher device ML–SC–2 (Ming Lee) and sieve with sieves of dimension 1.5 and 4 mm.

The process of beams forming from materials 1–6 was performed with the use of the laboratory high-pressure injection moulding machine BOY XS. The two cavity injection mould allowed forming 60 mm length beams with diameter of 6 mm.

The water soluble thermaplasticizer was chosen as its components are environmentally friendly and arising in debinding process waste water is well biodegradable. The channels that are opened up by the water debinding allow the residual binder to escape without damage to the microstructure of the cores. The binder remaining guarantees the adequate strength necessary for transport cores to the furnace and the residual binder is removed from the cores by pyrolysis during the sintering process. Application of soluble in water thermoplasticizer Siliplast HS required realizing the two stage debinding. Immersion of the beams in water bath for 8 h at temperature of 70 °C allowed to get rid of about 60% of thermoplasticizer and the remaining part was removed with thermal process. The electrical furnace FCF 14/160 M (Czylok) with debinding function was imposed, which was equipped with two fans enabling delivery of preheated air and its pull-off from the furnace chamber. Fig. 2 presents the thermal debinding and sintering curve for beams and cores.

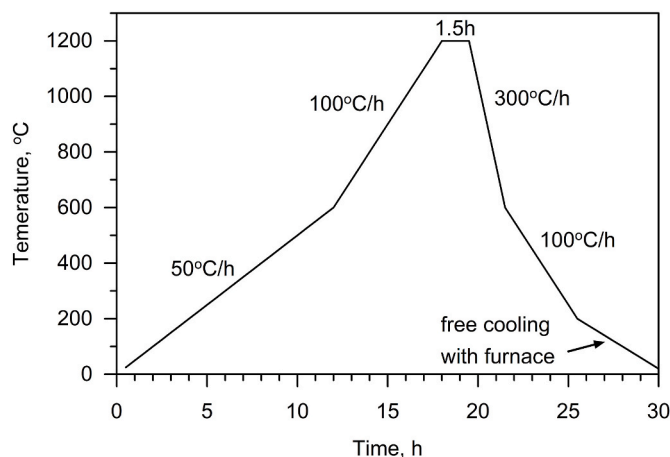The parameters of sintered materials characterizing the degree of

sintering as the apparent density, the open porosity and the water absorbability were determined with method based on Archimedes' law and boiling the samples until they become saturated with water. The bending strength was determined according to standard *P*N-EN 60672–2:2002 by three point method on sintered beams of diameter 6.0 mm and length of 60.0 mm with the use of the special constructed device, which measured the bending force *F*. The distance between support points *l* was equal to 50 mm and the bending strength was calculated with accordance to standard as $(8 \cdot F \cdot l)/(\pi \cdot d^3)$. The surface roughness was tested using a MarSurf PS 10 profilometer (Mahr Inc.). Evaluation of the thermal expansion coefficient in range of temperatures from 20 to 1300 °C was carried out with use of the high temperature dilatometer (BÄHR-Gerätebau GmbH). The loss of core weight was determined after 5 h of etching at 110 °C in a water solution with potassium hydroxide, which was treated as laboratory test of cores etching. The XRD phase analyses of sintered materials were performed with the use of X'Pert PRO diffractometer with CuKα radiation for 2θ ranging between 10° and 90°. The distribution of the pore size in the sintered material was determined using the mercury porosimetry method on a Micromeritics AUTO PORE IV 9500. The microstructure of fracture surface of cores was observed using a Hitachi S–3400 N scanning electron microscope with Energy Dispersive X-Ray Spectrometer (EDS), which allowed to make a chemical analysis of micro surfaces.

On the basis of the obtained results, the material of optimal properties for core fabrication was selected. In the process of cores forming from selected material, the high pressure injection moulding machine Sumitomo Demag was used, which is characterised by the injection mould contact force 600 kN, the maximal injection pressure 2024 bar and the maximal injecting volume 168 cm^3.

During the mould design for ceramic cores forming, two the most important aspects were taken into account. To receive high quality cores, it was necessary to protect them from deformation on the stage of their fabrication. The extraction system of injected cores was designed in the special manner. The core removal after injection and preliminary cooling in cavity was made by hand with turning the lever with the use of five extractors. Three of extractors of the diameter of 6 mm were situated at the two end and in the middle of the main part of core while two extractors of the diameter of 3 mm were placed at the narrow ends of core. Putting in motion at once all these five extractors, allow to remove core without any deformation. The second aspect during the mould designing was connected with the shape and dimension of the restrictor, which allow the flowing feedstock to fill in the cavity. In order to fully fill in the whole long cavity as in the case of this core, without any material burning, the shape of restrictor was modified as more oval and the size was increased for about 20% in comparison with typical restrictor for plastic injection.

The thin-walled long cores were formed by the high-pressure injection moulding method from material 3. The cores were initially injected at temperature ranging from 150 to 170 °C in order to determine the optimal injection temperature so that avoid any defect and imperfection in injected cores. Finally, the optimal temperature of the cylinder and nozzle in the cores forming process, was set as 160 °C, with a tolerance of 5 °C. The pressure of injection was set as 1000 bar, while the velocity of injection was equal to 38.7 cm^3/s. In order to protect cores from deformation the temperature of the mould was decreased to 40 °C, and the time that the cores stay in mould was increased to 360 s. As a result of the material composition and set parameters during injection process, the very favourable value of less than 0.1% of material shrinkage during the formation process was observed.

In order to receive the high quality cores after sintering, the time of water debinding was necessary to select in the experimental way. Therefore, the cores were immersed in water bath at temperature of 70 °C for 2, 4, 6, 8 and 10 h. The remaining part of thermoplasicizer was removed during the thermal process combined with the cores final sintering at 1200 °C. All cores debinded in water for 2, 4 and 6 h after the final sintering were covered on the surface of the biggest cross-section with the bubbles or fracture. These defects appeared as a result of not enough thermoplasticizer removal at the first stage in water bath. However, the surfaces of cores, debinded for 8 and 10 h, were smooth and free of any defects. Obviously, there was no point in increasing the time of cores immersing in the water bath because this caused the cores destruction as a result of too much of binder removal, which must hold the shape of cores in the process of thermal debinding. Fig. 3 presents the cores made from material 3 after the final sintering.

The cores after sintering were measured in three axes to evaluate the dimensional accuracy with the use of Mitutoyo Crysta ApexC7106 coordinate measuring machine. In the measurement process a tilt-rotary head and two measuring modules were utilised together with prepared programme that concludes all elements (points, distances, sections and chords) which were indicated by the core designer and for which the special tolerance requirements were imposed.

3. Results and discussion

Table 2 presents the results of the material properties after sintering at 1200 °C. The increase of borosilicate glass content at the expense of quartz glass in the input powders 2 and 3 in comparison with powder 1 at the same quantity of zirconium silicate and alumina caused an increase of density stage, bending strength, surface roughness and the shrinkage but the coefficient of thermal expansion and material weight loss in the etching test were decreased. This improvement of material

Fig. 3. The cores debinded for 8 h after the final sintering.

properties as a result of the borosilicate glass content increase was due to passing the borosilicate glass in the liquid phase and attracting grains of other raw materials. In the case of materials 2, 4 and 5, the borosilicate glass content was set at the same 8.0 wt% level, but the quantity of zirconium silicate and alumina changed. The 3.0 wt% reduction of zirconium silicate and alumina contents in material 4 in comparison with material 2 caused the slight decrease of apparent density, bending strength and shrinkage and increase of the coefficient of thermal expansion while the surface roughness and the weight loss in the etching test were on the same level. Almost the same changes in the material properties was created by the 3.0 wt% reduction of alumina content in material 5 in comparison with material 2. However the decease of mechanical strength was on the level of 2.7%. The positive influence of the increase of borosilicate glass content in material composition was also confirmed in the case of material 6 when comparing them to material 4. The 3.0 wt% increase of borosilicate glass at zirconium silicate and alumina contents equal to 10.0 and 9.0 wt%, respectively in material 6 brought almost 45.4% increase of mechanical strength and 18.4% shrinkage increase. However, the apparent density, the surface roughness, the coefficient of thermal expansion and the weight loss in the etching test were on the same level. It should be underlined that the surface roughness of ceramic cores are mainly affected by the quality of mould cavity. Therefore, the cavity of mould, which shapes the cores, were carefully polished. Moreover, the surface roughness of cores is also influenced by the distribution of particle size of input powders composed of different volume of raw materials, situated near boundary of mould cavity. In the process of cores forming by high pressure injection moulding method, segregation of coarse and fine particles can lead to small differences in surface roughness of cores, as in this case. Therefore, the surface roughness of all materials were measured in order to verify whether the acceptable level less than 3 μm were achieved. On the base of materials properties presented in Table 2 the material 3 was chosen as revealing the optimal parameters for cores fabrication. The material 3 is characterised by the highest stage of densification and bending strength as well as the lowest coefficient of thermal expansion among others materials.

The selected material 3 for cores manufacturing reveals the suitable apparent density (1.72 g/cm^3) and the open porosity (32.32%), which represents an expected level. The fabricated cores will be formed in the wax casting model and assembled in the casting mould as a result of obtained mechanical strength equal to 25.8 MPa. The high quality of mapping the internal surface of the blade channels after casting will be ensured by the surface roughness equal to 2.3 μm. The thermal shock resistance and the dimensional stability of cores at the temperature of liquid alloy casting will be ensured as the coefficient of thermal expansion is equal to $3.52.10^{-6}$ 1/K. The relatively low value of material shrinkage after sintering under 1.9% will protect the core deformation in the sintering stage. The process of core etching after blade casting in production conditions will run smoothly as the mass loss for material 3 after 5 h of etching at 105 °C in water potassium solution reached 54.5%

Fig. 4 presents XRD pattern of materials after sintering at 1200 °C with the dwell time equal to 1.5 h. According to the XRD patterns, all materials reveal presence of ZrSiO$_4$, Al$_2$O$_3$ and cristobalite phases. However, intensity of peaks is higher and better built in material structure for materials of greater borosilicate glass content. In the case of material 3 for cores manufacturing the intensity of peaks of all detected phases are the highest.
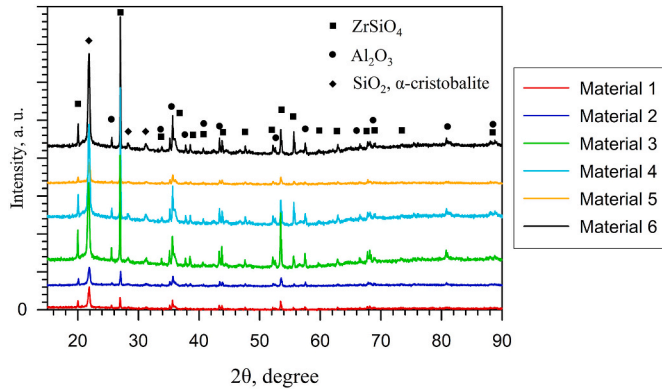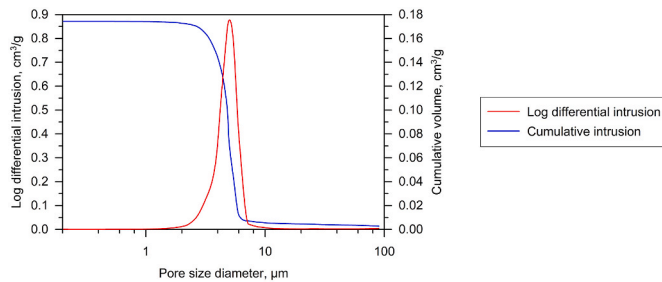
Fig. 5 presents the differential and cumulative curve as a function of the pore size diameter for material 3. The peak abscissa of differential curve points at the mean diameter of pore size, which in the case of material 3 is equal to 4.8 μm. However, the cumulative curve gives information on the cumulative pores volume, which for material 3 is equal to 179 mm^3/g. Such value should ensure the easy etching of material 3.

Fig. 6 presents photos of fracture surface of material 3 after sintering, in which large particles were observed with dimension from 20 to 50 μm and a structure composed of fine particles of size less than a few
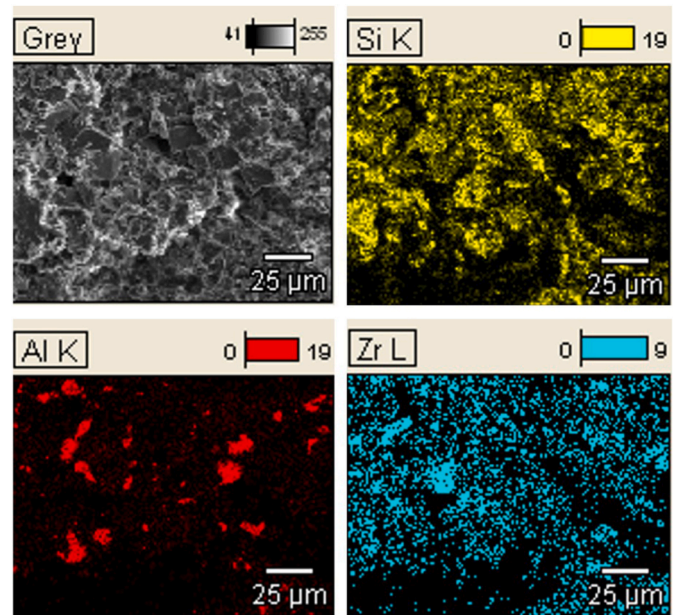
Table 2
The materials properties after sintering at 1200 °C.

Material	Water absorbability, %	Apparent density, g/cm³	Open porosity, %	Bending strength, MPa	Surface roughness, μm	Coefficient of thermal expansion, 1/K	Shrinkage, %	Weight loss in etching test, %
1	21.02	1.66	34.91	11.6	1.5	4.47·10⁻⁶	1.12	72.8
2	20.24	1.68	34.03	18.4	2.0	3.79·10⁻⁶	1.40	62.8
3	18.76	1.72	32.32	25.8	2.3	3.52·10⁻⁶	1.89	54.5
4	20.70	1.64	33.88	16.3	2.1	3.91·10⁻⁶	1.14	62.9
5	20.79	1.65	34.33	17.9	2.0	3.02·10⁻⁶	1.18	65.3
6	20.13	1.65	33.18	23.7	2.1	3.74·10⁻⁶	1.35	62.9

Fig. 4. XRD patterns of the materials sintered at 1200 °C.

Fig. 5. The differential and cumulative curve of pore size distribution of material for core fabrication.
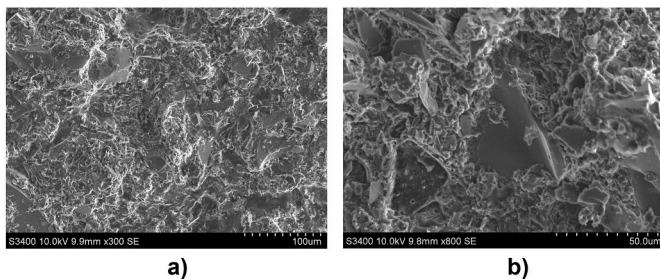
Fig. 6. The microstructure of fracture surface of optimal material 3 for core fabrication.

Fig. 7. The plot of distribution of chosen elements on the fracture surface of optimal material 3.

micrometres. The distribution of large particles is homogenous, and the visible voids and pores are due to the lack of complete compaction of the material. Such microstructure of cores should reveal the ease of their etching, which was confirmed by result of etching test in laboratory conditions.

Fig. 7 presents the map of distribution of chosen elements on the fracture surface of optimal material 3. Distribution of Si element is homogeneous, but visible places without yellow colour are the site, where pores and voids are situated. Al element is also quite spread in the surface but some bigger concentrations of this element are also visible, which point on appearance of alumina particles in material. The same state is noticeable with distribution of Zr element, which was added to the material in the form of zirconia silicate.

The optimal material 3 for cores manufacturing was additional sintered at 1250 and 1300 °C to investigate the change of cores properties at higher temperature. The apparent density increased to 1.77 and 1.84 g/cm³ and the open porosity decreased to 30.89 and 28.19%, respectively for material sintered at 1250 and 1300 °C, which was related with obtainment the higher stage of material density. As a result of higher density stage the bending strength reached 26.7 and even 27.6 MPa, respectively for material sintered at 1250 and 1300 °C. However, such improvement of mechanical strength takes places at a cost of higher shrinkage of material which achieved 2.59 and 3.31% for material sintered at 1250 and 1300 °C, accordingly. Such elevated shrinkage cannot be accepted for cores manufacturing because it causes cores deformation and it is very possible that dimensions of cores sintered at higher temperature will exceed the tolerance field. The values of weight loss in the etching test of material sintered at 1250 and 1300 °C are also not desirable, as they reached 49.2 and 46.6%, respectively. Such cores could reveal worse etching properties at productive conditions in autoclave and the possible application of additional cycle of cores removal can lead to the multivane clusters degradation. The values of surface roughness and coefficient of thermal expansion for material sintered at elevated temperatures were only insignificantly higher, which made evidence that these parameters were stable.

The desirable properties of material for ceramic cores are ensured by

the applying the special designed composition of raw materials and their particle size distributions. Application of the quartz glass as the basic raw material for a cores structure ensured the material for cores a low thermal expansion coefficient, good chemical resistance with molten alloy, sufficient refractoriness and resistance on thermal shock. The borosilicate glass improved the stage of cores sintering by passing in liquid phase and attracting grains of other raw materials, which caused the increase of sintering stage and the mechanical strength of material. Zirconium silicate similar to quartz glass ensured the material for cores the low thermal expansion coefficient and it improved the high temperature properties of cores such as the high thermal and chemical stability. The alumina in the cores material improved the high-temperature strength and reduces shrinkage of the ceramic core. The particle size distributions of raw materials has significant importance since great particles must be surrounded with smaller ones and such microstructure after cores sintering, together with liquid phase derived from borosilicate glass, ensures greater value of bending strength at open porosity less than 35% and appropriate pore size distribution. The high mechanical strength of cores enables their forming in the wax casting model and assembling in the casting mould and the appropriate value of open porosity and pores size ensures the cores etching after blade casting in production conditions. Reduction of cores shrinkage was performed by application of alumina and compaction of raw materials particles, which after sintering also decreases the shrinkage. The less value of cores shrinkage, protected cores from deformation and ensured their dimension stability.

Fig. 8a presents the measurement process of the ceramic core on a coordinate measurement machine while Fig. 8b exhibits the program window during operation with measured cross-sections of ceramic core. The measurement process of ceramic core presented in Figs. 3 and 8a consists of determination the coordinates of eight points, nine sections, nine chords and four distances, which were located in whole surface of core in order to eliminate core that exceed even one dimension. The highest deviation for all measured cores from the nominal dimension was occurred in the case of the widest chord, which was equal to -0.085 mm and represents the one-third range of tolerance. The trend in core thickness can be observed, which is related with the distance from the injection point. The cores thickness in the nearest part of injection point includes in the negative range of the tolerance field. In the middle part of cores, the deviation from nominal dimension is almost unnoticeable while at the furthest part from injection points, the cores thickness falls in the positive range of the tolerance field. This trend in cores thickness can be explained by the slight loss of closing force of mould in the high-pressure injection moulding process, which also increases in the region of injection point and weakens at the end of injected core.

On the base of the results analysis for cores measurements, one can conclude that dimension of cores falls within the tolerance field, which is as an effect of application the high pressure of injection, lower mould temperature and extended stay time of injected cores in mould. The high injection pressure allowed to obtain superior density in whole cavity volume, which avoided cores deformation during sintering process. Decreasing the mould temperature and increasing time at which cores stay in the mould protected cores from deformation at forming stage and eliminated expensive equipment for cores straightening.

4. Conclusions

The material elaborated in this paper for cores fabrication, which was composed of 64.0 wt% quartz glass, 11.0 wt% borosilicate glass, 13.0 wt% zirconium silicate (300 mesh) and 12.0 wt% alumina (325 mesh), satisfies rigorous requirements concerning its application for manufacturing multivane clusters for turbofan jet engine.

The increase of borosilicate glass content at the expense of quartz glass in the input powders at the same quantity of zirconium silicate and alumina caused an increase of density stage, bending strength, surface roughness and the shrinkage but the coefficient of thermal expansion
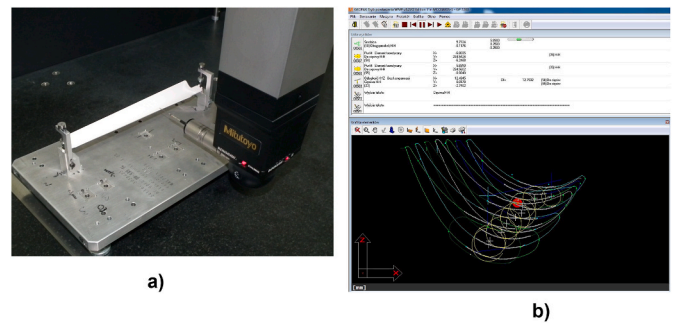
Fig. 8. The ceramic core in the measurement process on the CMM (a), the program window with measured cross-sections of ceramic core (b).

and material weight loss in the etching test were decreased. The reduction of zirconium silicate and alumina content caused the slight decrease of apparent density, bending strength and shrinkage and increase of the coefficient of thermal expansion while the surface roughness and the weight loss in the etching test were on the same level. Nearly the same changes in the material properties was created by the reduction of alumina content.

The developed technology based on high-pressure injection moulding method allowed to obtain thin-walled long ceramic cores with the high dimensional precision, which can be utilised in production of such precise and responsible multivane clusters for turbofan jet engine. This aim was realised as a result of application of the high injection pressure, decreasing the mould temperature and extending the stay time of injected cores in the mould, which protected cores from deformation and eliminated the use of expensive equipment for cores straightening.

CRediT authorship contribution statement

Magdalena Gromada: Conceptualisation, Methodology, Formal analysis, Investigation, Writing - original draft. Adam Świeca: Methodology, Formal analysis, Investigation, Resources. Rafał Cygan: Investigation, Validation, Writing - review & editing, Supervision.

Declaration of competing interest

The authors declare that they have no known competing financial interests or personal relationships that could have appeared to influence the work reported in this paper.

Acknowledgments

References

[1] H. Li, Y. Liu, Y. Liu, Q. Zeng, J. Liang, Silica strengthened alumina ceramic cores prepared by 3D printing, J. Eur. Ceram. Soc. 41 (2021) 2938–2947.

[2] Z. Zhao, Z. Yang, Z. Yin, B. Chen, J. Yu, Z. Ren, G. Yu, G. Zhang, Investigation of the properties and leaching characteristics of ceramic cores fabricated using BaZrO$_3$ as the raw material, Mater. Chem. Phys. 272 (2021), 124925.

[3] M. Gromada, A. Świeca, M. Kostecki, A. Olszyna, R. Cygan, Ceramic cores for turbine blades via injection moulding, J. Mater. Process. Technol. 220 (2015) 107–112.

[4] L.-Y. Wang, M.-H. Hon, The effect of cristobalite seed on the crystallization of fused silica based ceramic core – a kinetic study, Ceram. Int. 21 (1995) 187–193.

[5] A. Kazemi, M.A. Faghihi-Sani, H.R. Alizadeh, Investigation on cristobalite crystallization in silica-based ceramic cores for investment casting, J. Eur. Ceram. Soc. 33 (2013) 3397–3402.

[6] A. Kazemi, M.A. Faghihi-Sani, M.J. Nayyeri, M. Mohammadi, M. Hajfathalian, Effect of zircon content on chemical and mechanical behavior of silica-based ceramic cores, Ceram. Int. 40 (2014) 1093–1098.

[7] Y. Qin, W. Pan, Effect of silica sol on the properties of alumina-based ceramic core composites, Mater. Sci. Eng., A 508 (2009) 71–75.

[8] E.-H. Kim, G.-H. Cho, Y.S. Yoo, S.M. Seo, Y.-G. Jung, Development of a new process in high functioning ceramic core without shape deformation, Ceram. Int. 39 (2013) 9041–9045.

[9] H. Wu, D. Li, Y. Tang, B. Sun, D. Xu, Rapid fabrication of alumina-based ceramic cores for gas turbine blades by stereolithography and gelcasting, J. Mater. Process. Technol. 209 (2009) 5886–5891.

[10] J. Yu, Z. Yang, C. Li, K. Deng, Z. Ren, Investigation on properties of the silica ceramic cores for the hollow blades prepared by the conversion of the silicon resin, Key Eng. Mater. 680 (2016) 267–271.

[11] Z. Yang, Z. Zhao, J. Yu, Z. Ren, S. Ma, Z. Wang, Effect of silicone resin as precursor and binder on the properties of alumina based ceramic cores using ball-shaped powders, Ceram. Int. 45 (2019) 2170–2177.

[12] Z. Yang, Z. Yin, Y. Shi, Z. Zhao, X. Fei, J. Yu, Z. Ren, G. Yu, Microstructure and bending strength improvement of alumina-based ceramic cores by liquid silicone resin infiltration, Mater. Chem. Phys. 239 (2020), 122041.

[13] Q. Li, J. Liang, Y. Zhang, J. Li, Y. Zhou, X. Sun, Fused silica ceramic core based on network-structured zircon design via 3D printing, Scripta Mater. 208 (2022), 114342.

[14] Z. Pan, J. Guo, S. Li, J. Xiong, A. Long, Experimental study on high temperature performances of silica-based ceramic core for single crystal turbine blades, Ceram. Int. 48 (2022) 548–555.

[15] W. Zheng, J.-M. Wu, S. Chen, C.-S. Wang, C.-L. Liu, S.-B. Hua, K.-B. Yu, J. Zhang, J. X, Zhang, Y.-S. Shi, Influence of Al$_2$O$_3$ content on mechanical properties of silica-based ceramic cores prepared by stereolithography, J. Adv. Ceram. 10 (6) (2021) 1381–1388.

[16] Z. Yang, K. Li, S. Ma, J. Yu, Z. Ren, Preparation, mechanical, and leaching properties of CaZrO$_3$ ceramic cores, Int. J. Appl. Ceram. Technol. 18 (2021) 1490–1497.

[17] G. Lu, Y. Chen, Q. Yan, H. Zhan, P. Mao, D. Liu, Investigation of microstructure and properties in short carbon fiber reinforced silica-based ceramic cores via atmosphere sintering, J. Eur. Ceram. Soc. 41 (2021) 7339–7347.

[18] E.-H. Kim, H.Y. Park, C. Lee, J.B. Park, S.C.H. Yang, Y.-G. Jung, Single crystal casting of gas turbine blades using superior ceramic core, J. Mater. Res. Technol. 9 (2020) 3348–3356.

[19] B. Ozkan, F. Sameni, F. Bianchi, H. Zarezadeh, S. Karmel, D.S. Engstrøm, E. Sabet, 3D printing ceramic cores for investment casting of turbine blades, using LCD screen printers: the mixture design and characterisation, J. Eur. Ceram. Soc. 42 (2022) 658–671.

[20] W. Tang, T. Zhao, R. Dou, L. Wang, Additive manufacturing of low-shrinkage alumina cores for single-crystal nickel-based superalloy turbine blade casting, Ceram. Int. 48 (2022) 15218–15226.

[21] S. Huang, C. Ye, H. Zhao, Z. Fan, Additive manufacturing of thin alumina ceramic cores using binder-jetting, Addit. Manuf. 29 (2019), 100802.

[22] G.S. An, S.W. Choi, T.G. Kim, J.R. Shin, Y.-I. Kim, S.-C. Choi, Y.-G. Jung, Amino-functionalization of colloidal alumina particles for enhancement of the infiltration behavior in a silica-based ceramic core, Ceram. Int. 43 (2017) 157–161.

[23] Y.-H. Kim, J. Yeo, S.-C. Choi, Shrinkage and flexural strength improvement of silica-based composites for ceramic cores by colloidal alumina infiltration, Ceram. Int. 42 (2016) 8878–8883.

[24] J.J. Liang, Q.H. Lin, X. Zhang, T. Jin, Y.Z. Zhou, X.F. Sun, B.G. Choi, I.S. Kim, J. H. Do, C.Y. Jo, Effects of alumina on cristobalite crystallization and properties of silica-based ceramic cores, J. Mater. Sci. Technol. 33 (2017) 204–209.

[25] X. Wang, Y. Zhou, L. Zhou, X. Xu, S. Niu, X. Li, X. Chen, Microstructure and properties evolution of silicon-based ceramic cores fabricated by 3D printing with stair-stepping effect control, J. Eur. Ceram. Soc. 41 (2021) 4650–4657.

[26] V. Piotter, W. Bauer, R. Knitter, M. Mueller, T. Mueller, K. Plewa, Powder injection moulding of metallic and ceramic micro parts, Microsyst, Technol. 17 (2011) 251–263.

[27] R. Wick-Joliat, M. Tschamper, R. Kontic, D. Penner, Water-soluble sacrificial 3D printed molds for fast prototyping in ceramic injection molding, Addit. Manuf. 48 (2021), 102408.